Forschungsbericht 2019-16

The DLR Project Land-Based and Onboard Wake Systems L-bo*ws*

Frank Holzäpfel, Carsten Schwarz
(Projektleiter und Editoren)

Deutsches Zentrum für Luft- und Raumfahrt
Oberpfaffenhofen, Braunschweig und Hamburg

DLR Deutsches Zentrum für Luft- und Raumfahrt

Wirbelschleppe, L-bows, hybride LES, Landung, Plate Line, Wirbeleinflug, Vorhersage, Warnung, Lidar

DLR Forschungszentren Oberpfaffenhofen, Braunschweig und Hamburg
Frank Holzäpfel, Carsten Schwarz (Projektleiter und Editoren)

(Veröffentlicht in englischer Sprache)

Das DLR Projekt Land-Based and Onboard Wake Systems – L-bo*ws*

DLR-Forschungsbericht 2019-16, 2019, 189 Seiten, 112 Bilder, 27 Tabellen, 336 Literaturstellen, 39,00 € zzgl. MwSt.

Das Projekt Land-Based and Onboard Wake Systems (L-bows) setzte sich die bodengebundene Vorhersage optimierter Wirbelschleppen-Sicherheitsabstände und die flugzeuggestützte Vermeidung gefährlicher Wirbelschleppeneinflüge in allen Flugphasen auf taktischen und prätaktischen Zeitskalen zum Ziel. Hierzu wurden innovative Methoden entwickelt, um die Effizienz dieser Vorhersagesysteme maßgeblich zu steigern und damit deren Wirtschaftlichkeit zu erhöhen. Um den Luftverkehr effektiv, Kapazitäten schonend und sicher zu planen und zu führen, kommt der korrekten Vorhersage des Absinkens, der Lateraldrift und des Zerfalls von Wirbelschleppen und den daraus resultierenden Mindestabständen zwischen Flugzeugen eine immer größere Bedeutung zu und zwar sowohl in Flughafennähe als auch im Reiseflug. Die durchgeführten Arbeiten widmen sich der Initiative von ICAO, FAA und EUROCONTROL zur Rekategorisierung der Wirbelschleppenabstände, den erwarteten Kapazitätsengpässen der Landebahnen großer europäischer Flughäfen, den reduzierten vertikalen Mindestabständen im Reiseflug, der wachsenden Diversifizierung von Flugzeugtypen von Very Light Jets bis zu Super Heavy Aircraft sowie der in SESAR und NextGen angestrebten Liberalisierung des Luftraums.

Wake vortex, L-bows, hybrid LES, landing, plate line, encounter, prediction, warning, lidar

DLR Research Centres Oberpfaffenhofen, Braunschweig and Hamburg
Frank Holzäpfel, Carsten Schwarz (Project Managers and Editors)

The DLR Project Land-Based and Onboard Wake Systems – L-bo*ws*

DLR-Forschungsbericht 2019-16, 2019, 189 pages, 112 figs., 27 tabs., 336 refs., 39.00 €

In order to plan and control air traffic effectively and safely the correct prediction of wake vortex descent, lateral drift and decay as well as the resulting minimum separations between aircraft have become increasingly important in the vicinity of airports as well as in cruise. The DLR project Land-Based and Onboard Wake Systems (L-bows) aimed at the ground-based prediction of optimized wake vortex separation distances and the airborne avoidance of hazardous wake encounters in all flight phases. Innovative methods have been developed to increase the efficiency of prediction systems in order to significantly increase their economic benefits. The project addressed the initiative of ICAO, FAA, and EUROCONTROL for the recategorisation of wake vortex related aircraft separation distances, the expected capacity gaps of the runways of the major European airports, the reduced vertical separation minima in cruise flight, the growing diversification of aircraft types from very light jets to super heavy aircraft as well as the target in SESAR and NextGen of further liberalisation of airspace.

Forschungsbericht 2019-16

The DLR Project Land-Based and Onboard Wake Systems – L-bo*ws*

Frank Holzäpfel, Carsten Schwarz
(Projektleiter und Editoren)

Deutsches Zentrum für Luft- und Raumfahrt
Oberpfaffenhofen, Braunschweig und Hamburg

189 Seiten
112 Bilder
27 Tabellen
336 Literaturstellen

Deutsches Zentrum
DLR für Luft- und Raumfahrt

Forschungsbericht 2019-16

The DLR Project Land-Based and Onboard Wake Systems L-bo*ws*

Collection of Reports

Das DLR Projekt Land-Based and Onboard Wake Systems L-bo*ws*

Sammlung von Berichten

Frank Holzäpfel, Carsten Schwarz
Project Managers and Editors

Deutsches Zentrum
DLR für Luft- und Raumfahrt

The DLR Project Land-Based and Onboard Wake Systems – L-bo*ws*

In order to plan and control air traffic effectively and safely the correct prediction of wake vortex descent, lateral drift and decay as well as the resulting minimum separations between aircraft have become increasingly important in the vicinity of airports as well as in cruise. The DLR project Land-Based and Onboard Wake Systems (L-bo*ws*) aimed at the ground-based prediction of optimized wake vortex separation distances and the airborne avoidance of hazardous wake encounters in all flight phases. Innovative methods have been developed to increase the efficiency of prediction systems in order to significantly increase their economic benefit. The project addressed the initiative of ICAO, FAA, and EUROCONTROL for the recategorisation of wake vortex related aircraft separation distances, the expected capacity gaps of the runways of the major European airports, the reduced vertical separation minima in cruise flight, the growing diversification of aircraft types from very light jets to super heavy aircraft as well as the target in SESAR and NextGen of further liberalisation of airspace.

Das DLR Projekt Land-Based and Onboard Wake Systems – L-bo*ws*

Das Projekt Land-Based and Onboard Wake Systems (L-bo*ws*) setzte sich die bodengebundene Vorhersage optimierter Wirbelschleppen-Sicherheitsabstände und die flugzeuggestützte Vermeidung gefährlicher Wirbelschleppeneinflüge in allen Flugphasen auf taktischen und prätaktischen Zeitskalen zum Ziel. Hierzu wurden innovative Methoden entwickelt, um die Effizienz dieser Vorhersagesysteme maßgeblich zu steigern und damit deren Wirtschaftlichkeit zu erhöhen. Um den Luftverkehr effektiv, Kapazitäten schonend und sicher zu planen und zu führen, kommt der korrekten Vorhersage des Absinkens, der Lateraldrift und des Zerfalls von Wirbelschleppen und den daraus resultierenden Mindestabständen zwischen Flugzeugen eine immer größere Bedeutung zu und zwar sowohl in Flughafennähe als auch im Reiseflug. Die durchgeführten Arbeiten behandeln die Initiative von ICAO, FAA und EUROCONTROL zur Rekategorisierung der Wirbelschleppenabstände, die erwarteten Kapazitätsengpässe der Landebahnen großer europäischer Flughäfen, die reduzierten vertikalen Mindestabständen im Reiseflug, die wachsende Diversifizierung von Flugzeugtypen von Very Light Jets bis zu Super Heavy Aircraft sowie die in SESAR und NextGen angestrebte Liberalisierung des Luftraums.

Table of Contents

1 Introduction

The DLR Project Land-Based and Onboard Wake Systems (L-bo*ws*) was accomplished in the timeframe from April 2014 to March 2017 with contributing teams from the Institute of Aerodynamics and Flow Technology, the Institute of Air Transportation Systems, the Institute of Atmospheric Physics, the Institute of Flight Guidance, the Institute of Flight Systems and Flight Experiments.

L-bo*ws* aimed at the ground-based prediction of optimized wake vortex separation distances and the airborne avoidance of hazardous wake encounters in all phases of flight. In order to plan and control air traffic effectively and safely, the correct prediction of wake vortex descent, lateral drift and decay as well as the resulting minimum separations between aircraft have become increasingly important in the vicinity of airports as well as in cruise. For these purposes innovative methods have been developed to increase the efficiency of prediction systems in order to significantly increase their economic benefit.

With this the project addressed the initiative of ICAO, FAA, and EUROCONTROL for the re-categorisation (RECAT) of wake vortex related aircraft separation distances, the increasing capacity gaps of the runways of the major European airports, the reduced vertical separation minima in cruise flight, the growing diversification of aircraft types from very light jets to super heavy aircraft as well as the target in SESAR and NextGen of the further liberalisation of airspace.

The L-bo*ws* project structure is displayed in Figure 1. The project was split into the main work packages coordination, ground-based systems and airborne systems. The articles in this collection are numbered following the work package numbers shown in Figure 1. For example the article numbered 1.1.3 corresponds to the third article related to work package 1.1. At least one article per work package with a maximum of three articles per work package are included in this collection. However, an impressive list of publications emerging from the project is found in the appendix which is complementing and exceeding by far the current collection.

One goal of the ground-based approach was the development of methods for pre-tactical predictions of safe wake vortex safety separations for the entire air traffic in Europe (see article 1.4). These methods can be used to optimize the planned flight routes including meteorological and traffic considerations. They also enable the integration of further conflicts like thunderstorms or volcanic ash and the related cascade effects in the complete air-traffic network.

Measurements and simulations reveal that during approach and landing aircraft frequently come close to or even encounter wake vortices. Actually, the probability to encounter wake vortices is the highest during final approach, because there wake vortices cannot descend unrestrictedly, but tend to rebound driven by the interaction with the ground. Under weak crosswind conditions these vortices may hover next to the flight path of the follower aircraft. So a vital goal of L-bo*ws*'s ground-based approach was to answer the fundamental question: „How can the current landing procedures be safe despite the obviously high number of close and sustained wake vortices?" A convincing answer to this question, which can be found in

articles 1.2.1 and 1.2.2, is prerequisite to the design and installation of an optimal wake vortex advisory system.

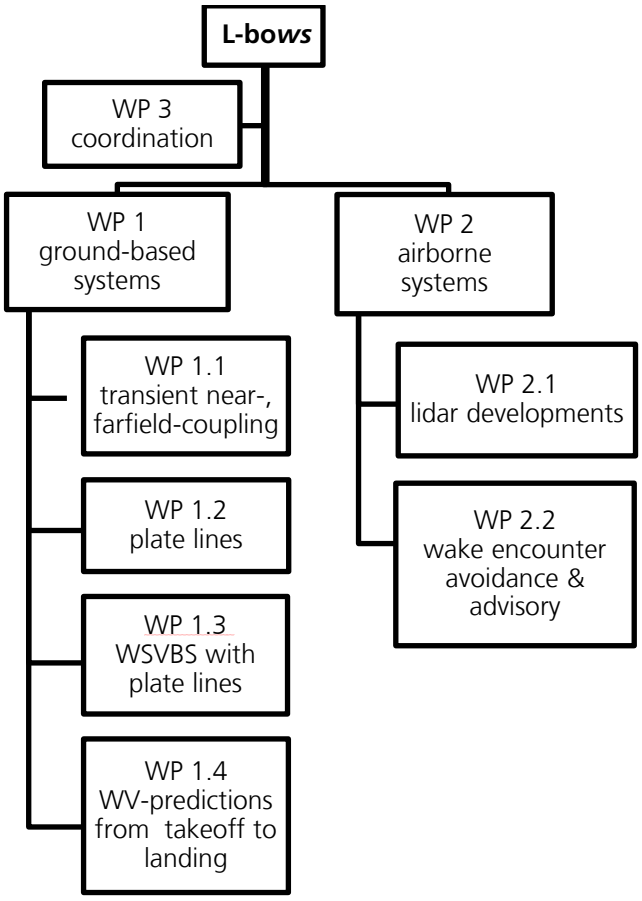

Figure 1: Project structure.

Other project targets were related to the patented plate line concept for the acceleration of wake vortex decay during final approach (see article 1.2.1). These targets comprise the optimization of the plate line dimensions for aircraft of different sizes (Anton et al., 2017), an improved understanding to which extent the accelerated vortex decay also results in reduced encounter severity in terms of aircraft reaction and pilot acceptance (article 1.2.2), and a study illustrating to which extent the installation of plate lines may accommodate more actual landings per time unit or reduce arrival delays (article 1.3).

Another goal connected to the final approach was the further development of a numerical simulation system covering vortex evolution from the flow around the aircraft until final decay for transient aircraft manoeuvres like landing and touchdown. The first step, described in article 1.1.1, consists of simulations of the flow around a realistic transport aircraft configuration in several altitudes above ground effect and, alternatively, a simplified touchdown maneuver using unsteady simulations. Remarkably, the subsequent large eddy simulations with landing gear (article 1.1.2) reveal the formation of a strong coherent vortex

modifying the interaction and longevity of the multiple vortex system in ground-proximity. The specific role of this vortex could be verified by lidar measurement data collected at Vienna airport.

The activities aiming at the airborne tactical avoidance of encounters in all phases of flight followed two different but connected strategies. On the one hand, the WEAA (wake encounter avoidance and advisory) system for the prediction and warning of imminent encounters and the provision of minimal evasion manoeuvres was further developed and demonstrated in two flight test campaigns involving the DLR Falcon and ATRA research aircraft as well as regular air traffic (article 2.2).

The other goal was the development and construction of prototypical elements of a lidar system for the airborne detection of wake vortices and clear air turbulence (article 2.1). Good measurement accuracy of the novel near-field UV direct-detection Doppler wind lidar system was demonstrated in a ground-based trial.

1.1.1 Numerical Simulation of the Influence of the Landing Gear and the Ground Effect on the Flow around a Transport Aircraft Configuration

David Rohlmann

Institute of Aerodynamics and Flow Technology

The ground effect and the landing gear show a strong influence on the flow around an aircraft configuration and on the expected wake vortices of the aircraft. Furthermore, the wake of the landing gear influences the generation and the development of the wake vortices. Within the DLR project L-bo*ws* (Land-based and onboard wake systems), among other topics, the prediction capabilities for wake vortices should be improved by the use of numerical simulations. For these simulations exact CFD data of the flow around the investigated aircraft configuration is needed. Therefore, numerical investigations on the flow around a realistic transport aircraft configuration with and without landing gear in several altitudes in ground effect were performed. In steady simulations the altitude of the aircraft above ground was varied in fixed steps. Furthermore, a simplified touchdown maneuver based on a real landing maneuver was simulated by the use of unsteady RANS simulations.

1. Introduction

The DLR project L-bo*ws* (Land-based and onboard wake systems) focuses on the prediction and manipulation of wake vortices in the field of commercial aviation (Schwarz and Holzäpfel, 2016). One of the project's work packages deals with high fidelity simulations of wake vortices of transport aircraft configurations using a coupled RANS LES approach. The main topic of these investigations is the simulation of the whole life time of the wake vortices during approach and touchdown of the vortex generating aircraft. Here, a special focus is set on the movement of the wake vortex system on the ground at different wind directions and speeds and on the possibilities to influence the decay of the vortices. Within the project L-bo*ws* an Airbus A320 in high lift configuration was used as the vortex generator.

Within the coupled RANS LES method (Misaka et al. 2015, Stephan et al. 2014), which was used in this project, the flow field around the vortex generating aircraft is generated by a RANS simulation. Afterwards, to initialize the LES simulation, the RANS field is moved through the LES domain. After this, the further development of the wake vortices and their interaction for example with the ground is simulated in the LES simulation. To enable an exact simulation of the wake vortices in the LES domain a highly accurate RANS field around aircraft generating the vortices is needed. Hence, for the RANS simulations a detailed CAD model of the Airbus A320 “ATRA” in high lift configuration including the landing gear was used. The simulations were performed with and without landing gear to investigate the influence of the landing gear on the flow around the aircraft. Furthermore, the influence of the ground effect on the flow around the aircraft during approach and touchdown was investigated by simulations in different altitudes of the aircraft above the ground.

In addition to the steady RANS simulations in different altitudes an unsteady simulation of a simplified touchdown maneuver was performed. This investigation was carried out to analyze the unsteady effects in the flow around the aircraft during the unsteady descent of the aircraft to the ground and the rotation of the aircraft after touchdown.

In this paper the steady and unsteady RANS simulations performed during the project L-bo*ws* and their results will be presented. The paper has been submitted for publication in the CEAS Aeronautical Journal.

2. Geometry and mesh

2.1 Geometry

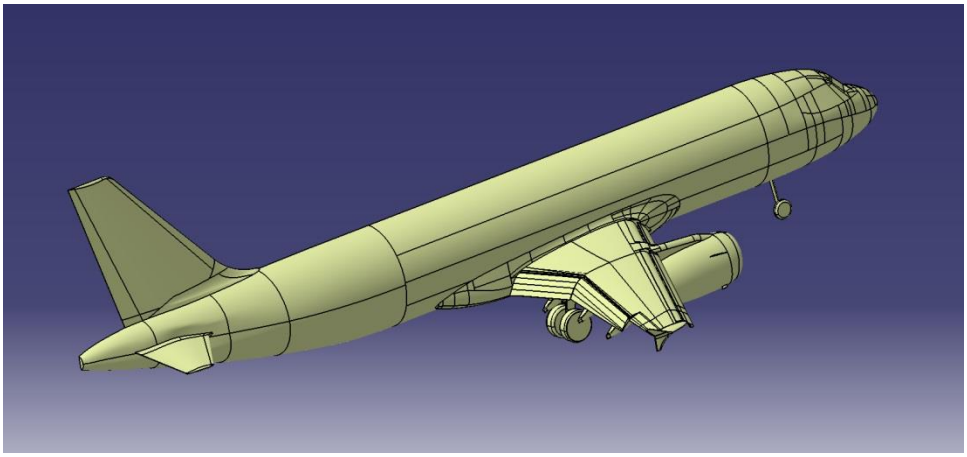

Figure 1: CAD model – overview

Within the project L-bo*ws* an Airbus A320 was used as the aircraft generating the wake vortex system. For the RANS simulations a very detailed CAD model of the Airbus A320 ”ATRA” operated by the German Aerospace Center (DLR) was available. All investigations shown in this paper were carried out using the high lift configuration “Full LDG”. This implies a deflection angle of δ_{flaps} = 40° for the flaps and a deflection angle of δ_{slats} = 27° for the slats. Besides the high lift elements, the CAD model also includes the slat tracks, the IAE V2500 turbofan engine, the flap track fairings and the vertical and horizontal tail planes. Furthermore, the CAD model also includes a slightly simplified main and nose landing gear. Figure 1 is giving an overview on the CAD model used. In Figure 2 the CAD model of the simplified main landing is shown.

The steady RANS simulations were performed with and without landing gear. For the unsteady RANS simulation of the simplified touchdown maneuver the configuration without landing gear was used.

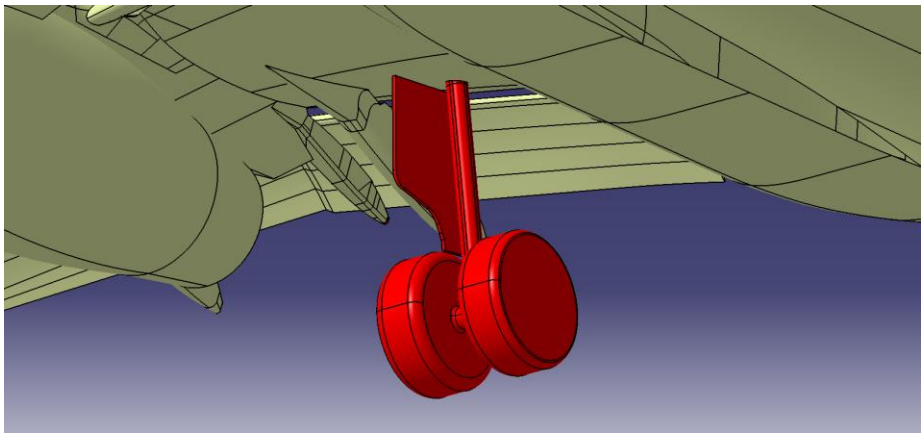

Figure 2: CAD model - Main landing gear

2.2 Mesh Generation

The RANS simulations within the project L-bo*ws* were performed using hybrid unstructured meshes. The meshes were built using the mesh generator Centaur (Centaursoft, 2017). They are based on the experiences made during the project HINVA (Rudnik et al. 2012, Bier et al. 2012, Rohlmann and Keye, 2015). The work in HINVA also was focused on the Airbus A320 high lift configuration. The meshing of the surfaces and the boundary layers in L-bo*ws* is based on the meshes used in HINVA. Additionally the volume meshes were strongly refined in the regions of wakes and vortex systems produced by the wing, the high lift devices, the landing gears and the tail planes. The boundary layers on all non-slip walls in the complete mesh were resolved by 40 prism layers. Thereby, the meshes used show a very high mesh resolution to resolve all relevant flow phenomena at the Airbus A320 high lift configuration. In Figure 3 in overview on the Centaur volume source setup is given. The surface mesh around the main landing gear is shown in Figure 4.

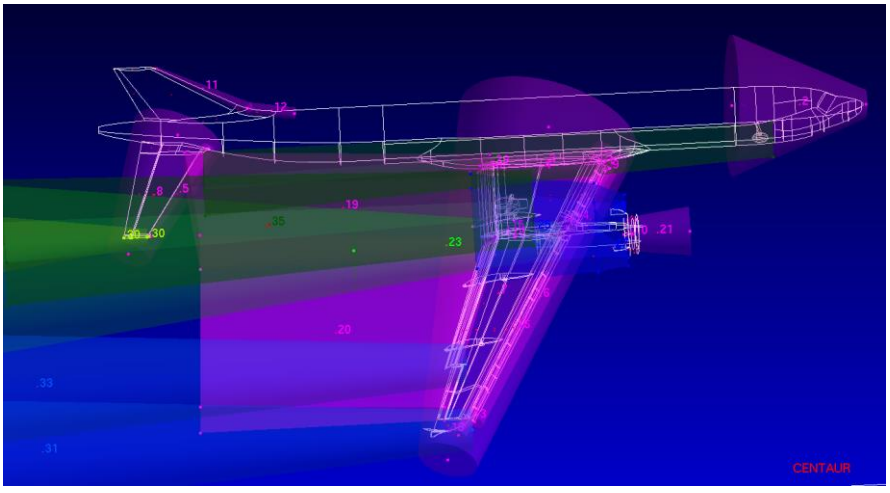

Figure 3: Centaur setup – Overview

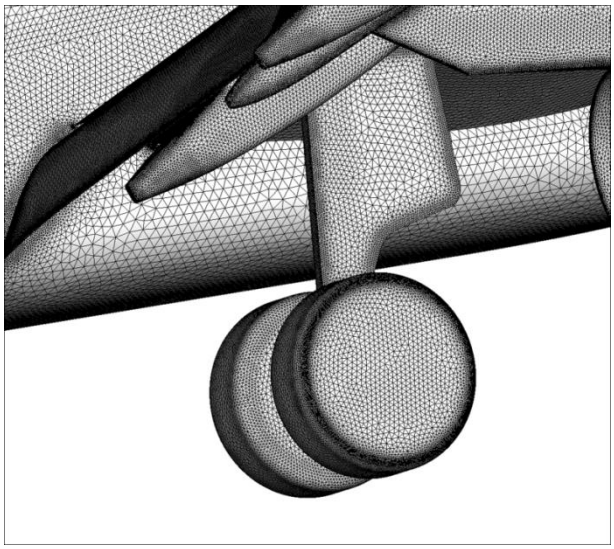

Figure 4: Surface mesh around main landing gear

To realize the simulation of different altitude steps, one approach using multiple mesh blocks was chosen for the meshing. For this approach, the simulated flow volume is divided in several overlapping mesh blocks. These blocks are meshed separately. After the meshing the relative position of the blocks is set up in the flow solver and the flow field is calculated for the whole domain. By using this meshing approach, it is possible to build one separate mesh block for the aircraft and one separate mesh block for the far field including the ground. The relative positioning of these blocks enables the possibility to realize different altitude steps by the use of identical meshes. In Figure 5 an overview of the mesh block setup for one altitude step is given. All mesh parts which are not needed for the simulation, like the mesh below the ground or behind the aircraft, are blanked by the flow solver.

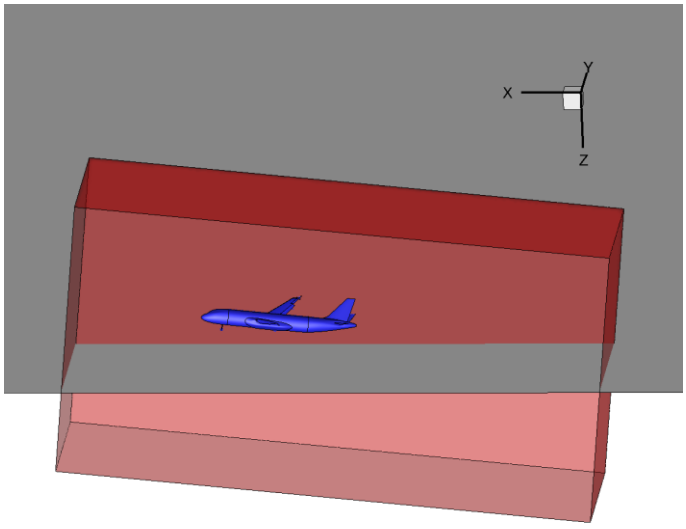

Figure 5: Block setup – Overview

To further improve the quality of the simulated flow field around the aircraft configuration, at each altitude step the meshes were locally refined during the simulation process. This was done by an automatic mesh adaptation process provided by the flow solver. The mesh

adaptation is based on a user defined sensor function and is restricted to user defined regions in the flow field. Within the simulations presented in this paper, the mesh adaptation is locally restricted to the regions around the tip vortices and the wakes of the configuration. As a sensor function the difference in total pressure between two neighboring mesh points was set. The meshes were adapted in up to nine steps for both configurations, with and without gears, for all altitude steps. In Figure 6 a slice through the volume mesh before the first and after nine adaptation steps is shown. An improvement of the mesh resolution in the wake of the wing and around the tip vortices of the wing and the high lift devices can clearly be seen.

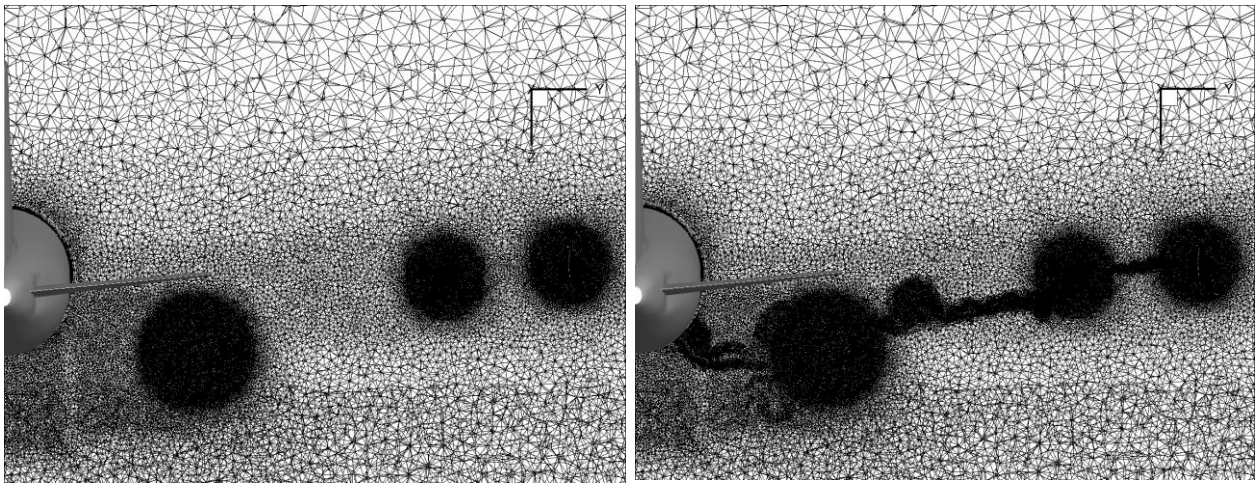

a) b)

Figure 6: Slice through mesh

Parameter	Value
Number of surface elements	2.7e+06
Number of prisms	72e+06
Total point number	61e+06

Table 1: Number of mesh points

In Table 1 the number of points and elements for the meshes before the automatic mesh adaptation during the simulation is shown. By the automatic mesh adaptation the number of total points is increased by about 15%.

3. Flow Solver and Flow Condition

3.1 Flow Solver

Within the current studies the DLR TAU Code (Kroll et al. 2009) was used as the flow solver for the RANS and URANS simulations. The DLR TAU Code is a compressible, unstructured finite volume solver for the Reynolds averaged Navier-Stokes equations.

For all simulations shown in this paper, the Spalart-Allmaras (SA) turbulence model (Spalart and Allmaras, 1992) was used. The SA turbulence model is robust and sufficiently validated for the simulation of the flow around complex high lift configurations (Bier et al. 2012, Rohlmann and Keye, 2015, Rumsey et al. 2011). The time-stepping was done by a lower-upper symmetric Gauß-Seidel (LU-SGS) scheme. A matrix dissipation scheme was used for the artificial dissipation for the central scheme used. A 3v multigrid cycle was applied to accelerate the convergence.

A dual time stepping approach was used for the unsteady Reynolds averaged Navier-Stokes equations for the simulation of the unsteady simplified touchdown maneuver. The unsteady movement of the aircraft during the maneuver was implemented by a relative movement of the mesh block around the aircraft and the far field block including the ground. All surfaces of the aircraft were modeled as non-slip Navier-Stokes walls. The ground was modeled as a slip Euler wall. The engine of the aircraft was treated as a through flow nacelle.

3.2 Flow Conditions

The used flow conditions are derived from a real touchdown maneuver of the Airbus A320 “ATRA”. They were converted to the International Standard Atmosphere (ISA) at the altitude of h = 0 m. The resulting flow conditions for the simulations are shown in Table 2.

Parameter	Value
Density	ρ = 1.225 kg/m^3
Pressure	p = 101325 Pa
Temperature	T = 288.15 K
Velocity	v = 64 m/s
Reynolds number	Re ≈ 18.4*10^6
Mach number	Ma ≈ 0.188

Table 2: Flow conditions

3.2.1 Steady Simulations

The steady RANS simulations were performed for the configurations with and without landing gears at a constant angle of attack for eight altitude steps between h = 0 m and h = 175 m. In this study the altitude is defined as the distance between the main landing gear and the ground. The angle of attack was set to α = 6°, which was the average angle of attack during the approach in the flight test data.

3.2.2 Unsteady Simulations

The movement of the aircraft during the simplified touchdown maneuver was derived from real touchdown maneuvers of the Airbus A320 “ATRA”. The simplified touchdown maneuver contains a constant descent with constant velocity and constant angle of descent. The angle of

attack is kept constant up to the touchdown. After touchdown the aircraft rotates to an angle of attack of α = 0°. During rotation the angular velocity as well as the x velocity are kept constant. During the descent to the ground, the angle of attack is kept constant at α= 6°, the same angle of attack as in the steady RANS simulations. In the unsteady maneuver simulation this angle of attack is achieved by the addition of the constant geometric angle of attack the aircraft geometry and a superposition of the x and z components of the aircraft velocity.

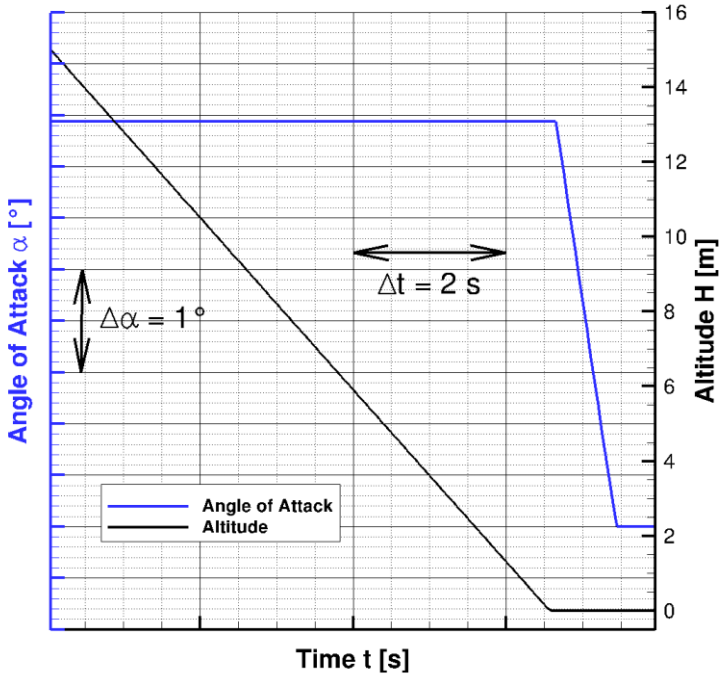

Figure 7: Altitude and geometric angle of attack during the touchdown maneuver

In Figure 7 the development of altitude and angle of attack during the maneuver is shown as a function of the physical maneuver time.

The physical time step for the unsteady simulation had to be set to a relatively high value of Δt = 0.05 s due to the long physical time span to simulate. According to the limited dynamics of the maneuver looked at and the very steady flow conditions during the maneuver, this relatively large time step still results in an acceptable convergence of the inner time steps of the URANS simulation.

4. Results

The results of the simulations will be discussed in the following sections. First of all an overview on the global flow in the steady simulations will be given. Then the influence of the landing gears on the flow around the aircraft configuration is shown. Afterwards, the influence of the ground effect will be discussed. In the end, the results for the simplified touchdown maneuver will be presented.

4.1 Results – Steady RANS

In Figure 8 the influence of the automatic mesh adaptation on the resolution of the wake of the wing is shown. Both figures show a slice through the flow domain a short distance behind the wing and are colored by the total pressure. Figure 8a shows the results before the automatic mesh adaptation and Figure 8b after nine steps of the automatic mesh adaptation. The comparison of both figures shows a strong effect of the mesh adaptation on the resolution of the smaller flow features in the wake of the wing. In Figure 8b more small flow features can be seen in the flow solution. Especially at the outer part of the wing the resolution of the smaller flow features is improved significantly.

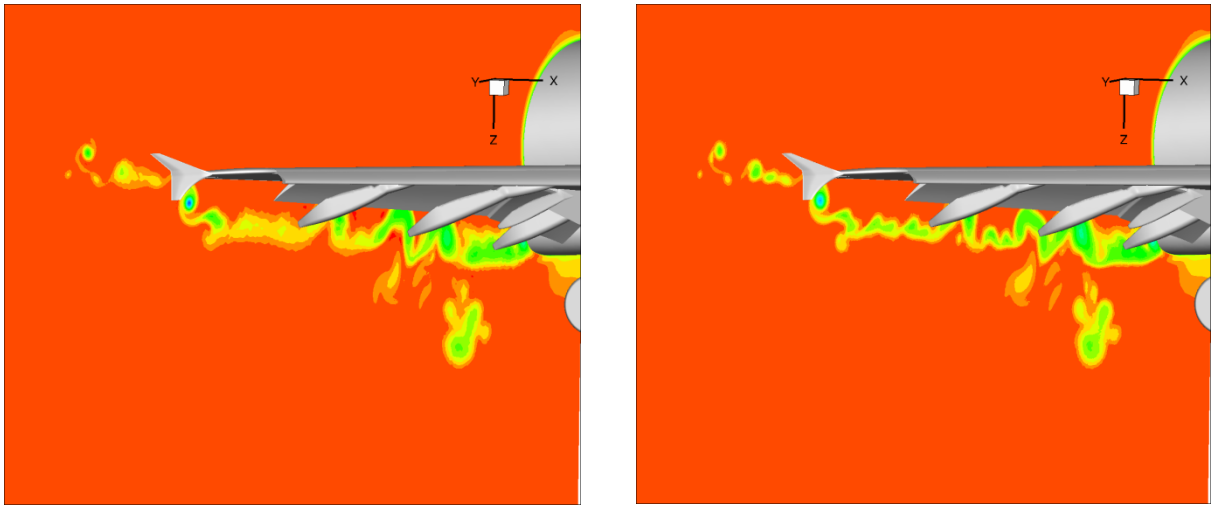

a) b)

Figure 8: Slice through flow solution - Colored by total pressure - h = 15 m

A typical convergence history of the density residual and the lift and drag coefficients for the steady RANS simulations performed within L-bo*ws* is shown in Figure 9. The density residual decreases for four orders of magnitude and the amplitudes of the lift and drag coefficient decrease to very small values. So the convergence level can be assumed to be sufficient. Furthermore, in this figure one can identify the steps of the automatic mesh adaptation as peaks in the density residual. Due to the fact that after the last mesh adaptation step the density residual levels to slightly higher values and the amplitudes of the aerodynamic coefficients remain slightly higher, another mesh adaptation step is not useful.

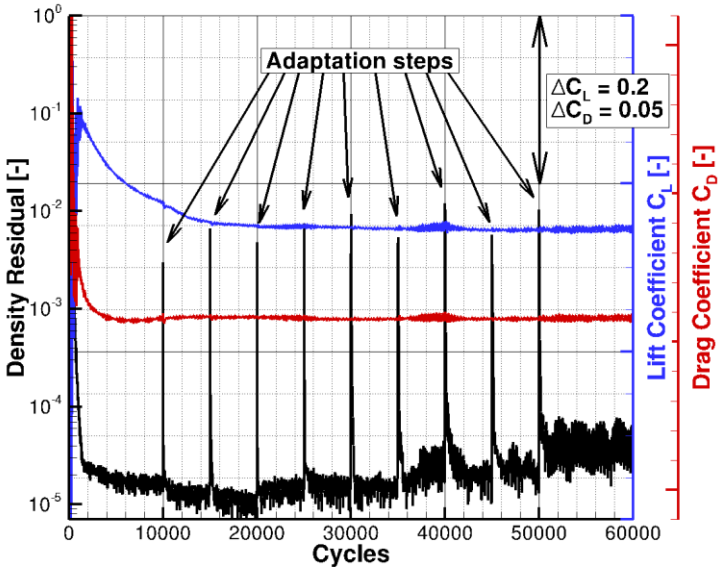

Figure 9: Typical convergence history for the steady RANS simulations

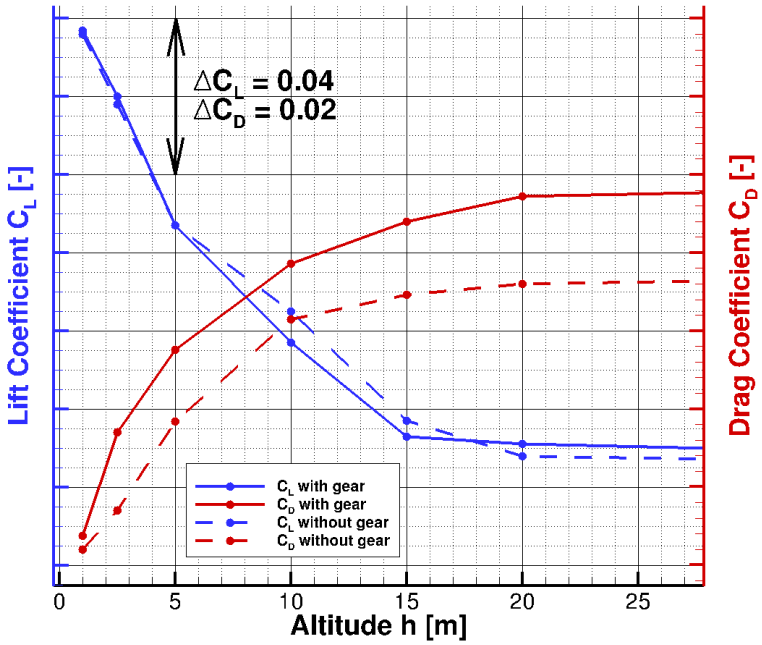

Figure 10: Influence of altitude and landing gear on C_L and C_D

In Figure 10 the influence of the ground effect and the presence of the landing gear on the lift and the drag coefficients for the simulated altitudes is shown. The diagram is cut at the altitude of h = 15 m because there is no significant change in the aerodynamic coefficients for higher values. In the following sections 4.1.1 and 4.1.2 the influence of the landing gear and the ground effect is investigated separately.

4.1.1 Influence of the Landing Gear

According to Figure 10 the landing gear has no significant influence on the lift coefficient of the Airbus A320 high lift configuration for all considered altitude steps. In contrast to the influence of the landing gear on the lift, the influence of the landing gear on the drag coefficient is clearly visible for all considered altitude steps. The influence of the landing gear on the lift coefficient is very limited due to the very small local disturbance of the flow field around the wing. The disturbance is only located at the lower side of the inner main wing respectively near the nose of the fuselage. Almost the complete wing, especially the upper side of the wing, the fuselage as well as the tail planes are not influenced by the landing gear. Furthermore, the surfaces of the landing gear itself are not producing a substantial amount of lift.

In contrast to the influence of the landing gear on the lift, the influence on the drag is clearly visible. For all altitudes steps looked at, the drag is significantly increased by the addition of the landing gear. The influence on drag is only a local effect at the landing gear itself because, as described above, the mean flow around the aircraft configuration is not strongly influenced by the presence of the landing gear. The drag is produced directly by the landing gear surfaces. The landing gear can be considered as a large blunt body located in nearly undisturbed flow producing a strong wake but almost no lift. The influence of the landing gear on the drag coefficient is decreasing with decreasing altitude. This can be explained by the growing influence of the ground effect on the flow in the area of the landing gear with decreasing altitude. The growing influence of the ground effect results in a reduced local flow velocity especially at the position of the main landing gear below the wing ending up with a reduced drag for the whole aircraft configuration for decreasing altitudes. This effect is described in detail in section 4.1.2.

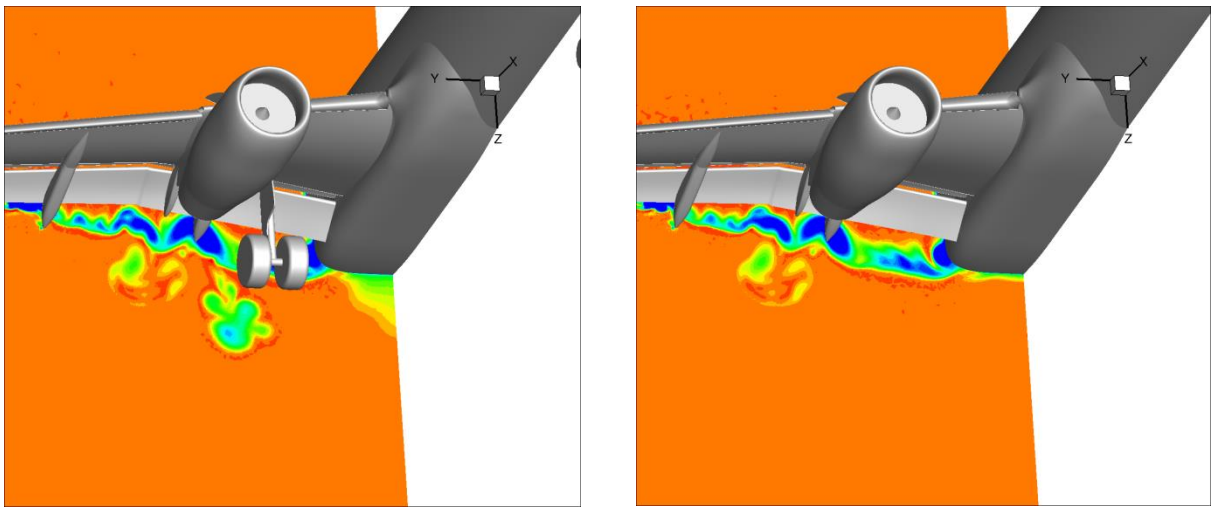

a) b)

Figure 11: Slice through flow solution - Colored by total pressure - h = 15 m

In Figure 11 the influence of the landing gear on the total pressure in the wake of wing is shown in a slice shortly behind the inboard wing for an altitude of h = 15 m for both configurations, with and without landing gear. The strong loss in total pressure in the wake of

the wing and the engine is clearly visible in both figures. Additionally, the extensive and strong loss in total pressure behind the landing gear can be seen in Figure 11a. The wakes of the wing and the nacelle are not influenced significantly by the presence of the main landing gear. But the strong wake of the main landing gear may have an influence on the formation and the development of the wake vortex system of the complete aircraft configuration. This topic will be evaluated by the ongoing coupled RANS LES simulation of the wake vortex system within this project. Besides the wake of the main landing gear, in Figure 11a, also the wake of the nose landing gear is visible below the fuselage. Compared to the wake of the main landing the total pressure loss of the nose landing gear is much smaller due to the smaller dimensions of the nose landing gear and the relative long distance between the nose landing gear and the slice through the volume presented here.

For an altitude of h = 15 m, the figures Figure 12 and Figure 13 show the pressure distributions of the wing including the high lift devices in two slices. In Figure 12 the pressure distribution at the inner wing close to the main landing gear is shown. Figure 13 is showing the pressure distribution in the middle of the outer wing. At the pressure side of the main wing at the inner wing the pressure level is slightly higher for the configuration without landing gear. This can be explained by a blockage of the flow between nacelle and fuselage by the presence of the landing gear. This blockage results in a reduced local flow velocity and, therefore, in a higher static pressure level. At the lower side of the flap a slightly reduced static pressure is visible for the configuration with landing gear caused by the loss of total pressure in the wake of the landing gear. At the slat and the upper sides of main wing and flap no difference in the pressure levels can be observed. The pressure distributions at the outer do not show any differences between the two configurations. These minor and local differences in the pressure distributions at wing also explain the non-existing effect of the landing gear on the lift.

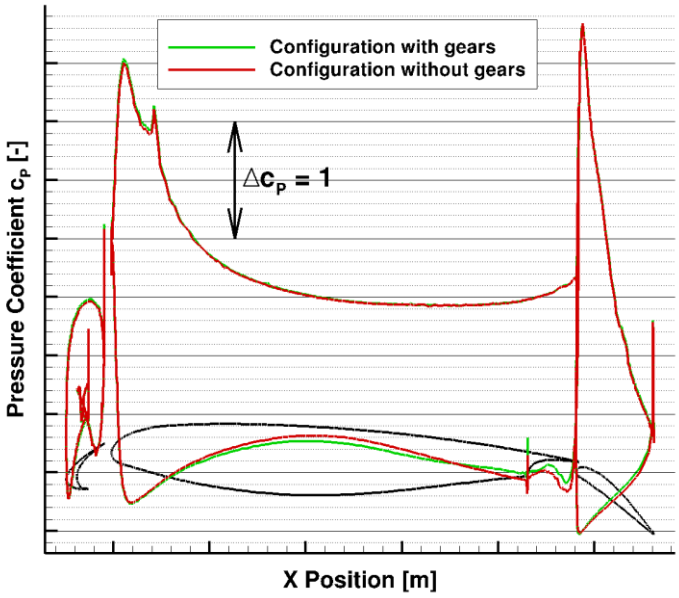

Figure 12: Pressure distribution inner wing - h = 15 m

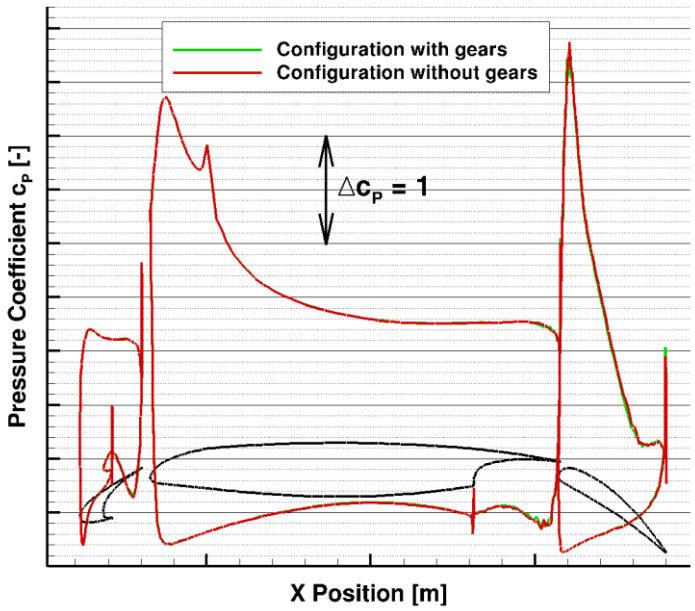

Figure 13: Pressure distribution outer wing - h = 15 m

4.1.2 Influence of the Ground Effect

The theory of the ground effect, for example (Torenbeek, 1976), explains the aerodynamic effects using the potential theory by a virtual mirroring of the vortical system of the aircraft configuration at the ground. When bringing an aircraft configuration at constant angle of attack closer to the ground, this approach predicts decreasing drag and increasing lift for moderate angles of attack and relatively small lift coefficients. For configurations at higher lift coefficients, with deflected trailing edge flaps or at very low altitudes above ground this approach results in a decrease of lift when decreasing the distance to the ground. In Figure 10 the influence of the decreasing ground distance on the lift and drag coefficients of the Airbus A320 high lift configuration can be seen. With decreasing altitude the drag also decreases while the lift increases. The simulations performed within L-bo*ws* use the Airbus A320 high lift configuration with deflected trailing edge flaps at the wing at a moderate angle of attack and cover a relatively large range of altitudes. Therefore, it is reasonable the take a closer look at the single components of the configuration to explain the observed effects on lift and drag correctly.

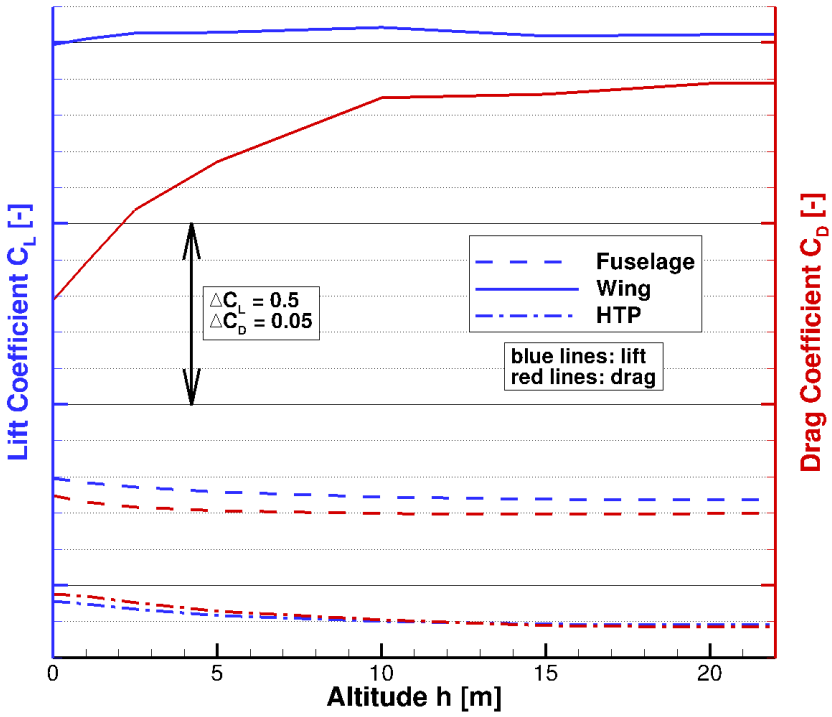

Figure 14: C_L and C_D for wing, fuselage and vertical plane of the configuration without landing gear wing plotted against the altitude

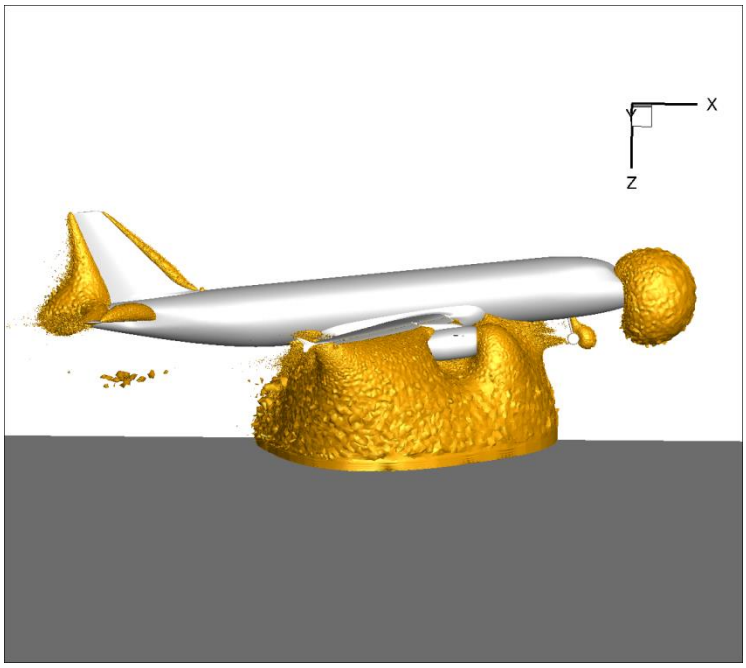

Figure 15: Iso surface of the static pressure, $0 < c_P < 1$, h = 5 m

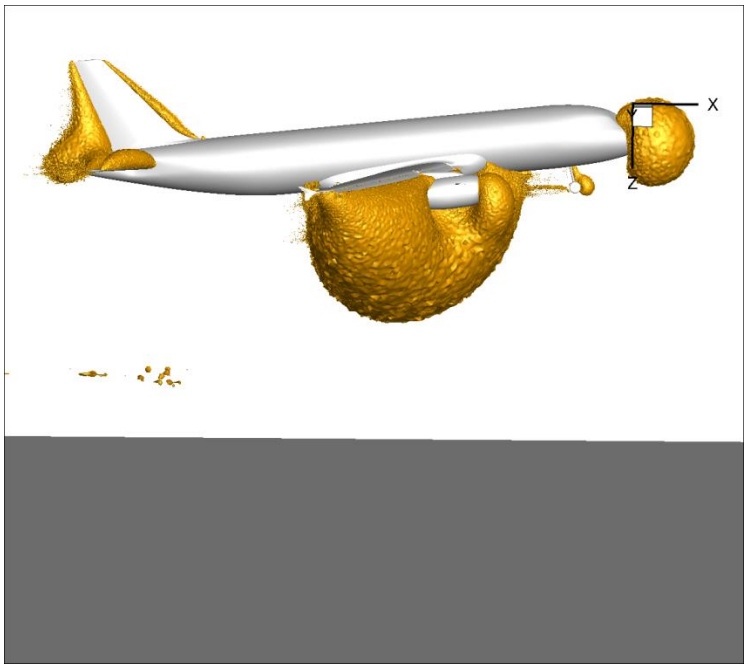

Figure 16: Iso surface of the static pressure, $0 < c_P < 1$, h = 15 m

Figure 14 shows the development of the lift and drag coefficients for the wing including the high lift devices, the fuselage and the vertical plane of the configuration without landing gear over the altitude. For the wing the lift coefficient increases with decreasing altitude. Only at very low altitudes a reverse effect can be observed and the lift coefficient of the wing slightly decreases. The lift coefficients for the fuselage and the vertical plane are increasing while decreasing the altitude for all altitudes simulated. With decreasing altitude, among other effects, the flow between aircraft and ground is decelerated and the static pressure between aircraft and ground is increased. This deceleration of the flow between aircraft and ground close the ground compared to free flight conditions can be explained by the mirroring of the vortical system of the aircraft at the ground resulting in an induced flow velocity against the actual flow velocity between aircraft and ground. This induced flow velocity slows down the flow between the aircraft and the ground resulting in a rise of the static pressure in this region and a higher lift for the aircraft configuration. For very low altitudes and high lift coefficients, for example at wings with deflected high lift devices, the reduction of the flow velocity between aircraft and ground also has a negative effect on the lift. The reduced flow velocity reduces the local stagnation pressure and the local circulation yielding to a negative effect on the lift. This negative effect on the lift superposes the positive pressure effect and can result in an inverse ground effect for very low altitudes and high lift coefficients. The effect of the increasing static pressure between aircraft and ground with decreasing altitude can be seen in Figure 15 and Figure 16. These figures show an iso surface of the static pressure $0 < c_P < 1$ for the altitudes h = 5 m and h = 15 m. With decreasing altitude the surface of the constant positive static pressure between aircraft and ground is growing. This increase of pressure between aircraft and ground, results also in the increasing lift of fuselage and vertical tail plane observed in Figure 14. But this cannot explain all effects at the wing. Although the pressure level at the lower side of the wing is increasing with decreasing altitude, see Figure

17 and Figure 18, also the pressure level at the upper side of the wing is increasing. Furthermore, with decreasing altitude a reduction of the circulation and the resulting lift at the trailing edge flap is visible in the pressure distributions. Only at the slat an increase of the suction peak and the circulation with decreasing altitude is visible. This can be explained by the ground effect resulting in an increased induced angle of attack at the leading edges. The effects described here are stronger at the inner wing, Figure 17, than at the outer wing, Figure 18, due to larger relation of local chord length and local distance to ground. In total these effects described above, lead to an increase of lift at the wing for the larger altitudes and a very small decrease of the lift for the very small altitudes investigated. Beside this, the ground effect also induces a small shift of the spanwise lift distribution in the direction of the inner wing by decreasing the altitude, see Figure 19.

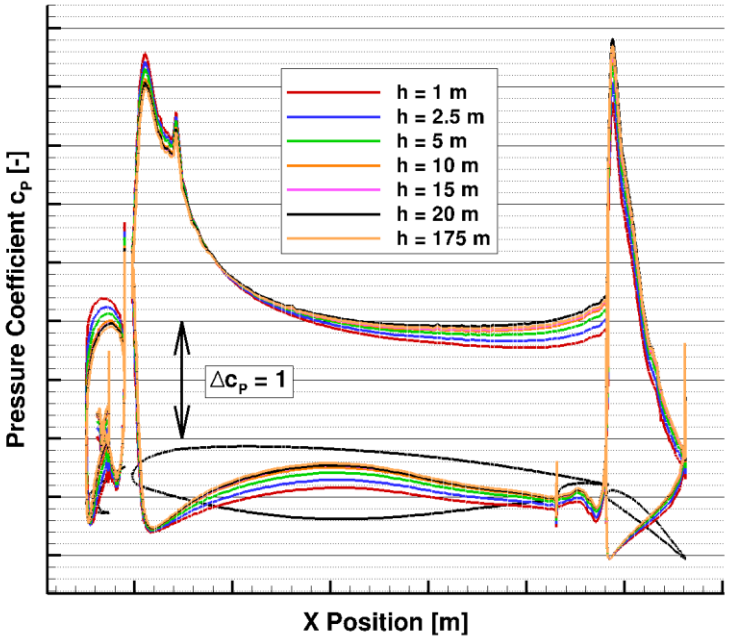

Figure 17: Pressure distribution at the inner wing

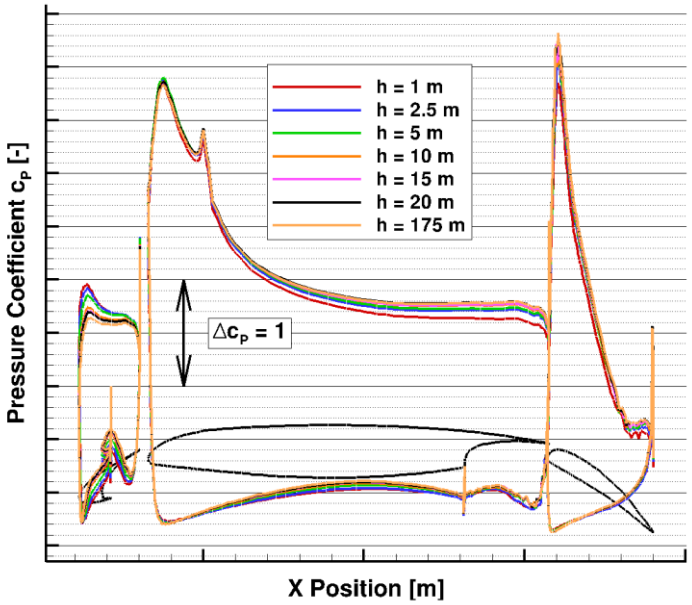

Figure 18: Pressure distribution at the outer wing

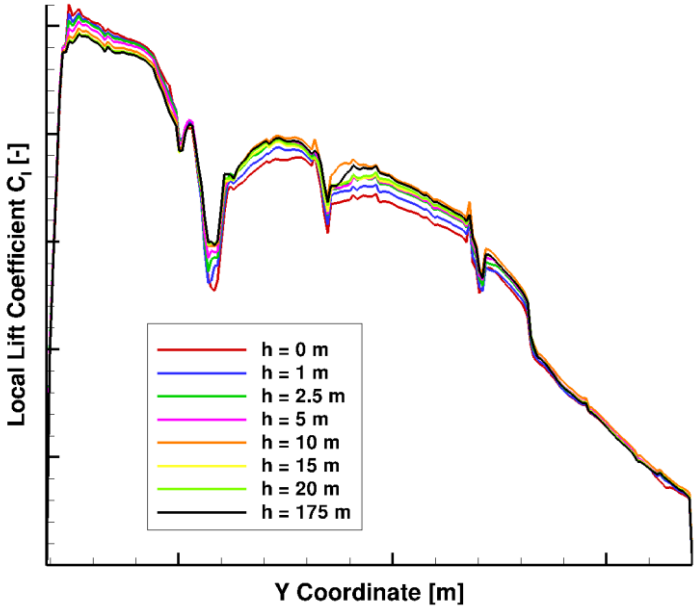

Figure 19: Influence of the ground effect on the spanwise lift distribution at the wing

Besides the influence on the total lift of the configuration, the reduction of the downforce at the vertical tail plane due to the ground effect also has an influence on the trimming of the configuration. In real flight conditions this reduction of downforce has to be compensated by an additional elevator deflection to retain in a trimmed state. This elevator deflection leads to a reduction of the overall lift gain for the complete configuration and was neglected in this study.

Also in Figure 14 it can be seen, that the reduction of total drag in ground effect is caused by a reduction of the drag of the wing. In contrast to the drag produced by the wing, the drag of fuselage and vertical tail plane increases with decreasing altitudes. The reduction of the drag of the wing can be explained the two effect. The first and main effect is a reduction of the induced drag of the wing due to weakening of the trailing vortices of the configuration caused by the presence of the ground. The second effect can be found in a reduction of the local flow velocity between ground and aircraft resulting in a slightly reduced friction drag at the wing. The small increase of the drag at the fuselage and the vertical tail plane can be explained by the increased static pressure at the lower side of the aircraft configuration. By taking the angle of attack of the configuration into account this increase of static pressure results in a small force component against the moving direction of the aircraft.

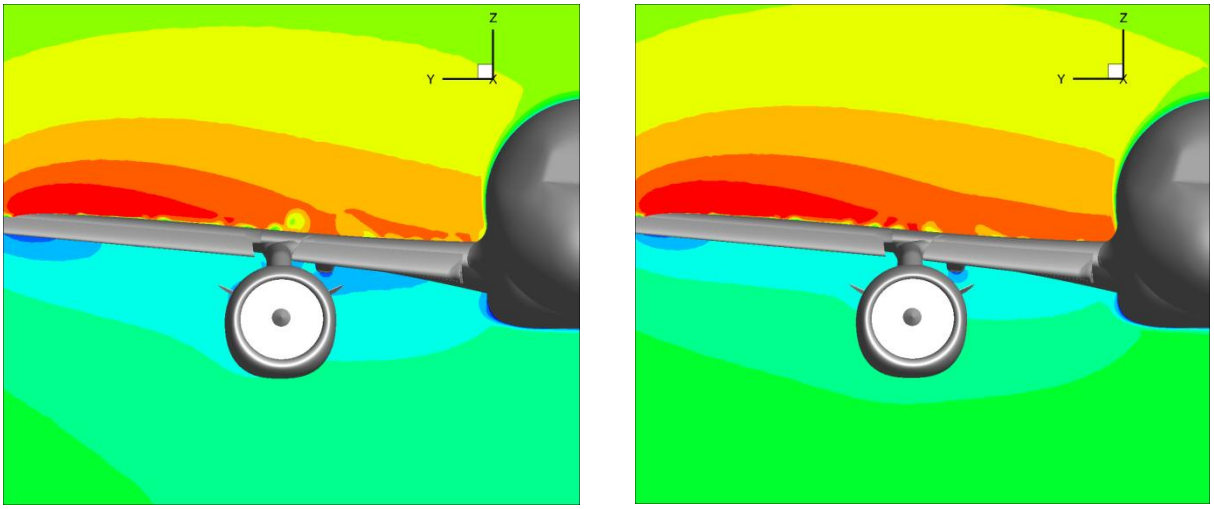

a) b)

Figure 20: X velocity in a x = const. slice at the position of the main landing gear

In section 4.1.1 the decreasing drag of the landing gear in ground effect was already briefly discussed. In this section this effect will be described in detail. The decrease of the landing gear's drag can be explained by the reduction of the local flow velocity in the region of the man landing gear when the altitude is decreased. This reduction of local flow velocity yields to a reduced drag of the main landing gear due to the reduction of the local stagnation pressure. This effect can be seen in Figure 20. In this figure for the configuration without landing gear the x component of the flow velocity is shown in a x = const. slice at the position of the main landing gear for two altitudes at h = 2.5 m and h = 20 m. The local x component of the flow velocity at the position of the main landing gear between the nacelle and the fuselage, which is mainly responsibility for the pressure drag of the main landing gear, is significantly reduced at the smaller altitude of h = 2.5 m compared to h = 20 m.

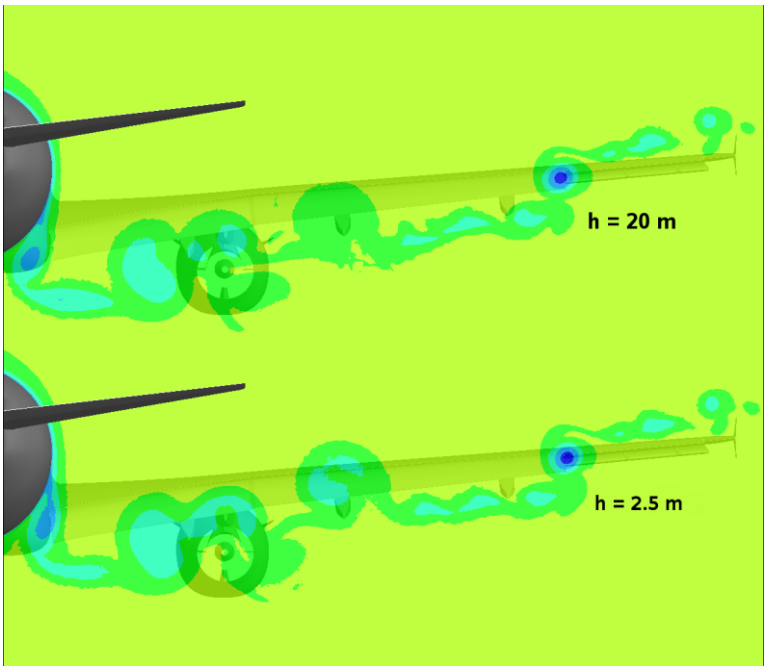

Figure 21: Influence of the ground effect on the wake of the wing

In Figure 21 the influence of the ground effect on the wake of the main wing is shown for h = 2.5 m and h = 20 m by the total pressure in a slice a few meters behind the wing. The biggest differences in the wake of the wing between those two altitudes are located in the region of the inner wing. At the outer part of the outer wing almost no influence of the altitude is visible. The position of the tip vortices of the trailing edge flap and wing tip as well as the strength of the loss of total pressure inside these vortices is also almost identical for the two altitudes shown in the figure. At the inner wing the loss in total pressure in the wake is slightly higher for the altitude of h = 2.5 m. Furthermore, the complete wake at the inner wing is shifted slightly upwards for this altitude. This shift can be explained by the reduced downwash behind wing for the smaller altitude. The increase of the total pressure loss of the wake of the inner wing can be explained by a spread of the boundary layer flow at the main wing and the wake of the slat due to the stronger pressure gradient above the wing for smaller altitudes, see Figure 17. The observed shift of the wake and the increased total pressure loss in the wake for smaller altitudes may has a significant influence on the formation of the wake vortices of the configuration looked at. In addition, the reduced downwash behind the wing due to the presence of the ground may also have an influence on the further development of the wake vortices.

4.2 Results – Unsteady RANS

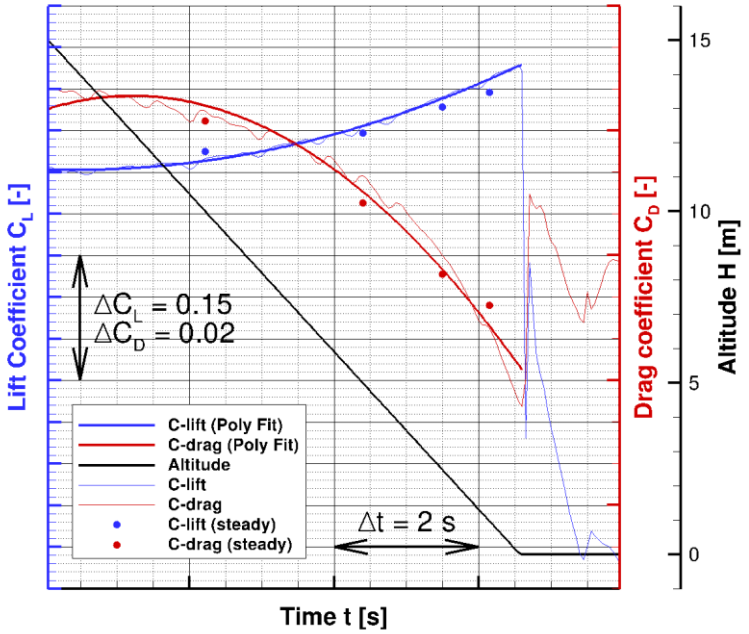

Figure 22: Development of C_L, C_D and altitude h over physical time

In Figure 22 the development of the lift and drag coefficients and the altitude is plotted against the physical maneuver time. The thin lines show the actual unsteady development of the coefficients during the simulation. The thick lines give a smoothed approximation of the unsteady values for altitudes above h = 0 m by a second degree polynomial. The dots in this figure show the aerodynamic coefficients of the steady RANS simulation described in the previous sections. The aerodynamic coefficients show only very limited unsteady oscillations during the simulation and are very close to the smoothed polynomial approximation. The smoothed curves are showing the behavior expected by the theory of the ground effect. The small unsteady oscillations observed in the unsteady aerodynamic coefficients can be explained by small flow separations at the trailing edge flap. Furthermore, the polynomial approximation of the unsteady aerodynamic coefficients is in very good agreement with the results of the steady RANS simulations. The small differences between the steady RANS and the unsteady maneuver simulation can also be explained by the small and unsteady flow separations at the trailing edge flap. These unsteady flow phenomena are not captured correctly by the steady RANS approach giving slightly different results. In the moment of the touchdown the z component of the aircraft movement switches to v_x = 0 m/s. Due to this, the angle of attack of the configuration is decreasing abruptly leading to an abrupt increase of lift and drag. During the rotation of the aircraft configuration to an angle of attack of α = 0° the induced angle of attack is increased by a superposition of the horizontal aircraft velocity and the rotation. This results in a slightly increased angle of attack during the rotation. At the beginning of the rotation the step in the angle of attack yields to a stepwise increase in lift. Afterwards during the rotation the lift decreases linear analog to the angle of attack until α = 0° is reached.

In the following, only the aerodynamic phenomena after touchdown be discussed in detail due to the fact that the phenomena observed in the unsteady maneuver simulation are not significantly different compared to the steady RANS results described in the sections above.

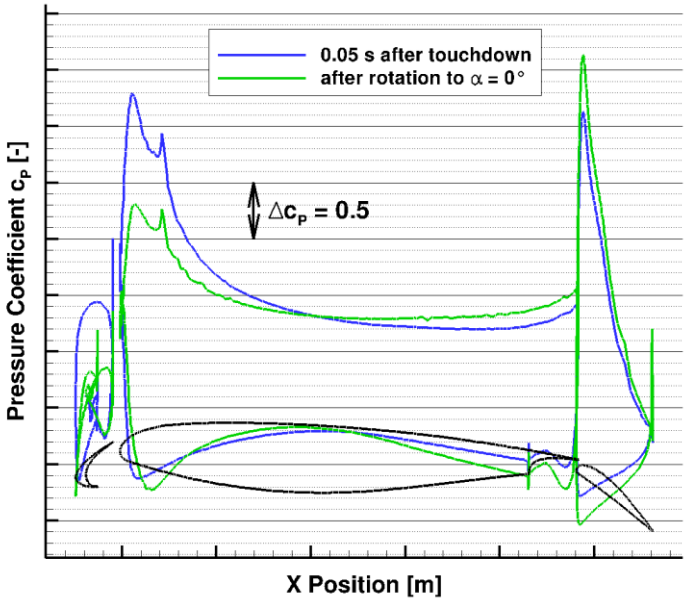

Figure 23: Pressure distribution at inner wing

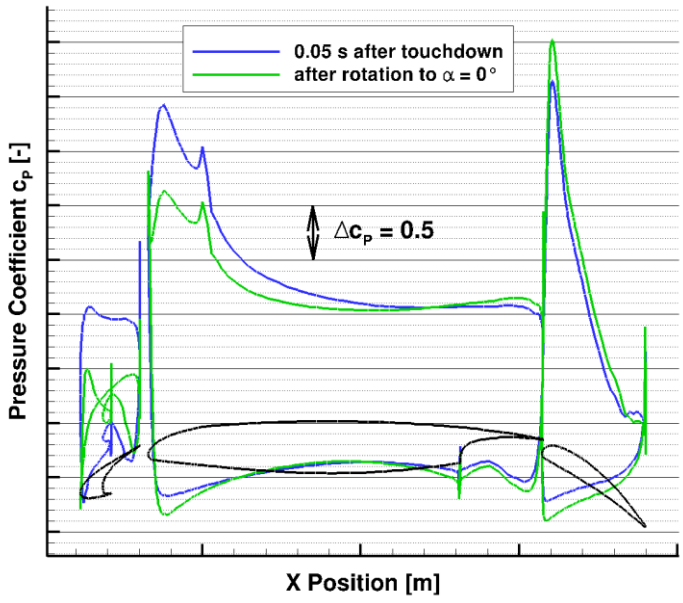

Figure 24: Pressure distribution at outer wing

The figures Figure 23 and Figure 24 show the pressure distributions in one slice at the inner wing and one slice at the outer wing for the time step directly after the touchdown and the

time step directly after the rotation. In both figures at the slat and at the leading edge of the main wing a reduction of the suction peak is visible due to the reduction of the angle of attack during the rotation. The pressure at the stagnation point at the main wing is increasing during the rotation. The increase of the pressure is caused by the increase of the local flow velocity between aircraft and ground. This results from a decreasing ground effect due to a decrease of lift during the rotation. This effect is also visible in both slices at the stagnation point of the trailing edge flap. Furthermore, the suction peak at the trailing edge flap is increasing in both slices during the rotation. This is caused by the increasing flow velocity between aircraft and ground. This results in an increase of circulation at the flap although the angle of attack is reduced during the rotation. As a result of the increasing suction peaks at the flap, in both slices the pressure level at the trailing edge of the main wing is also changing during the rotation. Due to the increase of circulation at the trailing edge flap, a flow separation at the upper side of the trailing edge flap is visible at the slice at the inner wing.

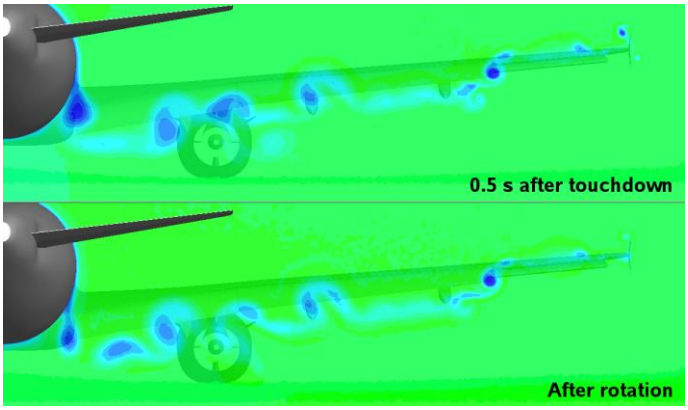

Figure 25: Total pressure in a slice behind the wing, 0.5 s after touchdown and after rotation

The wake of the wing for the first time step after touch down and the first time step after the rotation is shown in Figure 25 by the total pressure in a slice behind the wing. The figure shows the decrease of the wake of the wing caused by the rotation of the aircraft configuration to an angle of attack of $\alpha = 0°$. As a major effect the total pressure loss in the wing tip vortex and the vortex at the root of the wing is significantly reduced by the derotation. Furthermore, the loss in total pressure in the wake of the engine, mainly caused the vortical system induced by the engine, is also clearly reduced. However, the loss in total pressure in the tip vortex of the trailing edge flap is only slightly reduced after the rotation to $\alpha = 0°$. The wake of the inner wing in the region between the fuselage and the engine even is slightly increased. This is a result of the small flow separation observed at the trailing edge flap after the rotation. At the outer wing this effect is not visible because there is no flow separation at the trailing edge flap in this region. The vertical position of the wake behind the wing is not significantly modified by the rotation to $\alpha = 0°$.

5. Conclusions

The studies presented here involve the setup and realization of steady and unsteady RANS simulations of a realistic transport aircraft configuration in high lift configuration with and

without landing gear in ground effect. The investigation was focused on steady altitude steps and on a simplified unsteady touchdown maneuver. The test configuration used was a detailed model of the Airbus A320 high lift configuration as a typical transport aircraft configuration.

The results presented in this paper show a significant influence of the landing gear on the overall aerodynamic values of the configuration. Furthermore, a significant influence of the landing gear on the wake of the configuration was observed. Although the observed effects are clearly visible on all altitude steps investigated, the effect is decreasing with decreasing altitude. These effects may have a strong influence on the formation and development of the wake vortex system of configuration studied.

The ground effect was observed in the steady as well as in the unsteady simulations. The effect was consistent to the theory of the ground effect. As well as the landing gear, the ground effect has a clearly visible influence on the aerodynamic coefficients and on the wakes of the high lift configuration investigated. The effects observed also may have a significant influence on the formation and development of the wake vortex system of the configuration.

Additionally, in the unsteady maneuver simulation the development of the flow around the aircraft configuration after touchdown and during derotation on the ground to an angle of attack of $\alpha = 0°$ was studied. A clearly visible step in the aerodynamic coefficients in the moment of the touchdown was observed. During the rotation the aerodynamic coefficients change gradually analog to the angle of attack. Consistent effects were visible in the wakes of the configuration.

Overall the simulations shown in this study form a very good basis for the coupled RANS LES simulations ongoing within the project L-bo*ws*. These simulations will be performed to give a better understanding of the formation and development of the wake vortex system of a realistic high lift transport aircraft configuration during approach and after touchdown.

Acknowledgements

This report was also submitted to be published in the CEAS Aeronautical Journal. The final publication will be available at http://link.springer.com

References

Bier N., Rohlmann D., Rudnik R. (2012): Numerical Maximum Lift Predictions of a Realistic Commercial Aircraft in Landing Configuration, AIAA 2012-0279, 50th AIAA Aerospace Sciences, Nashville, USA.

Centaursoft (2017): CENTAUR Grid Generation Software, https://www.centaursoft.com/grid-generator.

Kroll N., Becker K., Rieger H., Thiele F. (2009): MEGADESIGN and MegaOpt - German Initiatives for Aerodynamic Simulation and Optimization in Aircraft Design, Springer-Verlag Berlin, Heidelberg.

Misaka T., Holzäpfel F., Gerz T. (2015): Large-Eddy Simulation of Aircraft Wake Evolution from Roll-Up Until Vortex Decay, Journal of Aircraft, Vol. 53, No. 9, pp. 2646-2670.

Rohlmann D., Keye S. (2015): Stall Maneuver Simulation of an elastic Transport Aircraft based on Flight Test Data, AIAA 2015-2570, AIAA Aviation, 33rd AIAA Applied Aerodynamics Conference, Dallas, USA.

Rudnik R., Reckzeh D., Quest J. (2012): HINVA - High lift IN-inflight VAlidation - Project Overview and Status, AIAA 2012-0106, 50th AIAA Aerospace Sciences, Nashville, USA.

Rumsey C.L., Slotnick J.P., Long M., Stuever R.A., Wayman T. R. (2011): Summary of the First AIAA CFD High-Lift Prediction Workshop, Journal of Aircraft, Vol. 48, No. 6, pp. 2068-2079.

Schwarz C., Holzäpfel F. (2016): Land-Based and Onboard Wake Systems - The DLR Project L-bo*ws*, Deutscher Luft- und Raumfahrtkongress, Braunschweig, Deutschland.

Spalart P., Allmaras S. (1992): A One-Equation Turbulence Model for Aerodynamic Flows, AIAA Paper 1992-0439.

Stephan A., Holzäpfel F., Misaka T. (2014): Hybrid simulation of wake-vortex evolution during landing on at terrain and with plate line, International Journal of Heat and Fluid Flow, Vol. 49, pp. 18-27.

Torenbeek E. (1976): Synthesis of Subsonic Airplane Design, University Press, Delft, p. 551ff.

1.1.2 Effects of Detailed Aircraft Geometry on Wake Vortex Dynamics During Landing

Anton Stephan[1], David Rohlmann[2], Frank Holzäpfel[1], Ralf Rudnik[2]

[1] *Institute of Atmospheric Physics*, [2] *Institute of Aerodynamics and Flow Technology*

The final approach and touchdown of a landing aircraft is studied numerically with different hybrid RANS/LES approaches. Particular emphasis is put on the ground effect and the wake vortex evolution before and after touchdown. Additionally, the effect of the landing gear on the aircraft's aerodynamics during landing is analyzed. The near field around the landing aircraft is generated using two different RANS methods. In a number of steady-state simulations the altitude of the aircraft above ground was varied in fixed steps. Furthermore, a simplified continuous landing maneuver was simulated by applying unsteady RANS simulations. The resulting RANS fields are then coupled with an LES simulation using three different approaches. The computed vortex circulation is compared with aircraft measurements. As a result we see that the new transient hybrid approach provides physically reasonable results. The landing gears have a notable effect on the aircraft's drag, as well as on the wake footprint. However, the effect on the wake vortex circulation evolution is moderate. Remarkably, the simulations with landing gear show a strong coherent vortex, merging late with the main vortex. A particular emphasis is put on the comparison with LIDAR measurement data collected in a recent campaign at Vienna airport. The vortex structures predicted by the simulations are clearly visible in those measurements. Simulated tangential velocity profiles are compared with vortex model profiles. It is observed that standard vortex models fail to capture the complex vortex structures emerging during the landing process but can be improved including mirror vortices.

1. Introduction

Wake vortices are generated by flying aircraft in a natural way through the creation of lift. The complex wake structures in the aircraft's near-field roll-up to a vortex system of two counter-rotating vortices further downstream. The generated two-vortex system can persist for several minutes, possessing a high amount of kinetic energy and thereby posing a potential hazard to following aircraft. In ground proximity the transport and decay of the wake vortices are mainly determined by the wind conditions and the interaction with the ground, Bricteux et al. (2016). To avoid wake-vortex encounters, regulatory separation distances between aircraft pairs have to be maintained based on the involved aircraft's weights, which limit the capacity at airports. Therefore, the investigation of wake-vortex decay is an important subject in aviation since the 1980s, Spalart (1998); Gerz et al. (2002).

Despite four decades of intensive research, the wake vortex issue is still a fascinating field of fluid dynamics research that is highly application-oriented. From theoretical, numerical and furthermore experimental points of view there are still many open questions relevant for the air traffic management. The aim of understanding wake vortices in ground proximity triggers new numerical and experimental developments. The high Reynolds number flow involving highly complex geometries, strong coherent structures and no distinguished mean flow direction makes it difficult to understand and predict accurately.

A landing aircraft generates a highly complex flow field in terms of structure and relevant scales. The flow around the main wing, fuselage, slat, flap, jet engine and tailplane, as well as the interaction with the ground and the sudden lift reduction during touchdown substantially affect the generated wake vortices.

We characterize the evolution of the aircraft's wake during landing by four main phases, *Final approach, Flare, Touchdown* and *Roll-out*, Stephan et al. (2014). Independently from this, the aircraft wake evolution is frequently considered to consist of three distinct phases, the *roll-up phase*, the *vortex phase* and the *decay phase* (Breitsamter, 2011). Usually, Reynolds-averaged Navier-Stokes (RANS) simulations are used for computing the flow field around the aircraft and the subsequent roll-up process of the wake (Stumpf, 2005). The dynamics of wake vortices after roll-up until decay have been mainly studied by large-eddy simulations (LES) considering various atmospheric conditions including turbu-

lence, thermal stability and wind shear (Holzäpfel, 2003; Misaka et al., 2012). In those studies a vortex pair with a constant velocity profile along flight direction was initialized in the computational domain. The interaction with the ground has also been simulated by initializing fully rolled-up vortices (Proctor et al., 2000; Georges et al., 2005). This approach neglects the vortex roll-up process, different vortex generation heights above ground, the effect of the touchdown maneuver and may not fully capture the three-dimensional vortex deformations appearing during ground interaction.

Complementary to simulations, real wake vortex flows have mainly been investigated by measurements using a *light detection and ranging* (LIDAR) device (Constant et al., 1994). An emitted laser beam is reflected and scattered by aerosols moving with the vortex flow. The detected signal provides the particle position and the phase shift of the photons, which reveals the velocity towards the detector by the Doppler-shift. A major challenge in experimental wake vortex physics is the development of accurate algorithms deducing the main vortex characteristics like position and circulation from the raw signal. It turns out that those algorithms are highly dependent on the LIDAR system and its technical specifications. For a $2\mu\,\mathrm{m}$ pulsed Doppler LIDAR system (Köpp et al., 2004; Smalikho & Rahm, 2010) the so-called *velocity envelope method* is most popular, whereas for the well-established $1.54\mu\,\mathrm{m}$ LIDAR systems the so-called *radial velocity method* is yielding the best results (Smalikho et al., 2015). These algorithms are using a Burnham-Hallock vortex profile as a model vortex to estimate the vortex circulation from the radial velocity scans. Far from the ground this model assumption is justified and leads to good results. Here we investigate if this assumption is still valid in ground proximity. New measurement techniques using *Particle Image Velocimetry (PIV)* systems at the airport have been proposed in Konrath et al. (2013), but applications to wake vortex flow still have to be demonstrated.

The first theoretical investigations on the ground effect have been performed by Wieselsberger (1922) and Prandtl (1923) employing a modification of Prandtl's lifting line theory. It can, however, only be applied for steady flows, that is, assuming a fixed altitude above ground, wing speed and angle of attack. An overview of various analytical approaches for the quantification of the wing in ground effect (WIG) can be found in Pistolesi (1937). Solutions for two- and three-dimensional wings may be found in Widnall & Barrows (1970). Daeninck et al. (2006) investigates the wake vortex roll-up in ground effect for different wing aspect ratios and span loadings at various altitudes above ground. A double elliptical chord distribution as a model for a high-lift configuration is also studied. The steady-state wing in ground effect is modeled using Prandtl's lifting line theory. All these considerations have been purely stationary and thus ignoring the flight path angle, the flare and the changing angle of attack.

Real aircraft landings are characterized by a complex coupled system of parameters like angle of attack, flight speed, flight altitude and attitude, etc. Such complex coupled systems can be derived from flight measurement data (Jategaonkar, 2006). An overview of the ground effect from the system identification view can be found in (Fischenberg, 1999). In the systemic approach analytical models for lift and drag coefficients in ground effect are considered. Model parameters are identified using flight test data and these are later validated in simulations.

Large-Eddy Simulations (LES) proved to be an effective method to study the dynamics of wake vortices after roll-up until decay. Those have been substantially developed since the first LES was applied to study the evolution of the potentially hazardous aircraft wake. With a pure LES approach, a vortex pair with a constant velocity profile along the flight direction is initialized. It may incorporate different vortex profiles and even multiple vortex systems. This technique was successfully applied for studying the dynamics of wake vortices after roll-up until decay, taking into account various atmospheric conditions like turbulence, thermal stability and wind shear, both out of ground, Holzäpfel (2003); Misaka et al. (2012), as well as in ground proximity, Proctor et al. (2000); Bricteux et al. (2016); Holzäpfel et al. (2016). This approach can also be applied to the problem of landing aircraft and the wake-vortex interactions in ground proximity. However, the pure LES method has its limitations, as it cannot capture the effects of the wake roll-up process, the touchdown maneuver and the wing in ground effect at varying vortex generation heights above the ground. Hence, the full three-dimensional vortex deformations and instability mechanisms, appearing during ground interaction, cannot be investigated.

The coupling of RANS and LES simulations is an innovative methodology to simulate the aircraft flight through a computational, generating a wake in a realistic way, Misaka et al. (2013, 2015). For this purpose a pre-computed high-fidelity steady RANS flow field is swept through the LES domain. This is done to initialize the aircraft wake in the LES domain and will be further referred to as "spatial LES". This method includes all stages of wake-vortex evolution, from roll-up to vortex decay. The results have

revealed valuable insights for cruise flight, Misaka et al. (2015), as well as flight in ground proximity during the landing phase, Stephan et al. (2014). With this study the focus is put on the wake-vortex physics, including three-dimensional effects of decaying vortices in ground proximity. Their evolution is driven by the complex interaction of many factors including ambient turbulence, turbulent wind, ground interaction, the touchdown maneuver and the triggered end effects, Stephan et al. (2017).

While Stephan et al. (2014) gives a first attempt to study wake vortices of a landing aircraft with hybrid RANS/LES methods, the current paper develops the method further. The unsteady nature of the flare is addressed in the current hybrid RANS/LES simulation using two different approaches. Firstly, different flight states at different heights above the ground are simulated in separate steady RANS simulations. These states are mapped into the LES domain at the respective instant of time and are then used for several consecutive time-steps in the LES. In contrast to Stephan et al. (2014), where the wing-in-ground effect was merely calculated by the LES, here an accurate RANS simulation is performed. This method is further referred to as multiple RANS/LES. Secondly, an unsteady RANS of the entire landing process is performed. From this simulation, fields are extracted at the same time steps as in the multiple RANS/LES, and used to initialize the flow-field in the LES. This method is referred to as URANS/LES. This investigation was carried out to analyze the transient effects in the flow field around the aircraft during the unsteady descent of the aircraft to the ground and the derotation maneuver after touchdown. Both methods are compared in this study with respect to the circulation development of the wake vortices after touchdown. Special attention is put on the instant of touchdown. While Stephan et al. (2014) models the instant of touchdown by fading the forcing term in the LES, this work simulates the instant of touchdown. Measurement results of a real A320 landing are presented and used for validation. Additionally, the question of the landing gear influence on the wake vortices is addressed and simulated with both multiple RANS/LES and URANS/LES.

To enable an exact simulation of the wake vortices in the LES domain, an accurate pre-computed RANS flow field around the aircraft generating the vortices is needed. Hence, for the RANS simulations a detailed model of the Airbus A320 “ATRA” in high-lift configuration, including the landing gear, was used, Rohlmann (2018). The simulations were performed with and without landing gear to investigate the influence of the landing gear on the flow around the aircraft. Furthermore, the influence of the ground effect on the flow around the aircraft during approach and touchdown was investigated by simulations at different altitudes of the aircraft above the ground.

2. RANS Methods

2.1. Geometry

Within the DLR project L-bo*ws* an Airbus A320 airplane was used as a wake vortex generator. For the RANS simulations a very detailed CAD model of the Airbus A320 “ATRA” operated by the German Aerospace Center (DLR) was available. All investigations shown in this paper were carried out using the high-lift configuration “Full LDG”. This implies a deflection angle of $\delta_{flaps} = 40^{\circ}$ for the flaps and a deflection angle of $\delta_{slats} = 27^{\circ}$ for the slats. Besides the high-lift elements, the CAD model also includes the slat tracks, the IAE V2500 turbofan engine cowling, the flap track fairings and the vertical and horizontal tail planes. Furthermore, the CAD model also includes a slightly simplified main and nose landing gear. Fig. 1 (a) gives an overview of the CAD model used. In Fig. 1 (b) the CAD model of the simplified main landing gear is shown. The steady RANS simulations were performed with and without landing gear. For the unsteady RANS simulation of the simplified touchdown maneuver, the configuration without landing gear was used.

2.2. Mesh

The RANS simulations within the project L-bo*ws* were performed using hybrid unstructured meshes. The meshes were build using the mesh generator Centaur, Centaur (2017). They are based on the experience gathered during the project HINVA Rudnik et al. (2012); Bier et al. (2012); Rohlmann & Keye (2015). The work in HINVA was also focused on the Airbus A320 high-lift configuration. The meshing of the surfaces and the boundary layers in L-bows is based on the meshes used in HINVA. Additionally, the volume meshes were strongly refined in the regions of wakes and vortex systems produced by the

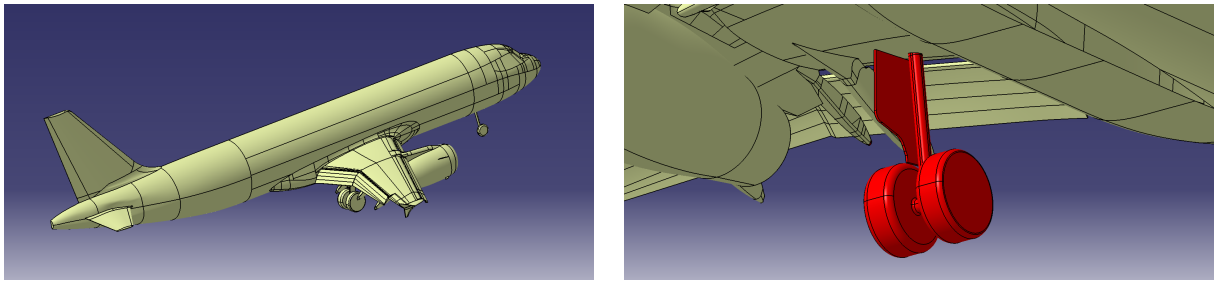

(a) Overview (b) Main landing gear

Figure 1: CAD model

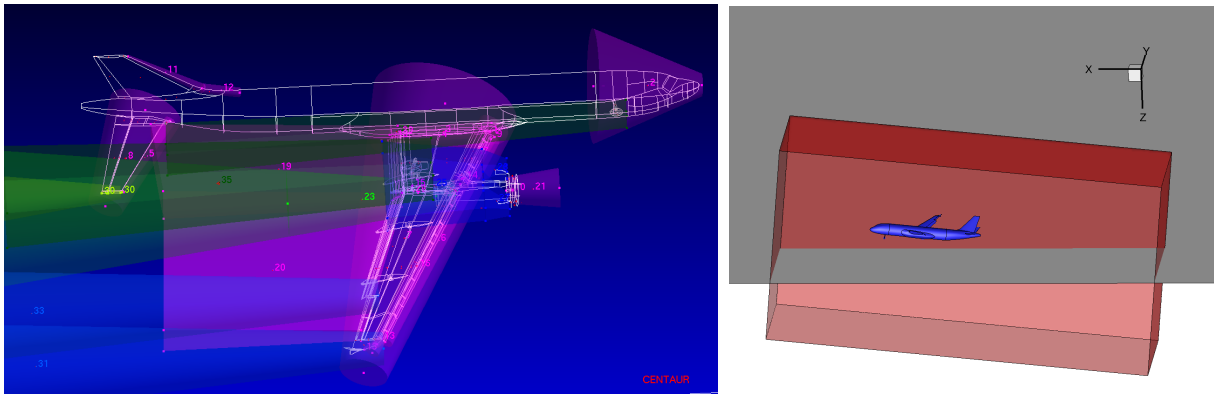

(a) Centaur setup (b) Block setup

Figure 2: Overview of volume source and mesh block setup

wing, the high-lift devices, the landing gears and the tail planes. To achieve a proper resolution of the boundary layers on the non-slip walls, 40 prisms layers were used on all non-slip walls in the complete mesh. The meshes are, thereby, of a very high resolution in order to resolve all relevant flow phenomena around the Airbus A320 high-lift configuration. Figure 2 (a) provides an overview of the Centaur volume source setup.

To realize the simulation at different altitude steps, an approach using multiple mesh blocks was chosen for the meshing. The simulated flow volume is divided in several overlapping mesh blocks, which are meshed separately. After the meshing, the relative position of the blocks is set up in the flow solver and the flow field is calculated for the whole domain using the Chimera technique for the exchange of flow data between the mesh blocks. By using this meshing approach, it is possible to build one separate mesh block for the aircraft and one separate mesh block for the far field including the ground. The relative positioning of these blocks enables realizing different altitude steps by the use of identical meshes. In Fig. 2 (b) an overview of the mesh block setup for one altitude step is given. All mesh parts which are not needed for the simulation, like the mesh below the ground or behind the aircraft, are blanked by the flow solver.

To further improve the quality of the simulated flow field around the aircraft configuration, at each altitude step the meshes were locally refined during the simulation process. This was done by an automatic mesh adaptation process provided by the flow solver. The mesh adaptation is based on a user defined sensor function and is restricted to user defined regions in the flow field. In the simulations presented in this paper, the mesh adaptation was locally restricted to the regions around the vortices and the wakes of the configuration. As a sensor function, the difference in total pressure between two neighboring mesh points was set. The meshes were adapted in up to nine stages for both configurations, with and without gears, for all altitude steps. In Fig. 3 (a) a slice through the volume mesh before the first and in Fig. 3 (b) after nine adaptation steps is shown. An improvement of the mesh resolution in the

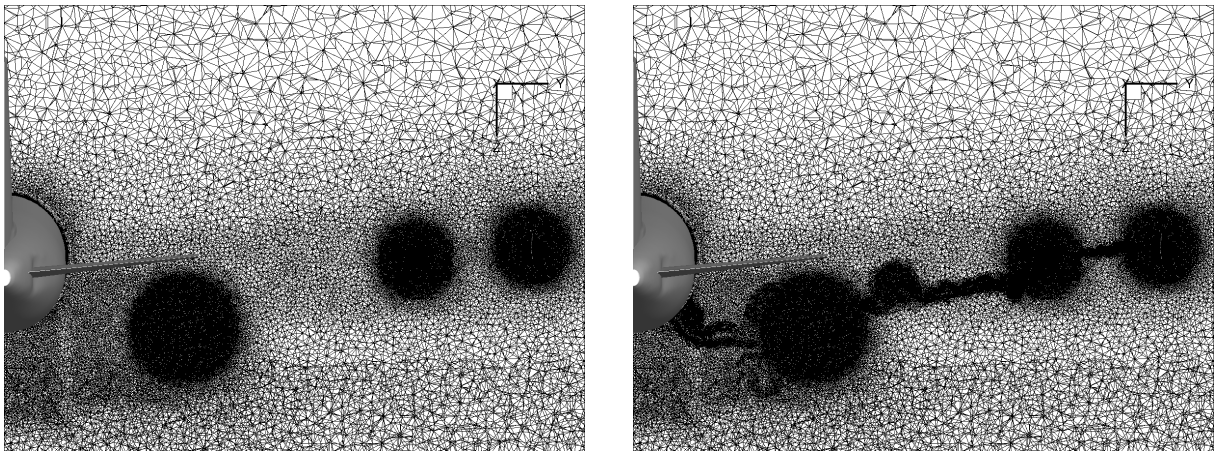

(a) Before automatic refinement (b) After automatic refinement

Figure 3: Slice through mesh

wake of the wing and around the tip vortices of the wing and the high-lift devices can clearly be seen.

Table I: Number of mesh points

Number of surface elements	2.7e+06
Number of prisms	72e+06
Total point number	61e+06

The number of points and elements for the meshes before the automatic mesh adaptation is shown in Tab. I. The automatic mesh adaptation accounts for a roughly 15% increase in total grid point count.

2.3. Flow Solver

Within the current studies the DLR TAU Code, Kroll et al. (2009) was used for the RANS and URANS simulations. TAU is a compressible, unstructured finite volume solver for the Reynolds-averaged Navier-Stokes equations.

For all simulations shown in this paper, the Spalart-Allmaras (SA) turbulence model Spalart & Allmaras (1992) was used. The SA model is robust and sufficiently validated for the simulation of the flow around complex high-lift configurations Bier et al. (2012); Rohlmann & Keye (2015); Rumsey et al. (2011). The time-stepping was done by an implicit lower-upper symmetric Gauß-Seidel (LU-SGS) scheme. A central second-order scheme with Matrix dissipation was employed. A standard "3v" multigrid cycle was applied to accelerate convergence.

A dual time stepping approach was used for the transient URANS simulation of the simplified touchdown maneuver. The unsteady movement of the aircraft during the maneuver was achieved by a relative movement of the mesh block around the aircraft and the far field block including the ground. All surfaces of the aircraft were modeled as non-slip Navier-Stokes walls. The ground was modeled as a slip (Euler) wall. The engine of the aircraft was treated as a through flow nacelle. A jet was not simulated.

2.4. Flow Conditions

The used flow conditions are derived from a real touchdown maneuver of the Airbus A320 “ATRA”. They were converted to the International Standard Atmosphere (ISA) at an altitude of $h = 0\ m$. The resulting flow conditions for the simulations are shown in Tab. II.

The reference values for an elliptic load distribution (Gerz et al., 2002), initial circulation, vortex

Table II: Flow conditions

Density	$\rho = 1.225\,\mathrm{kg}\,/\,\mathrm{m}^3$
Pressure	$p = 101325\,\mathrm{Pa}$
Temperature	$T = 288.15\,\mathrm{K}$
Velocity	$U_\infty = 64\,\mathrm{m}\,/\,\mathrm{s}$
Reynolds number	$Re \approx 18.4 * 10^6$
Mach number	$Ma \approx 0.188$
wing span	$b = 34.1\,\mathrm{m}$
wing plan-form area	$A = 122.6\,\mathrm{m}^2$
total lift coefficient	$C_L = 1.67$

spacing, vortex descent velocity, characteristic time, vorticity unit are given as

$$\Gamma_0 = \frac{2C_L U_\infty A}{\pi b}, \quad b_0 = \frac{\pi}{4} b, \quad w_0 = \frac{\Gamma_0}{2\pi b_0}, \quad t_0 = \frac{b_0}{w_0}, \quad \omega_0 = \frac{1}{t_0}, \tag{1}$$

resulting in $\Gamma_0 = 244.2\,\mathrm{m}^2\,/\,\mathrm{s}$, $b_0 = 34.1\,\mathrm{m}$, $w_0 = 1.45\,\mathrm{m}\,/\,\mathrm{s}$, and $t_0 = 18.45\,\mathrm{s}$, see Tab. III. For the sake of clarity physical quantities are not normalized in this work. We set $t = 0$ at the instant of the touchdown or the crossing of a surface, depending on the context. The maximum tangential velocity of the wake vortices is around $20\,\mathrm{m}\,/\,\mathrm{s}$.

Table III: Reference values

initial vortex separation	$b_0 = 26.8\,\mathrm{m}$
initial circulation	$\Gamma_0 = 244.2\,\mathrm{m}^2\,/\,\mathrm{s}$
vortex descent speed	$w_0 = 1.45\,\mathrm{m}\,/\,\mathrm{s}$
characteristic time	$t_0 = 18.45\,\mathrm{s}$

2.5. Steady Simulations

The steady RANS simulations were performed for the configurations with and without landing gears at a constant angle of attack for eight altitude steps between $h = 0\ m$ and $h = 175\ m$. In this study the altitude is defined as the distance between the main landing gear and the ground. The angle of attack was set to $\alpha = 6°$, which was the average angle of attack during the approach in the flight test data.

2.6. Simulation of the Touchdown Maneuver

The movement of the aircraft during the simplified touchdown maneuver was derived from real touchdown maneuvers of the Airbus A320 “ATRA”. The simplified maneuver features a constant angle of descent with constant velocity up to the touchdown. After that the aircraft rotates to an angle of attack of $\alpha = 0°$. During rotation the angular velocity, as well as the horizontal velocity, are kept constant. During the descent to the ground the angle of attack is kept constant at $\alpha = 6°$, the same angle of attack as in the steady RANS simulations. In the unsteady maneuver simulation this angle of attack is achieved by the addition of the constant geometric angle of attack the aircraft geometry and a superposition of the horizontal and vertical components of the aircraft velocity.

In Fig. 4 the development of altitude and angle of attack during the maneuver is shown as a function of time. The physical time step for the transient simulation had to be set to a relatively high value of $\Delta t = 0.05\ s$ due to the long simulated physical time span. Due to the limited dynamics of the maneuver and the quasi-steady flow conditions, this relatively large time step still results in an acceptable convergence of the inner time steps of the URANS simulation.

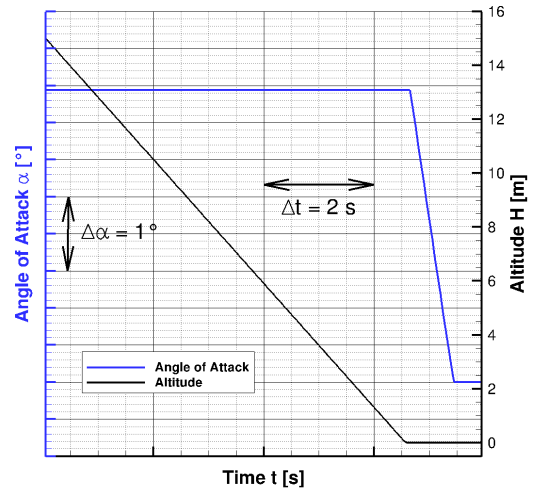

Figure 4: Altitude and geometric angle of attack during the touchdown maneuver

3. LES Methods

3.1. MGLET - Multi-Grid Large Eddy Turbulence

The Large Eddy Simulation is performed using the incompressible LES code MGLET, developed at the Technical University of Munich, Manhart (2004). It solves the incompressible Navier-Stokes equations:

$$\frac{\partial u_i}{\partial t} + \frac{\partial (u_i u_j)}{\partial x_j} = -\frac{1}{\rho}\frac{\partial p'}{\partial x_i} + \frac{\partial}{\partial x_j}\left((\nu + \nu_t) 2 S_{ij}\right) \quad , \tag{2}$$

$$\frac{\partial u_j}{\partial x_j} = 0\,. \tag{3}$$

Here u_i represents the velocity components in the three spatial directions $(i = 1, 2, \text{ or } 3)$, $S_{ij} = (\partial u_i/\partial x_j + \partial u_j/\partial x_i)/2$ denotes the strain rate tensor and $p' = p - p_0$ equals the pressure deviation from a reference state p_0. The kinematic viscosity is given as the sum of molecular viscosity ν and eddy viscosity ν_t, determined by means of a Lagrangian dynamic sub-grid scale model, Meneveau et al. (1996). Eqns. (2) and (3) are solved by a finite-volume approach, using a fourth-order compact scheme, Hokpunna & Manhart (2010). A split-interface algorithm is used for the parallel solution of the tri-diagonal system, Hokpunna (2009), resulting from the compact scheme. A third-order explicit Runge-Kutta method is used for the time integration. The simulations are performed in parallel, using a domain decomposition approach.

3.2. Wake initialization

A realistic aircraft wake is generated in an LES domain by sweeping a high-fidelity steady RANS flow field through the domain, which enables the simulation of the wake-vortex evolution from its generation until its final decay (Misaka et al., 2015). The RANS flow field delivers a forcing term for the Navier-Stokes equations solved in the LES. This approach is referred to as a fortified solution algorithm (Fujii, 1995), or a nudging technique used in data assimilation (Kalnay, 2003). The resulting velocity field in the aircraft vicinity consists of the weighted sum

$$\mathbf{V} = f(y)\mathbf{V}_{\text{LES}} + (1 - f(y))\mathbf{V}_{\text{RANS}} \tag{4}$$

of the LES and the RANS velocity fields, see Figure 5, with a transition function

$$f(y, \alpha, \beta) = \frac{1}{2}\left[\tanh\left[\alpha\left(\frac{y}{\beta} - \frac{\beta}{y}\right)\right] + 1.0\right]. \tag{5}$$

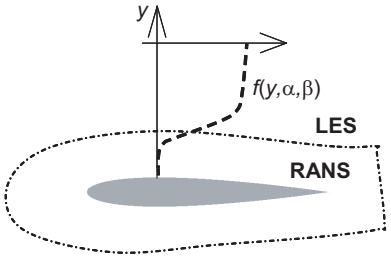

Figure 5: Schematic of a weighting function for a combination of RANS and LES flow fields (Misaka et al., 2015).

Here α and β represent the slope and the maximum wall-distance of the transition region, for which we employ similar values as in Misaka et al. (2015). The mapping of the RANS flow field from an unstructured mesh to the structured grid of the LES solver is performed by a linear interpolation conducted only once before the wake initialization. First the steady RANS solution is mapped to a Cartesian grid, a so-called frame, which is then mapped to the LES grid and shifted for every time step. As the frame can only be mapped at discrete grid positions of the LES grid, an inclined glide path can not be realized by a single fixed frame. Thirty-two frames have to be prepared in advance, interpolating the aircraft flow in between, leading to a smooth wake initialization. This way we meet the Courant-Friedrichs-Levy (CFL) condition and achieve a realistically small aircraft descent angle. This requires additional memory, but does not result in a significant increase of computational time for the simulation.

This hybrid method also enables us to study the effect of an ambient turbulent crosswind on the aircraft wake by initializing the wake within a pre-simulated turbulent wind field, Stephan et al. (2017). In the present work stratification effects are not taken into account.

3.3. Computational domain, approach and boundary treatment

The hybrid simulation approach and the switch to pure LES (large arrow) are sketched in Figure 6. The first part of the simulations includes the hybrid RANS/LES wake initialization until touchdown, Figure 6 (a). The second part is a pure LES of the wake-evolution, Figure 6 (b). We employ periodic boundary conditions in the flight and spanwise directions, a no-slip condition at the ground (bottom) and a free-slip condition at the top of the LES domain. The aircraft starts in the back part of the domain, passes the boundary and approaches the ground. Because of the periodicity the aircraft is placed in front of the domain in Figure 6 (a). After touchdown, the first slice of the domain is extended into the back part at the slope of the vortex and closed artificially to a horse shoe vortex, see Figure 6 (b). This procedure effectively minimizes disturbances generated at the starting point of the vortex initialization. Note that wake vortex linking due to Crow instability is frequently observed in cruise altitudes and may also occur in ground proximity. When the landing gear touches the ground the lift ceases quickly. Then the bound vortex, i.e. the circulation around the aircraft wings, and consequently the wake vortices are strongly reduced. We model the touchdown by removing the RANS flow field forcing term from the simulation. In the LES domain we employ uniform mesh spacing for all three spatial directions, with a resolution of $dx = dy = dz = 0.3\,\mathrm{m}$. The dimensions are $(L_x, L_y, L_z) = (614.4, 153.6, 57.6) = (22.9b_0, 5.7b_0, 2.1b_0)$ on a $(N_x, N_y, N_z) = (2048, 512, 192)$ grid, leading to a total of approximately 200 million grid points. The back part of the domain with a length of $5b_0$ is used as a ghost domain where the aircraft motion starts. Here, the subsequent reconnection of the vortex pair by a horseshoe vortex takes place. The aircraft passes the domain boundary at a height of $1.2b_0$. At touchdown the tail wing is at $x^* = 16.3$.

3.4. Reproduction of turbulent fluctuations

From Czech et al. (2004) and Stephan et al. (2013) it is evident that the transfer of turbulent fluctuations in the wake to the LES field is important for the simulation of the wake evolution. In this work we use the approach employed by Misaka et al. (2015). As turbulent velocity fluctuations are modeled in a RANS simulation, but resolved in an LES simulation, they have to be reconstructed in the LES domain from the RANS eddy viscosity during the mapping process.

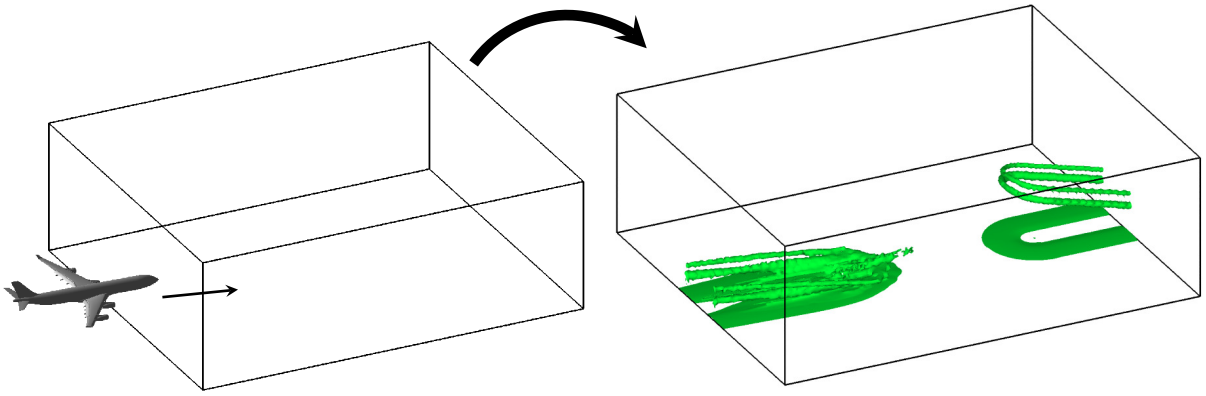

(a) Wake initialization until touchdown. (b) LES, vortex decay after touchdown, domain shortened.

Figure 6: Schematic of an aircraft landing displaying the computational domain and the wake evolution (a) before touchdown, during wake initialization, (b) after touchdown with artificial vortex reconnection (from Stephan et al. (2014)).

In a straightforward approach the velocity fluctuations are modeled as white noise fluctuations in the RANS-LES transition region, their magnitude being controlled by a proportional-integral (PI) controller during the movement of the RANS field through the LES domain.

$$\mathbf{V}_{\mathrm{RANS+WN}} = \mathbf{V}_{\mathrm{RANS}} + K\mathbf{V}_{\mathrm{WN}}, \tag{6}$$

$$K = a_1(\overline{k}_{t,\mathrm{LES}} - k_{t,\mathrm{RANS}}) \tag{7}$$

$$+ \; a_2 \int (\overline{k}_{t,\mathrm{LES}} - k_{t,\mathrm{RANS}})dt, \tag{8}$$

where V_{WN} denotes the white noise velocity field and K controls its magnitude. The constants are set to $a_1 = 10$ and $a_2 = 1.0$ in the simulations.

3.5. Hybrid RANS/LES cases

In this section three different hybrid RANS/LES approaches are presented. All together five hybrid simulations are performed, which are presented in the results section. First, a coupled simulation with a single RANS field, without any influence of the ground, obtained at a height of $h = 175\,\mathrm{m}$ is performed for both cases, with and without landing gear. These simulations are denoted by sRg and sRn respectively. This approach is presented in Stephan et al. (2014) and serves as a reference for the new approach.

In the second approach we take multiple RANS fields at different heights from the steady RANS simulations as listed in Tab. IV and initialize them at the respective positions, see Tab. IV. Here, again, the simulations are performed with and without landing gear. They are denoted by mRg and mRn, respectively. In the case without landing gear we also use the RANS field at the $h = 0m$ position, with an angle of attack $aoa = 6^o$, as well as the derotated RANS field at $h = 0m$ with $aoa = 0^o$.

In the last approach, the unsteady RANS simulation delivers multiple solution snapshots for the LES at different heights, as listed in Tab. IV. The simulation is only performed without the landing gear, denoted by URn. We also use the RANS flow field at the $h = 0m$ position with $aoa = 6^o$, as well as the derotated RANS field at $h = 0m$ with $aoa = 0^o$.

4. Flight measurement data

To study the flare and touchdown phases we employ flight test data from tests that have been performed by the *Institute of Aerodynamics and Flow Technology (DLR)* as validation experiments for the simulation model A320-ATRA on behalf of Airbus. The present flight test data of a landing (test No.12) was kindly provided by Christian Raab. Various parameters have been evaluated. All quantities are calculated from

Table IV: RANS field initialization heights.

RANS altitude	mRg	mRn	URn
$20\,\mathrm{m}$	$33.9\,\mathrm{m} \sim 17.4\,\mathrm{m}$	$33.9\,\mathrm{m} \sim 17.4\,\mathrm{m}$	–
$15\,\mathrm{m}$	$17.4\,\mathrm{m} \sim 12.6\,\mathrm{m}$	$17.4\,\mathrm{m} \sim 12.6\,\mathrm{m}$	$33.9\,\mathrm{m} \sim 12.6\,\mathrm{m}$
$10\,\mathrm{m}$	$12.6\,\mathrm{m} \sim 7.5\,\mathrm{m}$	$12.6\,\mathrm{m} \sim 7.5\,\mathrm{m}$	$12.6\,\mathrm{m} \sim 7.5\,\mathrm{m}$
$5\,\mathrm{m}$	$7.5\,\mathrm{m} \sim 3.9\,\mathrm{m}$	$7.5\,\mathrm{m} \sim 3.9\,\mathrm{m}$	$7.5\,\mathrm{m} \sim 3.9\,\mathrm{m}$
$2.5\,\mathrm{m}$	$3.9\,\mathrm{m} \sim 1.8\,\mathrm{m}$	$3.9\,\mathrm{m} \sim 1.8\,\mathrm{m}$	$3.9\,\mathrm{m} \sim 1.8\,\mathrm{m}$
$1\,\mathrm{m}$	$1.8\,\mathrm{m} \sim 0\,\mathrm{m}$	$1.8\,\mathrm{m} \sim 0.6\,\mathrm{m}$	$1.8\,\mathrm{m} \sim 0.6\,\mathrm{m}$
$0\,\mathrm{m}$	–	$0.6\,\mathrm{m} \sim 0\,\mathrm{m}$	$0.6\,\mathrm{m} \sim 0\,\mathrm{m}$
$0\,\mathrm{m}$, $aoa = 0^o$	–	$0\,\mathrm{m}$	$0\,\mathrm{m}$

the measured ones taking the ground effect into account. Though the data is fairly fluctuating, the overall behavior is very useful as a reference.

Figure 7 shows the altitude plotted against the time, including the flare and touchdown maneuvers. Note that the constant approach angle that we use in the LES turns out to be a good approximation of the flight path. The angle of attack is shown in the second plot. Being nearly constant during approach and flare, it decreases rapidly two seconds after the landing gear has touched the ground at $21\,\mathrm{s}$. The third plot of Fig. 7 shows the true airspeed slightly decreasing during approach, moderately decreasing during the flare and strongly decreasing after touchdown. The evolution of the lift and drag coefficients are depicted in the lower two plots of Fig. 7. The lift coefficient slightly increases during approach and flare and strongly increases at the instant of touchdown, where the aircraft experiences a strong vertical force. The drag coefficient stays nearly constant most of the time and only increases drastically after touchdown.

We would like to deduce the wake vortex strength from the flight data. The equations for the lift coefficient C_L (Eqn. 9) and the initial circulation Γ_0 (Eqn. 10) are coupled and deliver the relations (11):

$$C_L = \frac{L}{\frac{1}{2}\rho U^2 A}, \tag{9}$$

$$\Gamma_0 = \frac{L}{\rho b_0 U}, \tag{10}$$

$$L = C_L \frac{1}{2}\rho U^2 A, \qquad \Gamma_0 = \frac{C_L U A}{2 b_0}. \tag{11}$$

Beside the strong fluctuations we conclude from Fig. 8 (plot 1) that the vortex strength slightly increases during approach and flare, whereas the increase in the lift force L is negligible (plot 2). Instead, it fluctuates around a single level matching the weight force of the aircraft. Note that substantial fluctuations of Γ during approach and landing may, besides ambient turbulence, also contribute to the observed rapid deformation of wake vortices. Addressing the question of the wake-vortex strength during the flare we conclude: If we assume a nearly constant lift force L balancing the weight force, then Γ_0 increases corresponding to the decrease of U, by Eq. (11). However, this effect is moderate. The lift to drag ratio changes substantially more, see third plot in Fig. 8. It suggests an increase of lift forces with respect to drag forces, down to an aircraft altitude of $b_0/4$ $(t = 15s)$, similar to the results from the steady-state theory. Very close to the ground this effect seems to be reversed, which is not consistent with theory. After touchdown the flight data may not be correct. We assume a strong reduction of the wake-vortex circulation directly after touchdown.

5. Results

5.1. Influence of the Ground Effect

The theory of the ground effect, for example Torenbeek (1976), explains the aerodynamic effects using Potential theory. The ground can be seen as a mirror-plane where the system of aircraft vortices is

present on the other side of it. When bringing an aircraft configuration at constant angle of attack closer to the ground, this approach predicts decreasing drag and increasing lift for moderate angles of attack and relatively small lift coefficients. For configurations at higher lift coefficients, with deflected trailing edge flaps or at very low altitudes above ground, this approach results in a decrease of lift with decreasing distance to the ground. The influence of the decreasing ground distance on the lift and drag coefficients of the Airbus A320 in high-lift configuration can be deduced from Fig. 9 based on a RANS simulation. With decreasing altitude the drag also decreases while the lift increases.

In Fig. 9 the development of the lift and drag coefficients and the altitude are plotted against physical time. The thin lines show the actual unsteady development of the coefficients during the simulation, while the bold lines give a smoothed approximation of the unsteady values for altitudes above $h = 0\ m$ by a second degree polynomial. The dots in this figure show the aerodynamic coefficients of the steady RANS simulation described in the previous sections. The aerodynamic coefficients show only very limited fluctuations during the simulation and are very close to the smoothed polynomial approximation. The smoothed curves are showing the behavior predicted by the theory of the ground effect. The small unsteady oscillations observed in the aerodynamic coefficients can be explained by small flow separations at the trailing edge flap. Furthermore, the polynomial approximation of the unsteady aerodynamic coefficients is in very good agreement with the results of the steady RANS simulations. The small dif-

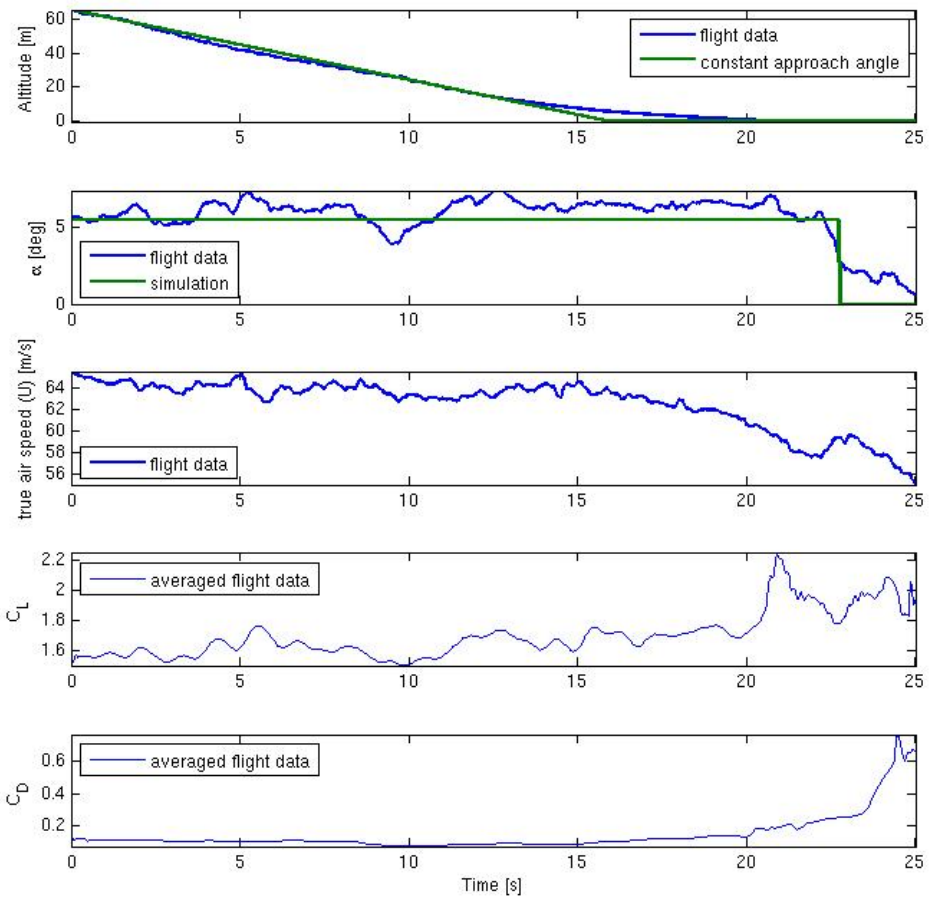

Figure 7: Aircraft altitude, angle of attack, true air speed, lift- and drag coefficients during landing from flight measurements with ATRA research aircraft.

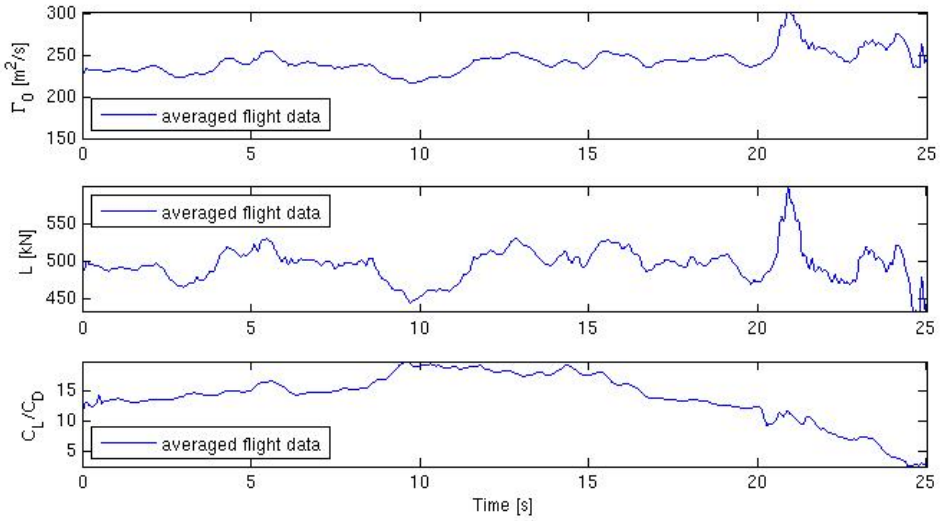

Figure 8: Lift force, wake-vortex circulation tendencies, as well as lift to drag ratio deduced from flight measurements with ATRA research aircraft.

ferences between the steady RANS and the unsteady maneuver simulation can also be explained by the small unsteady flow separations at the trailing edge flap. These transient flow phenomena are not captured correctly by the steady RANS approach.

In the moment of the touchdown the vertical aircraft movement switches to $v_z = 0\ m/s$. Due to this, the angle of attack is decreasing abruptly leading to an abrupt increase of lift and drag. During rotation to an angle of attack of $\alpha = 0°$ the induced angle of attack is increased by a superposition of the horizontal aircraft velocity and the rotation. This results in a slightly increased angle of attack during the rotation. At the beginning of the rotation the step in the angle of attack yields a step-wise increase in lift. Afterwards the lift decreases linearly similar to the angle of attack until $\alpha = 0°$ is reached.

With decreasing altitude, among other effects, the vertical flow between the aircraft and the ground is decelerated and the static pressure increases. This deceleration of the flow compared to free flight can be explained by the mirroring of the vortical system of the aircraft at the ground resulting in an induced flow velocity against the actual flow velocity between aircraft and ground. This induced velocity slows down the flow between the aircraft and the ground resulting in a rise of the static pressure in this region and a higher lift for the aircraft configuration. The effect of the increasing static pressure between the aircraft and the ground with decreasing altitude can be seen in Fig. 10 (a) and Fig. 10 (b). These figures show an iso-surface of the static pressure $c_P = 1$ for the altitudes $h = 5\ m$ and $h = 15\ m$. With decreasing altitude the surface of the constant positive static pressure between aircraft and ground is growing.

5.2. Circulation comparison with flight data

In this section we compare the different hybrid RANS/LES methods with respect to the circulation of the wake vortices after touchdown. The different realizations of the hybrid RANS/LES landing lead to different evolution of wake vortex circulation. The results are compared with the flight measurement data. First, note that steady RANS and URANS lead to very similar results in terms of lift coefficient C_L and drag coefficient C_D, see Fig. 9. The lift coefficient C_L is increasing with decreasing distance to the ground for steady RANS, as well as URANS. The diagram is clipped off at the altitude of $h = 15\ m$ because there is no significant change in the aerodynamic coefficients for higher values. We use different definitions for the circulation in the subsequent discussion. All of those are evaluated in the LES domain. First, Γ_0 as it is defined in Eq. (11) at different aircraft positions, depending on the lift coefficient C_L.

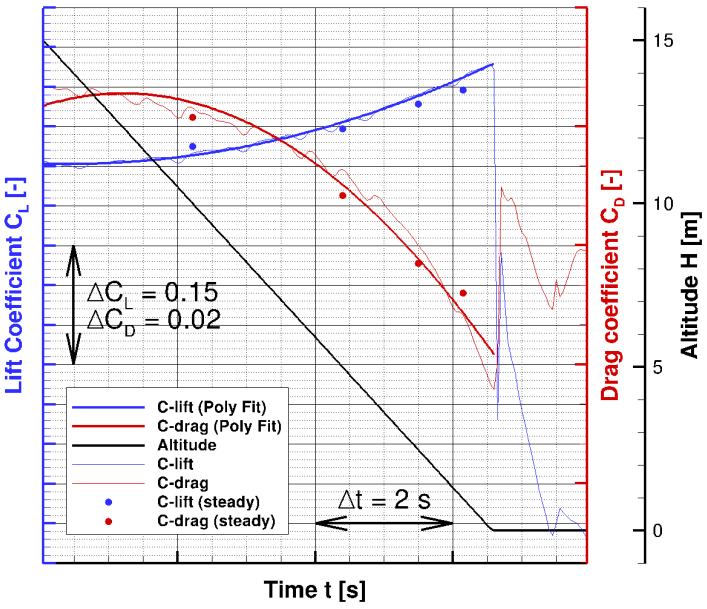

(a)

Figure 9: Development of C_L, C_D and altitude h over physical time, RANS simulations.

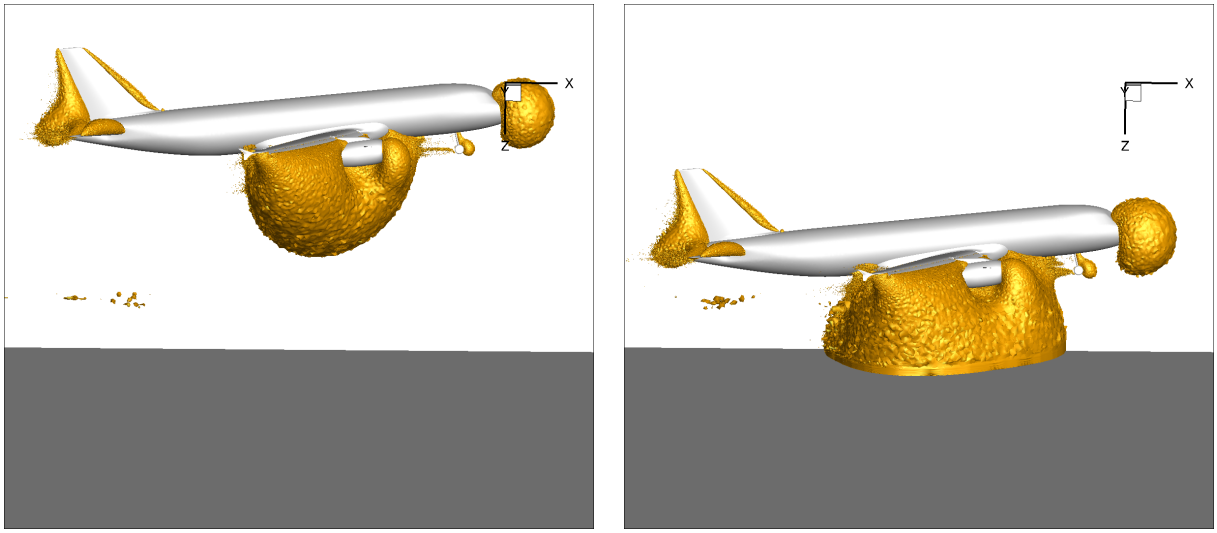

(a) $c_P = 1,\ h = 15\,\mathrm{m}$ (b) $c_P = 1,\ h = 5\,\mathrm{m}$

Figure 10: Iso-surfaces of the static pressure

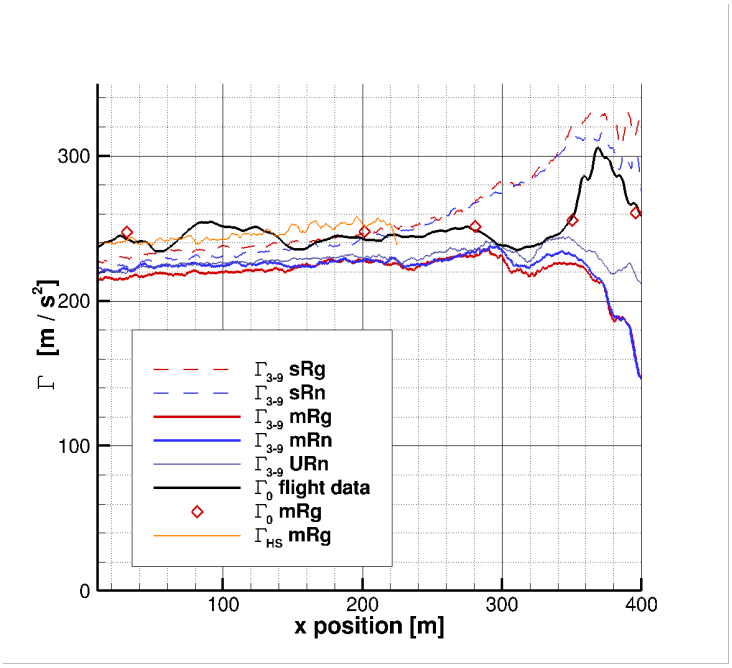

Figure 11: Circulation development for different hybrid techniques compared with flight data along the glide path.

Second, a scaled version of the widely used Γ_{5-15} is employed, namely

$$\Gamma_{3-9} = \frac{1}{6}\int_{3\,\mathrm{m}}^{9\,\mathrm{m}} \Gamma(r)dr, \tag{12}$$

where $\Gamma(r) = \int_{D_r} \omega_x \cdot dA$ denotes the circulation in a disc of radius r centered in the vortex core, which is evaluated in the flow field of the simulation. Third, we use $\Gamma_{HS} = \int_{HS} \omega_x \cdot dA$, the integral of the vorticity in flight direction, taken over the entire half-space of the simulated domain.

Figure 11 depicts Γ_{3-9} for all simulated cases sRn, sRg, mRn, mRg, URn. First, note that when entering the simulation domain, all circulation values are close together. While the transient approaches lead to a slight increase of the circulation, we have stronger circulation growth in the single RANS field hybrid simulations, even accelerating with a closer distance to the ground. As we use a ghost domain on the LES side, as described above, the circulation has already slightly increased for the single RANS simulation entering the domain, compared to the transient approaches. This effect shows that the RANS simulations should be conducted taking the ground into account and the LES cannot fully compensate the shortcomings of a RANS simulation without ground effect. mRn and URn have very similar behavior, especially in the beginning. For the mRn case we also evaluate Γ_0 and Γ_{HS}, which correspond very well with the flight data before touchdown. It turns out that Γ_{3-9} does only capture about 90% of the entire circulation, created by the aircraft, which is in agreement with former results Stephan et al. (2014); Misaka et al. (2015), indicating that vorticity patches may be distributed over relatively large areas. Due to the developing circulation boundary layer, Γ_{HS} does not show sensible results very close to the ground, therefore it is omitted in Fig. 11 for $x > 225\,\mathrm{m}$. Finally, Γ_0 from the landing experiments is plotted in Fig. 11, showing a very consistent behavior with Γ_0 in the mRg case. The circulation derived from flight data is slightly increasing during flare and strongly increasing shortly before touchdown where we actually cannot expect an elliptical wing loading. So, the instant before touchdown has to be analyzed carefully. As we do not have flight data statistics, we cannot consider the flight data graph as the only acceptable truth, but qualitative and quantitative behavior agree well.

All curves are slightly increasing until shortly before touchdown. After that the area used to calculate Γ_{3-9} is overlapping with the ground. Here, the respective disc segment above ground is used for integration. However, the developing secondary vorticity boundary layer at the ground leads to a reduction

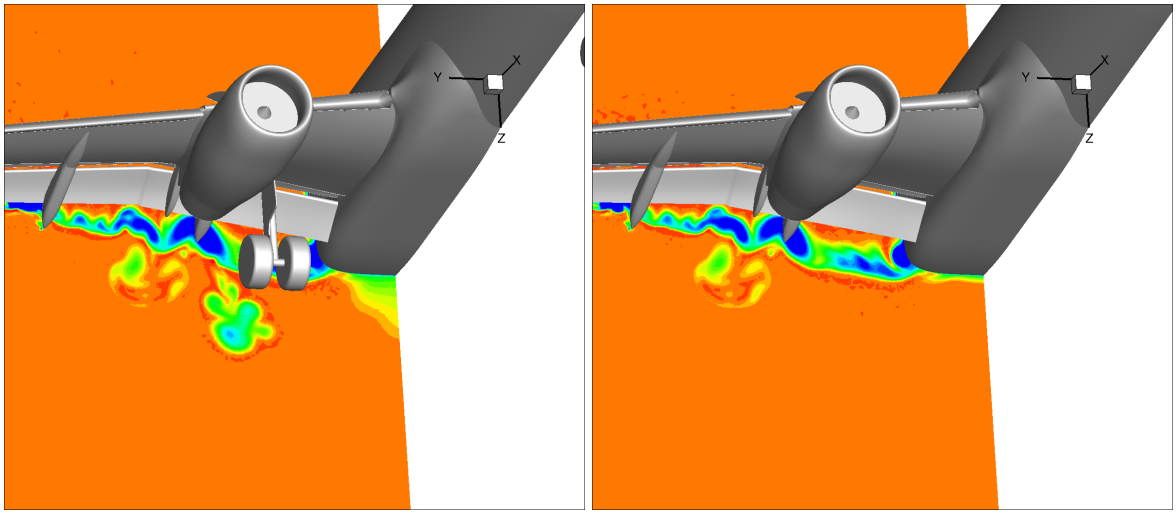

(a) With landing gear (b) Without landing gear

Figure 12: Slice through flow solution - Colored by total pressure - $h = 15\ m$

of Γ_{3-9}.

5.2.1. *Influence of the Landing Gear*

In Fig. 12 the total pressure in the wake of the wing is shown in a slice shortly behind the inboard wing, for an altitude of $h = 15\ m$ for both configurations, with and without landing gear. The strong loss in total pressure in the wake of the wing and the engine is clearly visible in both figures. Additionally, the extensive loss in total pressure behind the landing gear can be seen in Fig. 12 (a). The wakes of the wing and the nacelle are not influenced noticeably by the presence of the main landing gear. Observing the strong wake of the main lading gear we expect an influence on the formation and the development of the wake vortex system of the complete aircraft configuration. Besides the wake of the main landing gear, in Fig. 12 (a), also the wake of the nose landing gear is visible below the fuselage. Compared to the wake of the main landing gear the total pressure loss of the nose landing gear is much smaller due to its smaller dimensions of the nose landing gear and the relatively long distance between the nose landing gear and the slice through the volume presented here.

In Fig. 13 the influence of the ground effect and the landing gear on the lift and drag coefficients is shown for the simulated altitudes. According to Fig. 13 the landing gear has no significant influence on the lift coefficient of the Airbus A320 in high-lift configuration for all considered altitude steps. In contrast, the influence of the landing gear on the drag coefficient is clearly visible for all considered altitude steps. The landing gear accounts for an isolated local disturbance of the flow field around the wing and thus has only a minor impact on the lift coefficient. The small disturbance is located only at the lower side of the inner main wing near the nose of the fuselage. Most of the wing, especially its upper side, the fuselage and the tail planes are not influenced by the landing gear. Furthermore, the surfaces of the landing gear itself are not producing a substantial amount of lift.

In contrast to the minor influence of the landing gear on the lift, the drag is significantly increased by the addition of the landing gear for all altitude steps. This increase is also localized at the landing gear itself since, as described above, the mean flow around the aircraft configuration is only weakly influenced by the landing gear. The landing gear can be considered as a large blunt body located in nearly undisturbed flow producing a strong wake, but almost no lift. The influence of the landing gear on the drag coefficient is decreasing with decreasing altitude. This can be explained by the growing influence of the ground effect on the flow in the surrounding area with decreasing altitude. The growing influence of the ground effect results in a reduced local flow velocity, especially at the position of the main landing gear below the wing, resulting in reduced drag for the whole aircraft configuration for decreasing altitudes.

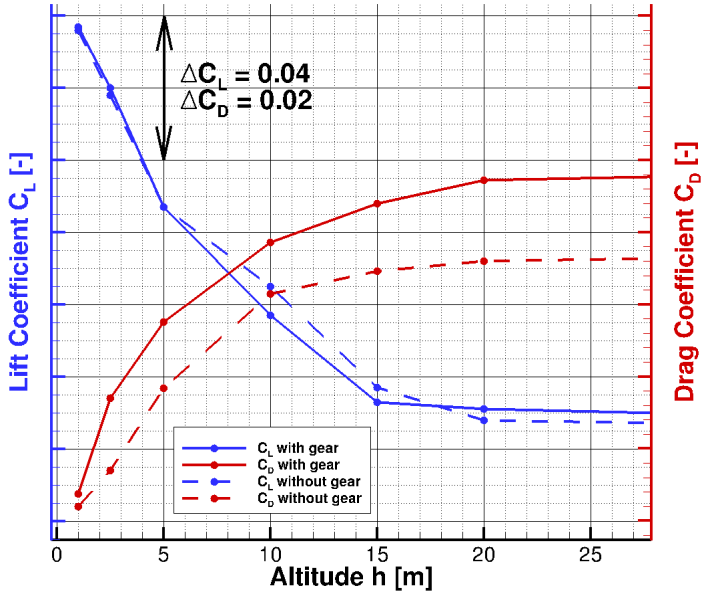

Figure 13: Influence of altitude and landing gear on C_L and C_D

The further propagation of the landing gear's wake is depicted in Fig. 14. Here the vorticity magnitude is plotted in five equidistant slices at positions in front of the touchdown point. The complex vortex system at different positions behind the aircraft is shown with and without the landing gear. We clearly see how the multiple vortex system evolves. We observe wing and flap-tip vortices merging to the main two counter-rotating wake vortices. Additionally, there are two vortices generated by the tailplane propagating downwards, and the wing-fuselage vortices that dissipate in the turbulent wake. Additionally, we see two vortices emerging from the gear wake. They form strong coherent structures and can clearly be seen at the level of the tailplane vortices. We call this vortex the engine-gear-vortex and analyze it. On the contrary, we have less coherency in the wake without the landing gear.

The long-time development of the circulation and the effect of the landing gear are depicted in Fig. 15, for the single and multiple RANS approaches. Here we average the circulation over the first $400\,\mathrm{m}$, where the vortices do not link with the ground. The less accurate one field RANS/LES approach does not reveal any difference caused by the gears, whereas a slightly faster decay is observed when using the multiple RANS/LES approach for the simulation with landing gears. This can be explained by the coherency of the engine-gear-vortex leading to a stronger vortex-ground interaction and a more turbulent decay phase. However, this effect is moderate.

The difference between the simulations with and without landing gear shall be worked out in Fig. 16 and Fig. 17. In both figures the axial vorticity is depicted in a slice perpendicular to the runway at $x = 50\,\mathrm{m}$. The aircraft is passing the slice $6.4\,\mathrm{s}$ before touchdown. Right after the wings crossed the slice $(t = -6.4\,\mathrm{s})$ we observe vorticity sheets behind them, with the wing and flap tip vortices becoming apparent, as well as vorticity shedding off the engine, slats and gears in Fig. 16 (a). The fuselage creates counter-rotating vorticity. After $0.2\,\mathrm{s}$ the tail wings cross the slice. The counter-rotating tailplane and fuselage-wing junction vortices are clearly visible. The main vortices have already established themselves. However, while one single vortex patch is forming behind the engine in the simulations with landing gear, we have two distinct vortices behind each engine in simulations without the landing gear. In the sequel the complex multi-vortex system is further developing. The coherency of the engine vortex is more pronounced with gears, Fig. 16 (c),(d), but without gears the two engine vortices smear out and form an incoherent vorticity sheet.

The wing and flap tip vortex merge quickly and descend, Fig. 16 and Fig. 17 (e)-(f), the inner vortices are transported by the vorticity of the main vortices. The fuselage junction vortices dissipate quickly for both cases. Remarkably, the engine vortices stay coherent in simulations including the landing gear, while dissipating in simulations without it. Note that $2.4\,\mathrm{s}$ before touchdown the tailplane vortices are also

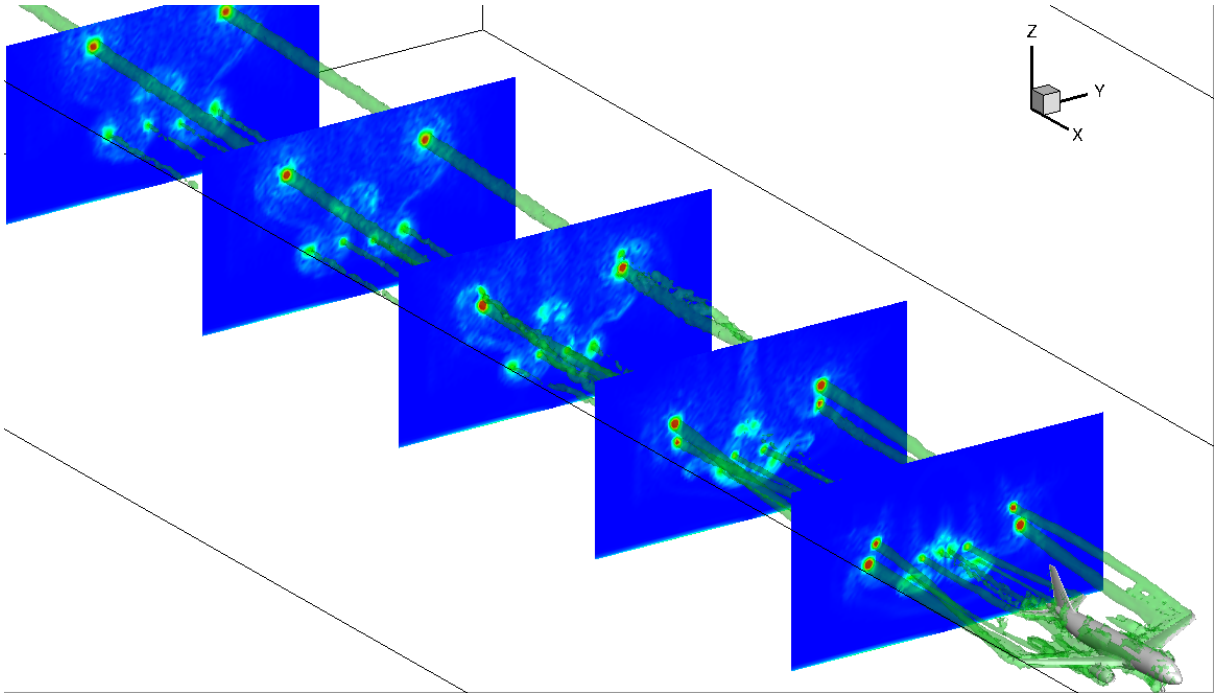

(a) With landing gear

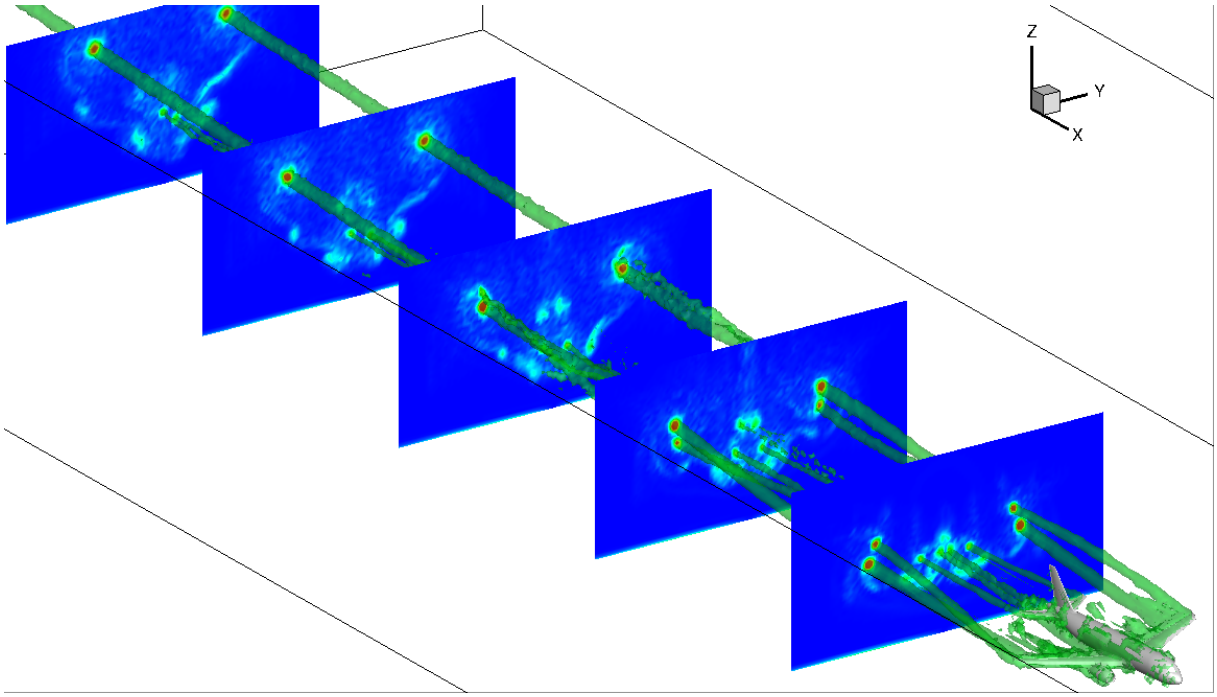

(b) Without landing gear

Figure 14: Multiple slices through the LES flow solution. Vorticity magnitude.

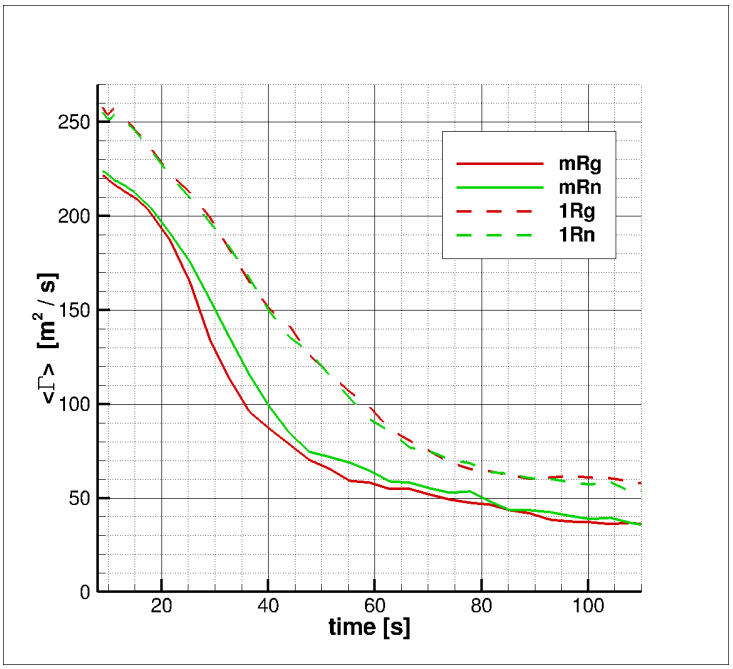

Figure 15: Circulation decay averaged, influence of the landing gear.

significantly less coherent in the case without gears and they also totally dissipate $3.7\,\mathrm{s}$ after touchdown. Due to the ground and the main vortices, the coherent engine vortices are transported quickly outboard in spanwise direction and even start to rebound from the ground, Fig. 16 (i) -(l). [1] We also observe a secondary vorticity layer emerging. Finally, we have three coherent vortices at $t = 3.7\,\mathrm{s}$ in the case with gears, which slowly merge in the sequel and we observe only one in the simulations without landing gear. As we could see, this effect translates to a stronger overall circulation reduction, see Fig. 15. On the one hand it is known that the behavior of multiple interacting vortices may substantially differ for slightly different vortex strengths and positions. On the other hand similar vortex structures can also be observed in LIDAR measurements, see Sec. 5.5., which provides evidence that the observed vortex constellation may occur.

5.3. The Touchdown Maneuver

The wake of the wing right after touchdown and right after the rotation maneuver is visualized in Fig. 18 by the total pressure in a slice behind the wing. The figure shows the decrease of the wake behind the wing, caused by the rotation of the aircraft to an angle of attack of $\alpha = 0°$. As a major consequence the total pressure loss in the wing tip vortex and the vortex at the root of the wing are significantly reduced by the derotation. Furthermore, the loss in total pressure in the engine wake is also apparent. However, the loss in total pressure in the tip vortex of the trailing edge flap is only slightly reduced after the rotation to $\alpha = 0°$. The wake of the inner wing in the region between the fuselage and the engine is even slightly increased. This is a result of the small flow separation observed at the trailing edge flap after the rotation. At the outer wing this effect is not visible because there is no flow separation at the trailing edge flap in this region. The vertical position of the wake behind the wing is not significantly modified by the rotation to $\alpha = 0°$.

[1] This effect of two vortices rolling-up close to the ground is thoroughly investigated in Stephan et al. (2014) for the wing and flap tip vortices of an A340 aircraft.

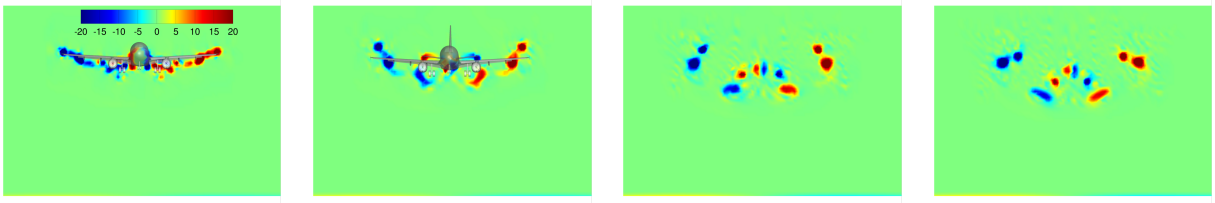

(a) $t = -6.4\,\mathrm{s}$ (b) $t = -6.2\,\mathrm{s}$ (c) $t = -5.7\,\mathrm{s}$ (d) $t = -5.4\,\mathrm{s}$

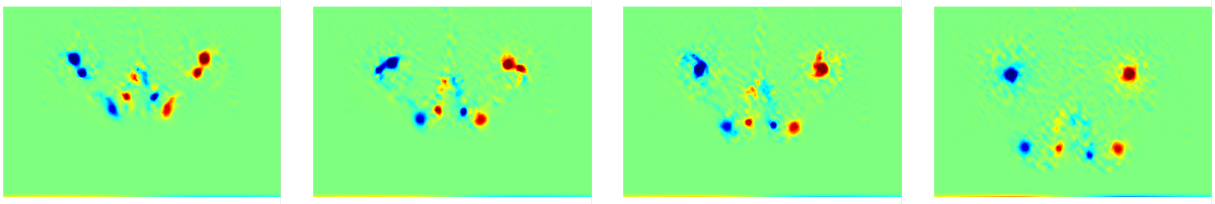

(e) $t = -5.0\,\mathrm{s}$ (f) $t = -4.5\,\mathrm{s}$ (g) $t = -4.0\,\mathrm{s}$ (h) $t = -2.4\,\mathrm{s}$

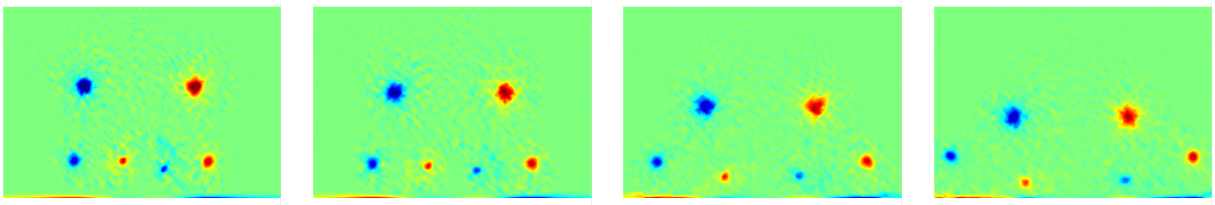

(i) $t = -0.4\,\mathrm{s}$ (j) $t = 0.5\,\mathrm{s}$ (k) $t = 2.3\,\mathrm{s}$ (l) $t = 3.7\,\mathrm{s}$

Figure 16: ω_x distribution - a slice where the aircraft with landing gears is passing through $6.4\,\mathrm{s}$ before touchdown.

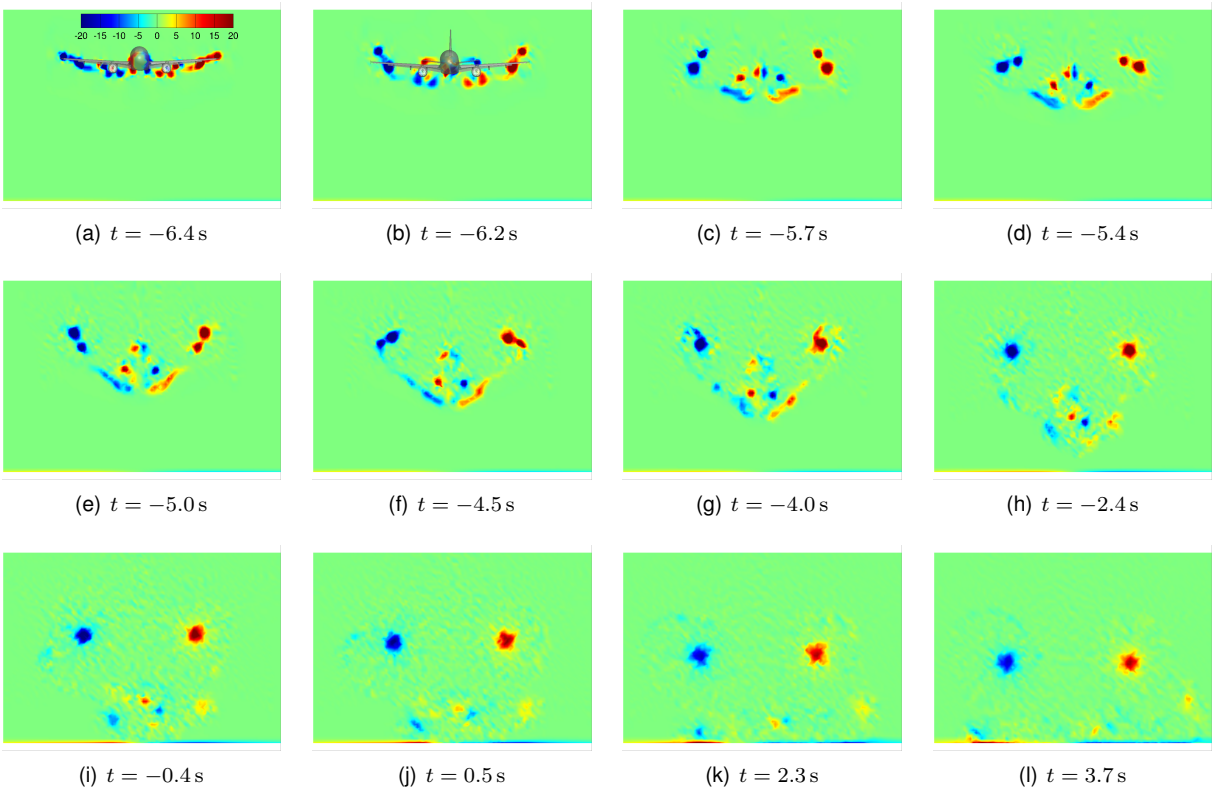

(a) $t = -6.4\,\mathrm{s}$ (b) $t = -6.2\,\mathrm{s}$ (c) $t = -5.7\,\mathrm{s}$ (d) $t = -5.4\,\mathrm{s}$

(e) $t = -5.0\,\mathrm{s}$ (f) $t = -4.5\,\mathrm{s}$ (g) $t = -4.0\,\mathrm{s}$ (h) $t = -2.4\,\mathrm{s}$

(i) $t = -0.4\,\mathrm{s}$ (j) $t = 0.5\,\mathrm{s}$ (k) $t = 2.3\,\mathrm{s}$ (l) $t = 3.7\,\mathrm{s}$

Figure 17: ω_x distribution - a slice where the aircraft without landing gears is passing through $6.4\,\mathrm{s}$ before touchdown.

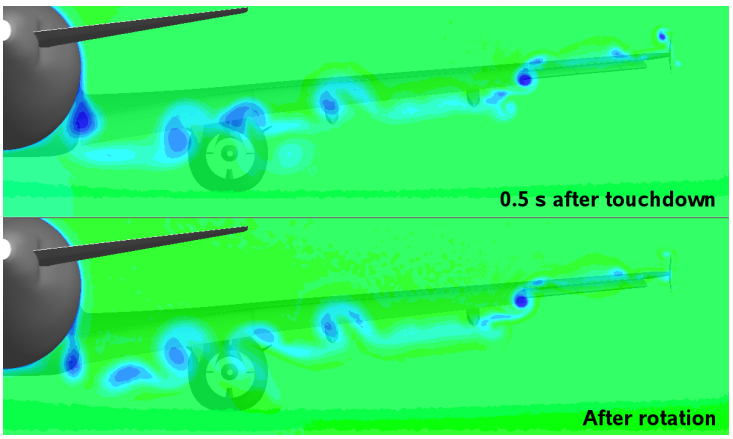

Figure 18: Total pressure in a slice behind the wing, $0.5\ s$ after touchdown and after rotation

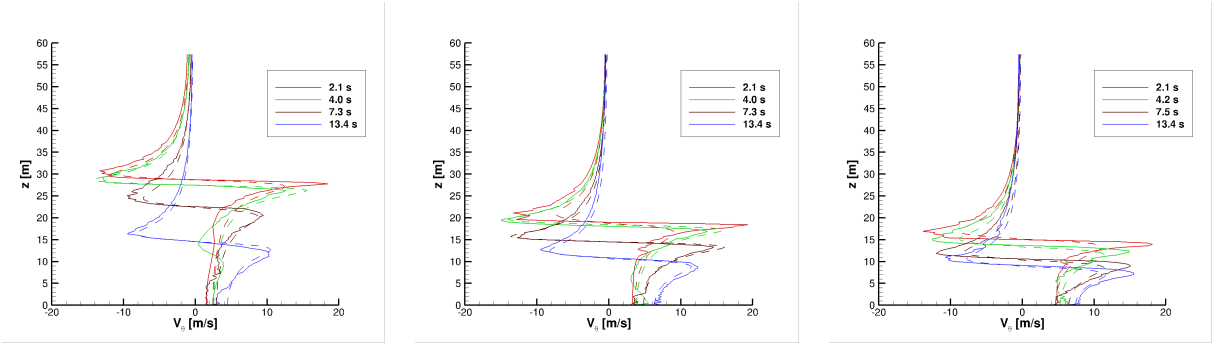

(a) gears, $x = 2\,\mathrm{m}$ (b) gears, $x = 154\,\mathrm{m}$ (c) gears, $x = 231\,\mathrm{m}$

(d) nogears, $x = 2\,\mathrm{m}$ (e) nogears, $x = 154\,\mathrm{m}$ (f) nogears, $x = 231\,\mathrm{m}$

Figure 19: Tangential velocity profiles compared to Burnham-Hallock model including mirror vortices.

5.4. Velocity profiles

In this section we analyze tangential velocity profiles, V_θ, in different slices along the glide path and compare them to the widely used Burnham-Hallock vortex model,

$$V_\theta = \frac{\Gamma_0}{2\pi r}\frac{r^2}{r^2 + r_0^2}, \tag{13}$$

where r_0 denotes the core radius. Figure 19 depicts V_θ profiles for different times after crossing planes at different planes in space, i.e. distances to the touchdown point. Note that we do not observe an anti-symmetric velocity profile, as the aircraft approaches the ground. This effect is mostly captured by the assumption of mirror vortices that model the effect of the wall. Therefore we compare all profiles with the Burnham-Hallock vortex model including a mirror vortex. The effect of the neighboring vortex can be neglected, since we only consider the horizontal velocity components.

This model fits very well at sufficiently for most situations, Fig. 19 (a) to (f). Note the influence of the engine-gear vortex in the simulation with landing gears, Fig. 19 (a) to (c), $4.0s$ after crossing. Particularly very close to the ground, the Burnham-Hallock vortex approximation is getting better with time. The influence of the landing gear is not apparent after $10\,\mathrm{s}$. We observe maximum velocities at the ground surface of about $8\,\mathrm{m}\,/\,\mathrm{s}$.

Indeed, vortex models are widely used for the post-processing of LIDAR wake vortex measurements, Smalikho & Rahm (2010); Smalikho et al. (2015). Especially the Burnham-Hallock model is used in an iterative process that minimizes the error to a certain model field. The presented results indicate that those models should be improved in ground proximity by using mirror vortices. Even the use of mirror vortices in the present algorithms does not entirely meet the character of the flow field very close to the ground when other vortices, like the engine-gear vortex are sufficiently coherent.

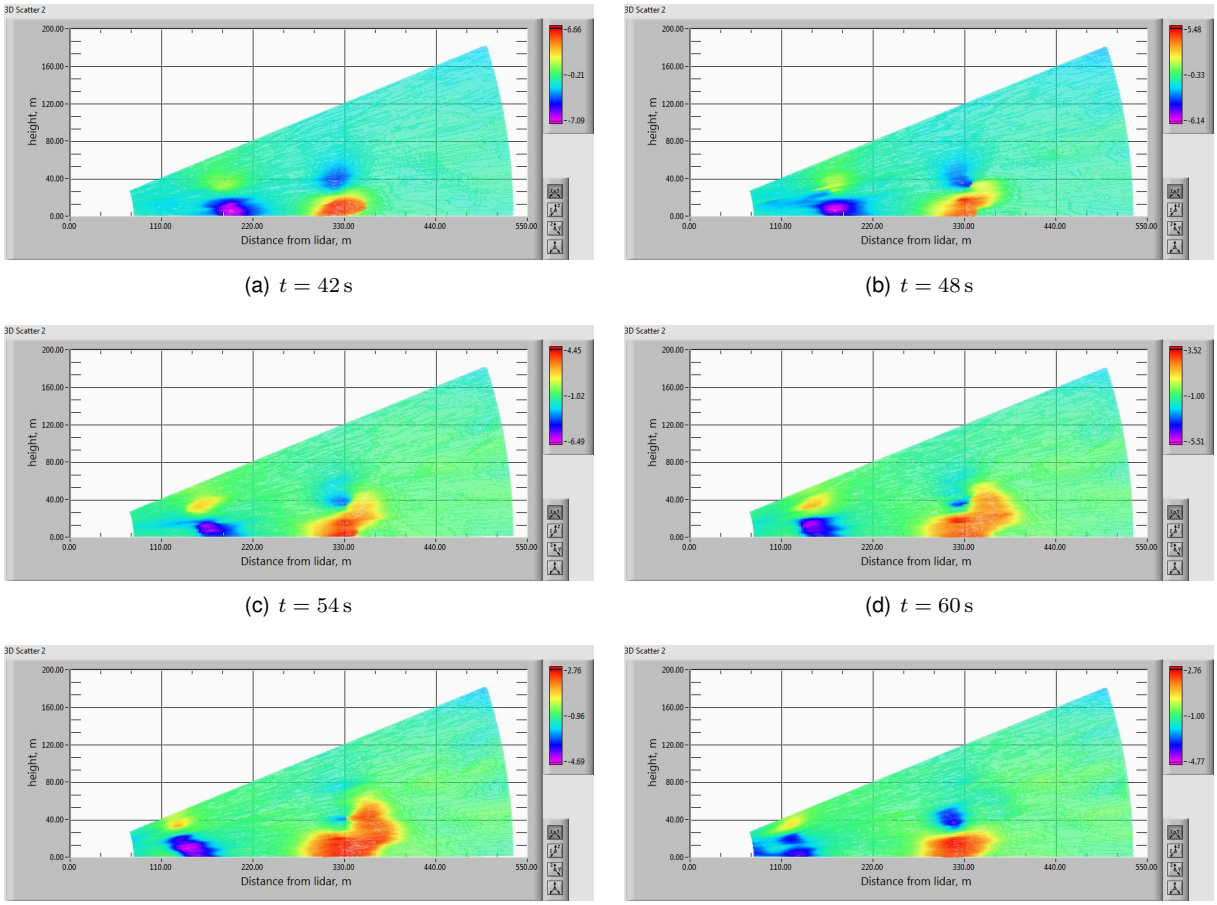

(a) $t = 42\,\mathrm{s}$ (b) $t = 48\,\mathrm{s}$

(c) $t = 54\,\mathrm{s}$ (d) $t = 60\,\mathrm{s}$

(e) $t = 66\,\mathrm{s}$ (f) $t = 72\,\mathrm{s}$

Figure 20: LIDAR RHi scan, radial velocity component in $\mathrm{m}\,/\,\mathrm{s}$, different times after the passage of a B747 aircraft

5.5. LIDAR discussion

As an application of the presented method we aim to investigate and interpret LIDAR measurements from a recent measurement campaign at Vienna international airport in November 2017. Pulsed coherent Doppler LIDARs (PCDLs) currently present a powerful technical instrument to study aircraft wake vortices. A $1.54\mu\,\mathrm{m}$ *Leosphere* Windcube 200 was thus used during the campaign. The LIDAR was positioned about $280\,\mathrm{m}$ away from the flight corridor. A range-height indicator (RHi) scan pattern from 0^o to 20^o perpendicular to the flight path was implemented, see Fig. 20.

The general theory of that kind of LIDARs and post-processing algorithms can be found in Smalikho et al. (2015) and Banakh & Smalikho (2013). The raw LIDAR data consists of Doppler velocity spectra for every point in the scanning plane. A straightforward retrieval of that kind of data employs the radial velocity component of the flow field towards the LIDAR, which is depicted in Fig. 20 and Fig. 21. In Fig. 20 we observe RHi scans for different time steps after a B747 has crossed the measurement plane, starting at a vortex age of $t = 42\,\mathrm{s}$. The plots depict the radial velocity V_r along the laser beam. Positive velocities point away from the LIDAR. The wake vortex system leads to a characteristic quadrupole pattern. We observe how the downwind vortex is advected towards the LIDAR, whereas the upwind vortex hovers above the initial position. In Fig. 20 (b) and (c) we clearly see blue streaks from the downwind vortex towards the LIDAR, that indicate the presence of another smaller vortex. Particularly significant is the outflow of the positive radial velocity of the upwind vortex in Fig. 20 (c) to (e). At a time of $t = 72\,\mathrm{s}$ that outflow suddenly vanishes, see Fig. 20 (f). We would not expect that flow field pattern generated by just one coherent vortex. A similar pattern is observed after a A320 landing, though not that

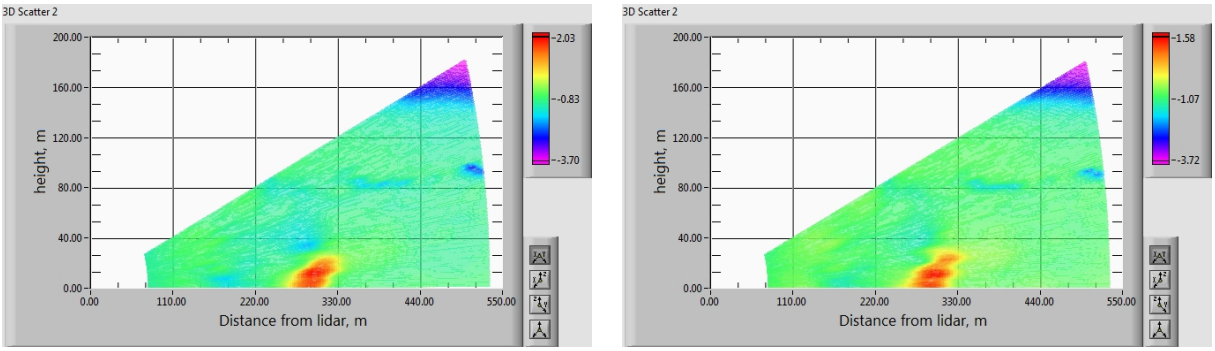

(a) $t = 78\,\mathrm{s}$

(b) $t = 84\,\mathrm{s}$

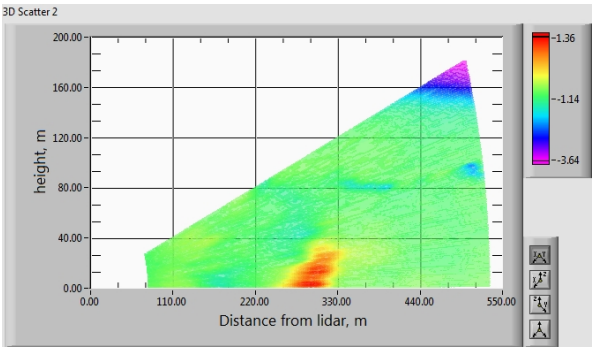

(c) $t = 90\,\mathrm{s}$

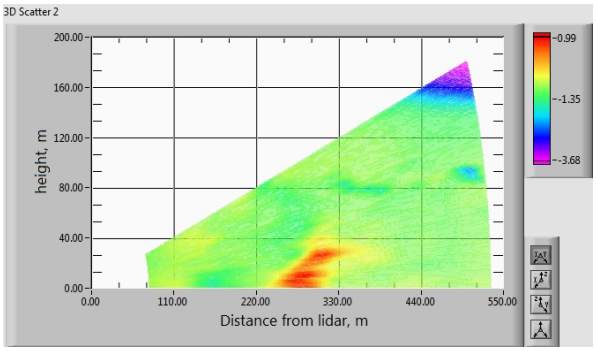

(d) $t = 96\,\mathrm{s}$

Figure 21: LIDAR RHi scan, radial velocity component, different times after the passage of a A320 aircraft

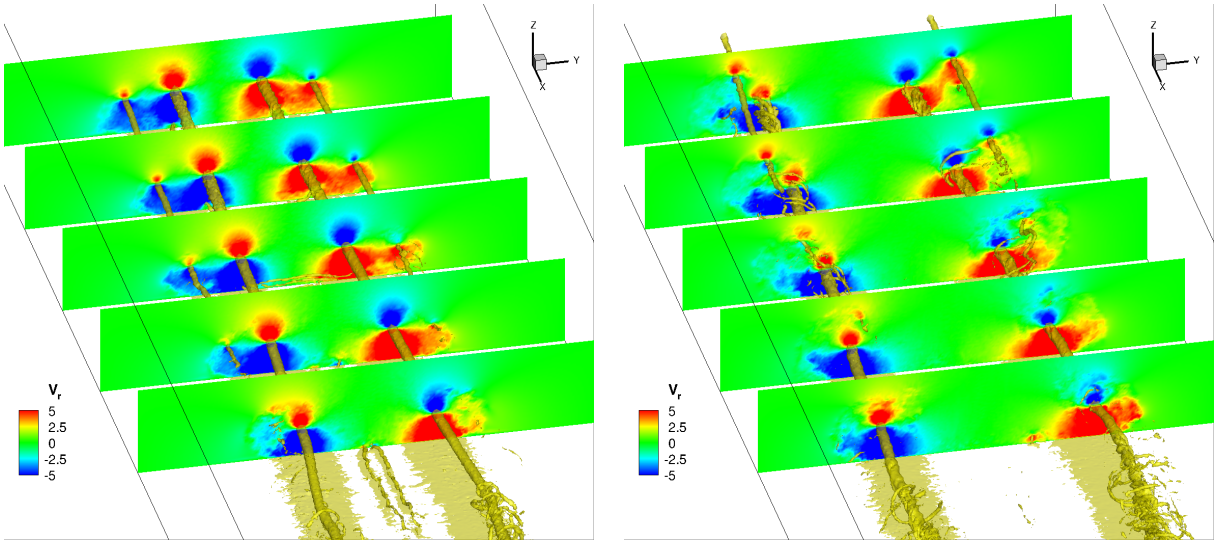

(a) $t = 6.5\,\mathrm{s}$ (b) $t = 13\,\mathrm{s}$

Figure 22: Simulated LIDAR RHi scans of radial velocity, vorticity magnitude iso-surface from hybrid RANS/LES simulation with landing gears

clear, Fig. 21. Here, the crossing height was higher, and the pattern was observed later after crossing. Generally speaking, the described effects cannot be observed in all cases, since they depend on the aircraft type and are more pronounced for larger aircraft. This is partly an effect of the LIDAR resolution, but has to be investigated further.

The LIDAR images can be simulated by calculating the radial velocity that a LIDAR would observe. Figure 22 depicts five instantaneous scans at different distances to the touchdown point, for two time steps after touchdown. As we do not include wind in these simulations we have an almost symmetric field, though the radial velocity image is asymmetric. We clearly see the quadrupole and the characteristic outflow, Fig. 22 (b), upper slice. A closer look at the upper slice of Fig. 22 (b) is given in Fig. 23. The radial velocity pattern is similar to the LIDAR measurements. Here we include additional information, namely a vorticity magnitude iso-surface and velocity vectors. We conclude that three vortices are involved in that pattern - the main vortex, the engine vortex, that stays stable due to the landing gears, as well as a the tailplane vortex rebounding from the ground.

6. Conclusion

This work was dedicated to studying the wake vortex evolution during an aircraft landing. A special emphasis was put on the effects of the landing gear. Various new hybrid methods were proposed with the objective to capture all relevant effects during flare and touchdown. The novel approaches have been compared with a previously employed one, as well as with flight measurement data. The results were used to interpret LIDAR measurement data of landing aircraft wake vortices.

The new hybrid RANS/LES method incorporates multiple steady-state solution fields created in advance by running a number of RANS simulations. A very detailed CAD model of the A320 “ATRA” research aircraft, operated by the DLR, was used in those RANS simulations. A high-lift configuration with deflected flaps and slats with and without main and nose landing gears was used. The RANS simulation used a hybrid unstructured mesh with adaptively refined regions behind the wing, flaps, slats, landing gears, and tailplane. The compressible, finite volume DLR TAU Code was used to solve the RANS equations, with the robust and accurate Spalart-Allmaras model. The LES domain was handled by MGLET, an incompressible code employing a forth-order accurate compact finite-volume scheme and a dynamic Lagrangian model for the unresolved scales. The RANS fields were used to initialize the flow-field in the LES domain at suitable height intervals. A similar approach was tested employing an unsteady RANS simulation by extracting a number of solution fields at different times and mapping them

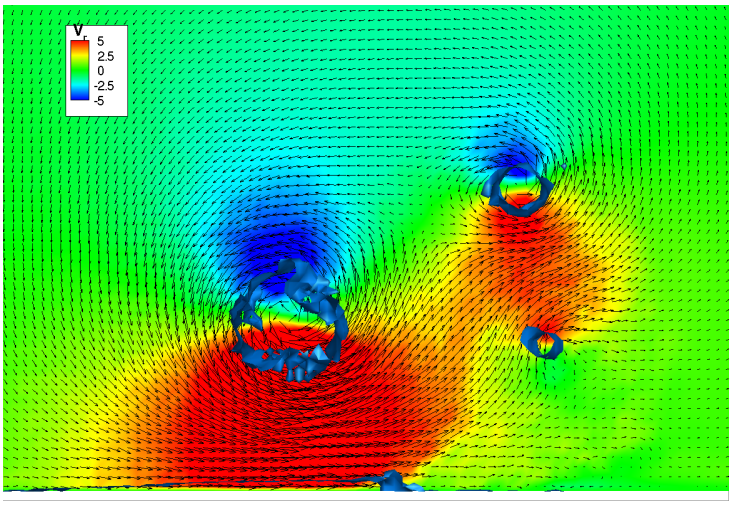

Figure 23: Close-up of the simulated LIDAR RHi scan, Fig. 22, vorticity iso-surface visualizing vortices and velocity vectors.

into the LES domain. The unsteady simplified touchdown maneuver was realized by a URANS simulation, where a dual time stepping approach and moving meshes, realized using the Chimera technique, were used.

Flight measurement data from validation experiments were presented. From parameters like the lift coefficient and the true air speed a theoretical value for the circulation of the wake vortices was deduced. The ground effect was clearly visible in the simulations, as well as in the flight data, when comparing the lift coefficient. The RANS and the URANS simulations yielded very similar lift and drag coefficients. As a good indicator to validate the hybrid simulation method the circulation of the wake vortices was evaluated. Indeed, a good agreement between the circulations resulting from the new hybrid RANS/LES coupled computation and flight measurements was achieved. It was observed that this approach notably improves the landing simulation, compared to the previously employed hybrid approach.

The simulations have shown a surprising effect that may be induced by the landing gears. Though their impact on the circulation decay was moderate, a relatively strong coherent structure forms out of the engine - landing gear system whereas the engine wake dissipates quickly in the simulations without landing gears. The Burnham-Hallock model that was used to approximate tangential velocity profiles out of ground, has to be completed by mirror vortices close to the ground. However, this model did not capture the above mentioned engine vortex seen in the simulation with landing gear.

LIDAR measurements from a measurement campaign at Vienna international airport reveal interesting vortex patterns behind various types of aircraft after touchdown. The measured radial velocity patterns obtained by RHi scans could not be explained by just one vortex pair. The measurements were qualitatively compared to simulation results where a similar setup was employed. Indeed, the pattern matched very well. It could be shown that it was generated by a three vortex pair system, the main vortices, the tailplane vortices and the engine-gear-system vortices, presented above.

This study motivates the usage of LES data for the optimization of LIDAR post-processing algorithms of aircraft wake vortices in ground proximity.

Acknowledgments

The CPU time on the HPC Cluster SuperMUC, provided by the Leibniz Supercomputing Centre (LRZ) as well as the cooperation with AustroControl are greatly acknowledged. We thank Igor Smalikho and Norman Wildmann for their valuable contributions in the LIDAR measurement campaign.

References

Banakh, V., Smalikho, I. N. (2013), *Coherent Doppler WInd Lidars in a Turbulent Atmosphere*. Artech House, Boston & London.

Bier, N., Rohlmann, D., Rudnik, R. (2012), Numerical Maximum Lift Predictions of a Realistic Commercial Aircraft in Landing Configuration. *AIAA 2012-0279, 50th AIAA Aerospace Sciences, Nashville, USA*.

Breitsamter, C. (2011), Wake vortex characteristics of transport aircraft. *Progress in Aerospace Sciences*, Vol. 47, pp. 89–134. doi:https://doi.org/10.1016/j.paerosci.2010.09.002.

Bricteux, L., Duponcheel, M., De Visscher, I., Winckelmans, G. (2016), LES investigation of the transport and decay of various-strengths wake vortices in ground effect and subjected to a turbulent crosswind. *Physics of Fluids*, Vol. 28, no. 065105. doi:https://doi.org/10.1063/1.4954150.

Centaur (2017), Centaursoft: CENTAUR Grid Generation Software.

Constant, G. D. J., Foord, R., Forrester, P. A., Vaughan, J. M. (1994), Coherent laser radar and the problem of aircraft wake vortices. *Journal of Modern Optics*, Vol. 41, pp. 2153–2173. doi: https://doi.org/10.1080/09500349414552021.

Czech, M. J., Miller, G. D., Crouch, J. D., Strelets, M. (2004), Near-field Evolution of Trailing Vortices Behind Aircraft with Flaps Deployed. *AIAA Paper*, Vol. 2149.

Daeninck, G., Desenfans, O., Winckelmans, G. (2006), FAR-Wake Technical Report 3.1.1-1, Span loading variations and wake roll-up in ground effect. Techn. Ber., Université catholique de Louvain (UCL).

Fischenberg, D. (1999), Ground Effect Modeling Using a Hybrid Approach of Inverse Simulation and System Identification. *AIAA Paper 99-4324*.

Fujii, K. (1995), Unified Zonal Method Based on the Fortified Solution Algorithm. *Journal of Computational Physics*, Vol. 118, pp. 92–108. doi:https://doi.org/10.1006/jcph.1995.1082.

Georges, L., Geuzaine, P., Duponchel, M., Bricteux, L., Lonfils, T., Winckelmans, G., Giovannini, A. (2005), Technical Report 3.1.1-3, LES of two-vortex system in ground effect with and without wind. Techn. Ber., Université catholique de Louvain (UCL), Institut de Mécanique des Fluides de Toulouse(IMFT).

Gerz, T., Holzäpfel, F., Darracq, D. (2002), Commercial aircraft wake vortices. *Progress in Aerospace Sciences*, Vol. 38, No. 3, pp. 181–208. doi:10.1016/S0376-0421(02)00004-0ö.

Hokpunna, A. (2009), *Compact Fourth-order Scheme for Numerical Simulations of Navier-Stokes Equations*. PhD Thesis, Technische Universität München (Germany).

Hokpunna, A., Manhart, M. (2010), Compact Fourth-order Finite Volume Method for Numerical Solutions of navier-Stokes Equations on Staggered Grids. *Journal of Computational Physics*, Vol. 229, No. 20, pp. 7545–7570. doi:https://doi.org/10.1016/j.jcp.2010.05.042.

Holzäpfel, F. (2003), Probabilistic Two-Phase Wake Vortex Decay and Transport Model. *Journal of Aircraft*, Vol. 40, No. 2, pp. 323–331. doi:https://doi.org/10.2514/2.3096.

Holzäpfel, F., Tchipev, N., Stephan, A. (2016), Wind Impact on Single Vortices and Counterrotating Vortex Pairs in Ground Proximity. *Flow, Turbulence and Combustion.*, pp. 1–20. doi: https://doi.org/10.1007/s10494-016-9729-2.

Jategaonkar, R. V. (2006), *Flight Vehicle System Identification*. Progress in Astronautics and Aeronautics.

Kalnay, E. (2003), *Atmospheric Modeling, Data Assimilation and Predictability*. Cambridge University Press.

Konrath, R., Agocs, J., Geisler, R., Otter, D., Roosenboom, E., Wolf, T., Quest, J. (2013), Flow Field Measurements by PIV at High Reynolds Numbers. *AIAA Paper 2013-0869, 51st AIAA Aerospace Sciences Meeting,*. Grapevine, Texas, USA.

Köpp, F., Rahm, S., Smalikho, I. (2004), Characterisation of Aircraft Wake Vortices by 2-μm Doppler Lidar. *Journal of Atmospheric and Oceanic Technology*, Vol. 21, pp. 194–206. doi: https://doi.org/10.1175/1520-0426(2004)021<0194:COAWVB>2.0.CO;2.

Kroll, N., Becker, K., Rieger, H., Thiele, F. (2009), *MEGADESIGN and MegaOpt - German Initiatives for Aerodynamic Simulation and Optimization in Aircraft Design*. ISBN 978-3-642-04092-4.

Manhart, M. (2004), A Zonal Grid Algorithm for DNS of Turbulent Boundary Layers. *Computer and Fluids*, Vol. 33, No. 3, pp. 435–461. doi:https://doi.org/10.1016/S0045-7930(03)00061-6.

Meneveau, C., Lund, T. S., Cabot, W. H. (1996), A Lagrangian dynamic subgrid-scale model of turbulence. *Journal of Fluid Mechanics*, Vol. 319, pp. 353–385. doi: https://doi.org/10.1017/S0022112096007379.

Misaka, T., Holzäpfel, F., Gerz, T. (2013), Wake Evolution of High-Lift Configuration from Roll-Up to Vortex decay. *51st AIAA Aerospace Sciences Meeting, Grapevine, Texas,USA*.

Misaka, T., Holzäpfel, F., Gerz, T. (2015), Large-Eddy Simulation of Aircraft Wake Evolution from Roll-Up until Vortex Decay. *AIAA Journal*, Vol. 53, pp. 2646–2670. doi:10.2514/1.J053671.

Misaka, T., Holzäpfel, F., Hennemann, I. Gerz, T., Manhart, M., Schwertfirm, F. (2012), Vortex bursting and tracer transport of a counter-rotating vortex pair. *Physics of Fluids*, Vol. 24, pp. (025104–1) – (025104–21). doi:https://doi.org/10.1063/1.3684990.

Pistolesi, E. (1937), Ground Effect - Theory and Practice, Technical Memorandum no. 828. Techn. Ber., National Advisory Committee for Aeronautics, Washington.

Prandtl, L. (1923), Der induzierte Widerstand von Mehrdackern. Techn. Ber., Ergebnisse der Aerodynamischen Versuchsanstallt Göttingen, II. Lieferung.

Proctor, F. H., Hamilton, D. W., Han, J. (2000), Wake Vortex Transport and Decay in Ground Effect: Vortex Linking with the Ground. *AIAA, 2000-0757, 38th Aerospace Sciences Meeting & Exhibit, Reno*.

Rohlmann, D. (2018), Numerical Simulation of the Influence of the Landing Gear and the Ground Effect on the Flow around a Transport Aircraft Configuration. *CEAS Aeronautical Journal*, Vol. accepted.

Rohlmann, D., Keye, S. (2015), Stall Maneuver Simulation of an elastic Transport Aircraft based on Flight Test Data. *AIAA 2015-2570, AIAA Aviation, 33rd AIAA Applied Aerodynamics Conference, Dallas, USA*.

Rudnik, R., Reckzeh, D., Quest, J. (2012), HINVA - High lift INflight VAlidation - Project Overview and Status. *AIAA 2012-0106, 50th AIAA Aerospace Sciences, Nashville, USA*.

Rumsey, C. L., Long, M., Stuever, R. A., Wayman, T. R. (2011), Summary of the First AIAA CFD High-Lift Prediction Workshop. *Journal of Aircraft*, Vol. 48, No. 6, pp. 2068–2079. doi: https://doi.org/10.2514/1.C031447.

Smalikho, I., Rahm, S. (2010), Lidar Investigations of the Effects of Wind and Atmospheric Turbulence on an Aircraft Wake Vortex. *Journal of Atmospheric and Oceanic Technology*, Vol. 23 No.2, pp. 137–146. doi:https://doi.org/10.1134/S1024856010020107.

Smalikho, I. N., Banakh, V., Holzäpfel, F., Rahm, S. (2015), Method of radial velocities for the estimation of aircraft wake vortex parameters from data measured by coherent Doppler lidar. *Optics Express*, Vol. 23, pp. A1194–A1207. doi:https://doi.org/10.1364/OE.23.0A1194.

Spalart, P. (1998), Airplane trailing vortices. *Annual Review of Fluid Mechanics*, Vol. 30(1), pp. 107–138. doi:https://doi.org/10.1146/annurev.fluid.30.1.107.

Spalart, P., Allmaras, S. (1992), A one-equation turbulence model for aerodynamic flows. *30th Aerospace Sciences Meeting and Exhibit, Aerospace Sciences Meetings*. doi: https://doi.org/10.2514/6.1992-439.

Stephan, A., Holzäpfel, F., Misaka, T. (2013), Aircraft Wake Vortex Decay in Ground Proximity - Physical Mechanisms and Artificial Enhancement. *Journal of Aircraft*.

Stephan, A., Holzäpfel, F., Misaka, T. (2014), Hybrid simulation of wake-vortex evolution during landing on flat terrain and with plate line. *International Journal of Heat and Fluid Flow*, Vol. 49, pp. 18–27. doi:https://doi.org/10.1016/j.ijheatfluidflow.2014.05.004.

Stephan, A., Holzäpfel, F., Zholtovski, S. (2017), The effect of gusts on aircraft wake vortices. *Aircraft Engineering and Aerospace Technology*, Vol. 89, pp. 692–702. doi:https://doi.org/10.1108/AEAT-01-2017-0032.

Stumpf, E. (2005), Study of Four-Vortex Aircraft Wakes and Layout of Corresponding Aircraft Configurations. *Journal of Aircraft*, Vol. 42, pp. 722–730. doi:https://doi.org/10.2514/1.7806.

Torenbeek, E. (1976), *Synthesis of Subsonic Airplane Design*. University Press, Delft.

Widnall, S., Barrows, T. M. (1970), An analytic solution for two- and three-dimensional wings in ground effect. *Journal of Fluid Mechanics*, Vol. 41, part 4, pp. 769–792. doi: https://doi.org/10.1017/S0022112070000915.

Wieselsberger, C. (1922), Wing Resistance near the ground. *NACA TM-77*, Vol. 77.

1.1.3 Hybrid numerical simulation of the jet-wake-vortex interaction of a cruising aircraft

Anton Stephan[1], David Rohlmann[2], Frank Holzäpfel[1], Ralf Rudnik[2]

[1] *Institute of Atmospheric Physics*, [2] *Institute of Aerodynamics and Flow Technology*

The aircraft wake of an A320 aircraft from roll-up until decay is investigated with hybrid Reynolds averaged Navier-Stokes/Large-eddy simulation methods. The turbulent jet as well as the heat emission is included. The dynamics of the wake vortices interacting with the jet exhaust is investigated as well as the heat evolution in the wake. The results show that the jet engines influence the near field as well as the far field. They disturb the coherency of the wake particularly the relatively strong engine vortex is getting turbulent very fast. This leads to a slower decay of the entire system, as the Crow-instabilities are suppressed and develop later. The heat dissipates very fast. The descending vortex system leaves a vertical heat plume, where the maximal temperature is in the turbulent jet first, but is captured inside the vortex core for later vortex ages.

1. Introduction

The interaction of the exhaust jet with the wake vortices at cruise is relevant for two different reasons. On the one hand aircraft wake vortices pose a substantial risk to following aircraft due to strong coherent vortical flow structures which can persist in the atmosphere for a long time Jaquin et al. (2001); Gerz et al. (2002). On the other hand the environmental impact of air traffic has been investigated for already two decades Minnis et al. (1998).

The potential risk of encountering wake vortex turbulence at cruise has lead to the development of wake vortex prediction systems aiming to increase aviation safety. They rely on a comprehensive and detailed understanding of the wake vortex behavior under different atmospheric conditions. However, as recent investigations indicate, the detailed aircraft geometry, particularly the flap position and deployment and the resulting wing loading distribution, have a substantial impact on the wake vortex evolution Hallock & Holzäpfel (2018). Hence, it is not sufficient to exclude the roll-up phase and to confine to fully rolled up wake vortices in numerical studies.

The environmental impact is mainly driven by the generation of condensation trails (contrails), emerging from water vapor and soot particles from the engine. The formation and detrainment of ice crystals during the wake vortex descent as well as the turbulent mixing process influence the generation and evolution of the contrail. Wind shear leads to an effective extension of the contrail, such that contrail clusters generated by multiple aircraft may trigger, under favorable weather conditions the formation of long-lived cirrus clouds. They been identified to contribute to global climate issues as they modify the radiation budget of the atmosphere Burkhardt et al. (2010). The ice crystal density distribution is strongly dependent on the early water vapor entrainment into the co-rotation wake vortices. Hence, a comprehensive understanding of the environmental impact has to include the roll-up phase.

In view of the safety issue, the dynamics of wake vortices after roll-up until decay have numerically been studied by large-eddy simulations (LES) considering various atmospheric conditions including turbulence, thermal stability and wind shear (Holzäpfel, 2003; Misaka et al., 2012). In those studies a vortex pair with a constant velocity profile along flight direction was initialized in the computational domain. The coupling of Reynolds-averaged Navier-Stokes (RANS) and LES simulations is an innovative methodology to simulate the aircraft flight through a computational, generating a wake in a realistic way, Misaka et al. (2013, 2015). For this purpose a pre-computed high-fidelity steady RANS flow field is swept through the LES domain. This is done to initialize the aircraft wake in the LES domain and will be further referred to as "spatial LES". This method includes all stages of wake-vortex evolution, from roll-up to vortex decay. The results have been validated and revealed valuable insights for cruise flight, Misaka et al. (2015), as well as flight in ground proximity during the landing phase, Stephan et al. (2014).

The numerical investigation of the jet- wake vortex interaction and the analysis of emission distribution has been performed for at least two decades. The first LES investigations Gerz & Ehret (1997); Gerz

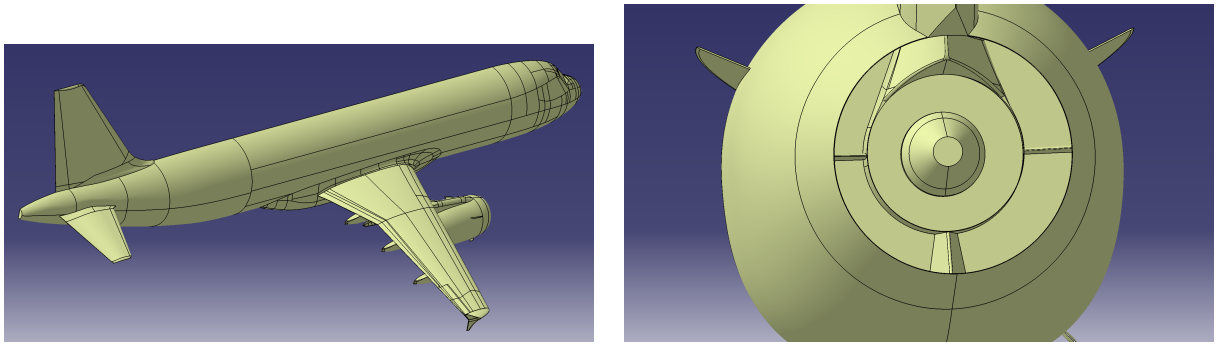

(a) (b)

Figure 1: CAD model - aircraft geometry (a) and engine nozzle geometry (b)

& Holzäpfel (1999) initialized fully rolled-up wake vortices and jet emissions constantly in flight direction. These LES do not simulate the early roll-up phase which is essential for an accurate ice crystal distribution. Recent work Kolomenskiy & Paoli (2018) tackles this problem employing a coupled RANS/LES approach. The authors realize, that "One of the difficulties that the wake modeling presents is the fact that the length scale of the complete roll-up of the vortex sheet is larger than the wing span and much larger than the vortex core size and the boundary-layer thickness." The authors menage to extend the simulated roll-up phase from the typical RANS scale of one chord length to 3.33 wingspans downstream from the wing tips. As they employ a very fine grid resolution they have to confine themselves to a relatively short domain. They use a inflow approach, which keeps the inertial system from the RANS to the LES.

In this work we use the method presented in Misaka et al. (2015) coupling additionally the potential temperature. As before the RANS solution is swept through a ground fixed domain. From the RANS to the LES the inertial system is switched from a aircraft fixed to a ground fixed system. After initializing the wake can develop for several seconds freely in space. This way we capture all temporal and spatial scales relevant to understand the jet - wake vortex interaction in a turbulent environment.

2. Geometry and Mesh - RANS

2.1. Geometry - RANS

Within the DLR project L-bo*ws* an Airbus A320 was used as the aircraft generating the wake vortex system. For the RANS simulations in cruise conditions a very detailed CAD model of the Airbus A320 "ATRA" operated by the German Aerospace Center (DLR) was available. The CAD Model is based on the A320 cruise configuration. It includes the horizontal and vertical tail plane, the flap track fairings and the IAE V2500 engine including two nacelle strakes and a very detailed nozzle including also the core nozzle, struts and the pylon extension. Figure 1 (a) is giving an overview on the CAD model used. For the simulations the horizontal tail plane is trimmed to an angle typical for cruise flight. In Fig. 1 (b) the geometry in the nozzle of the engine including the parts of the core engine and the struts is shown.

2.2. Mesh - RANS

The RANS simulations within the project L-bows were performed using hybrid unstructured meshes. The meshes were build using the mesh generator Centaur Centaur (2017). The meshes are build using a typical meshing approach for cruise flight RANS simulations. Additionally the volume meshes were strongly refined in the regions of wakes, vortex systems and shear layers produced by the wing, the engine and the tail planes. The boundary layers on all non-slip walls in the complete mesh were resolved by 40 prism layers. The first cell height is set to $y+ \approx 1$. Thereby, the meshes used show a very high mesh resolution to resolve all relevant flow phenomena at the Airbus A320 cruise configuration. In Fig. 2 an overview on the Centaur volume source setup is given.

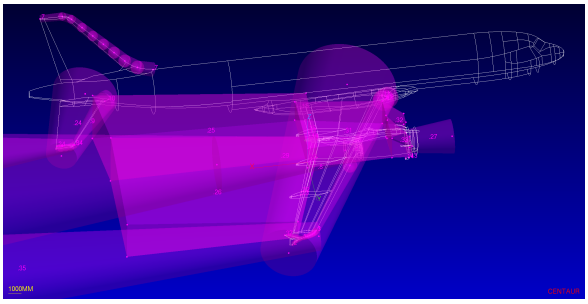

Figure 2: Centaur setup - overview

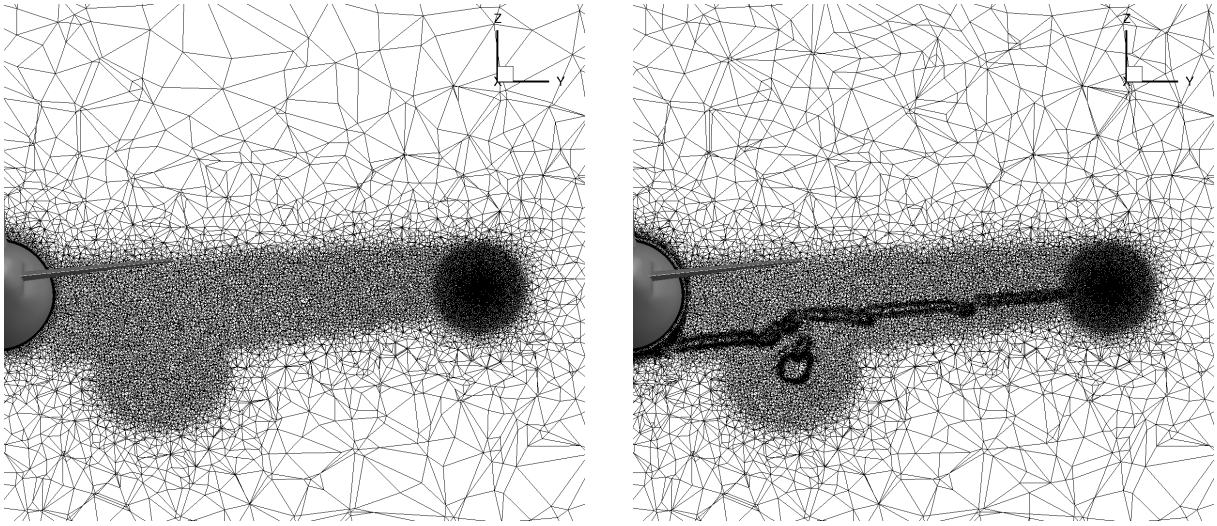

(a) Before automatic refinement (b) After automatic refinement

Figure 3: Slice through mesh

To further improve the quality of the simulated flow field around the aircraft configuration, the meshes were locally refined during the simulation process. This was done by an automatic mesh adaptation process provided by the flow solver. The mesh adaptation is based on a user defined sensor function and is restricted to user defined regions in the flow field. Within the simulations presented in this paper, the mesh adaptation is locally restricted to the regions around the tip vortices and the wakes of the configuration. As a sensor function the difference in total pressure between two neighboring mesh points was set. The meshes were adapted in nine steps. In Fig. 3 a slice through the volume mesh before the first and after nine adaptation steps is shown. An improvement of the mesh resolution in the wake of the wing and around the tip vortices of the wing devices can clearly be seen.

Table I: Number of mesh points

Number of surface elements	1.7e+06
Number of prisms	51e+06
Total point number	38e+06

In Tab. I the number of points and elements for the meshes before the automatic mesh adaptation during the simulation is shown. By the automatic mesh adaptation the number of total points is increased by about 25%.

3. Flow Solver and Flow Conditions - RANS

3.1. Flow Solver - RANS

Within the current studies the DLR TAU Code Kroll et al. (2009) was used as the flow solver for the RANS simulations. The DLR TAU Code is a compressible, unstructured finite volume solver for the Reynolds averaged Navier-Stokes equations. For all simulations shown in this paper, the Spalart-Allmaras (SA) turbulence model Spalart & Allmaras (1992) was used. The SA turbulence model is robust and sufficiently validated for the simulation of the flow around complex configurations Bier et al. (2012); Rohlmann & Keye (2015); Rumsey et al. (2011). The time-stepping was done by a lower-upper symmetric Gauß-Seidel (LU-SGS) scheme. A matrix dissipation scheme was used for the artificial dissipation for the central scheme used. A 3v multigrid cycle was applied to accelerate the convergence.

All surfaces of the aircraft were modeled as non-slip Navier-Stokes walls. The engine of the aircraft was treated in two different ways. One simulation was performed with the engine boundary conditions set similar to a through flow nacelle. In a second simulation the engine boundary conditions were approximated to real engine settings during cruise flight. In this simulation the thrust of the engine is approximately equal to the drag of the aircraft configuration. Furthermore, due to the complex CAD geometry of the engine, a realistic engine jet was modeled including the core and the bypass jet. The mass flow ratio of core and bypass jet was set as in the real engine and the temperature of the core jet was set similar to real flight conditions.

3.2. Flow Conditions - RANS

The used flow conditions for the cruise simulations are derived from typical cruise flight conditions of the Airbus A320 "ATRA" at $Ma = 0.78$. They were converted to the International Standard Atmosphere (ISA) at the altitude of $h = 36000\ ft$. The resulting flow conditions for the simulations are shown in Tab. II. Furthermore, the angle of attack was adjusted using the target C_L function of the TAU Code far

Table II: Flow conditions

Density	$\rho = 0.366\ kg/m^3$
Pressure	$p = 22797\ Pa$
Temperature	$T = 216.95\ K$
Velocity	$v = 230.31\ m/s$
Reynolds number	$Re \approx 24.8 * 10^6$
Mach number	$Ma \approx 0.78$
wing span	$b = 34.1\,\mathrm{m}$
wing plan-form area	$A = 122.6\,\mathrm{m}^2$
total lift coefficient	$C_L = 0.495$

field boundary conditions. Therefore a typical Airbus A320 cruise flight mass of $m = 60\ t$ was assumed. this results in a lift coefficient of $C_L \approx 0.495$. The target lift function was used in the simulation with the engine modeled as through flow nacelle. This results in a specific angle of attack which also was used for the simulation using a realistic thrust setting. For both simulations this approach gives realistic flight conditions of an Airbus A320 in cruise flight.

The reference values for an elliptic load distribution (Gerz et al., 2002), initial circulation, vortex spacing, vortex descent velocity, characteristic time, vorticity unit are given as

$$\Gamma_0 = \frac{2C_L U_\infty A}{\pi b}, \quad b_0 = \frac{\pi}{4} b, \quad w_0 = \frac{\Gamma_0}{2\pi b_0}, \quad t_0 = \frac{b_0}{w_0}, \quad \omega_0 = \frac{1}{t_0}, \tag{1}$$

resulting in $\Gamma_0 = 260.1\,\mathrm{m}^2\,/\,\mathrm{s}$, $b_0 = 26.8\,\mathrm{m}$, $w_0 = 1.55\,\mathrm{m}\,/\,\mathrm{s}$, and $t_0 = 17.295\,\mathrm{s}$, see Tab. III. We normalize physical quantities with the respective values. Vorticity ω is normalized by the time unit $\omega^* = \omega \cdot t_0$. We set $t = 0$ at the instant of crossing a surface, depending on the context. The maximum tangential velocity of the wake vortices is around $20\,\mathrm{m}\,/\,\mathrm{s}$.

Table III: Reference values

initial vortex separation	$b_0 = 26.8\,\mathrm{m}$
initial circulation	$\Gamma_0 = 260.1\,\mathrm{m}^2\,/\,\mathrm{s}$
vortex descent speed	$w_0 = 1.55\,\mathrm{m}\,/\,\mathrm{s}$
characteristic time	$t_0 = 17.295\,\mathrm{s}$

4. Geometry and Mesh - LES

4.1. MGLET - Multi-Grid Large Eddy Turbulence

The Large Eddy Simulation is performed using the incompressible LES code MGLET, developed at the Technical University of Munich, Manhart (2004). It solves the incompressible Navier-Stokes equations. Additionally an equation for the potential temperature is solved which models buoyancy effects and stratification employing the Boussinesq approximation Bannon (1995):

$$\frac{\partial u_i}{\partial t} + \frac{\partial (u_i u_j)}{\partial x_j} = -\frac{1}{\rho}\frac{\partial p'}{\partial x_i} + \frac{\partial}{\partial x_j}\left((\nu + \nu_t) 2 S_{ij}\right) + g\frac{\theta'}{\theta_0}\delta_{i3} \quad , \tag{2}$$

$$\frac{\partial \theta'}{\partial t} + \frac{\partial (u_j \theta')}{\partial x_j} = \frac{\partial}{\partial x_j}\left((\kappa + \kappa_t)\frac{\partial \theta'}{\partial x_j}\right) + u_3 \frac{d\theta_s}{dx_3} \tag{3}$$

$$\frac{\partial u_j}{\partial x_j} = 0\,. \tag{4}$$

Here u_i represents the velocity components in the three spatial directions $(i = 1, 2, \text{ or } 3)$, $S_{ij} = (\partial u_i/\partial x_j + \partial u_j/\partial x_i)/2$ denotes the strain rate tensor, $p' = p - p_0$ and $\theta' = \theta - \theta_0$ equals the deviation from a reference state of the pressure p_0 and the potential temperature θ_0 respectively. We recall that the potential temperature is coupled with the absolute temperature through

$$\theta = T\left(\frac{p_e}{p}\right)^{\frac{R_L}{c_p}} , \tag{5}$$

with $p_e = 1013.25hPa$ denotes the pressure at the earth surface, $R_L = 287J/(kg \cdot K)$ the specific gas constant and $c_p = 1005J/(kg \cdot K)$ the heat capacity of air.

In the Boussinesq approximation, the potential temperature is coupled to momentum equations through the vertical velocity component and the buoyancy term. The background potential temperature θ_s in Eq. (3) is used to specify the vertical gradient of potential temperature. The kinematic viscosity in Eq. (2) is given as the sum of molecular viscosity ν and eddy viscosity ν_t, determined by means of a Lagrangian dynamic sub-grid scale model, Meneveau et al. (1996). The corresponding thermal diffusivity κ in Eq. (3) are obtained by assuming constant molecular and turbulent Prandtl numbers of 0.7 and 0.9, respectively.

Eqns. (2) and (3) are solved by a finite-volume approach, using a fourth-order compact scheme, Hokpunna & Manhart (2010). A split-interface algorithm is used for the parallel solution of the tri-diagonal system, Hokpunna (2009), resulting from the compact scheme. A third-order explicit Runge-Kutta method is used for the time integration. The simulations are performed in parallel, using a domain decomposition approach.

The ambient atmospheric conditions are characterized by the Brunt-Väisälä frequency $N = (g/\theta_0 d\theta/dz)^{1/2}$, representing the stability of the temperature stratification. We employ a typical $N = 0.01$ at an altitude of $h = 36000ft$. Normalizing N by $N^* = Nt_0$ leads to $N^* = 0.17$.

4.2. Wake initialization

In a similar way as proposed in Misaka et al. (2015) the aircraft's wake is initialized by mapping RANS flow fields around the aircraft consecutively into the ground fixed LES domain. This way we "fly" the RANS field at a prescribed trajectory, see Fig. 4. The forward movement of the aircraft is represented by simply shifting mapped flow field through a given mesh spacing. The high fidelity pre-simulated RANS

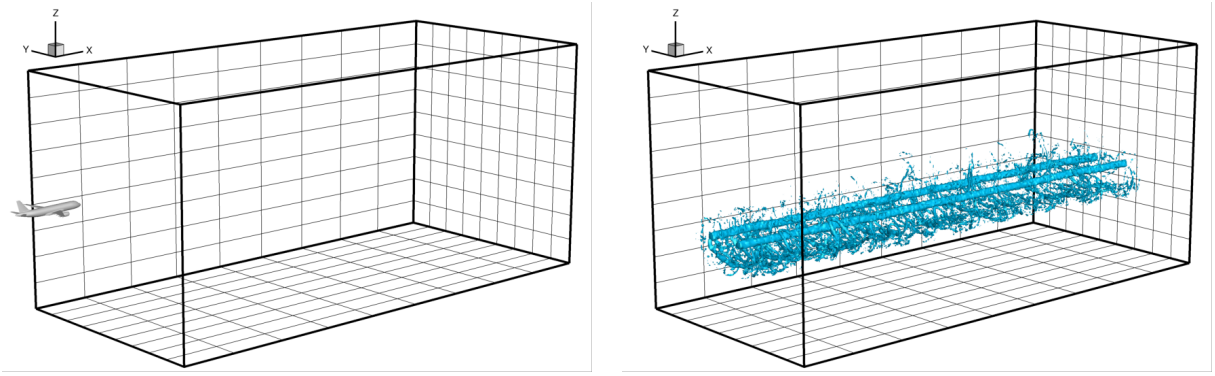

(a) wake initialization (b) wake evolution

Figure 4: Schematic of wake initialization (a) and subsequent wake evolution (b)

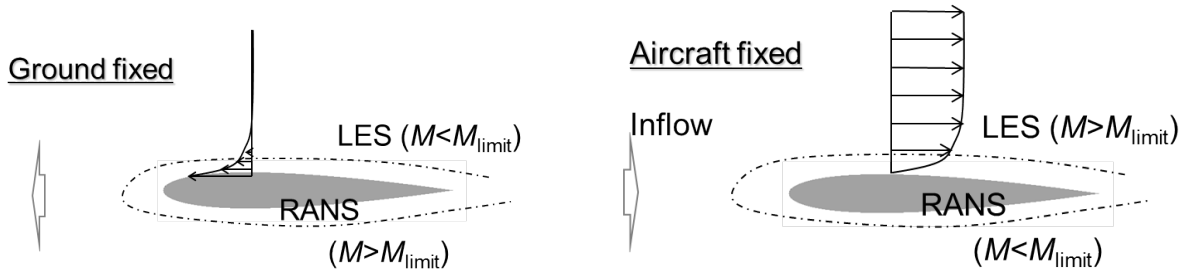

(a) (b)

Figure 5: Schematic of wake initialization (a) and subsequent wake evolution (b)

field $(\mathbf{V_{RANS}}, \theta_{\mathbf{RANS}})$, calculated on unstructured grid, is first mapped to a Cartesian grid and then is used as a constant but moving forcing term in the Navier-Stokes equations. The mapping of the unstructured RANS flow field to Cartesian LES mesh is performed by a linear interpolation once before the wake initialization.

The velocities as well as the potential temperature is updated every Rung-Kutta time step:

$$\mathbf{V} = f(y)\mathbf{V}_{\mathrm{LES}} + (\mathbf{1} - \mathbf{f}(\mathbf{y}))\mathbf{V}_{\mathrm{RANS}} \quad (6)$$

$$\theta = f(y)\theta_{\mathrm{LES}} + (\mathbf{1} - \mathbf{f}(\mathbf{y}))\theta_{\mathrm{RANS}}, \quad (7)$$

where f is a suitable smooth cut-off function depending on the wall distance y, with $f \to 0$ as $y \to 0$ and $f \sim 1$ for $y > D$. Here D denotes the distance from the aircraft, where the influence of the RANS field is negligible, defining the so-called RANS area. This approach requires additional computer memory to store the mapped RANS flow field, however, the additional computational costs for the forcing term is marginal. After the wake initialization the, Fig. 4 (a), which captures the short-time evolution the simulation is completed as a pure LES for arbitrary times, see Fig. 4 (b). Hence, this method is not limited in time and captures all relevant flow situations.

The schematic in Fig. 5 describes the advantage of that technique, that switches the inertial system which is aircraft fixed in the RANS simulation to the ground fixed system in the LES. In the ground fixed approach the high velocities in the order of v in the simulation, Fig. 5, appear in the boundary layer of the aircraft, whereas in the aircraft fixed system the flow field is away from the aircraft geometry shows velocities in the order of the aircraft speed v. With an Mach number of $Ma = 0.78$ we can tackle this simulation problem with an incompressible LES applying the first approach. Here, the area inside the RANS area is blocked in the incompressible LES computation. Finally, it is straight forward to simulate the aircraft flight through a controlled turbulence, by pre-simulating a turbulent field with LES before the aircraft initialization step. To sum up we can list the advantages of the system changing approach

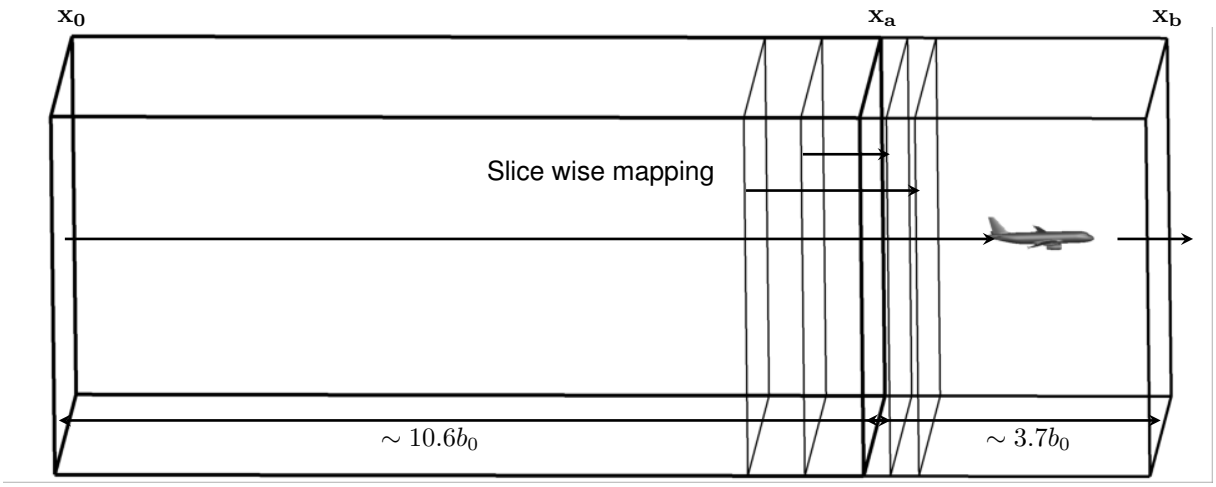

(a)

Figure 6: Schematic of the boundary treatment in flight direction

- arbitrary times of the wake evolution after roll-up can be computed
- an incompressible LES code can be used, which reduces computational cost
- the ambient turbulence can be treated straight forward by pre-simulation.

4.3. Boundary treatment and Computational settings

The boundary conditions in vertical and spanwise directions are periodic. In flight direction the computational setup leads to two major problems. First, the aircraft initialization has to start at some point of the domain. Similar to towing tank experiments so-called end effects are generated Bao & Vollmers (2005); Stephan et al. (2014). As vortices may not end freely in space disturbances at the main vortex ends propagate upstream. Therefore, the part where is initialization starts has to be cut off, in Fig. 6 the back part of the domain [$\mathbf{x_a}$, $\mathbf{x_b}$]. The main simulation box is in [$\mathbf{x_0}$, $\mathbf{x_a}$], which the aircraft is entering at $\mathbf{x_0}$ and leaving at $\mathbf{x_a}$ Second, periodic boundaries are not appropriate in flight direction, since after leaving the domain the wake has an older age at $\mathbf{x_0}$ than at $\mathbf{x_a}$. The flow is not periodic in flight direction. Here we add the removed part of the domain without the aircraft footprint. To close the wake mapping the entire field to slices in the ghost domain, as depicted in Fig. 6. This way the field is interpolated from $\mathbf{x_a}$ to $\mathbf{x_b}$. Now, we again apply periodic boundary conditions in flight directions, since the flow field is artificially made periodic.

In the LES domain we employ uniform mesh spacing for all three spatial directions, with a resolution of $dx = dy = dz = 0.25\,\mathrm{m}$. The dimensions are $(L_x, L_y, L_z) = (384.0, 128.0, 256.0) = (14.3b_0, 4.8b_0, 9.6b_0)$ on a $(N_x, N_y, N_z) = (1536, 512, 1024)$ grid, leading to a total of approximately 805 million grid points. The back part of the domain with a length of $5b_0$ is used as a ghost domain where the aircraft motion starts.

5. Results - RANS

In Fig. 7 the convergence history for the configuration without thrust is shown. The convergence of lift and drag is very good. In the convergence of the density residual, the different automatic mesh refinement steps can clearly be seen as big peak in the curve. The smaller peaks in the density residual curve indicate a change in the angle of attack due to the target lift function.

Surface stream lines and the pressure coefficients at the upper side of the wing and the nacelle for the case without thrust and the case with thrust are shown in Fig. 8. On the upper side of the wing no significant differences between these two cases are visible. Both simulations only show one small flow separation in the edge between the fuselage and the upper trailing edge of the wing. Also the pressure distribution at the upper side of the wing is not directly affected by the engine thrust setting. On the upper side of the nacelle, especially at the lip, strong differences in the pressure distribution are visible.

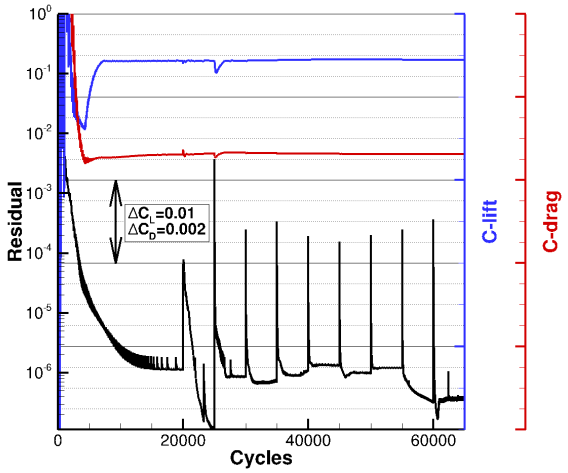

Figure 7: Convergence history case without thrust

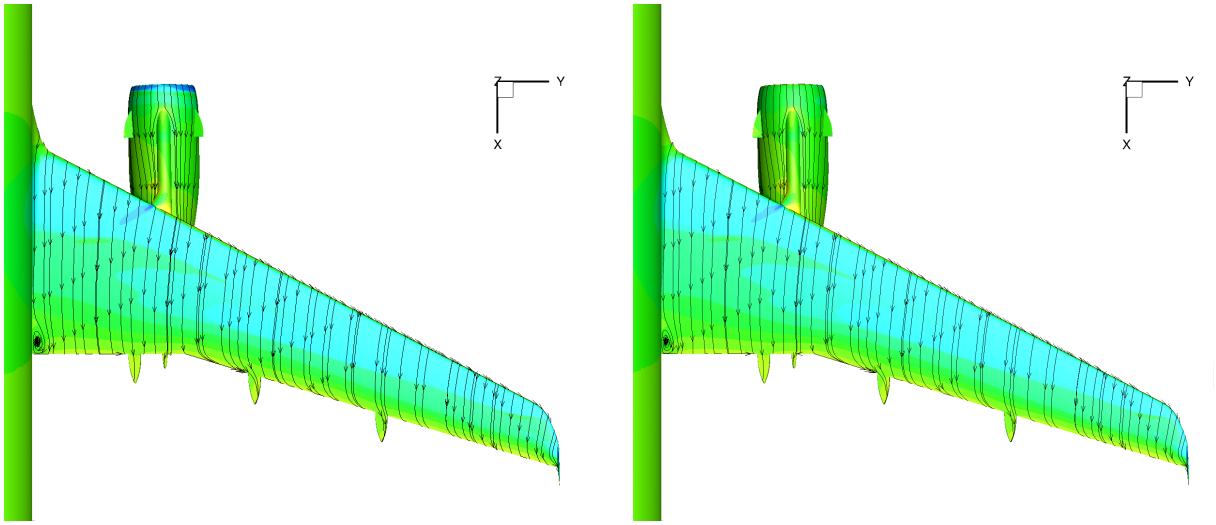

(a) Without thrust (b) With thrust

Figure 8: Surface stream lines and pressure coeffecients

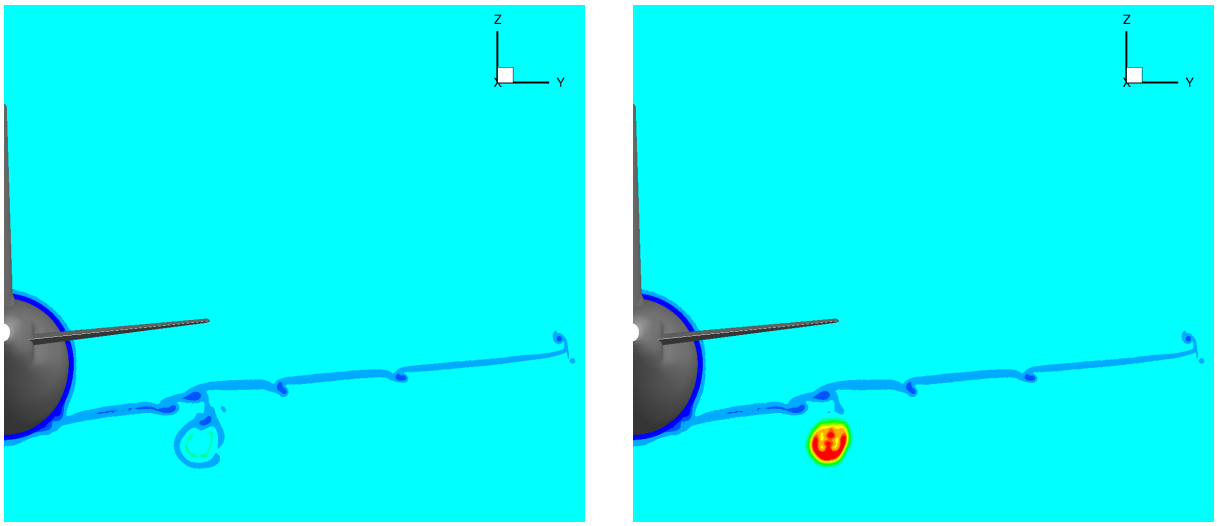

(a) Without thrust (b) With thrust

Figure 9: Total pressure in cut behind the wing

The case using the through flow nacelle engine settings shows a strong suction peak at the upper lip of the nacelle. In the simulation with realistic thrust setting only a very weak suction peak is visible. This can be explained the much higher engine mass flow rate in the case of the realistic thrust setting. The higher mass flow moves the stagnation line at the lip of the nacelle closer to the front of the nacelle. This directly results in a reduction of the suction peak at the lip.

In Fig. 9 the total pressure in a cutting plane behind the wing is shown. Although almost the complete wake does not show an influence of the engine jet, under wing in the kink region an influence of the jet of the engine is clearly visible. The engine jet introduces a strong increase of total pressure. This additional momentum leads to a disappearance of the wake of the engine visible in the simulation without thrust. Due to the high mesh resolution in the wake regions, the wake of the wing is still visible far behind the wing in a cutting plane showing the total pressure behind the horizontal tail plane, shown in fig. 10. Also the wake of the engine, see Fig. 10a, in the simulation without thrust and the jet of the engine, fig. 10b, in the simulation with thrust are still visible. In addition the thin wake of the horizontal tail plan is visible in this cutting plane. In fig. 11, the development of the jet of the engine in the near field behind the engine is shown by cutting planes coloured by the total pressure. It can be seen that the shear layers at the boundaries of the jet and the inner structure of the jet flow are propagated far behind the engine and the aircraft configuration.

6. Results - RANS/LES coupling

6.1. Qualitative Analysis of the Flow Field

6.1.1. *Near field*

A turbulent jet substantially influences the aircraft footprint. Figure 12 depicts the instant of vortex roll-up at $5b_0$ in flight direction. The vorticity magnitude visualizes the flow field qualitatively. Two strong vortices detach at the wing-tips, however the roll-up process is more complex as two secondary vortices detach from the wings rotating around the wing tip vortices and merging in a distance. The aircraft fuselage generates turbulence in the wake as well as the jet engines, see Fig. 12 (a). However, the engine thrust generates a strong jet which widens with the distance, see Fig. 12 (a). The iso-surface of $\omega* = 260$ is colored by θ', the potential air temperature background deviation. Additionally, a slice $3.5b_0$ behind the aircraft shows the vertical temperature footprint. We clearly see the effect of the hot engine exhausts in Fig. 12 (b), leading to high temperatures in the jet, and the cold area of the primary

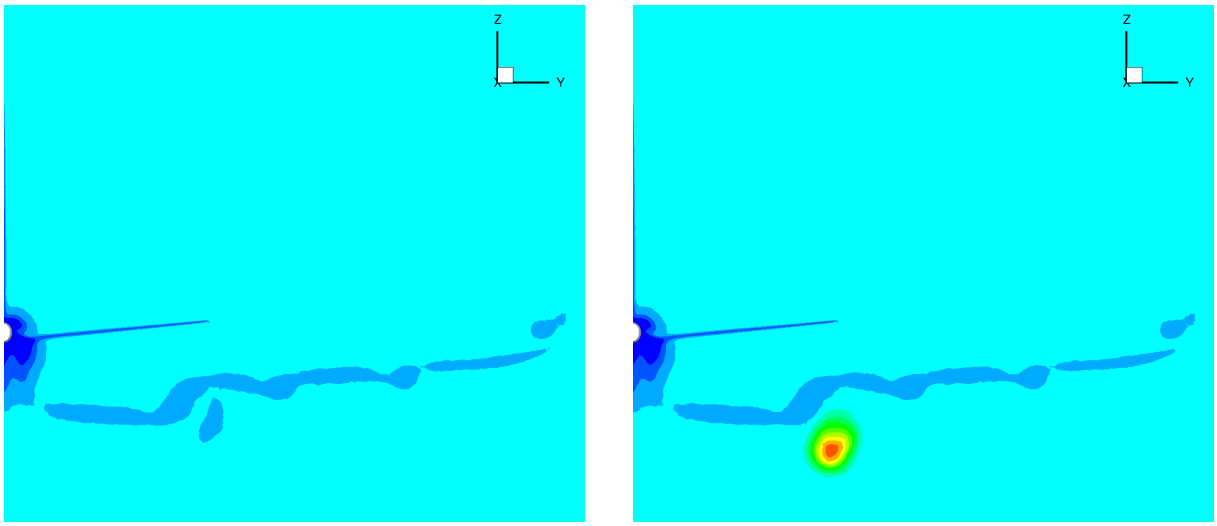

(a) Without thrust (b) With thrust

Figure 10: Total pressure in cut behind the horizontal tail plane

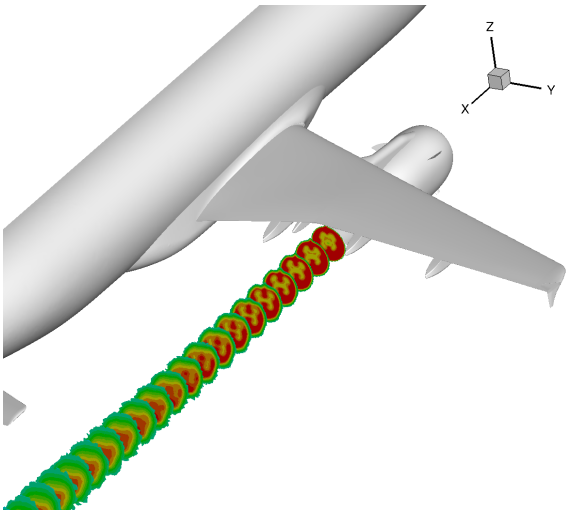

Figure 11: Total pressure distribution within the engine jet

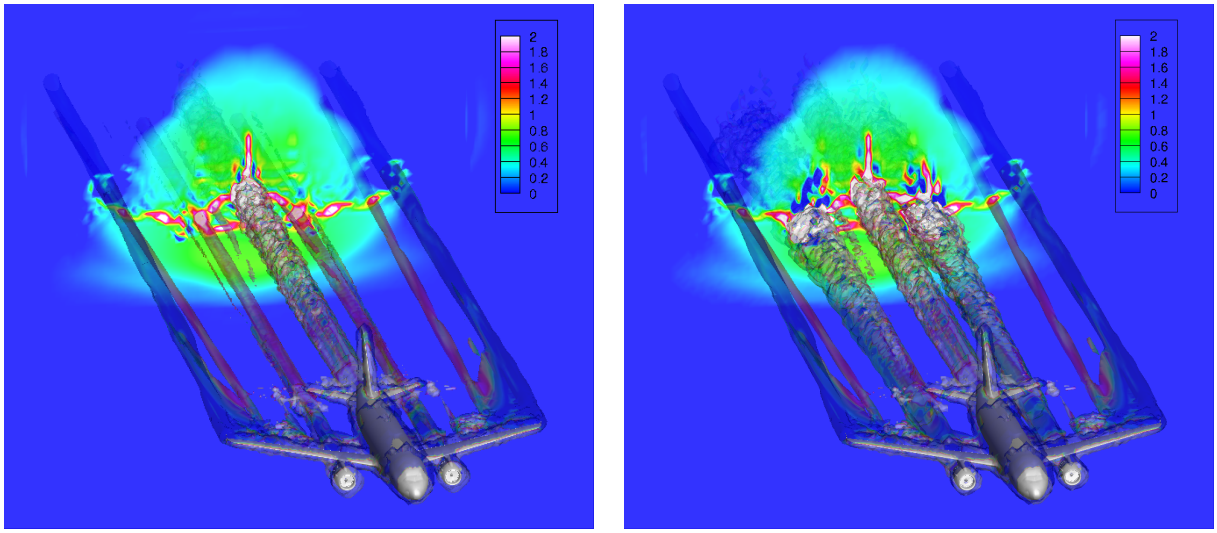

(a) without thrust (b) with thrust

Figure 12: Roll-up process and potential temperature distribution behind a cruising aircraft, $t* = 0.05, \omega* = 260$.

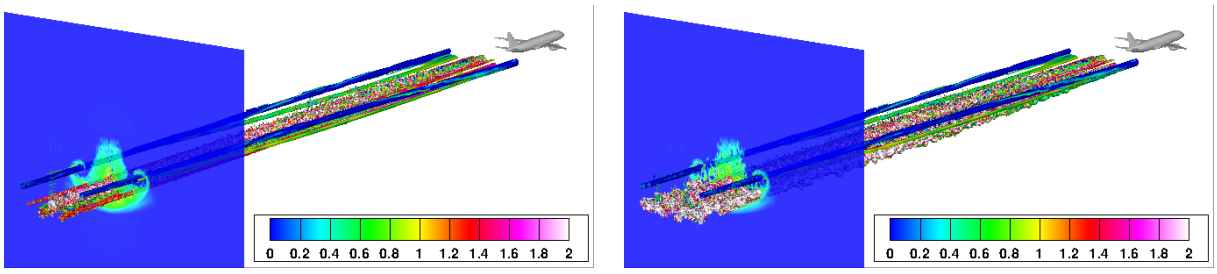

(a) without thrust (b) with thrust

Figure 13: Roll-up process and potential temperature distribution after the aircraft has left the simulation domain, $t* = 0.09, \omega* = 173$.

wake vortices. Air masses closer to the fuselage are warmer than apart. Note, that the mixing process already begins at distances to about $3b_0$. Wake vortices and jet do not mix in the near field, however the fuselage turbulence as well as the jets are transported downwards in the flow field of the strong primary vortices, see Fig. 13. Vorticity magnitude iso-surface at a level of $\omega* = 173$ colored by the temperature is depicted in Fig. 13 viewed from a different perspective at a later time step. The vortex oval is fully developed as wing tip vortices have merged with the secondary vortices in a distance of $10.5b_0$ behind the aircraft (green and blue vortex). The fuselage - and jet turbulence is transported the bottom of the oval, still being very hot in the case of the engine thrust. The jet turbulence directly destroys the coherent structures of the wake, as can be observed in Fig. 14. Here, the vorticity in flight direction is plotted in a slice perpendicular to flight direction in a distance of $6.7b_0$ from the aircraft. The coherent structures of the wake a preserved in the case without thrust. The wind-tip vortices, the secondary vortices from the wings, two vortices from each engine pylon, the fuselage wing junction vortex and finally the turbulent fuselage wake can clearly be distinguished, see Fig. 14 (a). On the contrary, most coherent structures in the wake are destroyed by the jet leaving only the wing-tip vortices, see Fig. 14 (b). It is worth mentioning that relatively strong engine vortices, see Fig. 14 (a), can be observed during aircraft landing, where the thrust is switched off. Numerical simulation as well as Lidar measurements examine the gear vortex in detail in Stephan et al. (2018).

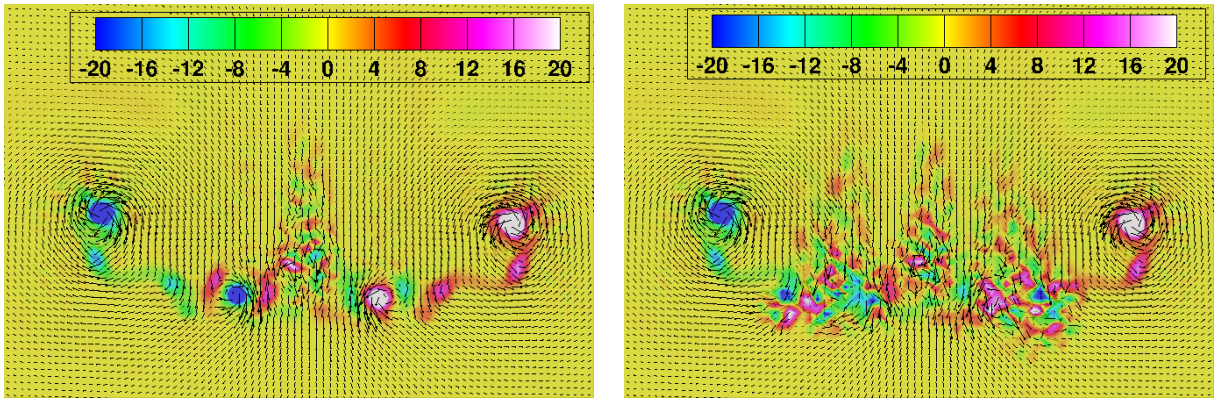

(a) without thrust (b) with thrust

Figure 14: x-vorticity at slice perpendicular to flight direction, distance to aircraft $6.7b_0$.

6.1.2. *Far field*

The wake evolution after roll-up in space is depicted in Fig. 15 for both with (b), (d), (f) and without thrust (a),(c),(e). As it can be observed, the vortices are parallel first. The turbulence inside the vortex oval is stretched and tilted under the influence of the two primary vortices. Note, that vortex streaks appear in both cases being warmer in the case with thrust, see Fig. 15 (a),(b). After a time of about $t^* = 3.4$ the turbulence generated by the aircraft weakens and the main vortices get unstable, see Fig. 15 (c),(d). The vortices link in the case without thrust at about $t^* = 6.0$, Fig. 15 (e), whereas the thrust turbulence stabilizes the main vortices, which are not linked at $t^* = 6.6$, Fig. 15 (f). This confirms the idea that Crow-linking can triggered be coherent multi vortex systems, as in the case without thrust. The heat evolution of the jet exhaust in a slice perpendicular to the flight direction is depicted in Fig. 16, the later images are zoomed out, such that the image captures the heated area. Velocity vectors show the flow field and especially the position of the main vortices. First most of the heat is concentrated behind the jet engines, but also other parts of the aircraft heat the ambient air. As already seen before, the heat is transported to the bottom of the oval and smears out to left and right. The fuselage generated heat is transported downwards. The heat dissipates very fast and wraps together with the air around the main vortices. After $t^* = 1$ the maximal occurring temperature is about one degree above the background temperature. The descending oval leaves a trace of warm air which leaks out of the downward moving oval. For comparison the same images are presented for the case without the jet exhaust, see Fig. 16. Here the entire heat stems from the aircraft itself. Although the roll up process, as well as the resulting heat plume is very similar, the total amount as well as the maximum temperature is reduced in that case.

7. Conclusion

This study investigates jet-wake-vortex interaction of a cruising aircraft, with hybrid numerical Reynolds averaged Navier-Stokes/Large-eddy simulation (RANS/LES) techniques. The method allows a detailed consideration of the aircraft geometry, the entire roll-up phase and to continue the simulation of a certain ground fixed area up to arbitrary reasonable times. Hence, the entire vortex and heat plume formation process is captured in detail. The hybrid approach consists of to major simulation parts. First high-fidelity steady RANS simulation with inflow conditions is performed. The computed RANS fields, velocity and potential temperature, serve as forcing term inside a ground fixed LES domain. The field is shifted with time in flight direction which simulates the aircraft flight through the domain. The switch of the coordinate system has three major advantages

- arbitrary times of the wake evolution after roll-up can be computed
- an incompressible LES code can be used, which reduces computational cost

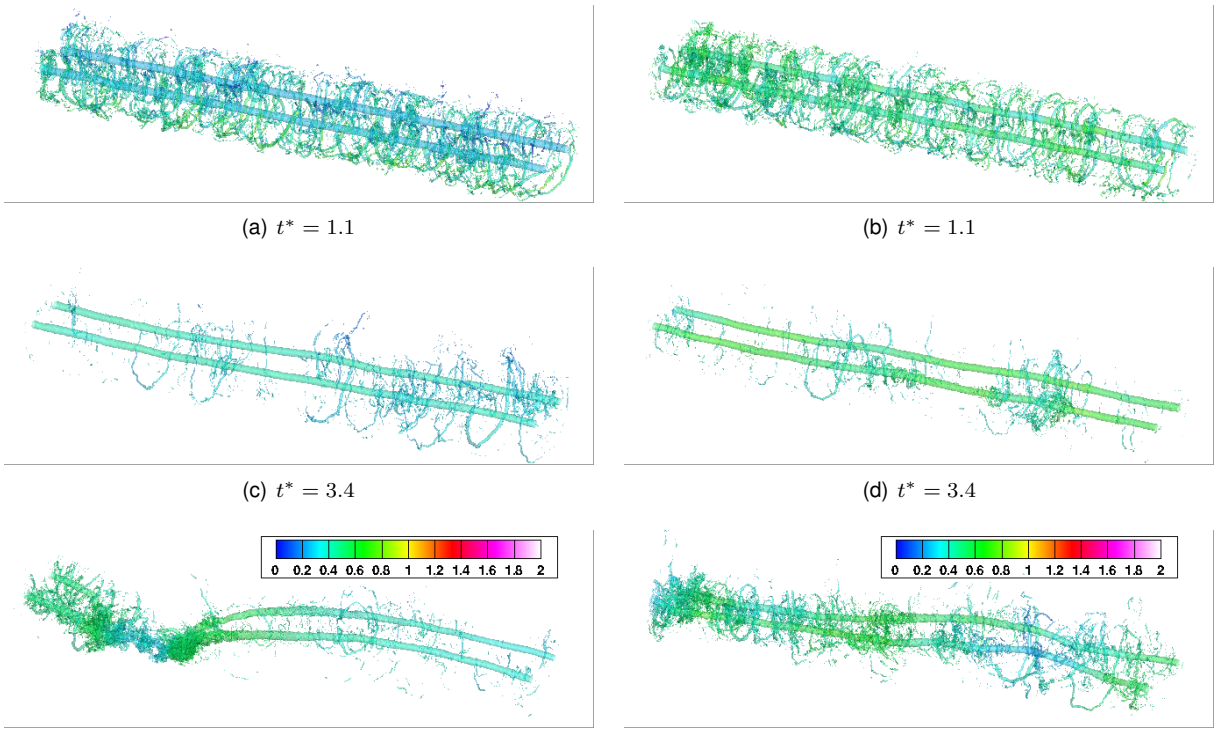

(a) $t^* = 1.1$ (b) $t^* = 1.1$

(c) $t^* = 3.4$ (d) $t^* = 3.4$

(e) $t^* = 6.6$ (f) $t^* = 6.6$

Figure 15: Wake vortex evolution after roll-up, without thrust (left) and with thrust (right).

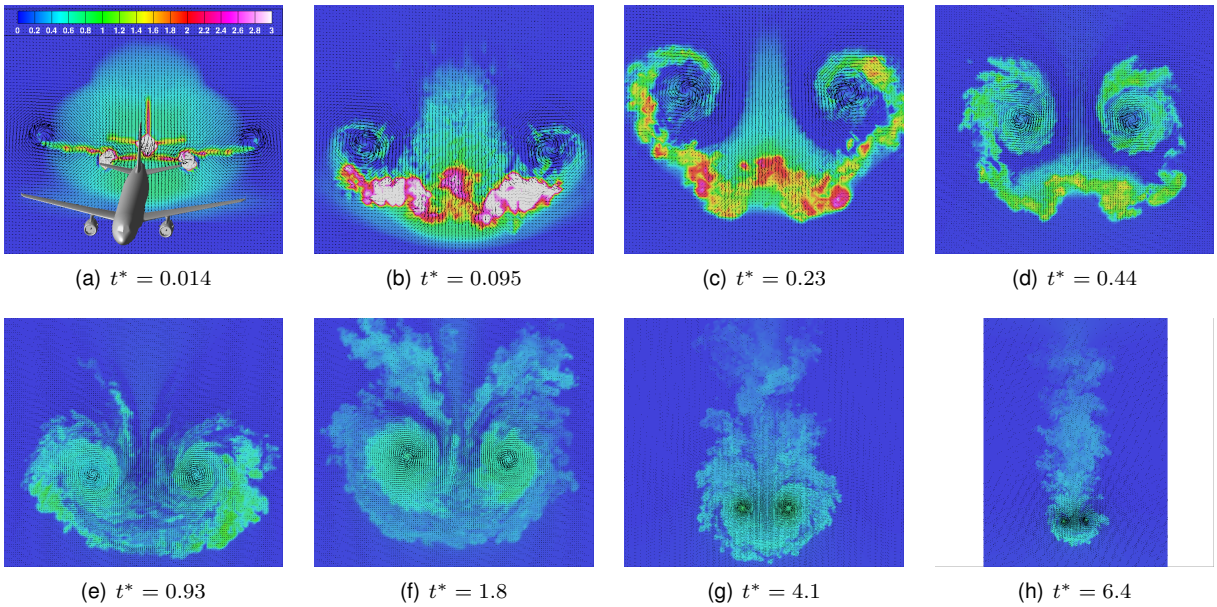

(a) $t^* = 0.014$ (b) $t^* = 0.095$ (c) $t^* = 0.23$ (d) $t^* = 0.44$

(e) $t^* = 0.93$ (f) $t^* = 1.8$ (g) $t^* = 4.1$ (h) $t^* = 6.4$

Figure 16: Heat evolution after roll-up, thrust.

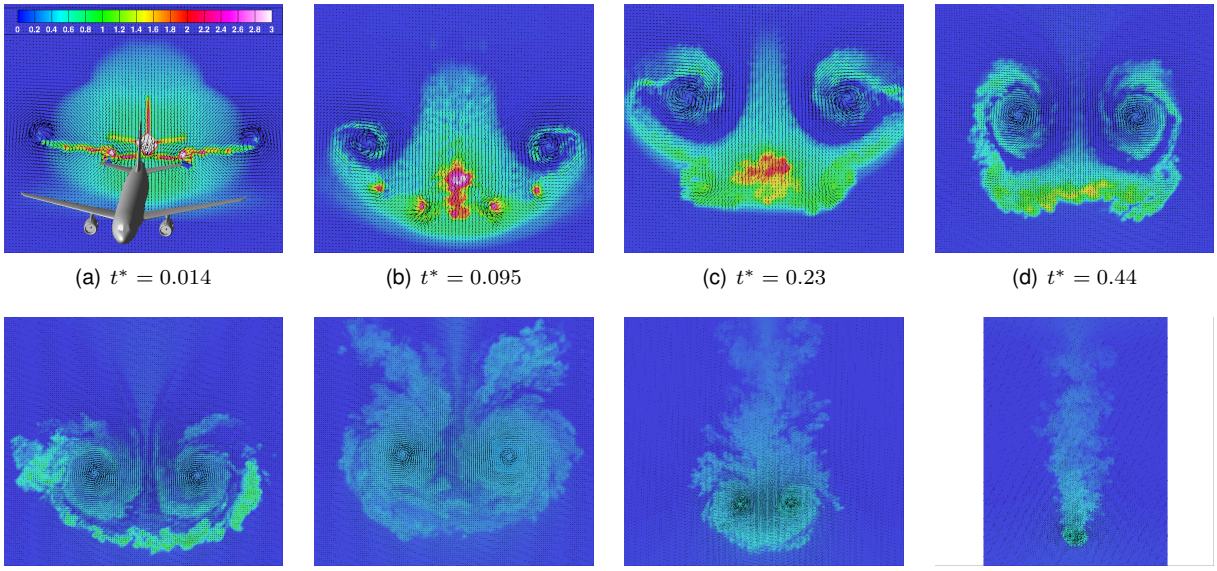

(a) $t^* = 0.014$ (b) $t^* = 0.095$ (c) $t^* = 0.23$ (d) $t^* = 0.44$

(e) $t^* = 0.93$ (f) $t^* = 1.8$ (g) $t^* = 4.1$ (h) $t^* = 6.4$

Figure 17: Heat evolution after roll-up, thrust.

- the ambient turbulence can be treated straight forward by pre-simulation.

The employed DLR TAU RANS code uses unstructured finite volume meshes. The mesh generation employs an automatic mesh adaptation technique increasing the total number of point by about 25%. The code captures compressible flow and incorporates the Spalart-Allmaras (SA) turbulence model. The Airbus A320 “ATRA” model was incorporated at typical cruise flight conditions. The incompressible LES code MGLET was coupled to TAU by the potential temperature additionally to the existing velocity coupling. The results show that the jet engines influence the near field as well as the far field. The hot turbulent plume behind the engines clearly superposes the coherent engine vortices. They disturb the coherency of the wake particularly the relatively strong engine vortex is getting turbulent very fast. This leads to a slower decay of the entire system, as the Crow-instabilities are suppressed and develop later. This confirms the idea that Crow-linking can triggered be coherent multi vortex systems, as in the case without thrust. The heat dissipates very fast. The descending vortex system leaves a vertical heat plume, where the maximal temperature is in the turbulent jet first, but is captured inside the vortex core for later vortex ages.

Acknowledgments

The work was performed within the DLR project L-bo*ws*. The CPU time on the HPC Cluster SuperMUC, provided by the Leibniz Supercomputing Centre (LRZ) are greatly acknowledged.

References

Bannon, P. R. (1995), Potential Vorticity Conservation, Hydrostatic Adjustment, and the Anelastic Approximation. *Journal of the Atmospheric Sciences*, Vol. 52, No. 12, pp. 2302–2312. doi:10.1175/1520-0469(1995)052<2302:PVCHAA>2.0.CO;2.

Bao, F., Vollmers, H. (2005), Alleviation of End-effects in Facilities for Far Wake Investigations. *43rd AIAA Aerospace Sciences Meeting and Exhibit*. Reno, Nevada.

Bier, N., Rohlmann, D., Rudnik, R. (2012), Numerical Maximum Lift Predictions of a Realistic Commercial Aircraft in Landing Configuration. *AIAA 2012-0279, 50th AIAA Aerospace Sciences, Nashville, USA*.

Burkhardt, U., KÃd'rcher, B., Schumann, U. (2010), Global Modeling of the Contrail and Contrail Cirrus Climate Impact. *Bulletin of the American Meteorological Society*, Vol. 91, No. 4, pp. 479–484. doi: 10.1175/2009BAMS2656.1.

Centaur (2017), Centaursoft: CENTAUR Grid Generation Software.

Gerz, T., Ehret, T. (1997), Wingtip vortices and exhaust jets during the jet regime of aircraft wakes. *Aerospace Science and Technology*, Vol. 1, No. 7, pp. 463 – 474. ISSN 1270-9638. doi: https://doi.org/10.1016/S1270-9638(97)90008-0.

Gerz, T., Holzäpfel, F. (1999), Wing-Tip Vortices, Turbulence, and the Distribution of Emissions. *AIAA Journal*, Vol. Vol. 37, No. 10, pp. 1270–1276.

Gerz, T., Holzäpfel, F., Darracq, D. (2002), Commercial aircraft wake vortices. *Progress in Aerospace Sciences*, Vol. 38, No. 3, pp. 181–208. doi:10.1016/S0376-0421(02)00004-0ö.

Hallock, J. N., Holzäpfel, F. (2018), A review of recent wake vortex research for increasing airport capacity. *Progress in Aerospace Sciences*, Vol. 98, pp. 27 – 36. ISSN 0376-0421. doi: https://doi.org/10.1016/j.paerosci.2018.03.003.

Hokpunna, A. (2009), *Compact Fourth-order Scheme for Numerical Simulations of Navier-Stokes Equations*. PhD Thesis, Technische Universität München (Germany).

Hokpunna, A., Manhart, M. (2010), Compact Fourth-order Finite Volume Method for Numerical Solutions of navier-Stokes Equations on Staggered Grids. *Journal of Computational Physics*, Vol. 229, No. 20, pp. 7545–7570. doi:https://doi.org/10.1016/j.jcp.2010.05.042.

Holzäpfel, F. (2003), Probabilistic Two-Phase Wake Vortex Decay and Transport Model. *Journal of Aircraft*, Vol. 40, No. 2, pp. 323–331. doi:https://doi.org/10.2514/2.3096.

Jaquin, L., Fabre, D., Geffroy, P., Coustols, E. (2001), The properties of a transport aircraft wake in the extended near field: an experimental study. *AIAA Conference Proceedings*, 2001-1038.

Kolomenskiy, D., Paoli, R. (2018), Numerical Simulation of the Wake of an Airliner. *Journal of Aircraft*.

Kroll, N., Becker, K., Rieger, H., Thiele, F. (2009), *MEGADESIGN and MegaOpt - German Initiatives for Aerodynamic Simulation and Optimization in Aircraft Design*. ISBN 978-3-642-04092-4.

Manhart, M. (2004), A Zonal Grid Algorithm for DNS of Turbulent Boundary Layers. *Computer and Fluids*, Vol. 33, No. 3, pp. 435–461. doi:https://doi.org/10.1016/S0045-7930(03)00061-6.

Meneveau, C., Lund, T. S., Cabot, W. H. (1996), A Lagrangian dynamic subgrid-scale model of turbulence. *Journal of Fluid Mechanics*, Vol. 319, pp. 353–385. doi: https://doi.org/10.1017/S0022112096007379.

Minnis, P., Young, D. F., Garber, D. P., Nguyen, L., Smith, W. L., Palikonda, R. (1998), Transformation of contrails into cirrus during SUCCESS. *Geophysical Research Letters*, Vol. 25, No. 8, pp. 1157–1160. doi:10.1029/97GL03314.

Misaka, T., Holzäpfel, F., Gerz, T. (2013), Wake Evolution of High-Lift Configuration from Roll-Up to Vortex decay. *51st AIAA Aerospace Sciences Meeting, Grapevine, Texas,USA*.

Misaka, T., Holzäpfel, F., Gerz, T. (2015), Large-Eddy Simulation of Aircraft Wake Evolution from Roll-Up until Vortex Decay. *AIAA Journal*, Vol. 53, pp. 2646–2670. doi:10.2514/1.J053671.

Misaka, T., Holzäpfel, F., Hennemann, I. Gerz, T., Manhart, M., Schwertfirm, F. (2012), Vortex bursting and tracer transport of a counter-rotating vortex pair. *Physics of Fluids*, Vol. 24, pp. (025104–1) – (025104–21). doi:https://doi.org/10.1063/1.3684990.

Rohlmann, D., Keye, S. (2015), Stall Maneuver Simulation of an elastic Transport Aircraft based on Flight Test Data. *AIAA 2015-2570, AIAA Aviation, 33rd AIAA Applied Aerodynamics Conference, Dallas, USA*.

Rumsey, C. L., Long, M., Stuever, R. A., Wayman, T. R. (2011), Summary of the First AIAA CFD High-Lift Prediction Workshop. *Journal of Aircraft*, Vol. 48, No. 6, pp. 2068–2079. doi: https://doi.org/10.2514/1.C031447.

Spalart, P., Allmaras, S. (1992), A one-equation turbulence model for aerodynamic flows. *30th Aerospace Sciences Meeting and Exhibit, Aerospace Sciences Meetings*. doi: https://doi.org/10.2514/6.1992-439.

Stephan, A., Holzäpfel, F., Misaka, T. (2014), Hybrid simulation of wake-vortex evolution during landing on flat terrain and with plate line. *International Journal of Heat and Fluid Flow*, Vol. 49, pp. 18–27. doi:https://doi.org/10.1016/j.ijheatfluidflow.2014.05.004.

Stephan, A., Rohlmann, D., Holzäpfel, F., Rudnik, R. (2018), Effects of Detailed Aircraft Geometry on Wake Vortex Dynamics During Landing. *Journal of Aircraft*, Vol. submitted.

1.2.1 Enhanced Wake Vortex Decay in Ground Proximity Triggered by Plate Lines

Frank Holzäpfel, Anton Stephan, Tobias Heel and Stephan Körner

Institute of Atmospheric Physics

From pilot reports, field measurements and numerical simulations it is known that wake vortices may persist within the glide path in ground proximity leading to an increased encounter risk. This paper investigates wake vortex behaviour during final approach and landing in order to understand why landings can be safe nevertheless. Further, it is investigated whether and to what extent the installation of plate lines beyond the runway tails may further accelerate wake vortex decay and thus improve safety by reducing the number of wake vortex encounters. A hybrid numerical simulation approach is employed to investigate vortex evolution from roll-up until final decay during the landing manoeuvre. The simulations are complemented by field measurement data accomplished at Munich airport and at special airport Oberpfaffenhofen. During touchdown so-called end effects trigger pressure disturbances and helical vortex structures that appear to ensure vortex decay rates in ground proximity needed to guarantee the required safety targets of aviation. Lidar measurements indicate that vortex decay indeed can be accelerated by a plate line installed on the ground surface. The lifetime of the most safety relevant long-lived and strongest vortices can be reduced by one third. The installation of plate lines beyond the runway tails may improve safety by reducing the number of wake vortex encounters and increase the efficiency of wake vortex advisory systems.

1. Introduction

Aircraft trailing vortices, generated as an unavoidable consequence of lift, pose a potential risk to following aircraft. The current separation standards between consecutive aircraft are still heavily influenced by the early studies carried out in the 1970s, with additional refinements introduced in the 1980s and 1990s (Hallock et al., 1998). These aircraft separations limit the capacity of congested airports in a rapidly growing aeronautical environment. The most likely economic scenario for the future European airport demand (EUROCONTROL, 2013) indicates that there will be around 1.9 million unaccommodated flights in 2035, constituting approximately 12% of the expected demand. Future air traffic increase and the deregulation of the airspace targeted by SESAR (SESAR, 2009) and NextGen (NextGEN, 2007) employing novel concepts such as trajectory-based operations and self-separation together with the increasing diversity of aircraft types from very light jets to super heavy aircraft might raise the probability to encounter wake vortices.

A few years ago ICAO initiated a process for the harmonization of wake turbulence separations termed RECAT. RECAT phase 1, which is the classification into six categories considering besides the weight, the approach speed, wing characteristics and in parts also the rolling moment exerted on following aircraft, has been implemented at the four US airports Memphis, Louisville, Cincinnati, and Atlanta followed by others (SAFO, 2014). The long-term

goal of the RECAT initiative plans for dynamic pair-wise separations that consider the aircraft type pairing and the environmental conditions. For an optimum exploitation of the dynamic pair-wise separations concept, full understanding of wake vortex behaviour during final approach and touchdown is mandatory.

The highest risk of encountering wake vortices prevails in ground proximity, where the vortices cannot descend below the glide path but tend to rebound due to the interaction with the ground surface (Holzäpfel and Steen, 2007). Weak crosswinds may compensate the self-induced lateral propagation of the upwind vortex, such that it may hover over the runway directly in the flight path of the following aircraft. From large eddy simulation as well as from lidar field measurements it is known that wake vortices may live significantly longer than the 2 minutes corresponding roughly to the 5 NM separation between a leading heavy weight class aircraft and a medium follower (Misaka et al., 2012). Consequently, the incident reporting scheme established by NATS reports most encounters at flight altitudes below 300 ft (Elsenaar et al., 2006, Critchley and Foot, 1991). Long-term lidar measurements of wake vortices at Charles de Gaulle airport indicate that in 3% of the cases the vortices are at least as close as 25 m to following landing aircraft within a vertical measurement plane close to the threshold (Treve, 2011). An analysis of DLR's wake vortex advisory system WSVBS demonstrates that in 57% – 70% of landings wake vortex behaviour in ground proximity impedes reduced separations (Holzäpfel et al., 2012)). Moreover, the possibilities of the pilot to recover from a vortex encounter are limited by the low flight altitude.

All these findings suggest that we do not yet understand wake vortex behaviour in ground proximity at a sufficiently good level and that comprehensive understanding of vortex evolution during the last seconds of a flight is of primary interest. With this paper we are asking two questions:

"Why is approach and landing safe under these conditions?"

"Can we actively promote wake vortex decay in ground proximity?"

Appropriate answers to these questions are crucial for the design of an optimal wake vortex advisory system (WVAS) (Gerz et al., 2002; Holzäpfel et al., 2009; Gerz et al., 2009; Hinton et al., 2000). Clearly, this paper cannot fully answer these questions but may substantially contribute to the answers based on advanced numerical simulation and the analysis of data of two field measurement campaigns.

After the introduction we present results of a new hybrid simulation method where an aircraft model and its surrounding flow field, obtained from high-fidelity Reynolds-averaged Navier-Stokes (RANS) simulation, are swept through a ground-fixed computational domain to initialize the wake whose further evolution is computed employing large eddy simulation (LES) (Misaka et al., 2015). This hybrid approach allows the simulation of vortex evolution from roll-up until final decay. The new method has been extended to the approach and landing of an aircraft in high-lift configuration (Stephan et al., 2013a). With the RANS/LES method we investigate the speed up of the interaction of the wake vortices with the ground at very low flight altitudes, the so-called end effects induced at the instant of touch-down when vortex circulation ceases abruptly, and the effects of a patented plate line deployed on the airfield in order to accelerate wake vortex decay. The installation of plate lines beyond the runway tails

may improve safety by reducing the number of wake vortex encounters and increase the efficiency of wake vortex advisory systems.

In the next section the numerical simulations are compared to results of field measurement campaigns conducted at Munich airport between 11 March and 12 May 2011 and at special airport Oberpfaffenhofen on 29 and 30 April 2013. The Munich data comprises 779 landings at vortex generation altitudes between 0.5 and 3 initial vortex separations, b_0, above ground. The data indicates that vortex decay on average progresses significantly faster at lower vortex generation heights. On one hand, the accelerated decay is related to an acceleration of the ground effect at very low altitudes; on the other hand, it can be attributed to end effects propagating from touch-down into the lidar measurement domain.

The final section describes the WakeOP campaign which was accomplished at special airport Oberpfaffenhofen in order to demonstrate the functionality of the plate line. Lidar measurements of the wake vortices generated during 74 overflights of the research aircraft HALO indicate that vortex decay indeed can be accelerated by a plate line installed on the ground surface. The field measurements are compared to simulations of HALO flights over the plate line accomplished with the new hybrid RANS/LES approach.

The paper has been published in Aircraft Engineering and Aerospace Technology (Holzäpfel et al. 2016).

2. Numerical Simulation of Approach and Landing

A new hybrid method for the simulation of wake vortex evolution from early roll-up until final decay is applied for approach and landing of an aircraft including touch-down. The effects of a plate line installed beyond the runway tails are also investigated. The acceleration of wake vortex decay in ground proximity triggered by plate lines has been investigated before experimentally in a towing tank (Stephan et al., 2013b), with classic LES (Stephan et al., 2013b; Stephan et al., 2013c), and with the hybrid LES approach presented here (Stephan et al., 2013a). A respective patent has been filed under number DE 10 2011 010 147; further international patents are pending.

The hybrid LES method initializes a realistic aircraft wake in a LES domain by sweeping a high-fidelity RANS aircraft flow through the domain, which enables to simulate wake-vortex evolution from generation until final decay (Misaka et al., 2013; Misaka et al., 2015). The simulations are performed for a large transport aircraft model in high-lift configuration previously used in ONERA's catapult facility during the European AWIATOR project. The RANS flow field, which has been established before with the DLR TAU code, serves as a forcing term or inner boundary in the LES domain. This approach can be referred to as a fortified solution algorithm or as a nudging technique used frequently for data assimilation in numerical weather prediction models. For generality all results are presented in normalized form denoted by an *, where the characteristic scales are based on initial vortex separation, b_0, and circulation, Γ_0, leading to the timescale $t_0 = 2\pi b_0^2 / \Gamma_0$.

Figure 1 depicts the wake evolution during approach and after touchdown at the times $t^* = -0.15$, 0.1, 0.5, and 1.0, where the time stamp $t^* = 0$ is assigned to the instant of touchdown. Figure 1 top left displays the complex vorticity distribution emerging directly behind the aircraft and the subsequent vortex roll-up to a single counter-rotating vortex pair.

In the near wake flow the outer flap-tip vortices, the wing-tip vortices, the inner engine-nacelle vortices, and the vortices detaching from the wing-fuselage junction can be differentiated. Out of ground effect the wing-tip and flap-tip vortices merge at a distance of about x* = 13 from the aircraft.

The wake vortices as well as the bound vortex along the wing instantaneously induce a vorticity layer of opposite sign at the ground surface already at the initial flight altitude of z* = 1.2. This vorticity layer subsequently detaches from the ground and is wrapped around the primary vortices. Due to the small distance between the vortices and the ground surface this process starts with almost no delay at the point of touchdown (Figure 1 top right, t* = 0.1). The turbulent wake of the fuselage is transported towards the ground by the downwash between the main vortices, where it disturbs the vorticity layer at the ground surface (t* = 0.1, 0.5). As a consequence, the secondary vorticity detaching from the ground is organized in omega-shaped / hairpin vortices wrapping around the primary vortices (bottom left).

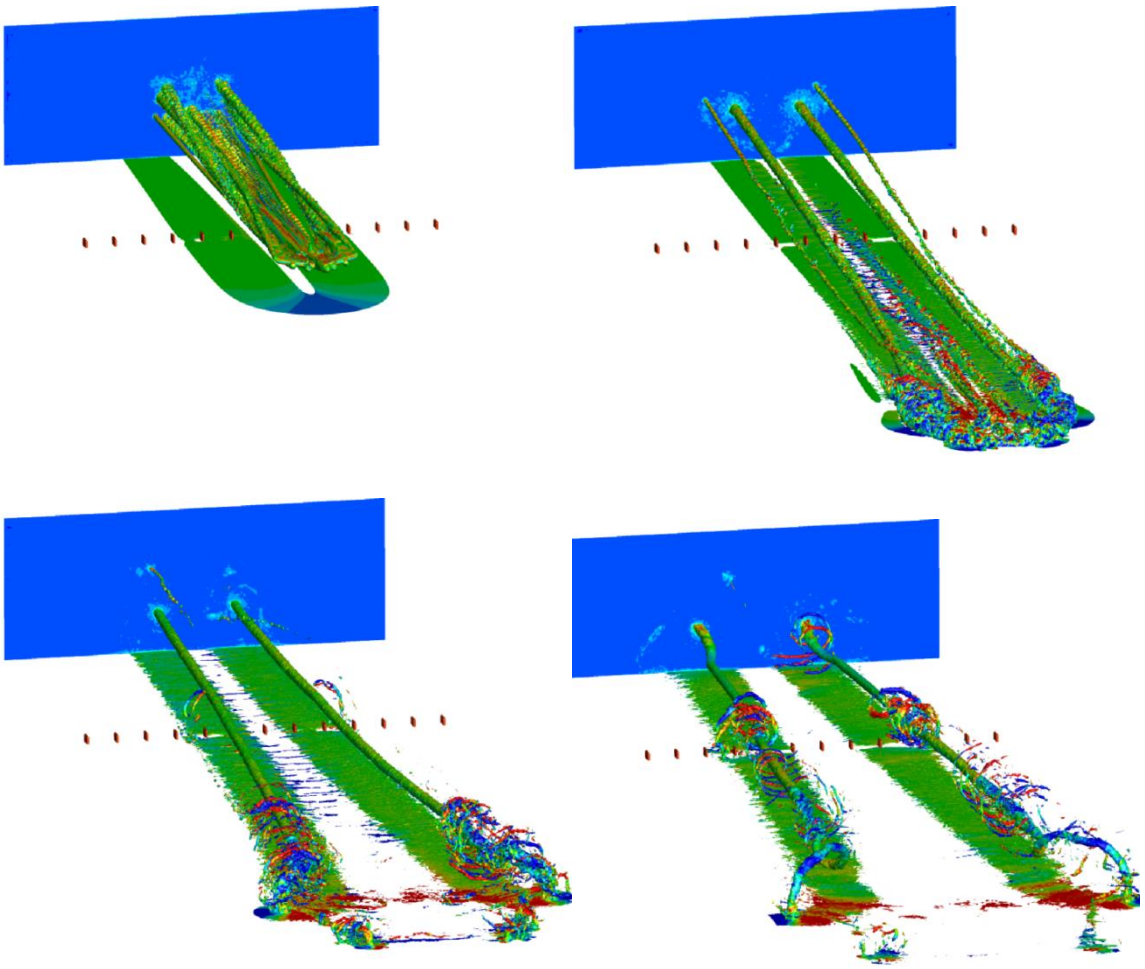

Figure 1 Wake vortex evolution during final approach with plate line at t* = -0.15, 0.1, 0.5, and 1.0. Iso-vorticity surface ||ω*|| = 110 coloured by vorticity strength in spanwise direction.

Note that the hybrid approach requires neither environmental turbulence nor surface inhomogeneities to trigger the turbulence in the wake vortices and the consequential coherent secondary vorticity structures that are vital for vortex decay characteristics in ground

proximity (Stephan et al., 2013c). Further consequences of the low vortex generation altitude are the rapid divergence of the vortices reaching a maximum vortex separation of more than 7 b_0 already at t* = 2.2 and a speed up of the merger of flap-tip and wing-tip vortex by a factor of four (Stephan et al., 2014).

Immediately after touchdown the bound vortex vanishes and the unconnected ends of the wake vortices get highly disturbed. Due to the pressure imbalance between the core of the freely decaying vortex ends and their environment, an axial flow is induced within the vortex cores and a corresponding pressure disturbance is propagating against flight direction. Simultaneously, helical disturbances are wrapped around the vortices and are propagating along the wake as well. The pressure disturbances and the helical structures constitute the so-called end effects (Bao and Vollmers, 2005).

End effects can occasionally be observed when condensation trails form in humid air marking the vortex cores that adopt helical shapes and quickly disappear after touchdown. An analysis of the video YouTube (2008) suggests that the propagation speed of the pressure disturbances may be on the order of 60 m/s. However, this estimate involves substantial uncertainty. Condensation trails may occur when the temperature, lowered by the pressure decrease in the vortex core, leads to supersaturation of water vapour and thus to condensation. So the rapid disappearance of the condensation trail is directly related to the pressure and consequential temperature increase in the vortex cores.

In accordance with the Helmholtz vortex theorem the free vortex ends cannot persist but connect rapidly with the ground (see Figure 1 below) where they turn up vertically. Vortex connection with the ground has been reported at low vortex generation altitudes and increased levels of environmental turbulence (Proctor et al., 2000).

The first effect of the plate line can already be identified at t* = -0.15 via a small gap of the vorticity layer generated at the ground. Already at t* = 0.5 omega-shaped secondary vortices have detached from the plates and approach the primary vortices driven by self-induction. A half vortex time scale later vigorous helical secondary vorticity structures have wrapped completely around the wake vortices and travel to either side of the plate line again driven by self-induction. The plate line concept exploits vortex dynamics by generating powerful secondary vortices that first actively approach the primary vortices and then actively propagate along the primary vortices finally leading to accelerated vortex decay (Stephan et al., 2013c).

Figure 2 shows the spatial and temporal evolution of radii-averaged circulation, $\Gamma_{5\text{-}15}$*. The propagation of the end effects can be discerned by the transition from orange to yellow along a line with a slope of about -8 x*/t*, whereas the sharp transition between yellow and blue represents the propagation of the vertical vortex segments against flight direction. The circulation evolution without plates on the left indicates rapid circulation decay at the touchdown position (x* = 16.3) propagating against flight direction. At t* = 3 the circulation has decreased to about $\Gamma_{5\text{-}15}$* = 0.7. The circulation decay triggered by the plates situated at x* = 5.1 commences already at times before one directly above the plates and quickly propagates to either side. At t* = 3 the circulation has decreased to below 0.4 along a considerable part of the considered approach path. Only residual vortex segments near x* = 12, which have linked on both sides with the ground, are disconnected from the disturbances and thus retain higher circulation values.

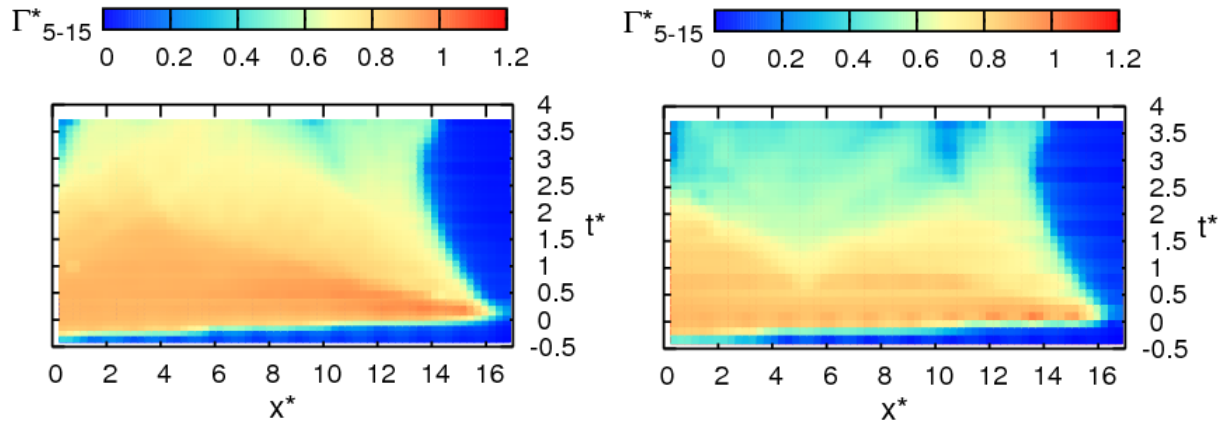

Figure 2 Temporal and spatial evolution of normalized radii-averaged circulation without (left) and with (right) plate line.

For operational application at an airport the plate line dimensions and arrangement need to be optimized such that the interaction of the disturbances stemming from the end effects and the plates proceed sufficiently fast to accelerate vortex decay at a usable rate all along the area between the first plate line and the touchdown zone. Additional plate lines located further away from the runway shall reduce vortex lifetime in the whole area where vortex rebound may lead to potentially hazardous encounters.

3. Measurement Campaign WakeMUC at Munich Airport – Ground Effect and End Effects

Wake vortex behaviour during final approach is investigated employing field measurement data gathered during the WakeMUC campaign accomplished between 11 March and 12 May 2011 at Munich airport. In that time frame lidar measurements of 779 landings of heavy aircraft and medium type aircraft on runway 26L have been collected. The 2 μm pulsed lidar was situated at a distance of about 850 m to the runway centreline in northerly direction. Different azimuth angles of the lidar beam have been adjusted during the 12 measurement days in order to capture wake vortices at different generation heights. Close to the threshold a METEK SODAR with a RASS extension provided 10-minute averages of vertical profiles of the three wind components, vertical fluctuation velocity, and virtual temperature with a vertical resolution of 20 m. The SODAR/RASS system was complemented by an ultrasonic anemometer (USA) mounted on a 10 m mast. Vortex generation altitudes reached from 0.5 initial vortex separations up to 3 b_0. Most of the measured wake vortices have been generated by medium type aircraft belonging for example to the A320 or B737 families and only a few by heavy aircraft.

Figure 3 displays measured wake vortex evolution in terms of vertical transport, circulation evolution, and vortex separation. Besides the scatter plot covering the complete data set, average developments of these parameters for seven different vortex generation altitude intervals are plotted. The employed height intervals are detailed in Table 1.

Figure 3 top left indicates that the mean minimum height above ground decreases from 1 b_0 at flight heights of about 3.2 b_0 to 0.5 b_0 at flight heights of 0.6 b_0. Also the maximum rebound

heights are ordered according to the vortex generation heights. As expected the lee vortex initiates its rebound earlier and at higher altitudes, because the crosswind shear supports the formation of the respective secondary vorticity layer at the ground (Stephan et al., 2013c). In agreement with the numerical simulations (see Figure 1) the generation and detachment of secondary vorticity at the ground proceeds almost immediately at very low vortex generation altitudes (in Figure 3 this is inferred from the supressed vortex descent and the immediate vortex decay and divergence). Figure 3 below indicates that vortex separation progresses the faster the lower the vortex generation height. This trend together with the maximum observed separations of about 8 b_0 again is well in line with simulations.

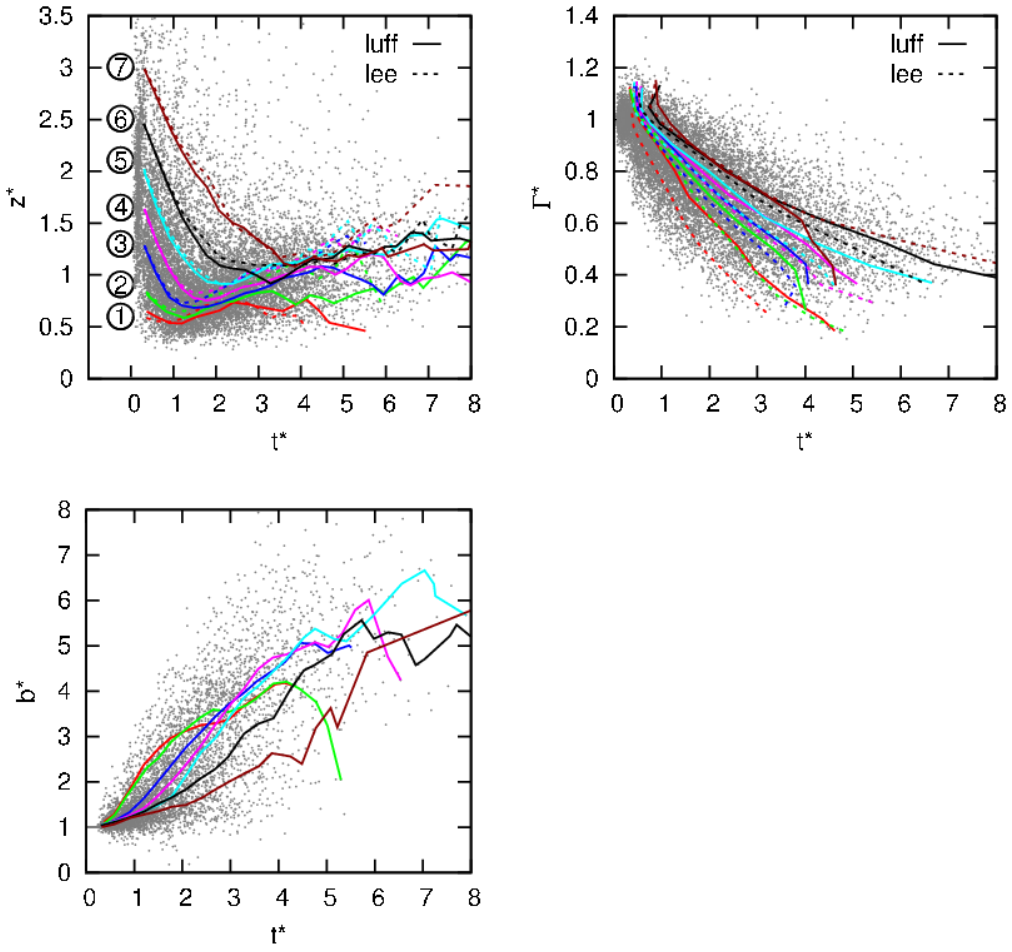

Figure 3 Vortex behaviour measured during WakeMUC campaign. Vortex generation heights detailed in table 1.

Table 1 Vortex generation height range intervals employed in Figure 3.

number	normalized height range
1	0.4 – 0.8
2	0.8 – 1.2
3	1.2 – 1.6
4	1.6 – 2.0
5	2.0 – 2.4
6	2.4 – 2.8
7	2.8 – 3.5

The circulation evolution related to the different vortex generation altitudes is shown in Figure 3 top right. The circulation curves are determined employing circulation binning instead of time binning in order to avoid that the curves level off towards the longest-lived vortex observations. Except for the highest vortex generation height, the decay rate of the lee vortex is increased compared to the luff vortex as expected (Holzäpfel and Steen, 2007; Stephan et al., 2013c).

The lower the flight altitude the faster the vortex decay. Comparing vortex generation heights 1 and 6 indicates that maximum vortex observation times for the operationally relevant luff vortex are about halved and that despite these disparate vortex observation times the circulation is even reduced by 50% at the lowest flight height. This drastically accelerated decay close to the ground corroborates qualitatively the numerical simulations. Most notably it indicates that end effects very likely actually play a distinguished role for the safety of the final approach as already revealed by the numerical simulations.

A comparison of Figures 2 and 3 shows that the circulation decay related to the propagating end effects is even faster in the measurements than in the simulations (flight heights of Figure 2 cover height ranges 1 and 2 in Figure 3). Potential reasons for this mismatch are that the turbulent kinetic energy in the aircraft wake predicted by the RANS simulation has not yet been assimilated into the resolved LES field and that in the simulation the vortex cores are too wide caused by the limited grid resolution leading to higher pressure in the core centre and thus lower pressure gradients driving the end effects. Investigations without the impact of the ground indicate that the wake turbulence is essential to achieve the circulation decay rates during the early wake vortex evolution observed with lidar in the so-called decay phase (Misaka et al., 2013). Other potential reasons are the lack of environmental turbulence and of headwind.

4. Measurement Campaign WakeOP at Oberpfaffenhofen Airport – Plate Line

The WakeOP campaign has been accomplished at special airport Oberpfaffenhofen with the research aircraft HALO, a modified Gulfstream G550, on 29 - 30 April 2013. The purpose of the

campaign was to demonstrate the functionality of the plate line patent DE 10 2011 010 147 to significantly accelerate vortex decay in ground proximity. A comparison of wake vortex behaviour with and without the patented obstacles at the ground employing towing tank experiments and LES is available in Stephan et al. (2013b). Effects of obstacle geometry and dimensions have been investigated in Stephan et al. (2013c). The 74 overflights of HALO over the plate line were divided into four flights. The sketch in Figure 4 illustrates the experimental setup, whereas the photo in Figure 5 provides an impression of a HALO overflight and the subsequent vortex roll-up in ground proximity visualized by white fog and red smoke.

HALO with its wing span of 28.48 m was operated in high-lift configuration with the landing gear deployed at approach speeds around 75 m/s. In order to generate strong wake vortices the refueling was adjusted such that the HALO was landing after the traffic patterns close to its maximum landing weight of 34,156 kg. HALO was flying across the plate line at a constant altitude of nominally one vortex separation b_0 = 22 m above ground. HALO avionic data was used to assess the time, height, lateral position, flight speed and aircraft weight of the plate line passages. Nose boom measurements deliver wind speed, turbulence and temperature data. The flight times were scheduled to the times of the day with minimum wind speeds and turbulence. The remaining impact of the environmental conditions on vortex behaviour was minimized by folding the plates up and down alternatingly after every second overflight.

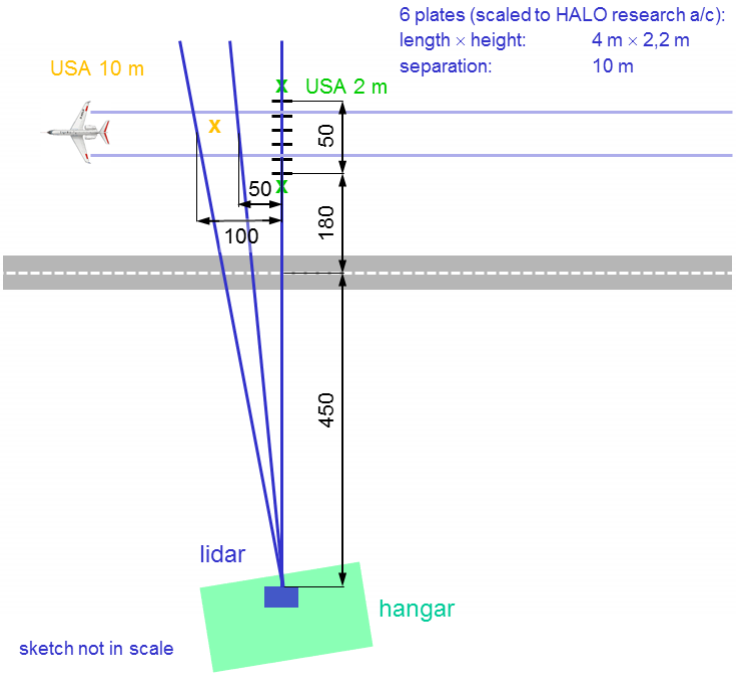

Figure 4 Sketch of WakeOP flight experiment setup at special airport Oberpfaffenhofen. All dimensions in meters.

Figure 5 Overflight of HALO aircraft and vortex roll-up in ground proximity visualized by white fog and red smoke.

The plate line consists of six wooden plates fixed by steel ropes at the ground (see Figure 6). Hinges are allowing folding the plates up and down. The plate dimensions have been scaled down to the wing span of HALO and amount to a length of 4 m and a height of 2.2 m. The separation between adjacent plates has been adjusted to 10 m leading to a length of the overall plate line of 50 m. For application to wake vortices generated by heavy aircraft, the plate line dimensions will be roughly doubled.

Figure 6 Plate line consisting of 6 plates with dimensions of 2.2 m × 4 m displaced by 10 m.

The 2 µm pulsed lidar was situated in the hangar at a distance of about 600 m (see Figure 4). The azimuth angle of the vertical scanning plane was adjusted such that measurements directly above the plates and at offsets of 50 m and 100 m were supported. The measurements with offsets were intended for the determination of the propagation speed of the disturbances triggered by the plates. Two ultrasonic anemometers (USA) equipped with microphones at a sensor height of 2 m have been lined up with the plate line. The operational USA of the airport mounted on a 10 m mast was separated by about 50 m from the plate line and complemented the measurements of wind, turbulence, and temperature at 2 m and at flight level by an intermediate height. Red smoke and white fog was released at the ground in order to visualize the vortex behaviour which has been documented by video and photo. An impression of the WakeOP campaign is available in the BBC 2 production “Airport Live - Episode 2” starting from minute 17 (BBC 2, 2013).

Already during the campaign the smoke and fog visualizations of the vortex evolution indicated that with the plate line the formed vortex structures are less coherent. Figures 7 and 8 display the quantitative vortex evolution measured by lidar without and with the plate line, respectively. Further, LES results are shown for comparison which will be discussed subsequently.

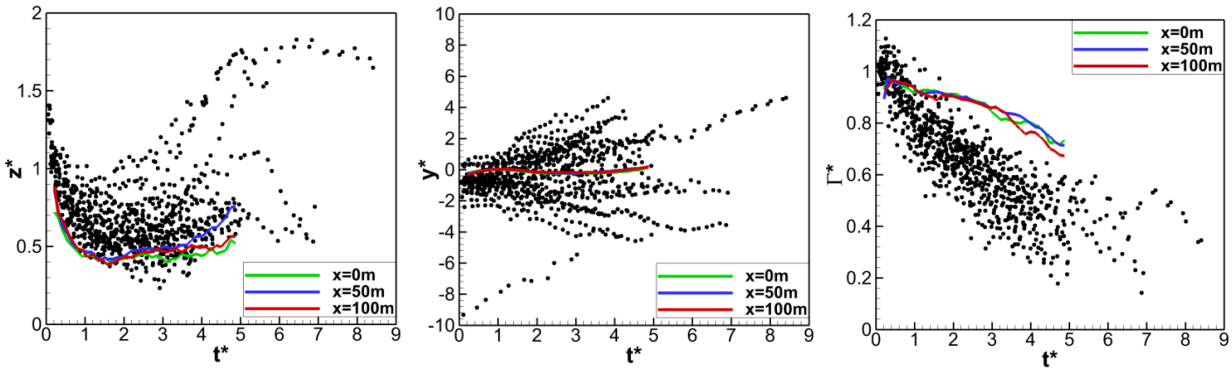

Figure 7 Measured (dots) and simulated (lines) evolution of luff vortex without plate line.

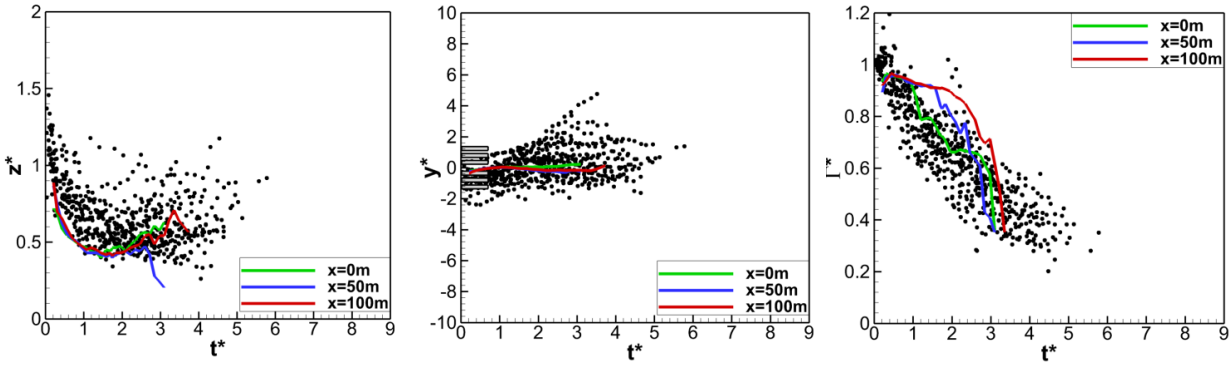

Figure 8 Measured (dots) and simulated (lines) vortex evolution with plate strikes.

Figure 7 displays data of the operationally relevant luff vortex, whereas Figure 8 presents cases where the vortices (mostly the luff vortex) encountered some plates at least temporarily. Figure 8 centre indicates that despite weak wind and turbulence conditions the plates were not perfectly hit by a large fraction of the vortices (plate positions are indicated by small rectangles). The atmospheric variability modified vortex transport in a complex way such that reliable plate line strikes were frequently prevented.

The comparison of Figures 7 and 8 reveals that vortex lifetimes and vortex rebound heights are clearly reduced by the plates. Also the average decay rate is increased by the plates. It is found that at all three axial offsets the circulation decay proceeds faster with the plate line. However, the propagation speed of the disturbances triggered by the plates cannot be inferred from the circulation evolutions. Actually, the measurements displaced by 100 m from the line feature the strongest and a very early impact of the obstacles. This surprising conjuncture can be explained by the fact that for the largest offset the plate line was coincidentally hit best. Although the propagation speed of the disturbances triggered by the plates cannot be determined quantitatively it is obvious that this speed is very high.

Selected overflights have been simulated by the hybrid LES method described above. Figure 9 depicts exemplarily a simulated flight of the HALO aircraft over the plate line with a weak crosswind. The cases plotted in Figure 7 and 8 employ a constant flight height of b_0 above ground and a crosswind of w_0 directed towards positive y-direction. The LES employs the Grötzbach-Schumann wall model (Grötzbach, 1987) in order to achieve a realistic Reynolds number of $Re_\Gamma = \Gamma/\nu = 10^7$. However, the wall model combined with the limited grid resolution in ground proximity do not support the formation of sufficiently strong secondary vortices with the consequences that the rebound altitude and vortex decay are underestimated whereas vortex divergence is overestimated.

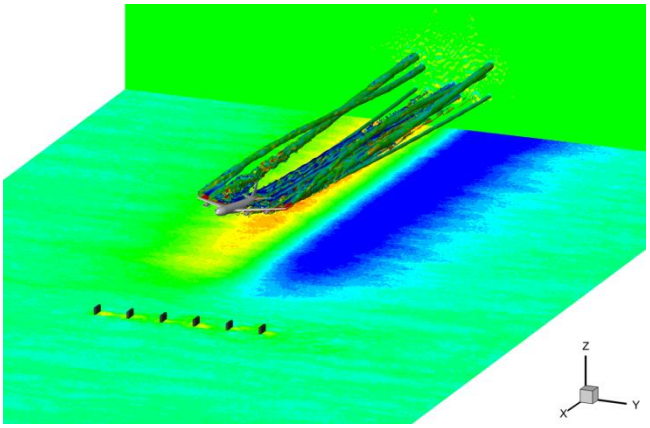

Figure 9 LES of the overflight of the HALO aircraft above the plate line at a weak crosswind. Wake vortices visualized by vorticity magnitude coloured by lateral vorticity component. Ground coloured according to crosswind speed.

The simulated vortex descent bounds vortex observations from below. This is partially due to the higher flight altitudes, turbulence and wind shear effects in the experiment, and the

underestimated secondary vortices in the simulation. Also the underestimated circulation decay may be attributed to the weak secondary vortices and weaker atmospheric turbulence.

At a distance of 50 m from the plate line the simulated vortices link with the ground; an effect which is less obvious but still conceivable in the observations. Directly above the plates (x = 0 m) the simulated circulation decay lies within the scattered measurement data. The delay of vortex decay at distances of 50 m and 100 m from the plate line observed in the LES is not present in the lidar data. A plausible explanation is that the LES underestimates the propagation speed of the disturbances triggered by the plates. A similar observation has also been made for the propagation speed of end effects (previous sections).

Figure 10 depicts cumulative distributions of measured circulation at vortex ages ranging from 40 s to 110 s with (lines with symbols) and without (lines) the plates. At every vortex age the circulation distribution with the plates indicates weaker and/or less detected wake vortices. Although the beneficial effects of the plates are not as pronounced as in laboratory experiments and LES, Figure 10 clearly indicates that a safety gain can be achieved by the installation of plate lines at an airport. The dissimilar efficiencies of the plate lines in laboratory, LES, and field experiment can be explained primarily by the atmospheric variability that prevented full plate strikes during the WakeOP campaign. This is not a flaw for operational application at an airport, because wake vortices advected out of a safety corridor around the glide path are not relevant for safety. Conversely, those vortices that remain in a critical part of the flight corridor will also be influenced by the plates.

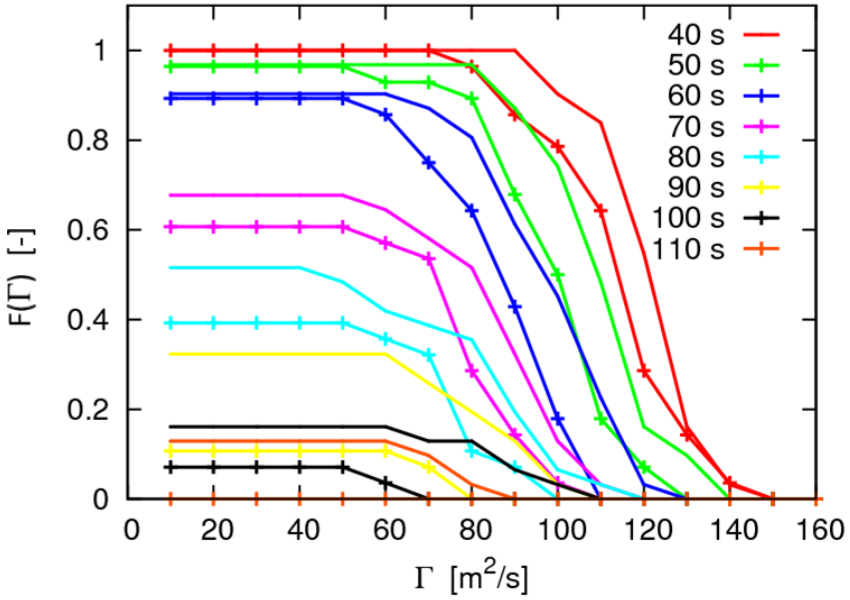

Figure 10 Cumulative circulation distributions at different vortex ages with and without plate line.

The benefits of the plate line appear much more conclusive if not the average behaviour is considered but only the most safety relevant most long-lived and strongest vortices (see Figure 11). The maximum circulation measured at different vortex ages reveals very

pronounced differences between the cases with and without plate line. While with the plate line no vortex survives longer than 100 s, without the plates a vortex with strength of more than 50% of its initial value is observed at an age of 130 s and the longest vortex duration amounts to 150 s. It can be concluded that the plate lines can be considered as a means that substantially reduces vortex lifetimes in situations where the vortices reside within the flight path and when environmental conditions support long-lasting and thus potentially hazardous vortices.

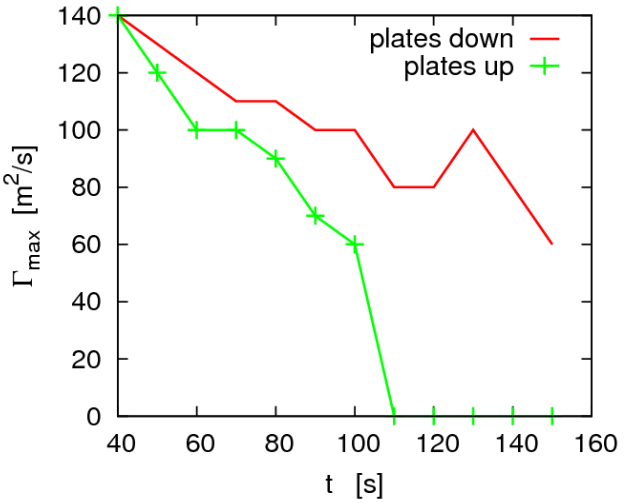

Figure 11 Maximum circulation measured at different vortex ages with and without plate line.

5. Conclusion

The current paper hypothesizes that with the given inefficacy of vortex descent below the glide slope in close ground proximity and the longevity of wake vortices observed in simulations and experiments, the probability of critical encounters during final approach should be much higher than reported in reality. Numerical simulations and field experiments are exploited in order to resolve this apparent contradiction.

A new hybrid simulation method that assimilates the highly accurate flow around an aircraft geometry in high-lift configuration into the domain of a large eddy simulation is used to capture wake vortex evolution from early roll-up to final decay in ground proximity. The simulations reveal that the sudden loss of lift during touchdown triggers so-called end effects that quickly propagate along the wake vortices and significantly accelerate vortex decay. The underlying mechanisms of the end effect appear to ensure vortex decay rates in ground proximity needed to guarantee the required safety targets of aviation.

In detail the following processes are identified. The roll-up and merger of the flap-tip vortices, the wing-tip vortices, and various other vortices to a single counter-rotating vortex pair is significantly accelerated close to the ground. The wake vortices as well as the bound vortex along the wing instantaneously induce a vorticity layer of opposite sign at the ground surface. The downwash of the turbulent fuselage wake disturbs this vorticity layer, such that the secondary vorticity detaching from the ground becomes organized in omega-shaped / hairpin

vortices wrapping around the primary vortices, leading to rapid decay. Due to the small distance between the vortices and the ground surface this process starts with almost no delay at the point of touchdown. A further consequence of the low vortex generation altitude is the rapid divergence of the vortices.

Immediately after touchdown the bound vortex vanishes and the unconnected ends of the wake vortices get highly disturbed. Due to the pressure imbalance between the core of the freely decaying vortex ends and their environment, an axial flow is induced within the vortex cores and a corresponding pressure disturbance is propagating together with helical disturbances against flight direction. The pressure disturbances and the helical structures constitute the so-called end effects. In accordance with the Helmholtz vortex theorem the free vortex ends cannot persist but connect with the ground.

Lidar measurements of the wake vortices generated by 779 arrivals at Munich airport during the WakeMUC campaign corroborate the findings of the simulations. In particular, it is shown that vortex decay rates are significantly increased at flight altitudes below one initial vortex separation. Headwinds, typically prevailing during landings, additionally advect the disturbances propagating from the touchdown zone against flight direction.

The beneficial effects of the touchdown on vortex decay can be extended along the whole airport area where vortices may rebound to the glide slope by installing a series of plates in lines perpendicular to the flight direction. The so-called plate lines trigger the early detachment of strong Ω-shaped secondary vortices that actively approach the wake vortices and subsequently propagate along the primary vortices. These dedicated secondary vortices lead to an accelerated wake vortex decay independent from natural external disturbances.

The lidar measurements accomplished during the WakeOP campaign at special airport Oberpfaffenhofen confirm the functionality of the plate line. Numerical simulations of flights over the plate line support the analysis of the field experiment. In many cases the atmospheric variability prevented reliable plate strikes such that on average vortex decay was augmented less in the field trial than in the previous laboratory experiments and numerical simulations. The benefits of the plate line appear much more conclusive if not the average behaviour is considered but only the most safety relevant long-lived and strongest vortices whose lifetime can be reduced by one third. It can be concluded that in potentially hazardous situations caused by persistent wake vortices within the glide path, plate lines may substantially reduce vortex lifetimes and thus increase safety.

The plate line design needs to be further optimized regarding the application to aircraft of different sizes and the compatibility with airport requirements. Once criteria like obstacle clearance, stability, frangibility, interference with the localizer, requirements of wildlife, and grounds maintenance are resolved and approved by authorities, it is planned to demonstrate the functionality of the plate line concept in an operational environment at Munich airport.

References

Bao, F. and Vollmers, H. (2005), “Alleviation of end-effects in facilities for far wake investigations”, AIAA-Paper 2005-0907.

BBC 2 (2013), “Airport Live - Episode 2”, available at https://www.youtube.com/watch?v=eHqdTddJQvQ (accessed 18 August 2015).

Critchley, J. and Foot, P. (1991), “UK CAA Wake Vortex Database: Analysis of Incidents Reported Between 1982 and 1990,” Civil Aviation Authority, CAA Paper 91.

Doligalski, T. L., Smith, C. R. and Walker, J. D. A. (1994), “Vortex Interactions with Walls,” *Annual Review of Fluid Mechanics*, Vol. 26, pp. 573–616.

Elsenaar B., van der Geest P., Speijker L., de Bruin A., Wolf S., Braun N., Gerz T., Holzäpfel F., Hahn K.-U., Schwarz C., Frech M., Köpp F., Mutuel L., Bourrez A., Barny H., Barbaresco F., Konopka J., Winckelmans G., Desenfans O., Pugh C., Davies H., Galpin D., Nicolaon J.-P., Vidal A., Harvey A., Wennerberg A., Schumacher J., Luckner R., Höhne G., Fuhrmann M., Laporte F., Hinsinger R., Schrauf G., Turp D., Agnew P., Hill C., Young R., Coustols E., Dolfi A. and Jacquin L. (2006): Wake Vortex Research Needs for "Improved Wake Vortex Separation Ruling" and "Reduced Wake Signatures", Part II, Specialists's Reports, Final Report of the Thematic Network "WakeNet2-Europe", 6th Framework Programme, 114 pages.

EUROCONTROL (2013), “Challenges of Growth 2013”, Summary Report, available at: http://www.eurocontrol.int/statfor.

Gerz T., Holzäpfel F. and Darracq D. (2002), “Commercial Aircraft Wake Vortices”, *Progress in Aerospace Sciences*, Vol. 38, No. 3, pp. 181-208.

Gerz T., F. Holzäpfel, W. Gerling, A. Scharnweber, M. Frech, K. Kober, K. Dengler and S. Rahm (2009), “The Wake Vortex Prediction and Monitoring System WSVBS - Part II: Performance and ATC Integration at Frankfurt Airport”, *Air Traffic Control Quarterly*, Vol. 17, No. 4, pp. 323-346.

Grötzbach, G. (1987) “Direct numerical and large eddy simulations of turbulent channel flows”, *Encyclopedia of Fluid Mechanics*, ed. N. Cheremisinoff, West Orange, NJ, pp. 1337-1391.

Hallock, J.N., Greene, G.C. and Burnham, D.C. (1998) “Wake Vortex Research – A Retrospective Look”, *Air Traffic Control Quarterly*, Vol. 6, No. 3, pp. 161-178.

Hinton, D.A., Charnock, J.K. and Bagwell, D.R. (2000) “Design of an Aircraft Vortex Spacing System for Airport Capacity Improvement,” AIAA Paper 2000-0622, 38th AIAA Aerospace Sciences Meeting & Exhibit, Reno, NV.

Holzäpfel, F. and Steen, M. (2007) “Aircraft Wake-Vortex Evolution in Ground Proximity: Analysis and Parameterization”, *AIAA Journal*, Vol. 45, No. 1, pp. 218-227.

Holzäpfel F., T. Gerz, M. Frech, A. Tafferner, F. Köpp, I. Smalikho, S. Rahm, K.-U. Hahn and C. Schwarz (2009) “The Wake Vortex Prediction and Monitoring Ssytem WSVBS - Part I: Design”, *Air Traffic Control Quarterly*, Vol. 17, No. 4, pp. 301-322.

Holzäpfel, F., Dengler, K., Gerz, T. and Schwarz, C. (2011) "Prediction of Dynamic Pairwise Wake Vortex Separations for Approach and Landing", AIAA Paper 2011-3037.
Misaka, T., Holzäpfel, F., Gerz, T., Manhart, M. and Schwertfirm, F (2012) "Vortex bursting and tracer transport of a counter-rotating vortex pair", *Physics of Fluids*, Vol. 24, No. 2, pp. 25104-1 - 25104-21, doi: 10.1063/1.3684990.

Holzäpfel, F., Stephan, A., Heel, T., Körner, S. (2016) "Enhanced Wake Vortex Decay in Ground Proximity Triggered by Plate Lines", Aircraft Engineering and Aerospace Technology, Vol. 88, Issue 2, pp. 206-214, doi: 10.1108/AEAT-02-2015-0045.

Misaka, T., Holzäpfel, F. and Gerz, T. (2013) "Wake Evolution of High-Lift Configuration from Roll-Up to Vortex Decay", AIAA Paper 2013-0362.

Misaka, T., Holzäpfel, F. and Gerz, T (2015) "Large-Eddy Simulation of Aircraft Wake Evolution from Roll-Up until Vortex Decay", accepted for publication in *AIAA Journal*, DOI: 10.2514/1.J053671.

NextGEN (2007), "Concept of Operations for the Next Generation Air Transportation System", Version 2.0, Joint Planning and Development Office, June.

Proctor, F.H., Hamilton, D.W. and Han, J. (2000) "Wake vortex transport and decay in ground effect: Vortex linking with the ground", AIAA-Paper 2000-0757.

SAFO 14007 (2014) "Safety Alert for Operators, Federal Aviation Administration", available at http://www.faa.gov/other_visit/aviation_industry/airline_operators/airline_safety/safo.

SESAR (2009) "European Air Traffic Management Master Plan of the Single European Sky ATM Research (SESAR) project", Edition 1, SESAR Consortium, March.

Stephan, A., Holzäpfel, F. and Misaka, T. (2013) "Towards Realistic Simulation of Wake-Vortex Evolution During Landing With Flat and Complex Terrain", 8th Int. Symposium on Turbulence and Shear Flow Phenomena, AER1A, August 28 - 30, Poitiers, France.

Stephan, A., Holzäpfel, F., Misaka, T., Geisler, R. and Konrath, R. (2013) "Enhancement of aircraft wake vortex decay in ground proximity - Experiment versus Simulation", *CEAS Aeronautical Journal*, Vol. 5, No. 2, pp. 109-125, DOI 10.1007/s13272-013-0094-8.

Stephan, A., Holzäpfel, F. and Misaka, T. (2013) "Aircraft Wake-Vortex Decay in Ground Proximity - Physical Mechanisms and Artificial Enhancement", *Journal of Aircraft*, Vol. 50, No. 4, pp. 1250-1260, doi/abs/10.2514/1.C032179.

Stephan, A., Holzäpfel, F. and Misaka, T. (2014) "Hybrid simulation of wake-vortex evolution during landing on flat terrain and with plate line", *International Journal of Heat and Fluid Flow*, Vol. 49, pp. 18-27.

Treve V., discussions during WakeNet3-Europe Workshop “Research Needs for Operational Concepts and Capacity Analysis”, London, UK, 8 - 9 Feb. 2011.

YouTube (2008) “A very wet arrival at Port Macquarie” available at https://www.youtube.com/watch?v=PpUftG_mxg8, (accessed 18 August 2015).

1.2.2 A simulation case-study on the influence of plate lines on the severity of wake vortex encounters in ground proximity

Dennis Vechtel[1], Anton Stephan[2], Frank Holzäpfel[2]

[1]*Institute of Flight Systems,* [2]*Institute of Atmospheric Physics*

Close to ground the behaviour of wake vortices changes in comparison to out of ground effect. Whilst vortices descend in free air due to their mutual induced velocities, they are hindered in sinking in presence of ground. This also changes the risk to encounter the wake of a preceding aircraft. Furthermore, wake encounters in ground effect are especially critical due to the nearness of the ground. Recent studies showed that vortex decay in ground proximity can be accelerated by installing a series of plates in lines perpendicular to the flight direction (so-called plate lines). This study analyses whether the accelerated vortex decay also results in lesser encounter severity in terms of aircraft reaction and pilot acceptance. Flow fields were generated by coupled RANS-LES simulations of an A340-sized aircraft in ground effect with light crosswind with and without plate lines for different vortex ages were implemented in a six-degrees-of-freedom aircraft simulation of an A320-sized aircraft. Offline simulations with autopilot engaged in autoland-mode showed a significant reduction of the aircraft response during the wake encounter with the plate lines. This reduction is indeed more pronounced with younger vortices but is still noticeable with old vortices. Simulations with pilots-in-the-loop in a full-flight simulator applying the same simulation model for the encountering aircraft also show a reduction of the aircraft response during manual landing as well as improved subjective pilot acceptance. Plate lines are therefore considered an effective means for either increasing flight safety with current minimum separations or maintaining the same level of safety in case that the minimum separations are reduced in the future.

Introduction

Vortices in proximity to a solid surface induce a boundary layer (vorticity layer) at the surface which causes the vortices to move along the surface driven by mutual velocity induction. Counter-rotating vortex pairs diverge during their approach to the ground following the hyperbolic trajectory of classical inviscid theory. Because of an adverse pressure gradient the vorticity layer may separate from the surface leading to the formation of secondary vortices. The detached secondary vortices may orbit around the primary vortices and the newly formed unequal vortex pairs rebound [1,2]. In contrast to headwind crosswind causes asymmetric rebound characteristics. Firstly, the crosswind shear vorticity supports the formation of the secondary vorticity at the lee (downwind) vortex, due to the same sign as the crosswind shear, and attenuates it at the luff (upwind) vortex, due to the opposite sign of the crosswind shear. Secondly, the primary vortices redistribute vorticity of the crosswind shear with which they mutually induce transport velocities [3]. These effects lead to an earlier and higher rebound and a more rapid decay of the lee vortex.

An increase in encounter probability close to ground was shown by various simulations [4-6]. Those results are confirmed by an increased encounter occurrence close to ground shown by pilot reports [7-10]. A potentially most dangerous situation for following aircraft arises if the longer-living luff vortex hovers above the runway because the self-induced lateral propagation speed of the luff vortex is just compensated by the crosswind. Numerical simulations [3] and

lidar measurements conducted at Frankfurt airport [11] indicate that a crosswind of about half the initial vortex descent speed roughly compensates the vortex-induced propagation speed of wake vortices generated at a height of about one initial vortex separation. The lower the vortex generation height the higher is the induced lateral vortex speed. In this study, with a generator aircraft of the ICAO HEAVY category, a crosswind of about 3 knots at a height of one initial vortex separation is chosen in order to compensate lateral vortex drift immediately before touchdown.

Recent studies showed that vortex decay in ground proximity can be accelerated by installing a series of plates in lines perpendicular to the flight direction (so-called plate lines) [35]. Plate lines [12] trigger the early detachment of strong Ω-shaped secondary vortices that actively approach the wake vortices and subsequently propagate along the primary vortices. These secondary vortices lead to an accelerated wake vortex decay independent from natural external disturbances [1,2]. Lidar measurements confirm the functionality of the plate line [3]. The benefits of the plate line are obvious if the most safety-relevant long-lived and strongest vortices are considered whose lifetime can be reduced by one third. It can be concluded that in potentially hazardous situations caused by persistent wake vortices on the glide path, plate lines may substantially reduce vortex lifetimes and thus increase safety.

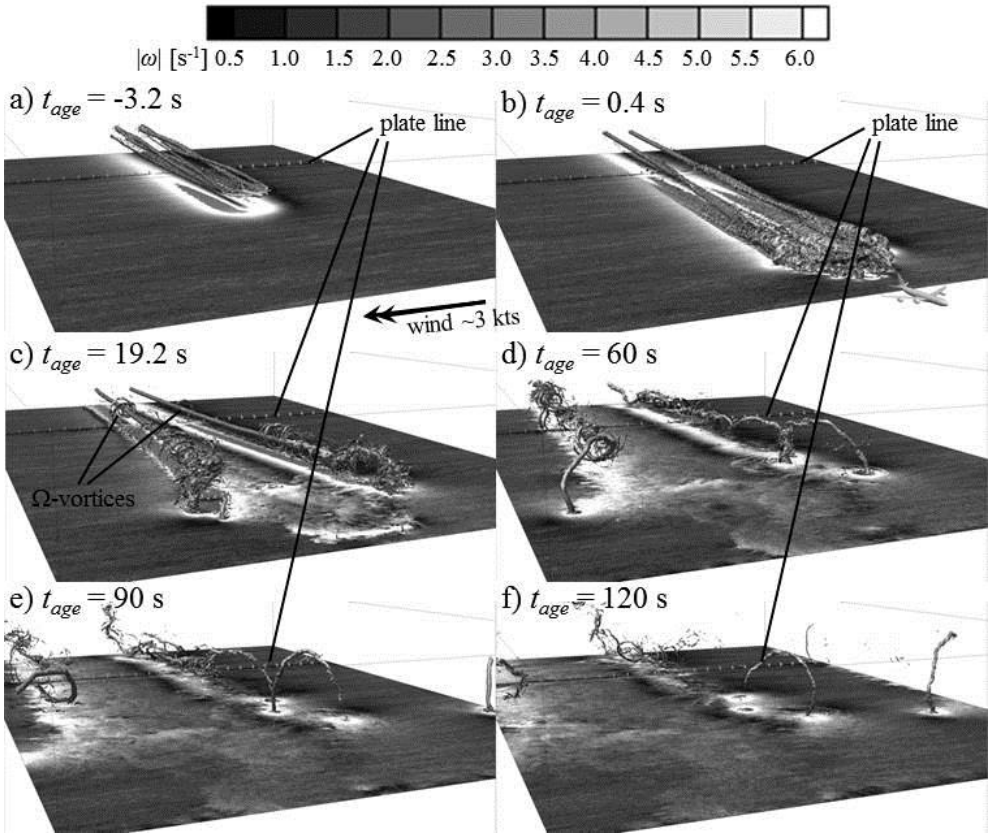

Figure 1 General overview on the simulation of wake vortex evolution of a landing aircraft at weak crosswind with plate line (iso-surfaces show vorticity of $|\omega| = 3.3\,\mathrm{s}^{-1}$, ground shaded by vorticity magnitude) [13].

The purpose of the simulations presented here is to analyse whether the accelerated vortex decay due to the plate line also affects the reaction of the encountering aircraft and the subjective hazard perception of pilots near ground. A more detailed analysis of the offline-simulations can be found in [13].

Aircraft Model

The DLR research aircraft A320 ATRA (Advanced Technologies Testing Aircraft) was chosen as encountering aircraft. For this aircraft a comprehensive simulation model exists at the DLR Institute of Flight Systems [14] usable for offline-simulations on usual desktop computers as well as for the motion-based full-flight simulator AVES [15]. The analysed aircraft pairing of an aircraft of the ICAO MEDIUM category following a wake generator of the HEAVY category is considered to be especially relevant at most highly frequented airports.

The simulation model of the ATRA comprises a two-point aerodynamics model for the longitudinal motion (wing and horizontal tail) and a one-point model for lateral motion. The aerodynamic model is based on stability and control derivatives identified from flight test data including nonlinear corrections for dynamic pressure, Mach number effect, stall, ground effect, etc. The aerodynamic model is validated by means of flight test data from ATRA within the flight envelope for normal operations. Besides this, the aircraft simulation model includes models of the V2500 engines, landing gear, control surface actuators and sensors (air data, navigation etc.), which are not yet validated by means of flight test data but which were adapted in a way to represent an A320. The sensor models for inertial and air data consider a specific time delay for each sensor and additionally the wind vanes for angle of attack and sideslip angle are modelled as PT2-system. The local influence of the vortex flow field on the wind vanes is considered in the sensor models as well (s. next section). However, as the angle of attack is not used for the flight control laws but only for engaging the high angle of attack protection (alpha-floor) the effect of the vortex flow field on the wind vanes is less relevant. Engagement of the high angle of attack protection did not occur during any simulation. The ATRA model incorporates a flight control system designed in analogy to the Airbus flight control architecture. The flight control system model of the ATRA simulation consists of an autopilot / auto-thrust system and provides a typical normal law with rate command / attitude hold control for manual flight.

One issue to keep in mind is that the reaction of the simulated flight control system to an external disturbance is difficult to validate. Whilst the response of the flight control system to control inputs shows a good conformity to the behaviour of the original flight control system of ATRA, its reaction to an external disturbance such as wake turbulence is likely to differ from the original one. However, the aircraft reaction appears plausible and is comparable with the aircraft reaction of the real aircraft in terms of magnitude and agility of the aircraft reaction on an external disturbance. All parameters, which are relevant for representing the flight dynamics of an aircraft correctly, are within the tolerances for Level-D-simulations [14,16]. Hence, the accuracy of the simulation model can be considered sufficient for scientific purposes. Also, even if the maximum aircraft response may be different from the response of the original A320 flight control system on the same external disturbance it can be assumed that relative assessment between cases with and without plate lines shows the correct tendency. For this reason the outcomes of the present simulation study can be considered as meaningful.

Generation of vortex flow fields and modelling of the aerodynamic interaction

A new hybrid method for the simulation of wake vortex evolution from early roll-up until final decay is applied for approach and landing of an aircraft including touchdown [12]. The hybrid LES (Large Eddy Simulation) initializes a realistic aircraft wake in an LES domain by sweeping a high-fidelity RANS (Reynolds Averaged Navier-Stokes) solution through the domain, which enables to simulate wake vortex evolution from generation until final decay [17]. Compared to the method used in previous studies [22,27], where fully rolled-up vortices were introduced in the LES-domain, this method considers all physical effects from the very creation and roll-up of the vortices right behind the generator aircraft and thus gives a much more realistic start point for the further simulation of the vortex evolution. Validation with data from windtunnel-measurements showed a very high accuracy of the simulation results [17].

The simulations are performed for an ICAO HEAVY transport aircraft of A340-size in high-lift configuration with deployed flaps and slats without landing gear. A landing mass of m = 190,000 kg, a wingspan of b = 60.3 m and a true airspeed of 75 m/s was employed, leading to an initial circulation of Γ_0 = 435 m^2/s and an initial vortex descent speed of w_0 = 1.46 m/s. The RANS flow field, which has been established before with the DLR TAU code [18], serves as a forcing term or inner boundary in the LES domain. The LES code MGLET from the TU Munich [19] calculates the flow in the ground fixed domain, incorporating a Lagrangian dynamic subgrid-scale model [20]. The LES are conducted with and without one plate line. A turbulent crosswind with a wind speed of 3 knots at a height of one initial vortex separation is allowed to develop prior to the wake initialization [21]. It is assumed that the encounter duration is short so that during an encounter the vortex age does not alter significantly. For this reason vortex flow fields for one specific vortex age are used for the entire encounter simulation.

The numerical results of the coupled RANS-LES simulations for three specific vortex ages (60 s, 90 s, 120 s) were transformed into three-dimensional look-up tables. These look-up tables were implemented in the simulation model of the encountering aircraft with a linear interpolation in order to give the velocity components in the three spatial directions (u,v,w) at a given position in space (x,y,z). The dimensions of these flow fields can be taken from Figure 2 which shows the shape of the vortices at three vortex ages with and without plate line. The plots in Figure 2 show the iso-surfaces of an absolute flow velocity of 5 m/s including the wind velocity. One can observe in the figure that in both cases (with and without plate line) the luff vortex remains nearly at a lateral position of y = 0 m (the runway centreline) throughout all vortex ages. Furthermore, the figure shows the quicker decay of the vortices due to the plate line located at a position of approximately x = 200 m.

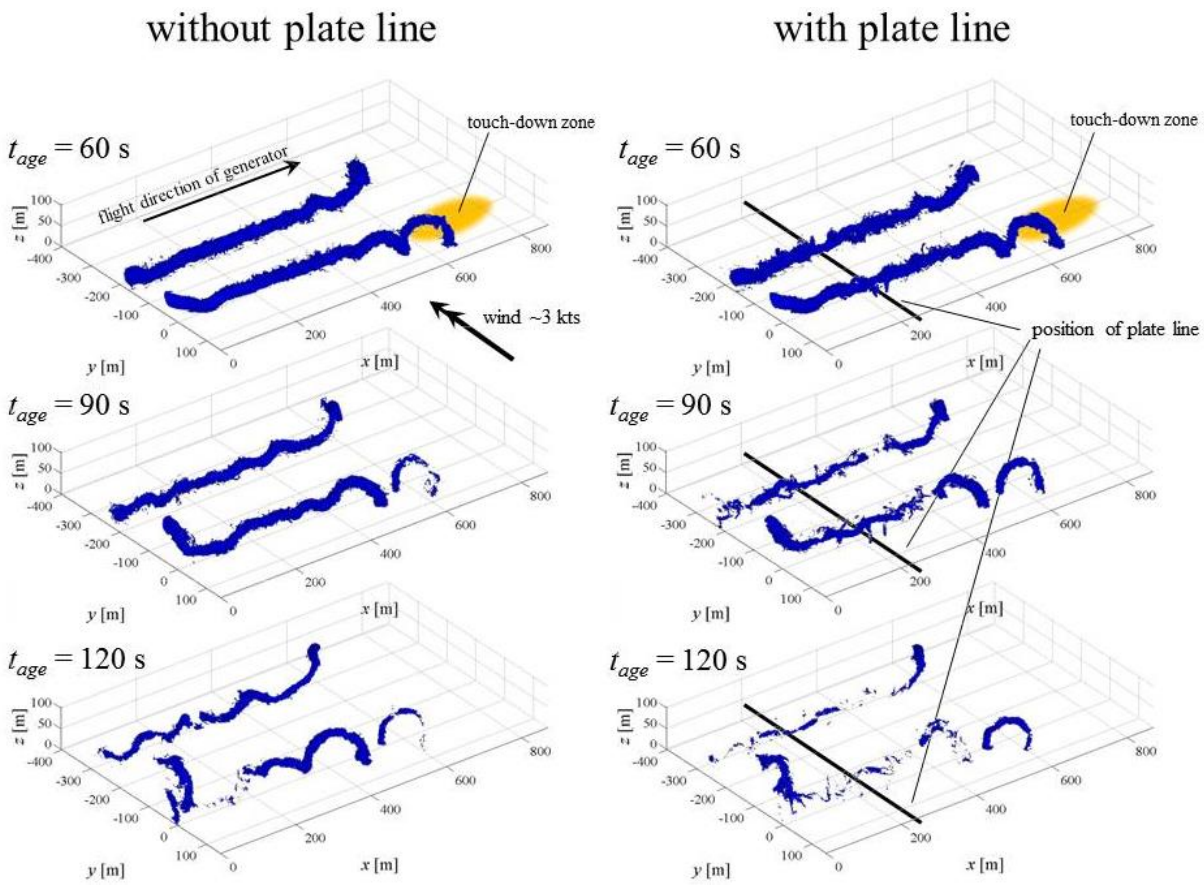

Figure 2 Vortex shapes (iso-surface of $|V| = 5\,\mathrm{m/s}$) for the investigated ages with and without plate line under light crosswind [13].

In order to simulate wake encounters with a dynamic aircraft simulation, an aerodynamic interaction model (AIM) is needed which calculates the vortex induced forces and moments acting on the encountering aircraft as a function of the aircraft position and attitude. The AIM used in this study is modelled as delta-aerodynamics model, which means that the basic aerodynamics model of the aircraft simulation is used for the calculation of the undisturbed flight, whereas the AIM solely calculates the additional forces and moments induced by the wake. The approach used for the AIM is the so-called strip method which divides the lift and side force generating surfaces of the aircraft (including wings, horizontal and vertical tail plane and fuselage) into single strips (see Figure 3).

For each strip an additional angle of attack (for wings and horizontal stabilizer) or angle of sideslip (for the fuselage and the vertical stabilizer) is calculated by means of the flow velocities of the vortices at the respective strip position. With the additional angles of attack and sideslip angles the incremental lift and side forces are calculated for each strip and with the respective lever arm of each strip the resulting moments as well. For the wings and the horizontal stabilizer an elliptical lift distribution is assumed and the resulting forces of each strip are weighed accordingly. Each strip is positioned according to the aircraft's geometry relative to the aircraft's centre of gravity. The forces and moments are assumed to apply at 25% of the strip's chord length. No dedicated stall model is included, instead for large angles of attack at the strips (>20°) the angle of attack is kept constant in order to prevent unrealistically high resulting forces. The forces and moments of all strips are summed up to

total induced forces and moments in all six degrees of freedom. These forces and moments are fed into the equations of motion of the aircraft simulation.

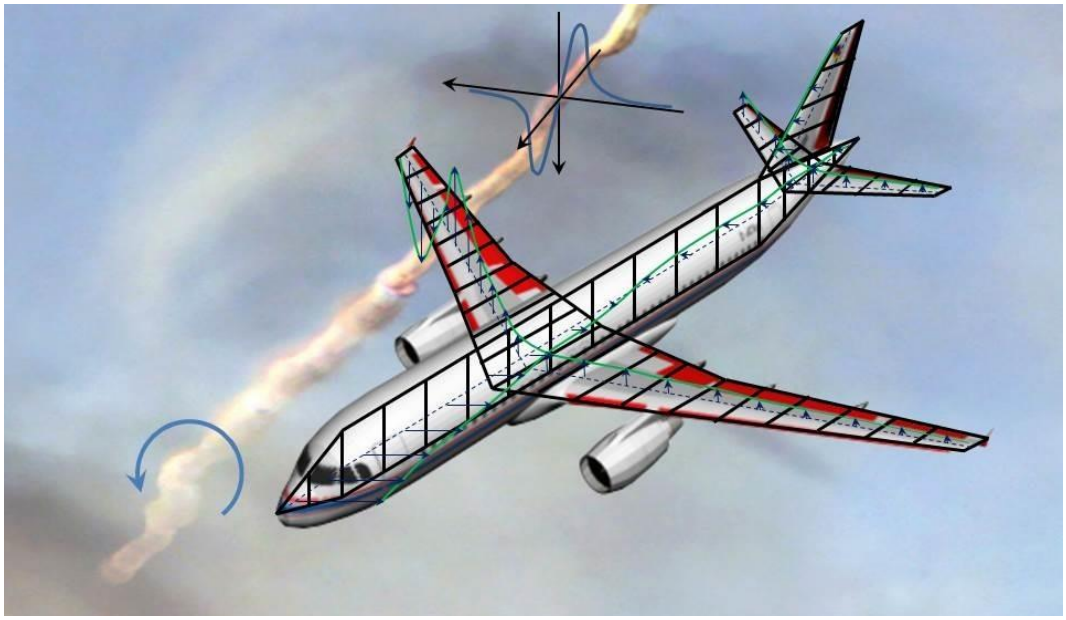

Figure 3 Depiction of the strip method with an exemplary lift distribution (green line) for each strip (black rectangles) [22].

This method was deemed feasible by Barrows [23], verified against wind tunnel tests by de Bruin [24], and further validated using flight test data by Fischenberg [25] and Jategaonkar [26]. The method was applied in various studies in the past [22,27-29] and is accepted to provide vortex induced forces and moments of acceptable accuracy.

As mentioned above, the vortex flow fields are not only used for the calculation of the forces and moments acting on the encountering aircraft, but also to calculate the influence of the wake encounter on the air data probes and vanes.

AVES Motion-Based Flight Simulator

The AVES (Air VEhicle Simulator) simulator centre was established by DLR Institute of Flight Systems in 2013 [15]. The simulator centre comprises a fixed-based and a motion-based simulator with variable cockpits. Figure 4 (left-hand side) shows the motion-based simulator of the AVES simulator centre from outside. As a major part one can observe the large dome which allows an enormously large visual projection area of 240° in horizontal and 95° in vertical direction. The large vertical expansion of the visual projection area is a requirement from the helicopter simulation, as helicopters require a much larger outside view as fixed-wing aircraft. Another detail of the motion-based simulator in Figure 4 is the motion system, which consists of an electrical hexapod-system. Figure 4 (right-hand side) shows the inside view of the A320 cockpit of AVES. The cockpit is a replica of the A320 cockpit, which represents the original in almost all details. In the aft part of the cockpit (not visible in Figure 4) an operator station is located, which allows full control of the simulation.

Figure 4 The AVES motion-based flight simulator

The whole software of the AVES was developed by DLR Institute of Flight Systems except the control of the motion platform. The flight simulation including the flight control system, autopilot, flight management system, flight warning computer, systems simulation as well as the simulator control software and the visual software was also developed by DLR Institute of Flight Systems. This guarantees highest flexibility for scientific purposes. Although the simulator is not certified for pilot training following JAA STD 1A [16], the simulation accuracy is considered to be well appropriate for scientific investigations.

Severity Assessment

For the assessment of the severity or hazard of a wake encounter suitable metrics are needed. During approach and landing aircraft usually fly the same nominal flight path, for which reason wake encounters typically occur under small encounter angles during this flight phase. As under small encounter angles the rolling moment induced by the vortices is the predominant disturbance acting on the encountering aircraft [30], it is reasonable to choose a metric that uses the rolling moment impact. An appropriate parameter is the so-called Roll Control Ratio *RCR*, i.e. the ratio between the vortex induced rolling moment coefficient $C_{\ell,ind}$ and the coefficient of the maximum rolling moment which can be generated by all roll control surfaces $C_{\ell,CTRL,\max}$ [31,32]

$$RCR = \frac{C_{\ell,ind}}{C_{\ell,CTRL,\max}}. \quad (1)$$

Consequently, an *RCR* greater than 1 means that the induced rolling moment cannot be fully compensated by the roll controls of the encountering aircraft. One important hazard metric used here is the maximum absolute *RCR* which occurred during the encounter $|RCR|_{\max}$. Other parameters used as metric represent the aircraft motion, e.g. the maximum bank angle Φ_{max}. Such metrics are useful when comparing different encounters or rating encounters on an objective level without any subjective pilot rating. However, a disadvantage of metrics like the maximum bank angle is that these values depend on the control inputs from the pilot or autopilot. The $|\mathrm{RCR}|_{\max}$ is independent from control inputs and can be interpreted as the potential maximum impact on the encountering aircraft. For pilot-in-the-loop investigations

with subjective pilot ratings as well as for offline simulation studies the $|RCR|_{max}$ has proven to be a suitable metric.

As the encounter scenario analysed here is close to ground, some additional criteria for non-acceptance are defined for the offline simulations, where no pilot rating on the encounter acceptance can be obtained. These additional criteria are based on the A320 geometry: a) wing strike (if $\Phi > 4.1872°/m \cdot H + 19°$), b) tail strike (if > 12° and $H < 20$ m), and c) hard landing (if $n_z \geq 2.6$ g [33]). A violation of any of these criteria in the offline simulations is rated as hazardous and therefore as unacceptable.

For the pilot-in-the-loop simulations a rating scale is needed which quantifies the subjective hazard perception of the pilot. For this reason a dedicated wake encounter rating scale was developed [34] (s. Figure 5). Right after each encounter the pilot has to rate the four items "aircraft control", "demands on the pilot", "aircraft deviations from flight state and flight path" and overall "hazard" on a scale from 1 to 4. These ratings are purely subjective and can therefore differ from pilot to pilot. In case that any rating item is rated with "4" the encounter is unacceptable by definition. Also, even as go-arounds may not inevitably be hazardous but should be prevented, the encounter is to be rated as unacceptable in case the pilot performs a go-around. In case of a go-around the aircraft deviations have to be rated with "4" by definition in order to numerically identify the encounter as unacceptable afterwards.

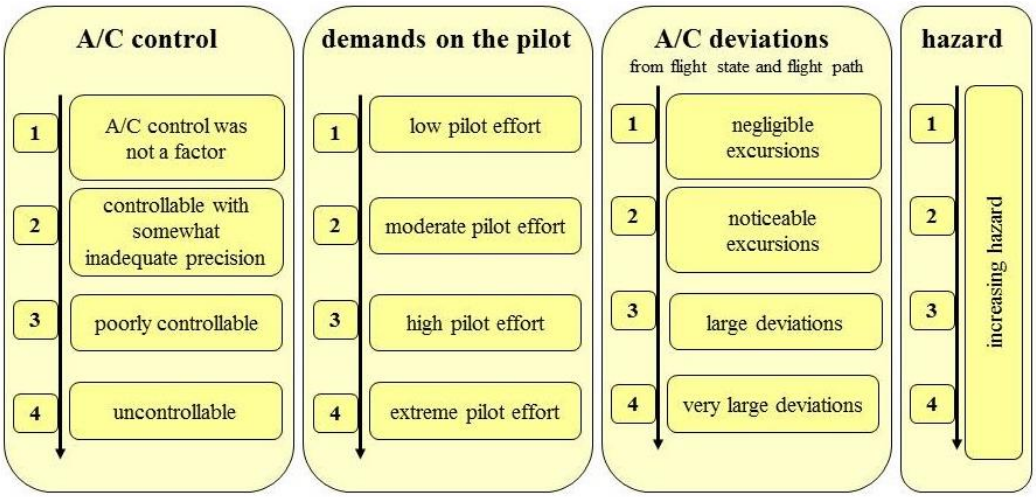

Figure 5 The wake encounter rating scale [34]

For the interpretation of the pilot ratings the practical experience from the experiments showed that if the average over all four rating items is below or equal "2" the encounter can be regarded as harmless. In this case the impact of the wake cannot be distinguished from other acceptable atmospheric disturbances such as light turbulence or gusts. On the other hand side the encounter has to be rated as unacceptable if one rating item is rated with "4" regardless from the other three rating items. Those encounters, which are not unacceptable by definition but with an average rating greater than "2" are indeed acceptable but cannot be regarded as harmless.

Offline Simulations

Offline simulations were conducted for analysis of the influence of plate lines on the aircraft reaction under variation of the encounter parameters. A more detailed analysis of the offline simulations described here is given in [13].

In all simulations the aircraft mass of the encountering A320 was 54 tons with a centre-of-gravity location of 25% of the mean aerodynamic chord (MAC). The aircraft is always fully configured with slats and flaps fully extended (slats at 27° and flaps at 40° deflection angle) and gear down. At simulation start the aircraft is trimmed with an approach speed of 137 kts true airspeed. The aircraft always lands in the autoland mode of the autopilot with glideslope and localizer hold engaged. In order to analyse different relative flight paths through the vortex flow field, the position of the flow field is varied in lateral and in longitudinal direction. This variation was performed between -500 m and 500 m in longitudinal direction (with a general step size of 100 m and a smaller step size of 20 m between -200 m and 200 m) and between -100 m and 100 m in lateral direction (with a general step size of 10 m and a smaller step size of 5 m between -50 m and 50 m). Altogether 868 encounters were simulated with different relative flightpaths through the vortex flow field, each with and without plate lines.

Table 1 shows the number of criterion violations with and without plate line as well as the relative improvement. Interestingly, no encounter at any of the analysed vortex ages resulted in a wing strike, neither with nor without plate line. One can observe that tail strikes occur only at a vortex age of 60 s. Hard landings occurred at vortex ages of 60 s and 90 s but not at 120 s. The table shows a significantly lower number of criterion violations with the plate line. The only slight increase is for hard landings at vortex ages of 90 s, when the criterion violations rise from 36 without plate line to 37 with plate line. However, this is a statistical issue at the boundaries of the investigated parameter space. All other criterion violations are significantly reduced.

	without plate line		
t_{age} [s]	wing strike	tail strike	hard ldg
60	0	38	110
90	0	0	36
120	0	0	0
	with plate line		
	wing strike	tail strike	hard ldg
60	0	7	95
90	0	0	37

120	0	0	0
	relative improvement		
	wing strike	tail strike	hard ldg
60	-	82 %	14 %
90	-	-	-3 %
120	-	-	-

Table 1 Number of criterion violations with and without plate line

Figure 6 shows the vortex impact, represented by $|RCR|_{max}$, and the aircraft reaction in the roll axis for all three investigated vortex ages. Comparing the vortex rolling impact in terms of $|RCR|_{max}$ during the encounter and the aircraft reaction in terms of maximum roll rate $|p|_{max}$ and maximum bank angle $|\Phi|_{max}$ one can observe that the scenarios with the highest $|RCR|_{max}$ values are not always those with the maximum aircraft reaction. This fact is very obvious at t_{age} = 60 s and can be explained by the duration of the vortex impact. The shorter the impact, the smaller the aircraft reaction can evolve. Hence, the maximum bank angles did not occur in the scenarios with the highest $|RCR|_{max}$ values of almost 2, but in those with smaller but longer-lasting rolling impact and $|RCR|_{max}$ values in the range between approximately 0.5 and 0.8 (the lower right corner of the figures). The maximum bank angle that occurred during the encounter simulations is about 20°. However, those events occurred at heights at which the wing could not hit the ground. Nevertheless, such large bank angles at very low altitude would be unacceptable for the pilot in reality and would most likely lead to a go-around.

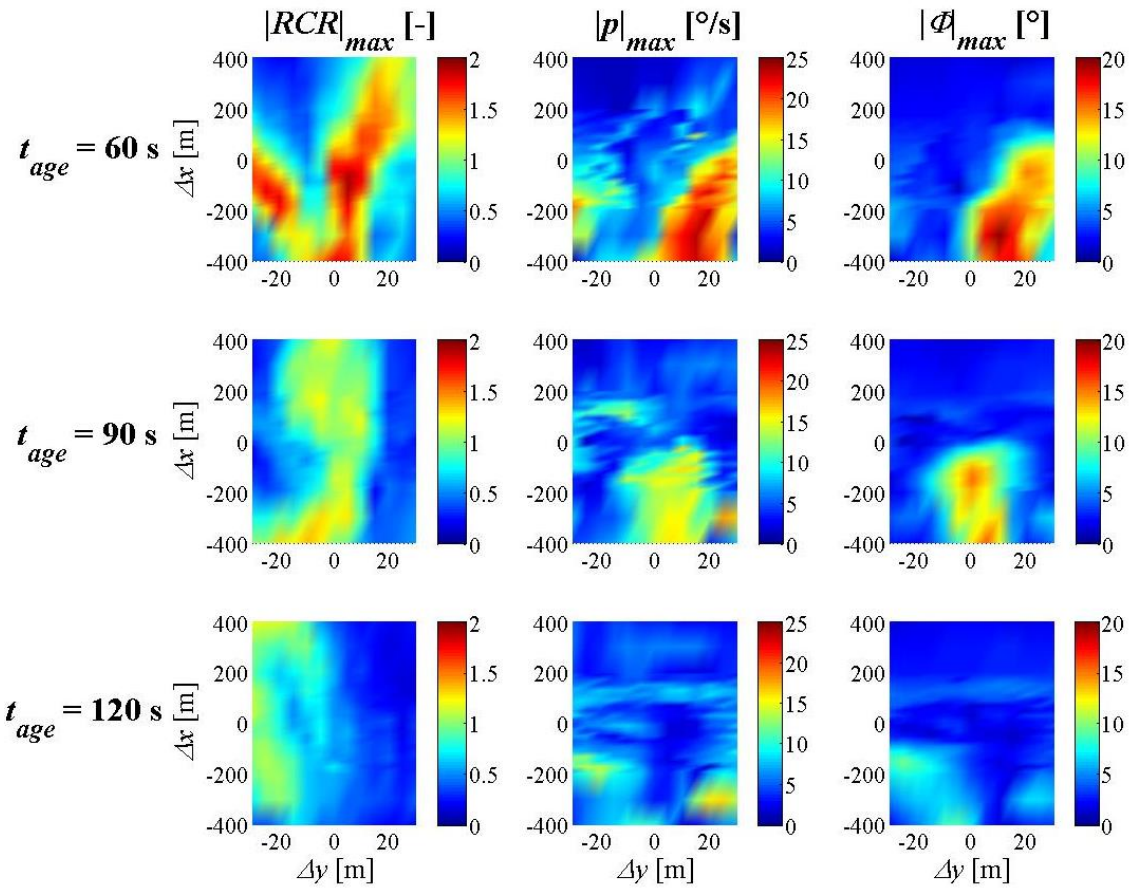

Figure 6 Distribution of $|RCR|_{max}$ and aircraft reaction in the rolling axis without plate line as a function of the relative longitudinal (Δ*x*) and lateral (Δ*y*) flow field position.

The analysis of the simulation results with plate line reveals similar general effects as without plate line. However, due to the lower vortex circulation as a result of the plate line the vortex impact is reduced. Again, Figure 7 shows the vortex impact represented by $|RCR|_{max}$ and the aircraft reaction in the roll axis for the simulations with plate line. In the figure the areas with relatively large aircraft reactions have a similar size, but the magnitudes of the aircraft reactions are significantly reduced in comparison to the case without plate line (s. Figure 6).

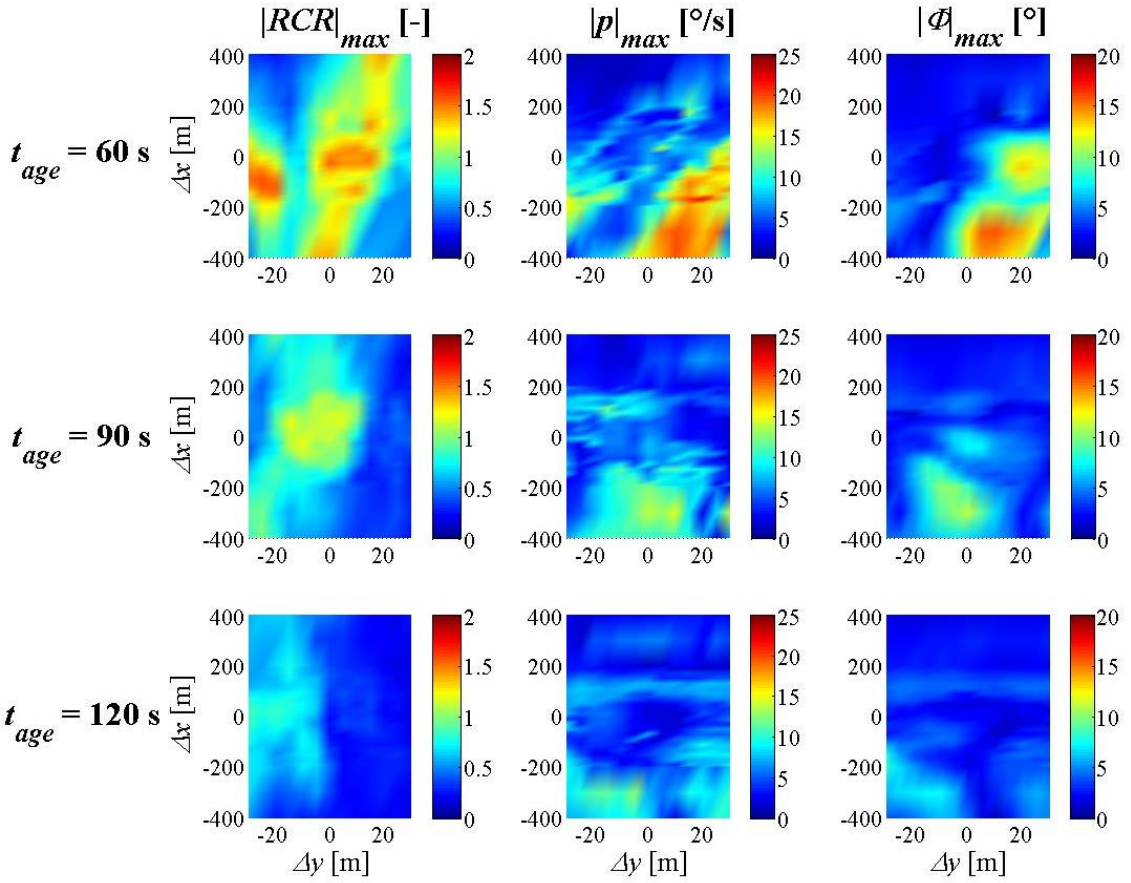

Figure 7 Distribution of $|RCR|_{max}$ and aircraft reaction in the roll axis with plate line as a function of the relative longitudinal (Δx) and lateral (Δy) flow field position.

Table 2 depicts the maximum and mean values of the $|RCR|_{max}$ and maximum bank angle $|\Phi|_{max}$, as well as the maximum values of the maximum vertical load factor $n_{z,max}$ and the maximum pitch angle Θ_{max} that occurred during all encounters as well as the relative improvement with the plate line. Interestingly, the positive effect of the plate line is more obvious for the younger vortices. Regarding the maximum $|RCR|_{max}$, one can observe that the values are significantly lower with plate line, especially for the old vortices. Nevertheless, this lower maximum impact in the roll axis does not result in the same reduction of aircraft reaction in terms of maximum bank angle $|\Phi|_{\max}$ (~30% reduction in $|RCR|_{max}$ compared to ~16% reduction in $|\Phi|_{max}$ and ~2% in $|\Phi|_{max}$ at t_{age} = 120 s). This implies that the duration of the maximum rolling impact is short, whereas the amount of smaller, but still considerable rolling impact that results in aircraft reaction is not lowered on a comparable level by the plate line. However, for t_{age} = 90 s the maximum bank angle could be reduced by almost 30% by the plate lines, which is a remarkable figure indeed.

	without plate line					
t_{age} [s]	max. $\|RCR\|_{max}$ [-]	mean $\|RCR\|_{max}$ [-]	max. $\|\Phi\|_{max}$ [°]	mean $\|\Phi\|_{max}$ [°]	max. $n_{z,max}$ [-]	max. Θ_{max} [°]
60	1.90	0.64	19.7	4.6	17.0	17.3
90	1.36	0.49	15.5	3.8	5.1	10.4
120	1.21	0.42	9.5	3.3	2.5	9.4
	with plate line					
t_{age} [s]	max. $\|RCR\|_{max}$ [-]	mean $\|RCR\|_{max}$ [-]	max. $\|\Phi\|_{max}$ [°]	mean $\|\Phi\|_{max}$ [°]	max. $n_{z,max}$ [-]	max. Θ_{max} [°]
60	1.59	0.62	15.6	4.2	15.5	14.0
90	1.19	0.46	11.2	3.6	5.0	10.2
120	0.86	0.38	8.0	3.2	2.2	9.3
	relative improvement					
t_{age} [s]	max. $\|RCR\|_{max}$ [-]	mean $\|RCR\|_{max}$ [-]	max. $\|\Phi\|_{max}$ [°]	mean $\|\Phi\|_{max}$ [°]	max. $n_{z,max}$ [-]	max. Θ_{max} [°]
60	16.3 %	3.3 %	20.8 %	8.7 %	8.8 %	19.1 %
90	12.5 %	6.1 %	27.7 %	5.8 %	2.0 %	1.9 %
120	28.9 %	10.6 %	15.8 %	2.3 %	12.0 %	1.1 %

Table 2 Maximum rolling impact and maximum aircraft reactions (with and without plate line) and their relative improvement

The very large numbers for the maximal $n_{z,max}$ at a vortex age of 60 s is assumed to be mainly from the modelling of the landing gear as a spring-damper-combination without modelling damping effects of the tire and a modelling of the aircraft as rigid-body. These large numbers would probably not occur at this magnitude in reality.

The significant reduction of $|RCR|_{max}$ is in accordance with the results of the WakeOP flight campaign [3], where Lidar measurements showed a reduction of the vortex circulation due to the plate line. As, for a given aircraft pairing, the vortex induced rolling moment, hence the *RCR*, is mainly influenced by the vortex circulation, the vortex separation and the encounter

geometry, a lower circulation is directly connected to a lower $|RCR|_{max}$ if all other influencing factors are kept the same.

All in all the results show a considerable influence of the plate line on the severity of wake encounters. Both the number of criterion violations and the magnitude of the aircraft reaction can be reduced by the plates.

Pilot-in-the-loop simulations

In addition to the offline simulations with autopilot engaged pilot-in-the-loop simulations were conducted in the AVES motion-based simulator for analysis of the influence of plate lines on the subjective hazard perception of pilots.

The analysed scenario was IFR approach under VMC at Frankfurt/Main airport (Germany). At simulation start the aircraft was trimmed at the final approach fix REDGO of runway 25C with an indicated airspeed of 180 kts in Config 2 (slats 22° / flaps 15°) with gear up. Initially, the autopilot was engaged in glideslope and localizer hold mode. The pilots were allowed to disengage the autopilot at their own discretion with the only limitation that the autopilot had to be disengaged below a height above ground of 500 ft in order to assure that the wake encounter was flown manually. During the approach the pilots had to configure the aircraft like in real flight and should perform a landing. In case that they decided to perform a go-around because of the wake encounter, they were allowed to do so. Same as for the offline simulations, the position of the flow field was varied in lateral and in longitudinal direction in order to analyse different relative flight paths through the vortex flow field. However, due to the limited number of possible simulation runs in the flight simulator, the variation was performed in a narrower range than in the offline simulations. In lateral direction the discrete positions y = (-25 m, 0 m, 25 m) and in longitudinal direction x = (-100 m, 0 m, 100 m) were applied. In the simulation campaign three DLR-internal pilots performed 55 encounters at the three vortex ages, each at the aforementioned flow field positions with and without plate lines.

The analysis of the encounters and pilot ratings shows that the pilot ratings correlate best with the aircraft reaction in the roll axis (Φ_{max} and p_{max}) and the maximum sink rate (or mathematically minimum vertical speed). These were also the main factors for the rating mostly mentioned by the pilots during the experiment. No correlations between the pilot ratings and other parameters, such as yaw rate, sideslip angle, load factors, etc. are found. Most unaccepted encounters were not accepted due to large bank angles. However, the data analysis shows that at very low heights above ground unacceptable bank angles means $\Phi > 5°$. Another reason for unacceptance was excessive sink rates.

All unaccepted encounters resulted in go-arounds. However, not every unaccepted encounter can be clearly explained by large bank angles or sink rates. Few unaccepted encounters show no excessive aircraft reaction but nevertheless resulted in a go-around. In some cases the pilots stated right after the encounter that they did not feel comfortable and that, although the aircraft reaction was not excessive, they decided to go-around as they could not anticipate how the encounter will evolve. Such ratings, which cannot be explained by quantitative figures, show the subjectivity of this kind of analysis. Such effects can only be handled through statistics, for which reason the limited database presented here can only outline preliminary

results. More simulation trials with more pilots are planned in the future in order to increase the statistical basis by more encounters. However, the current campaign already shows interesting results concerning the influence of the plate line.

Figure 8 shows the maximum bank angle as a function of $|RCR|_{max}$ for the three vortex ages with and without plates. Figure 9 shows the same for the maximum roll rate.

One can clearly observe in both figures that with and without plate line the average of Φ_{max} and p_{max} decreases with increasing vortex age. What is also obvious is that the number of unaccepted encounters decreases with increasing vortex age, both for cases with and without plate line. However, in direct comparison between the cases with and without plates for one single vortex age, one can observe that with the plate line the average value is usually lower than without plates. The same applies for the number of unaccepted encounters, which is always lower with plates than without.

The same tendency can be observed regarding the maximum sink rate during the encounter. Figure 10 depicts the minimum vertical speed (the maximum sink rate) again as a function of $|RCR|_{max}$ for the three vortex ages with and without plates.

Generally, Figure 10 shows higher maximum sink rates for younger vortices. In direct comparison for one vortex age, the average is in similar range with and without the plate line.

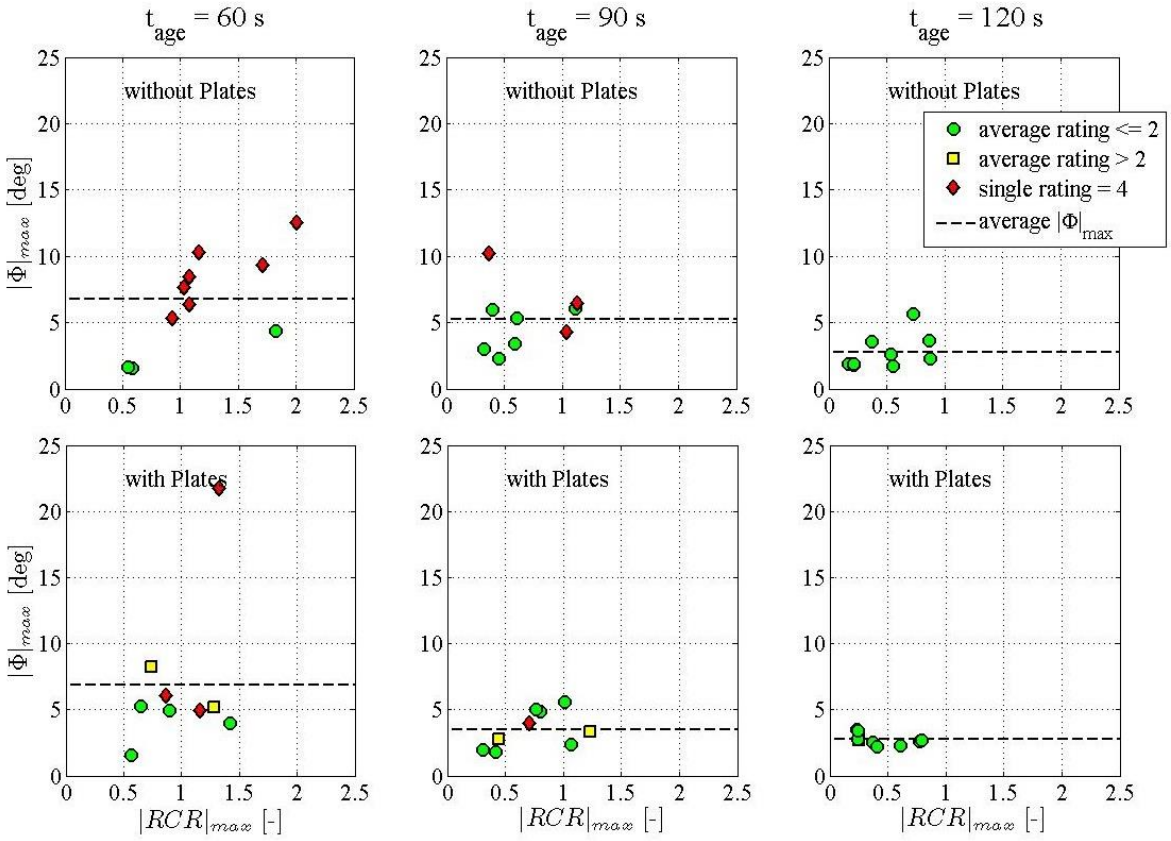

Figure 8 Maximum bank angles and pilot ratings as a function of $|RCR|_{max}$ with and without plate line

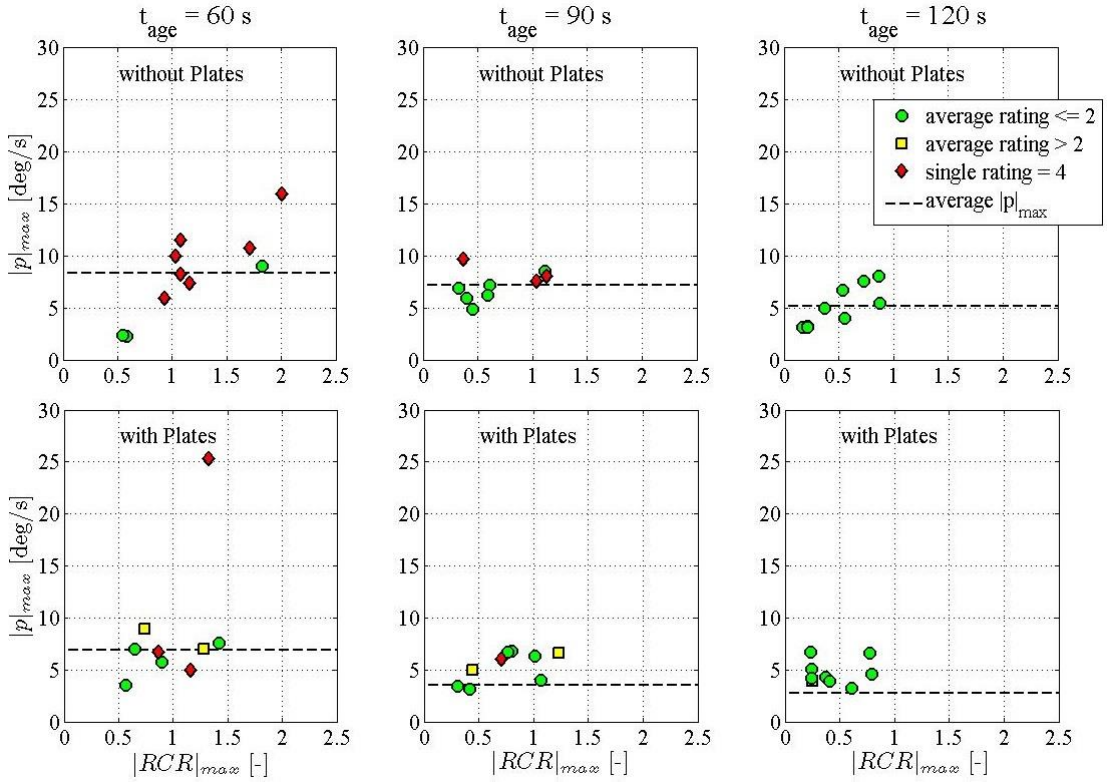

Figure 9 Maximum roll rates and pilot ratings as a function of $|RCR|_{max}$ with and w/o plate line

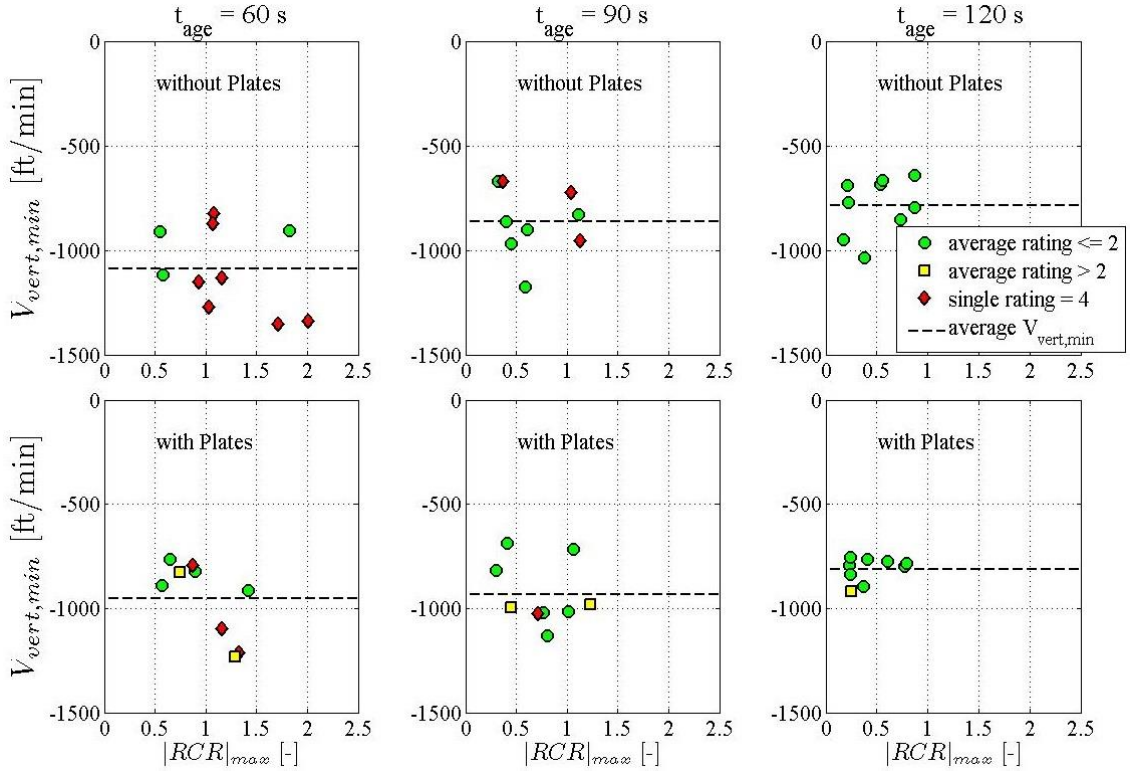

Figure 10 Minimum vertical speeds and pilot ratings as a function of $|RCR|_{max}$ with and without plate line

The simulator trials show the same tendency as the offline simulations, namely that the effect of the plate line to reduce the maximum vortex circulation also results in a reduction of the average aircraft response during the encounter and in an improved pilot acceptance. Obviously, the plate line is not able to fully eliminate unaccepted encounters; however, pilot acceptance is significantly improved due to the quicker vortex decay caused by the plates. Hence, the simulator trials also show that plate lines can be an effective means in order to reduce the severity of wake encounters close to ground.

Conclusions

A study with offline simulations and pilot-in-the-loop simulations in a motion-based full-flight simulator was performed for investigation of the influence of so-called plate lines on the encounter severity. Plate lines are a series of plates positioned in front of the runway that have shown to accelerate the vortex decay.

Wake vortex flow fields of an A340-sized aircraft were generated by coupling Reynolds-Averaged Navier-Stokes (RANS) simulations with Large-Eddy-Simulations (LES). With this method to simulate the evolution of wake vortices in ground proximity flow fields can be generated, which represent the special behaviour of wake vortices in ground effect very well. The accuracy of the simulation model of the encountering aircraft A320 is considered to be well acceptable for the present investigations. The aerodynamics model is validated by means of flight tests with the DLR research aircraft A320 ATRA. Other parts of the simulation model, such as landing gear, propulsion and the autopilot are not directly validated by flight test data, but were adapted in terms of their dynamics to represent an A320-size aircraft. The method to calculate the vortex induced forces and moments by using the so-called strip method has been widely used in the past and the confidence in the accuracy of this method is high. The autopilot and the control laws for manual flight used in this study were developed following the architecture of the original Airbus autopilot. However, only the behaviour of the autopilot on control inputs could be validated by means of real flight data. The flight control system's response on an external disturbance, such as wake vortices, could not be directly validated, but shows plausible results in counteracting external disturbances. The whole simulation framework can be considered accurate enough for representing wake encounters in ground proximity with autopilot of an A320-sized aircraft following an A340-sized one.

Both, the offline simulations and the trials in the flight simulator, showed a reduction of the aircraft reaction with the plate line. Especially for younger vortices the vortex impact and the aircraft reaction could be reduced considerably by the plates. Also, the piloted trials in the flight simulator revealed an improved pilot acceptance with the plate line. Hence, the dynamic encounter simulations showed that plate lines not only reduce the vortex circulation, as found out in previous studies, but also have a positive effect on the response of the encountering aircraft and the subjective hazard perception of the pilots.

The analysed aircraft pairing only represents A320-size MEDIUM aircraft following A340-size HEAVY aircraft. Other aircraft pairing were not investigated, which is why the results of the study cannot be generalized. However, it can be expected that the positive effect of the plate lines also applies to other categories of encountering aircraft as the plates generally accelerates the vortex decay.

Concluding, one can say that in case of a reduction of the separation minima plate lines could be an effective means in order to maintain safety. Also, there exist airports at which even with present separation procedures wake encounters occur more frequently than at other airports due to specific topographic, climatological or procedural reasons. Those encounters are mostly uncritical but nevertheless unwanted. For such airports plate lines could be a simple solution to reduce the encounter severity and thus increase flight safety.

References

[1] Doligalski, T. L., Smith, C. R., and Walker, J. D. A., "Vortex Interactions with Walls", Annual Review of Fluid Mechanics, Vol. 26, 1994, pp. 573–616.

[2] Stephan, A., Holzäpfel, F., and Misaka, T., "Aircraft Wake-Vortex Decay in Ground Proximity - Physical Mechanisms and Artificial Enhancement", Journal of Aircraft, Vol. 50, 2013, pp. 1250-1260. DOI: 10.2514/1.C032179.

[3] Holzäpfel, F., et. al., "Enhanced Wake Vortex Decay in Ground Proximity Triggered by Plate Lines", Aircraft Engineering and Aerospace Technology, Vol. 88, Issue 2, 2016, pp. 206-214. DOI: 10.1108/AEAT-02-2015-0045.

[4] Holzäpfel, F., et. al., "Aircraft wake vortex scenarios simulation package – WakeScene", Aerospace Science and Technology, Vol. 13, 2009, pp. 1-11.

[5] Kauertz, S., "Wake Vortex Encounter Risk Assessment using High-Fidelity Flight Simulation", German Aerospace Congress, 161301, Hamburg, 2010.

[6] Speijker, L.J.P., et al., "Probabilistic Wake Vortex Safety Assessment to Evaluate Separation Distances for ATM Operations", 22nd ICAS International Congress of Aeronautical Sciences, Harrogate, UK, 27 August – 1 September 2000.

[7] N. N., "Flight Safety Digest – Data Show That US. Wake-turbulence Accidents Are Most Frequent at Low Altitude and During Approach and Landing", Flight Safety Foundation, Vol. 21, No. 3-4, 2002.

[8] Critchley, J. B., and Foot, P. B., "United Kingdom Civil Aviation Authority Wake Vortex Database: Analysis of Incidents Reports Between 1982 and 1990", Civil Aviation Authority, CAA Paper 91015, London, 1991.

[9] Holzäpfel, F., "Analysis of potential wake vortex encounters at a major European airport", Proceedings of the International Conference of the EASN Association, 6th EASN International Conference on Innovation in European Aeronautics Research, Porto, Portugal, 18.-21. October 2016, pages 223-238.

[10] Holzäpfel, F., "Analysis of potential wake vortex encounters at a major European airport", Aircraft Engineering and Aerospace Technology, accepted for publication, 2017.

[11] Holzäpfel, F., and Steen, M., "Aircraft Wake-Vortex Evolution in Ground Proximity: Analysis and Parameterization", AIAA Journal, Vol. 45, No. 1, 2007, pp. 218-227.

[12] Stephan, A., Holzäpfel, F., and Misaka, T., "Hybrid simulation of wake-vortex evolution during landing on flat terrain and with plate line", International Journal of Heat and Fluid Flow, Vol. 49, 2014, pp. 18-27.

[13] Vechtel, D., Stephan, A., and Holzäpfel, F., “Simulation Study of Severity and Mitigation of Wake-Vortex Encounters in Ground Proximity”, Journal of Aircraft, (2017), doi: 10.2514/1.C033995.

[14] Raab, C., Flugdynamisches Simulationsmodell A320-ATRA – Validierungsversuche und Bewertung der Modellgüte (english: Flight Dynamics Simulation Model A320 ATRA – Validation Tests and Evaluation of the Model Accuracy), DLR internal report, IB 111-2012/43, 2012.

[15] Duda, H., et al., “Design of the DLR AVES Research Flight Simulator”, AIAA Modeling and Simulation Technologies Conference, AIAA Paper 2013-4737, 2013.

[16] N. N., “JAR-STD 1A Aeroplane Flight Simulators”, Joint Aviation Authorities, 1 June 1999.

[17] Misaka, T., Holzäpfel, F., and Gerz, T., “Large-Eddy Simulation of Aircraft Wake Evolution from Roll-Up until Vortex Decay”, AIAA Journal, Vol. 53, No. 9, 2015, pp. 2646 - 2670, DOI:10.2514/1.J053671.

[18] Keye, S., “Fluid-Structure Coupled Analysis of a Transport Aircraft and Flight-Test Validation” Journal of Aircraft 48, 2011, pp. 381–390.

[19] Manhart, M., “A Zonal Grid Algorithm for DNS of Turbulent Boundary Layer” Computers and Fluids 33, 2004, 435–461.

[20] Meneveau, C., Lund, T.S., and Cabot, W.H., “A Lagrangian Dynamic Subgrid-Scale Model of Turbulence” Journal of Fluid Mechanics 319, 1996, 353–385.

[21] Stephan, A., Zholtovski, S., and Holzäpfel, F., “The Effect of Gusts on Aircraft Wake Vortices”, Aircraft Engineering and Aerospace Technology, Vol.89, No 5, 2017.

[22] Vechtel, D., “Simulation study of wake encounters with straight and deformed vortices”, The Aeronautical Journal, Vol. 120, No. 1226, 2016, pp. 651-674.

[23] Barrows, T. M., “Simplified Methods of Predicting Aircraft Rolling Moments due to Vortex Encounters”, AIAA 14th Aerospace Sciencees Meeting, AIAA Paper 76-61, 1976.

[24] de Bruin, A. C., “WAVENC, Wake Vortex Evolution and Wake Vortex Encounter, Publishable Synthesis Report”, National Aerospace Laboratory NLR, NLR-TR-2000-079, 2000.

[25] Fischenberg, D., “Bestimmung der Wirbelschleppencharakteristik aus Flugmessdaten” (english: Determination of Wake Vortex Characteristics from Flight Test Data), German Aerospace Congress, Stuttgart, Germany, 2002.

[26] Jategaonkar, R., Fischenberg, D., and v. Gruenhagen, W., “Aerodynamic Modelling and System Identification from Flight Data – Recent Applications at DLR”, Journal of Aircraft, Vol. 41, No. 4, 2004, pp. 687-698.

[27] Vechtel, D., “In-flight simulation of wake encounters using deformed vortices”, The Aeronautical Journal, Vol. 117, No. 1196, 2013, pp. 997-1018.

[28] Schwarz, C. W., and Hahn, K.-U., “Full-flight simulator study for wake vortex hazard area investigation”, Aerospace Science and Technology, 2006, Vol. 10, 2006, pp. 136-143.

[29] Fischenberg, D., “A method to validate wake vortex encounter models from flight test data”, ICAS 2010 27th International congress of the aeronautical sciences, Nice, France, 2010.

[30] Rossow, V. J., “Lift-generated vortex wakes of subsonic transport aircraft”, Progress in Aerospace Sciences, Vol. 35, pp. 507-660, 1999.

[31] Schwarz, C., and Vechtel, D., “Wake Vortex Encounter Severity Criteria for RECAT“, DLR technical report IB 111-2012/44, Braunschweig, Germany, 2012.

[32] Crow, S. C., “Panel Discussion”, Symposium on Aircraft Wake Turbulence, Seattle, Washington, USA, 1-3 September 1970.

[33] N. N., “A320/A321 Aircraft Maintenance Manual AMM”, reference DG. AMM AEF, Issue 05-51-11.

[34] Schwarz, C., and Hahn, K.-U., “Subjective wake vortex encounter evaluation“, DLR technical report IB 111-2011/46, Braunschweig, Germany, 2011.

[35] Stephan, A., Holzäpfel, F. and Misaka, T., “Simulation of aircraft wake vortices during landing with decay enhancing obstacles”, ICAS 2014 29th International congress of the aeronautical sciences, St. Petersburg, Russia, 2014.

1.3 Assessment of dynamic pairwise separation benefits using an Airport-in-a-Lab concept

Franz Knabe[1], Frank Holzäpfel[2], Carsten Schwarz[3]

[1]*Institute of Flight Guidance,* [2]*Institute of Atmospheric Physics,* [3]*Institute of Flight Systems*

Today dynamic pairwise separations are considered the last evolutional step of research in order to alleviate the capacity reducing effects of wake-vortex-related aircraft separations. Within the L-bows project we employed DLR German Aerospace Center's wake vortex prediction and monitoring system WSVBS to predict safe minimum separations between arriving aircraft pairs depending on aircraft parameters and weather conditions. Based on an actual parameter set the dynamic pairwise separation values may be lower than separations from other frameworks. One resulting potential benefit is the possibility to accommodate more actual landings per time unit or to reduce arrival delay if demand is kept unchanged. Compared to other separation rule sets the challenge in utilizing and assessing this benefit is the short forecast lead time of the crucial weather conditions. We developed an assessment of the potential benefits of dynamic pairwise separations using an Airport-in-a-Lab concept. The paradigm of the concept is to combine real world airport data and future concepts in order to demonstrate the benefits in a laboratory environment. The results as exemplary benefits in terms of average arrival delays and their translation into direct cost savings were showing a range of 25% to 43%. Thus benefits were measurable within the Airport-in-a-Lab scenario but their realization in real life will strongly depend on the specific weather situation at an airport and the underlying demand-to-capacity ration for arrivals.

1. Introduction

Wake vortices are aerial turbulences generated during the flight of aircraft. Depending on the weight of the aircraft their power is strong enough to influence or even endanger a following aircraft flying on the same or a nearby flightpath. Based on ICAO guidelines longitudinal and vertical minimum separation rules are in place to avoid such effects. These increased separation values reduce the capacity values especially for succeeding arrivals landing on a single runway or on closely-spaced parallel runways. Hence research has been underway since the introduction of wake vortex separations in the early 70s to find opportunities to reduce the separations without decreasing the safety level ,,,,, .

NASA has been developing the Aircraft Vortex Spacing System (AVOSS) to produce weather dependent, dynamic wake vortex spacing criteria for aircraft categories. So AVOSS was not yet designed for the consideration individual aircraft types as foreseen by RECAT III. In a real-time field demonstration during July 2000 at the Dallas Ft. Worth International Airport functional elements for meteorological measurements, glide path adherence statistics, wake-vortex prediction, and wake-vortex monitoring were applied to a single runway system . An increase of runway throughput of 6% was predicted, where less than 1% of the predictions did not safely represent the observed wake behavior.

The DFS Deutsche Flugsicherung GmbH has developed the Wake Vortex Warning System (WVWS) to allow for the suspension of wake vortex separation between subsequent aircraft approaching the closely-spaced parallel runways 25L and 25R (renamed to 25C in 2006) at Frankfurt airport during favorable meteorological conditions. Based on wind and turbulence measurements of a 15 m anemometer array, the WVWS could predict whether or not wake vortices may reach the parallel runway in ground proximity.
The Wake Vortex Prediction and Monitoring System (Wirbelschleppen- Vorhersage- und Beobachtungssystem WSVBS) developed by DLR dynamically adjusts aircraft separations dependent on the prevailing weather conditions and the resulting wake vortex behavior , . The system predicts wake vortex transport and decay and the resulting safety areas along the glide slope. Initially, the system has been designed to optimize separations of aircraft categories for landings on the closely-spaced parallel runway system of Frankfurt airport. Later the WSVBS has been extended to predict dynamic pairwise separations for landings on single runways .
The current status of arrival separation regulations on final approach is that most states have adopted the ICAO guidelines and some states have introduced more detailed regulations (like in the United Kingdom). Since 2012 re-categorized schemes have been introduced at selected airports in Europe and in the US (RECAT I EU and RECAT I US). RECAT I separation schemes introduce 6 aircraft classes and safely reduce some of the minimum separation requirements in comparison with the ICAO guidelines. A further step will be the introduction of Pairwise Separations (PWS) as RECAT II with static separation parameters for individual pairs of aircraft types. A tailored RECAT II implementation has been running in the US since 2016 .
Dynamic Pairwise Separations (D-PWS) denoted as RECAT III currently are the last evolutional step of research in order to overcome the capacity reducing effects of wake vortex induced separation requirements. Within the D-PWS concept a safe minimum separation is predicted for each individual pair of arriving flights. Based on actual and forecast parameters the separation values may be lower than separations from other regulation frameworks and as such would increase the runway arrival capacity at least temporarily.
In this context the L-bo*ws* (Land-based and onboard wake systems) project of the German Aerospace Center (DLR) developed research approaches to predict safe minimum dynamic pairwise separations between arriving aircraft pairs depending on individual aircraft and weather parameters ,,. As part of the L-bo*ws* project an assessment of the potential benefits of dynamic pairwise separations in terms of delay and capacity was performed and the results are presented here.
As D-PWS separations are still under development they are not introduced anywhere to date. Thus benefit assessments are limited to hypothetical calculations using assumptions of the performance of the future system combined with expected demand patterns and operational concepts for the usage of D-PWS.
The effects of *individual pairwise* separations on the arrival situation of a single runway in terms of delay and capacity were studied in 2012 . Average daily delay reductions of 5 – 29 % against scenarios with application of standard ICAO separations were observed for individual aircraft based separations depending on the corresponding value of the runway occupancy time of the preceding aircraft. The results were achieved with the simulation of sample traffic days in a process simulation model.
Similar studies were carried out for *static* class-based re-categorized separation scenarios, which are introduced in Europe and the US already. In the capacity gain for the most

constrained European airports through the application of the RECAT I EU separation standard is estimated at 5% to 8%. A study on RECAT I US benefits computes benefits of 5.1% to 8.3% in arrival runway capacity for quarterly hours for four different US airports.
The study presented here is focusing on the future application of D-PWS for potential delay reductions in a tactical operational environment, to quantify the benefits in terms of operational savings and to set the potential of D-PWS in relation to other capacity improving measures. The terms tactical and strategic are used here to mark the day of operation (tactical) and one year to one week before operation (strategic) according to EUROCONTROL's ATCFM classification .
First, the benefit assessment using the Airport-in-a-Lab concept and the assessment goals are outlined. As arrival runway capacity is the core performance parameter which will be changed by D-PWS a short introduction is given on elements and influencing parameters. The assessment is based on tailored scenarios defined in an Airport-in-a-Lab concept and thus scenario elements like demand profile, separation sets, arrival speeds and separation buffers are presented in detail. An overview on the performance indicators used for the assessment and the tool to measure them in a model completes the materials and methods section. The results are presented in terms of delays and flows for different scenarios and in addition basic cost estimates are made to transfer delays into operating cost.

2. Data Sources and Methods

2.1 Assessment concept and assessment goals

Within the L-bo*ws* project the work presented here was aiming at the potential benefit of dynamic pairwise separations in terms of capacity enhancement and delay reduction for arrivals. The WSVBS has been used to predict reduced minimum separations in field tests at international airports and measurements proved the safety of its predictions. Accordingly the WSVBS can be considered within the process of achieving a technology readiness level of 5. As the predicted reduced separation values haven't been applied in real life flight operations benefits may be assessed in a laboratory environment only. For that purpose our Airport-in-a-Lab approach was used.

Airport-in-a-Lab is a concept to study airport airside related developments and improvements mainly in an early stage of development. The central idea of Airport-in-a-Lab is the tailoring of airport traffic models to the focus of the assessment in a laboratory environment. Tailoring here means the usage of a modular assembly system of scenario elements and modeling tools directly focusing on the needs of the assessment. The tailored approach can be seen as counterpart to a generic approach, which tries to capture a wide range of features in the model under study in order to be able to generalize the results.
The possible application of D-PWS including the amount of individual pairwise separation reductions have a forecast horizon of less than 30 minutes, i.e. the additional processing capacity of the runway will be used exclusively by arriving flights which are already near the airport. As a measurable result arrival delays due to temporal runway demand/capacity imbalances will be reduced or even avoided. Due to the nature of demand capacity balancing the gains will be the higher the more the ratio of demand and capacity reaches 1.
Therefore arrival delays within the airport vicinity are chosen here as the major performance indicator to quantify the capacity benefits of dynamic pairwise separations. Delay values are

then transferred into monetary benefits using standard operating costs of aircraft approaching an airport. In addition hourly saturation capacities are estimated using maximum throughput measurements.

2.2 The Wake Vortex Prediction and Monitoring System WSVBS

The Wake Vortex Prediction and Monitoring System (Wirbelschleppen- Vorhersage- und Beobachtungssystem WSVBS) was developed to tactically increase airport capacity for approach and landing ,,. The WSVBS dynamically adjusts aircraft separations dependent on measured and/or predicted weather conditions and the resulting wake vortex behavior without compromising safety. The system predicts wake vortex transport and decay and the resulting safety areas along the glide slope from final approach fix to threshold. Initially, the system has been particularly adapted to the closely-spaced parallel runway system of Frankfurt airport (runways 25L and 25C). Later the WSVBS has been further developed to predict dynamic pairwise separations for landings on single runways.

The elements of the WSVBS are generic and can well be adjusted to any runway system and airport location. The WSBVS assumes that all aircraft are established on the glide slope at a distance of 11 NM before the touchdown zone. The wake-vortex evolution is predicted within 13 gates along the final approach. In ground proximity the gate separation of 1 NM is reduced to 1/3 NM to properly resolve the interaction of wake vortices with the ground. The wake vortex advisory system employs a combination of meteorological instrumentation and numerical weather prediction to estimate the environmental conditions along the glideslope. For the current study, however, a synthetic weather database is used that was generated for the terminal area of Frankfurt airport (see next section). Based on glide path adherence statistics and estimated weather conditions the probabilistic wake vortex model P2P predicts upper and lower bounds for position and strength of vortices generated by individual aircraft types. These bounds are expanded by the safety area around a vortex that must be avoided by follower aircraft for safe and undisturbed flight (SHAPe) . The instant when all safety areas along the glide slope do not overlap anymore with the flight corridor define temporal aircraft separations.

The WSVBS has demonstrated its functionality at Frankfurt airport in the period from 18/12/06 until 28/02/07. At Munich airport the WSVBS has demonstrated the feasibility of dynamic pairwise separations for the first time (23/6/10 – 15/9/10) . In both campaigns the WSVBS was run in a test mode without adjusting aircraft separations. The performance tests in Frankfurt indicated that the WSVBS predictions were correct as for about 1100 landings observed during 16 days no warnings occurred from the LIDAR that measured wake vortex evolution in several planes with flight heights between about 30 m and 100 m .

The WSVBS combines several conservative elements like worst case combinations of aircraft parameters and conservative combinations of the probabilistic areas representing the approach corridors, wake vortex trajectories and safety distances between vortex and follower aircraft (see). For the current investigations the WSVBS setup 6 in table 1 of Ref. has been selected, corresponding to 1-σ allowances for the approach corridor dimensions and the wake vortex habitation areas combined with deterministic safety areas. A Monte Carlo simulation study demonstrates that for this setup the WSVBS is well adjusted to a reasonable level of safety by comparing the probability that wake vortices linger within a defined radius around the follower aircraft to measurement data collected at five major international

airports . Similar as for the introduction of RECAT-I EU at an airport, this validation could be complemented by long-term LIDAR observations of wake vortex behavior. Presumably, this would enable to further relax the current stringent safety allowances of the WSVBS with the benefit of increased operation times with reduced separations.

2.3 The Weather Database

The current study employs weather data from a one-year meteorological dataset established for the terminal area of Frankfurt Airport in Germany in the year 2004 with a numerical weather prediction system in order to provide a realistic database for various applications as the evaluation of new operational aircraft arrival procedures and their associated risks . The synthetic meteorological dataset has been validated against local surface wind climatology and against measurements of a sound detection and range/radio acoustic sounding system (SODAR/RASS).
The horizontal resolution of the simulation domain in the airport environment amounts to 2.1 km, such that every gate along the glide slope can be represented by different vertical profiles of meteorological parameters. Within the relevant height range the vertical resolution varies between 8 m in ground proximity and 50 m aloft. The dataset contains all parameters relevant for wake vortex transport and decay, namely air density, the three wind components, potential temperature, turbulent kinetic energy, and turbulence energy dissipation rate.

2.4 Arrival Runway Capacity

Runway capacity itself is a hypothetical average value for the number of aircraft which could be processed in average under certain assumptions and conditions in a given time interval. Especially in dynamic demand situations (which are the usual case on today's airports) the capacity is varying considerably from time interval to time interval. The introduction of dynamic pairwise separations by tendency will increase this variation even more because of the considerable influences of meteorological parameters like wind, turbulence and thermal stratification on wake vortex behavior and longevity .
Since the early 60s a whole lot of methods to compute runway capacity have been developed ranging from tabulation over analytical models and simulation models to the interpretation of actual traffic data. They are focusing mainly on hourly time intervals reflecting the anticipated purpose of operational, tactical and strategic demand-capacity-balancing,.
Today runway capacity is a scarce resource for most of the major airports and it will be even scarcer in the near and far future. Arrival runway capacity depends on a number of factors including aircraft performance, separation rules and their actual execution through pilots and controllers, as well as on the layout of runways and of arrival/departure routes. Weather parameters like visibility, precipitation or temperature affect these factors considerably. In addition capacity values are always coupled to assumptions on the demand to be expected in terms of quantity, composition and distribution over time.
A core element of runway capacity is the separation between two succeeding aircraft. The provision of separation between two aircraft is a main task in air traffic management either in the spatial dimension or in time when both aircraft are passing the same location
Looking on the arrival/arrival sequence on final approach the distance between the two aircraft in space as well as in time is influenced by a minimum longitudinal separation requirement, by the approach speed profile mainly of the following aircraft and by the

application of a safety buffer in order to guarantee the non-violation of minimum separations through variations and uncertainties during operation (see Figure 1).
Minimum approach separation values are dependent on the technical communication, navigation and surveillance (CNS) equipment as well as on the weight class and performance characteristics of the two aircraft in focus. The CNS equipment has an influence on the so called radar separation values whereas the weight classes of an aircraft pair determine the required wake vortex separations .
The approach speed profile of an actual flight is quite variable because it is dependent on the technical performance of the aircraft on the one hand and factors like headwind, aircraft weight, airline procedures and pilot commands on the other hand. The latter factors may vary from flight to flight.
The safety buffer as the third component is expressing implicitly the ability of controller and pilots to achieve a given arrival separation value during operation and their implicit acceptance of a non-achievement rate leading to e.g. increased missed approached rates.

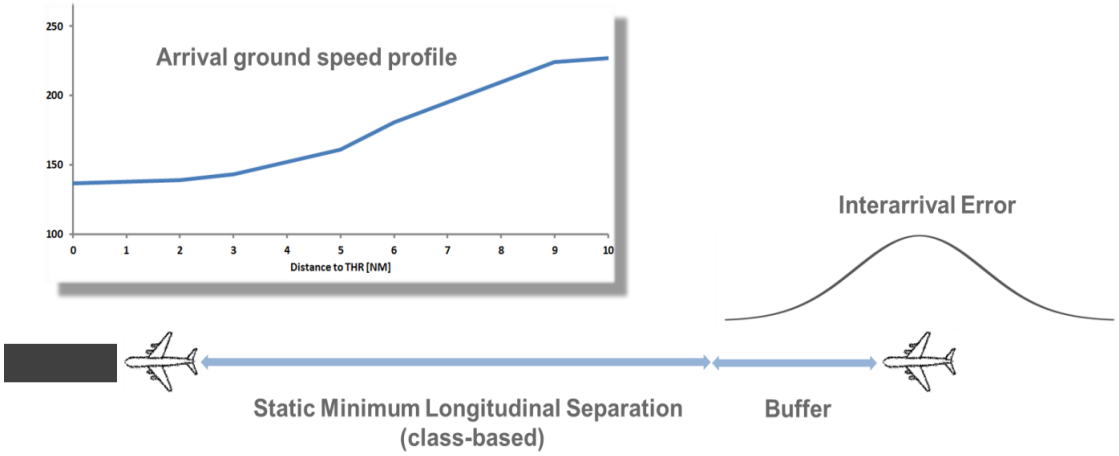

Figure 1: Parameters influencing arrival runway capacity in class based separation schemes

2.5 Scenario elements and Airport-in-a-Lab setup

Following the Airport-in-a-Lab concept sets of elements were assembled to represent the assessment scenarios for the study. Major element groups for this study are separation sets, traffic demand, arrival speed profiles and arrival/arrival separation buffers.

Separation sets

The application of minimum separations has proven as a recipe for safe arrival operations. Local mandatory implementations are based on guidelines of international bodies like ICAO or EUROCONTROL. For the purpose of this study, four sets of ***minimum wake turbulence separations*** were transferred into the Airport-in-a-Lab environment:

1. ICAO guidelines , as today they are the most implemented values including four weight categories Super (A380), Heavy, Medium and Light

2. RECAT-I EU as the European re-categorization scheme implemented e.g. at Paris Charles de Gaulle in 2016. RECAT I EU re-categorizes aircraft in six classes and introduces new minimum separation values between aircraft classes for safe operation.

3. The minimum dynamic pairwise separations (D-PWS) used here are called *WSVBS separations* to indicate them as outcome of the prediction methods developed in predecessor projects of the DLR project L-bo*ws*. The temporal separations were computed individually for each combination of lead aircraft type, follow aircraft type and meteorological data w.r.t. the time stamp of the lead aircraft over threshold. In cases where the prediction algorithm showed no reduction through dynamic pairwise separations in comparison to RECAT I EU values, the corresponding RECAT I EU minimum separations were used for the arrival pair in focus. The separation set is called *"RECAT I EU + WSVBS"*.

4. The WSVBS prediction method delivers the minimum separation exclusively based on the predicted wake vortex transport and decay. Accordingly, it also suggests safe minimum wake vortex separations smaller than the minimum radar separation of 2.5 NM. In order to make use of this capability an additional separation set was created with a minimum radar separation of 2.0 NM for cases where the WSVBS method delivered a safe minimum separation lower than 2.5 NM .

In cases where no wake vortex minimum separation was required in the ICAO or RECAT I EU separation sets, a minimum radar separation of 2.5 NM was applied.

Today visual separations may be applicable in specified weather conditions. They were not included in the study because activation periods and achievable separations are highly variable and thus lead to highly variable results with respect to arrival delay and arrival capacity.

Operational Concept

It is assumed that safe minimum dynamic pairwise separation values can be predicted reliably about half an hour to an hour before the touch downs of an aircraft pair . The operational concepts used for the airport-in-a-lab scenarios therefore cover the actions and elements involved during this time interval.

Actors are controllers and pilots, their role will not change significantly between scenarios with class-based minimum separation values and dynamic pairwise separation values. For the purpose of this study the actions of the controllers and pilots are limited to the task to establish the final approach sequence with the anticipated separation. Dynamic pairwise separation scenarios will require a controller support to realize the individual pairwise separation values like the LORD tool (Leading Optimized Runway Delivery) developed by EUROCONTROL. A sequence optimization is not considered in this stage of the development. It is assumed for all scenarios, that arriving aircraft will spend their runway queuing delay in the airport vicinity, be it in conventional holding stacks, linear holding trombones or point-merge structures. Each time the prediction system releases a possible reduced pairwise separation controller and pilot will be able to apply them if the follower flight is already delayed through runway queueing or would be delayed if the reduced separation could not be applied. This mechanism is the core beneficial effect of dynamic pairwise separation: to apply the reduced

separation to already delayed aircraft in the airport vicinity and hence reduce delays of the following aircraft.

Missed approaches are not modelled, it is assumed that the different separation buffer values used in the study will lead to comparable missed approach rates for all investigated scenarios, depending on the achievable separation delivery error in future environments.

Demand

Demand is a core element in a runway delay study . The more the demand approaches runway capacity the more minimum separations will have to be applied in order to guarantee safe operations and thus delay will be produced. In view of the Airport-in-a-Lab-scenario a high demand-to-capacity ratio will support the observation of expected delay reductions. Demand at an airport usually varies between different hours or different days in terms of absolute numbers and traffic mix e.g. of aircraft weight categories and hence will result in different average delay numbers between hours or between days even if the minimum separations stay constant. As dynamic pairwise separations will reduce wake vortex separations a high share of wake vortex relevant aircraft and of arrival only traffic streams to a runway will be beneficial to observe the performance of dynamic pairwise separations. London-Heathrow (LHR) represents an airport which covers these Airport-in-a-Lab requirements considerably and its traffic data are available from the EUROCONTROL Demand Data Repository for research purposes. An actual traffic sample of one month LHR traffic (March 2013) was used to generate a pseudo demand for the L-bo*ws* Airport-in-a-Lab scenarios. This demand traffic sample is denominated “High Load”. Pseudo demand here means a demand generated from the last flight track record of the actual traffic. Each of the 19,852 arrivals is represented by its unique flight-ID, aircraft type and the last flight track record as anticipated touch-down time. As LHR usually is operating its runways in segregated mode the arrival demand stream was considered as one landing stream to a single runway.

Figure 2 summarizes the distribution of the hourly arrival demand values of the month of 03/2013 plotted over the course of the 24 hours of the time of day. Values are varying between the days of the month in a range of about +/- 5 arrivals per hour during the main traffic period. The corresponding average hourly demand (solid black line) over the month as a function of the time of day predominantly stays between 35 and 40 arrivals per hour.

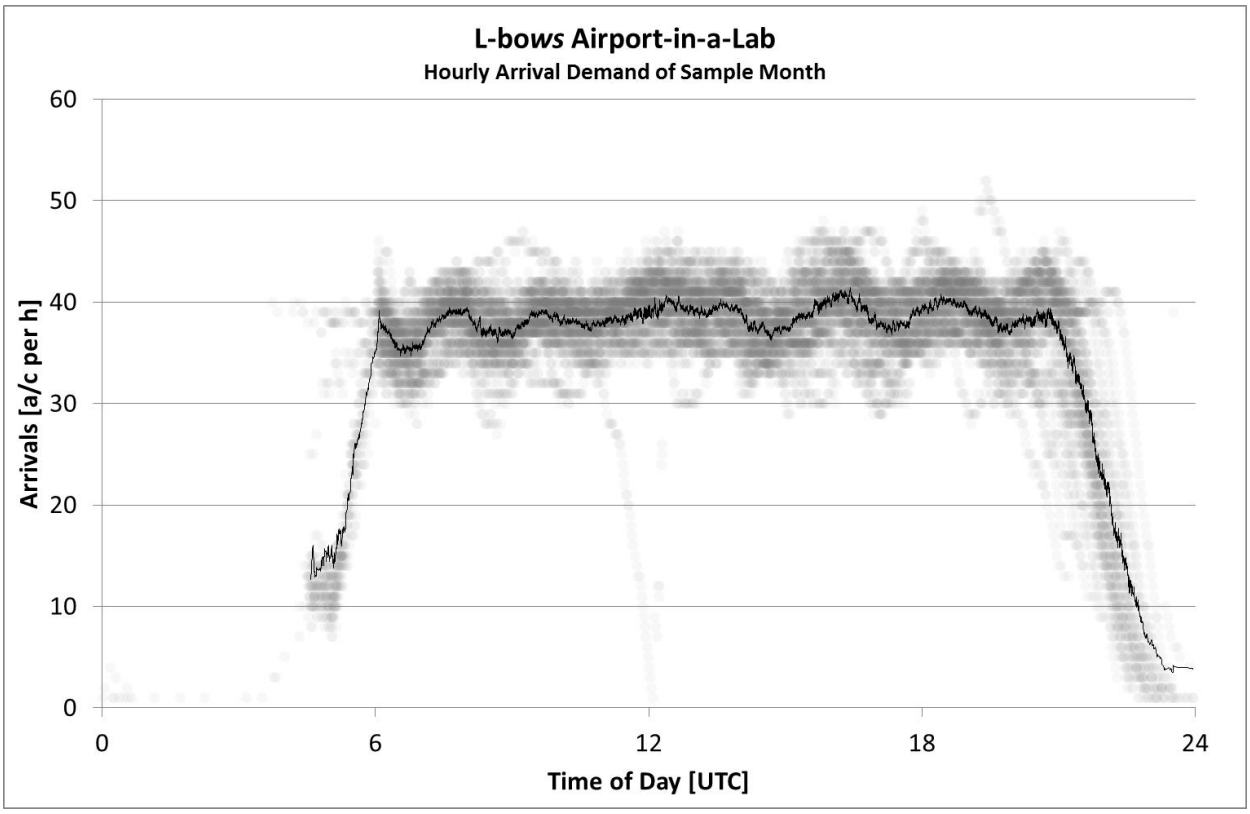

Figure 2: Hourly pseudo demand at threshold for L-bo*ws* Airport-in-a-Lab (values for all days of one month and corresponding moving average)

In addition a “High Load Compressed” demand sample is created from the “High Load” demand sample to be able to estimate saturation capacities of the different scenarios. The “High Load Compressed” demand is concentrating the scheduled arrival times of the whole month on a single point in time. The sequence of the landing operations is kept. Through this compression a steady and saturated demand is guaranteed for the complete traffic sample. The “High Load Compressed” demand sample is used to approximate the progress of hourly saturation capacity over the varying traffic mix of the traffic sample and the weather conditions during the selected month.

Arrival speed profiles

Speed profiles along the final approach paths (Figure 1) translate longitudinal distance based separation requirements (like ICAO or RECAT I-EU) into time intervals which in turn determine landing rates and in conjunction with demand influence arrival delays. Time-based minimum separation values like the ones from the WSVBS separation set can be used directly for capacity and delay calculations.

In order to translate longitudinal minimum separations into time intervals, recently published results of measurements at major European airports (,) were used as input to compile arrival speed profiles for the Airport-in-a-Lab usage. The speed profiles of individual aircraft types were clustered according to their traffic share in the traffic sample and time-to-fly versus distance-to-threshold were computed for two groups of aircraft corresponding to wake vortex class light/medium and heavy/super heavy. The results are presented in Table 1.

Average Time-to-Fly vs. Distance-to-Threshold		
Distance-to-Threshold [NM]	Time-to-Fly [s] (Light/Medium)	Time-to-Fly [s] (Heavy/Super Heavy)
2	53.3	51.5
2.5	66.4	64.3
3	79.1	76.9
3.5	91.4	89.1
4	103.2	101.1
4.5	114.6	112.7
5	125.5	123.9
5.5	136.1	134.8
6	146.5	145.3
6.5	156.8	155.7
7	166.9	165.9
7.5	176.9	176.0
8	186.9	185.9
8.5	196.7	195.8
9	206.5	205.5
9.5	216.2	215.1
10	225.7	224.7

Table 1: Average Time-to-Fly vs. Distance-to-Threshold Values used in the Airport-in-a-Lab scenarios

It has to be noted that these values are considerably higher than the time based separation values published in conjunction with the actual introduction at Heathrow airport due to the usage of local actual Heathrow specific arrival speed profiles (e.g. in).

Additional separation buffer

During the actual execution of immediate consecutive arrivals it is not possible for controllers and pilots to meet exactly the longitudinal minimum separation value between two aircraft. Therefore additional separation buffers are used in order to avoid violations of the minimum separation requirement. The size of these buffers directly influences the arrival capacity of an airport because it extends the average time to fly between two arrivals. The current practice of separation delivery at six major European hubs was studied in and . At 0.5 NM before threshold the observed mean spacing buffer was 0.5 NM ($\sigma = 0.7$ NM) on average for all airports with individual airport mean values between 0.2 NM and 1.2 NM. A study with data from seven airports in the US results in a mode value of 17 seconds for the excess inter-arrival time distribution, which corresponds to 0.67 NM buffer assuming an arrival speed of 140 kt and symmetrical distribution based on the lower half of the measurements .

In order to cover a range of possible separation buffers, the study here uses values of 0.5 NM, 0.75 NM and 1.0 NM. Lower values were not used because they imply a separation violation rate considerably higher than a commonly accepted theoretical rate of 5%.

Performance Indicators

The following performance indicators were chosen to compare the results of the different Airport-in-a-Lab scenarios:

Average Arrival Delay

The average arrival delay is the mean of all individual arrival delays of the traffic sample. The arrival delay of an individual flight is the difference between the planned landing time within the pseudo demand schedule and the actual simulated landing time. The average arrival delay indicates the overall performance of the demand capacity balancing process executed in the last phase of the arriving flights.

A reduction in average arrival delay may be transformed into monetary benefits by converting it through direct aircraft operating costs.

Hourly Flow

The maximum hourly flow is used as approximation for the hourly saturation capacity, if the demand is exceeding capacity clearly. The 95% hourly flow is used in addition to avoid outliers due to exceptional situations, 95% means that only 5% of the hourly intervals exceed this flow.

The benefit of arrival separation reduction is often stated in additional hourly capacity, so this value can be used for comparison purposes.

Delay Costs

Delay costs are estimated by converting cumulated arrival delays via direct operating costs into possible savings through the introduction of dynamic pairwise separations. Simulated tactical average delays were converted into tactical delay costs per month using EUROCONTROL recommended values for Airborne Arrival Management Costs from . For short delays up to 30 minutes per flight the costs are 71 € per minute per flight.

Runway Capacity and Delay Computation

The scenarios under study are straight arrival streams. Demands as well as the separation values in the D-PWS scenarios are dynamically changing. Therefore the Runway Capacity Simulation Model (RucsimX) was used to build properly separated sequences and to measure flows and delays over time. RucsimX was developed to build timely separated sequences of runway operations from a given demand schedule and a set of separations between runway operations. Its intended use covers runway capacity and delay studies of an arbitrary airport with multiple runways. RucsimX is a proprietary development of DLR.

3. Results

The results of the simulation runs are presented as

- average delays and maximum flows/95% flows for the “High Load” demand,
- maximum flows/95% flows, average flows, average and peak capacities for the “High Load Saturated” demand,
- tactical delay costs per month for selected scenarios.

3.1 Average Delays and Flows for “High Load” demand

The “High Load” demand scenario is based on the actual arrival traffic demand of one month at Heathrow airport in March 2013. The traffic peaks implicitly are adjusted to the then actual hourly arrival capacity of the airport which in turn depended on the then achieved time separations between arriving aircraft.

Separation Set (WV / Radar / D-PWS)	Avg. Delay [s]	Max Flow [ac/h]	95% Flow [ac/h]
ICAO / 2.5 / none	959	45	41
RECAT I EU / 2.5 / none	137	45	41
RECAT I EU / 2.5 / WSVBS	117	46	42
RECAT I EU / 2.0 / WSVBS	101	48	42

Table 2: Average Delay and Flow results for “High Load” scenarios with buffer size 0.5 NM

The maximum flows of the scenarios ICAO/2.5/none, RECAT I EU/2.5/none and RECAT I EU/2.5/WSVBS are comparable due to the fact that these values are the result of hours with a high share of radar separated aircraft pairs. Within the “High Load” scenarios the achievable maximum flow values depend on the demand situation which in turn varies with the actual delay situation. Therefore reduced minimum separation sets may not necessarily produce higher maximum flow rates.

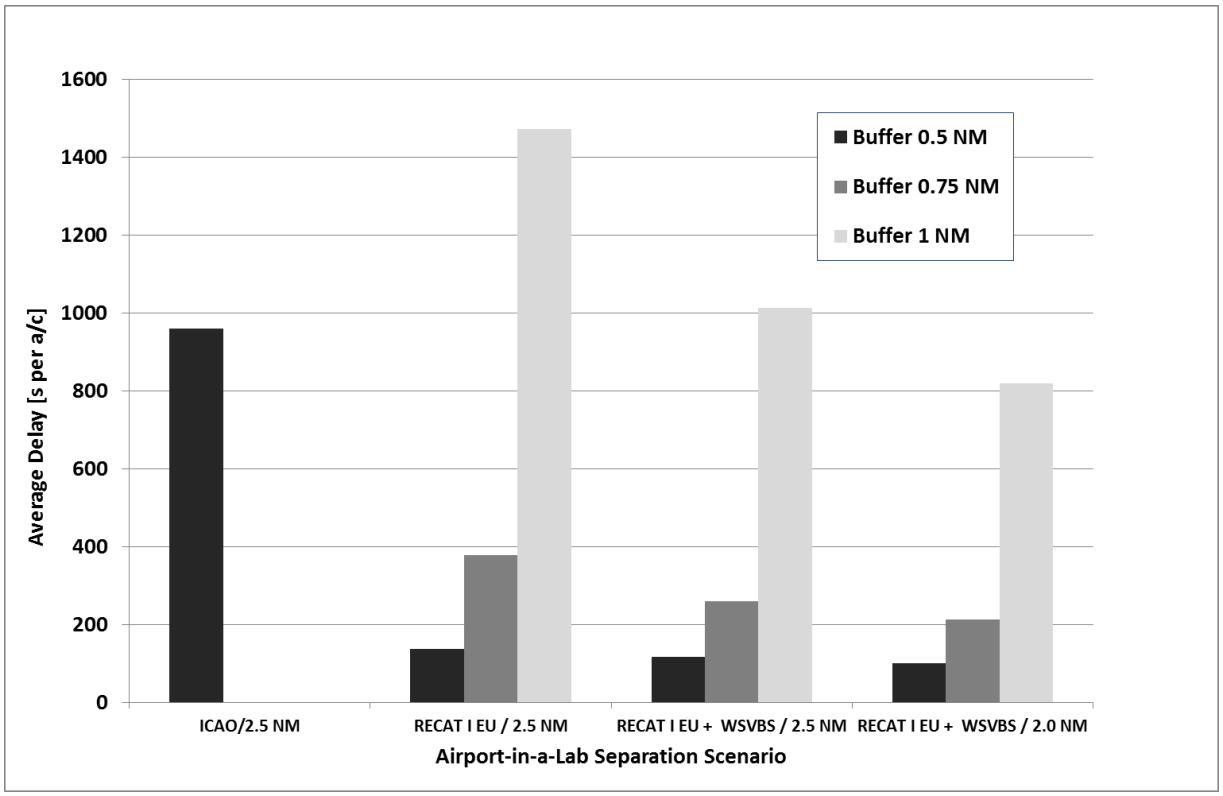

Figure 3: Average delay results depending on separation set and buffer size

Separation Set (WV / Radar / D-PWS)	Avg. Delay [s]	Max Flow [ac/h]	95% Flow [ac/h]
ICAO / 2.5 / none	2466	43	39
RECAT I EU / 2.5 / none	378	42	40
RECAT I EU / 2.5 / WSVBS	261	43	41
RECAT I EU / 2.0 / WSVBS	214	47	41

Table 3: Average Delay and Flow results for "High Load" scenarios with buffer size 0.75 NM

Looking on the absolute value of the average delay from the perspective of a normal operation day, values below 10 minutes per flights per day seem to be realistic for tactical arrival delay. It is expected that in a future system higher values, though they may be possible in disrupted situations, will not be accumulated in the airport vicinity but on their departure airports or en-route. Therefore this kind of delays will not be available for reduction through the application of D-PWS.

Separation Set (WV / Radar / D-PWS)	Avg. Delay [s]	Max Flow [ac/h]	95% Flow [ac/h]
RECAT I EU / 2.5 / none	1471	40	38
RECAT I EU / 2.5 / WSVBS	1013	42	40
RECAT I EU / 2.0 / WSVBS	819	48	41

Table 4: Average Delay and Flow results for "High Load" scenarios with buffer size 1.00 NM

3.2 Saturated Flows for "High Load Compressed" demand

The "High Load Compressed" demand was used to explore the saturation limits of the different scenarios. The time compression of the demand induces a continuous demand without gaps. Thus each combination of two aircraft will land with the smallest separation possible depending on the separation set. The resulting Maximum Flows and 95%-Flows are an approximation of the hourly saturation capacity. The Maximum Flow depicts the hour of the traffic sample month with the highest hourly saturation capacity and the 95%-Flow approximates an hourly saturation capacity, which could be reached in 5% of the time during the simulation.

In addition an hourly Peak Saturation Capacity and an hourly Average Saturation Capacity were computed using an analytical model. The Peak Saturation Capacity uses the lowest minimum separation values (i.e. 2.5 NM or 2.0 NM) to indicate maximum flows without any wake vortex related restrictions for reference purposes as an upper limit. The Average Saturation Capacity was computed analytically using the average traffic mix of the complete demand sample of one month. Scenarios with D-PWS application are considered as too heterogeneous to compute an Average Saturation Capacity .

	Simulation results		Analytical Model	Simulation results	Analytical Model
Separation Set	**Max Flow [ac/h]**	**95% Flow [ac/h]**	**Peak Sat. Cap. [ac/h]**	**Avg. Sat. Flow [ac/h]**	**Avg. Sat. Cap. [ac/h]**
ICAO / 2.5 / none	45	42	46.8	36.1	36.7
RECAT I EU / 2.5 / none	46	44	46.8	39.5	41.0
RECAT I EU / 2.5 / WSVBS	47	46	46.8	40.6	n/a
RECAT I EU / 2.0 / WSVBS	59	57	60.0	42.6	n/a

Table 5: Hourly Flow and Capacity results for saturated "High Load Compressed" demand with buffer size 0.5 NM

In addition two graphical representations were developed to show the distribution of the saturated hourly flow over time. Figure 4 is showing the progression of saturated hourly flow rates over simulation time using the "High Load Compressed" demand. Depicted are the following curves

- ICAO wake vortex separation set + minimum radar separation of 2.5 NM + buffer size 0.5 NM
- RECAT I EU wake vortex separation set + minimum radar separation of 2.5 NM + buffer size 0.5 NM
- RECAT I EU wake vortex separation set with WSVBS wake vortex separations where applicable + minimum radar separation of 2.0 NM + buffer size 0.5 NM.

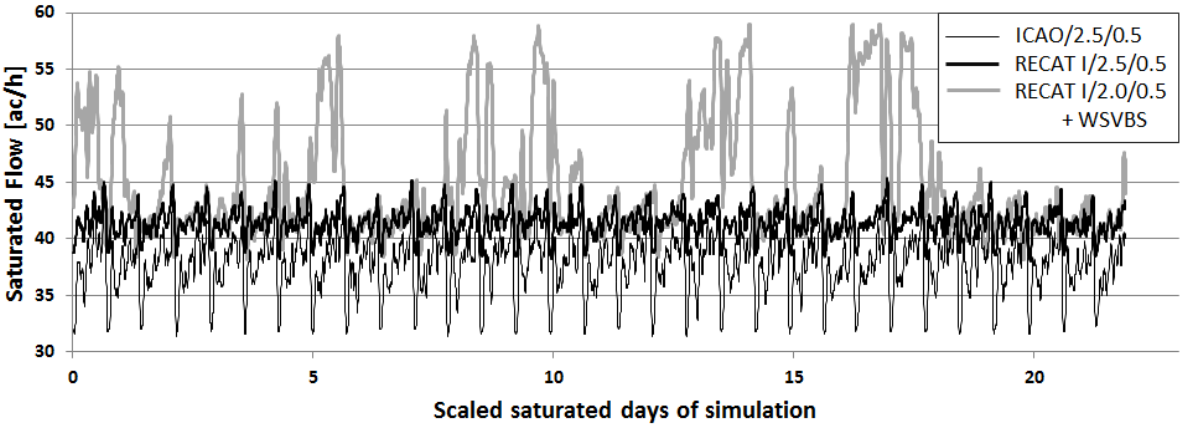

Figure 4: Progression of saturated flow over simulation time using "High Load Compressed" demand

Figure 5 is showing the cumulated percentage of simulation hours reaching a specified saturated flow

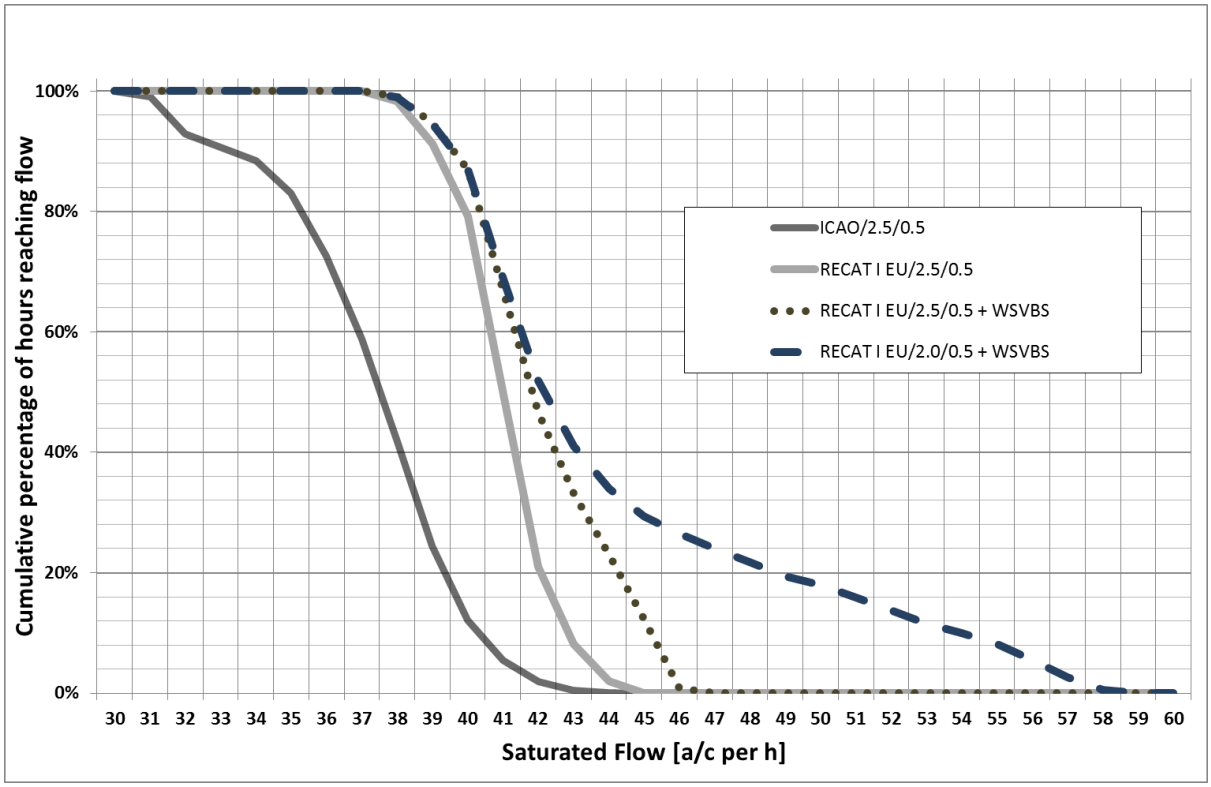

Figure 5: Cumulated percentage of simulation hours reaching a specified saturated flow using "High Load Compressed" demand

3.3 Tactical Delay Cost Savings

Simulated tactical average delays were converted into tactical delay costs per month using EUROCONTROL recommended values for Airborne Arrival Management Costs from . For short delays up to 30 minutes per flight the costs are 71 € per minute per flight and the scenarios are containing 19852 flights in one month. The results are presented exemplarily to show the dimension of possible savings. As stated earlier, a value of 10 minutes per flight can be treated as reasonable upper limit for tactical delays which can be used for savings through D-PWS. The results for the following high load scenarios are summarized in Table 6 and Table 7:

- ICAO wake vortex separation set + minimum radar separation of 2.5 NM + buffer size 0.5 NM
- RECAT I EU wake vortex separation set + minimum radar separation of 2.5 NM + buffer sizes 0.5 NM and 0.75 NM
- RECAT I EU wake vortex separation set with WSVBS wake vortex separations where applicable + minimum radar separation of 2.5 NM + buffer size 0.5 NM and 0.75 NM.

- RECAT I EU wake vortex separation set with WSVBS wake vortex separations where applicable + minimum radar separation of 2.0 NM + buffer size 0.5 NM and 0.75 NM.

Scenario	Avg. Delay [s]	Tactical Delay Costs per Month [M€]
ICAO/2.5/0.5	959	22.55
RECAT I EU/2.5/0.5	137	3.22
RECAT I EU/2.5/0.5/WSVBS	117	2.75
RECAT I EU/2.0/0.5/WSVBS	101	2.37

Table 6: Estimated tactical delay costs for selected scenarios with a buffer of 0.5 NM

Scenario	Avg. Delay [s]	Tactical Delay Costs per Month [M€]
RECAT I EU/2.5/0.75	378	8.88
RECAT I EU/2.5/0.75/WSVBS	261	6.13
RECAT I EU/2.0/0.75/WSVBS	214	5.03

Table 7: Estimated tactical delay costs for selected scenarios with a buffer of 0.75 NM

For increased demands the cost saving margins of course would be higher.

4. Discussion

The results presented in the preceding section are completely based on Airport-in-a-Lab Scenarios tailored to a demonstration of the benefits of D-PWS application employing DLR's wake vortex advisory system WSVBS. The following statements therefore are based solely on these results and cannot be seen as generally valid for the application of D-PWS at arbitrary airports.

In general it was observed, that D-PWS application using the WSVBS was able to reduce average tactical arrival delays. The amount of possible reduction was depending on two factors mainly. The first one is the base level of the average delay which is not surprising due to the exponential progression of delay when the demand to capacity ratio is approaching one and thus the base level of delay is already high. The second factor is the combination of D-PWS with a reduction of the minimum radar separation from 2.5 NM to 2.0 NM which enables the application of wake vortex separation values well below the actual radar separation.

The effects of a higher demand-to-capacity ratio on average arrival delay are demonstrated through the application of different buffer sizes (cf. Table 2 to Table 4). The capacity is decreased by extending the buffers and as the demand stays the same the demand-to-capacity ratio increases.

The Airport-in-a-Lab scenarios are containing three substantial groups of changes or improvements in the separation values:

1. Wake Vortex separation reduction: ICAO -> RECAT I EU-> RECAT I EU/WSVBS

2. Radar separation reduction: 2.5 NM -> 2.0 NM

3. Buffer size variations: 1.0 NM -> 0.75 NM -> 0.5 NM

Comparing these three groups, it can be concluded that the biggest ***delay reduction effects*** are generated through the switch from ICAO to RECAT I EU and the buffer size variation. The additional effect through the introduction of WSVBS separation even in combination with a radar separation of 2.0 NM where applicable is considerably smaller (cf. Table 2 to Table 4). Considering the maximum flows, however, improvements brought along by RECAT 1 EU and by the application of the WSVBS are on the same order of magnitude.

Looking at the ***maximum flows and peak saturation capacities*** in the "High Load Compressed" demand scenarios, the achieved flows and peak saturation capacities are showing a considerable gain in hourly peak values of more than 28% when comparing the RECAT I EU/2.5/0.5 scenario with the RECAT I EU+WSVBS/2.0/0.5 scenario (Table 5, Figure 4). The maximum flows achieved with the WSVBS approximately reach the peak saturation capacities that can be achieved by suspension of wake vortex related restrictions. In the case of D-PWS an increase in maximum achievable flows and peak saturation capacities can be used to reduce queues in the arrival area of the airport due to the prediction horizon of less than 1 h.

For strategic and tactical demand capacity balancing the available capacity should be as independent as possible on traffic mix or on time of day. Figure 4 and Figure 5 are showing that the RECAT I EU/2.5/0.5 separation scenario has a smoother progression in saturated flows than the ICAO/2.5/0.5 set on the one hand and the WSVBS separation sets on the other hand. For the WSVBS separations the potential capacity gains and their temporal distributions depend heavily on the prevailing weather conditions. Other weather situations may lead to significantly different characteristics of the achievable capacity gains. In particular, airports with higher frequencies of strong winds compared to the situation at Frankfurt airport may benefit from larger tactical capacity gains .

The benefits in terms of tactical arrival delay costs heavily depend on the base level of delay. Reasonable upper levels for the expected savings in the Airport-in-a-Lab scenarios studied are values of 2.75 Mill. € per month for the introduction of WSVBS in an RECAT I EU scenario and an additional saving of 1.1 Mill. € per month with the additional introduction of 2.0 NM radar separations where applicable.

The Airport-in-Lab environment established for the study may be easily modified to study additional future changes in the ATM system like parameter changes (e.g. minimum wake vortex separation sets, minimum radar separation, buffer sizes or demand patterns) or varying demand patterns.

5. Conclusions

Dynamic pairwise separations currently are the most advanced research step in reducing wake vortex minimum separation requirements. Within DLR's L-bo*ws* project it was shown that tactical arrival delay savings are achievable with D-PWS employing DLR's wake advisory system WSVBS and hourly peak saturation capacity can be improved substantially. Due to the

short prediction time the effective benefit of D-PWS in actual traffic situations will depend heavily on the congestion level of the flights arriving at an airport. The worse the delay situation is the more savings are generated once D-PWS are applicable. Airports with high frequencies of strong winds, that blow the wake vortices out of the flight corridor, may achieve higher tactical capacity gains.

Short-term capacity increases like the ones generated by D-PWS in the L-bo*ws* context may not be used to increase mid-term and long-term planning capacity parameters but there may be other ways to use the capacity gains during actual operation. One example is a situation on an airport with two or more arrival runways in use. If the capacity of one runway temporarily can be increased with D-PWS, it could be used to process arrivals from another runway where landings may be more sensitive from a noise perspective.

Acknowledgements

This report was also submitted to be presented at the AIAA Aviation Forum 2019 and to be published in the proceedings.

References

[1] J. N. Hallock, G. C. Greene and D. C. Burnham, "Wake vortex research – A retrospective look," *Air Traffic Control Quarterly,* Vol. 6, p. 161–178, 1998.

[2] Spalart and P. R., "Airplane trailing vortices," *Annual Review of Fluid Mechanics,* Vol. 30, p. 107–138, 1998.

[3] T. Gerz, F. Holzäpfel and D. Darracq, "Commercial aircraft wake vortices," Progress in Aerospace Sciences, Vol. 38, 2002.

[4] B. Elsenaar and et al., "Wake Vortex Research Needs for "Improved Wake Vortex Separation Ruling" and "Reduced Wake Signatures". Part II, Specialist's Reports," 2006.

[5] "Aircraft Wake Vortex State-of-the-Art & Research Needs. WakeNet3-Europe," compiled by F. Holzäpfel et al., issued by A. Reinke, 2011, 157 pages.

[6] J. N. Hallock and F. Holzäpfel, "A review of recent wake vortex research for increasing airport capacity," *Progress in Aerospace Sciences,* Vol. 98, pp. 27-36, 2018.

[7] D. Hinton, J. Charnock and D. Bagwell, "Design of an Aircraft Vortex Spacing System for Airport Capacity Improvement," in *AIAA Paper 2000-0622*, Reno, NV, USA, 2000.

[8] D. Rutishauser and C. O'Connor, "Aircraft Wake Vortex Spacing System (AVOSS) Performance Update and Validation Study," NASA, Langley Research Center, Hampton, VA, 2001.

[9] T. Gurke and H. Lafferton, "The development of the wake vortex warning system for Frankfurt Airport: Theory and implementation," *Air Traffic Control Quarterly,* Vol. 5, 1997.

[10] F. Holzäpfel, T. Gerz, M. Frech, A. Tafferner, F. Köpp, I. Smalikho, S. Rahm, K.-U. Hahn and C. Schwarz, "The Wake Vortex Prediction and Monitoring System WSVBS Part I: Design," *Air Traffic Control Quarterly,* Vol. 17, pp. 301-322, 2009.

[11] T. Gerz, F. Holzäpfel, W. Gerling, A. Scharnberger, M. Frech, K. Kober, K. Dengler and S. Rahm, "The Wake Vortex Prediction and Monitoring System WSVBS Part II: Performance

and ATC Integration at Frankfurt Airport," *Air Traffic Control Quarterly,* Vol. 17, pp. 323-346, 2009.

[12] F. Holzäpfel, K. Dengler, T. Gerz and C. Schwarz, "Prediction of Dynamic Pairwise Wake Vortex Separations for Approach and Landing," in *AIAA Paper 2011-3037*, Honolulu, Hawaii, USA, 2011.

[13] ICAO, "Procedures for Air Navigation Services - Air Traffic Management, 16th Edition," Doc 4444, ICAO, 2016.

[14] NATS/CAA, "Aeronautical Information Circular P 001/2015 Wake Turbulence," NATS, 2015.

[15] F. Rooseleer and V. Treve, "RECAT-EU European Wake Turbulence Categorisation and Separation Minima on Approach and Departure," EUROCONTROL, 2015.

[16] FAA Federal Aviation Administration, "SAFO Re-categorization (RECAT) of FAA Wake Turbulence Separation Categories at Specific Airports," FAA, Washington, 2013.

[17] FAA, "FAA Aircraft Wake Turbulence Re-Categorization (RECAT) Phase II Implementation within Southern California Terminal Radar Approach Control (TRACON) airspace," FAA, San Diego, 09/26/2016.

[18] A. Lau, S. Lorenz and F. Holzäpfel, "Individual Wake Vortex Separations: Capacity and Delay Impact on Single and Dual Dependent Runway Systems," in *12th AIAA Aviation, Technology, Integration, and Operations (ATIO) Conference*, Indianapolis, USA, 2012.

[19] T. Kolos-Lokatos and R. J. Hansman, "THE INFLUENCE OF RUNWAY OCCUPANCY TIME AND WAKE VORTEX SEPARATION REQUIREMENTS ON RUNWAY THROUGHPUT," MIT International Center for Air Transportation (ICAT), Cambridge, MA 02139 USA, 2013.

[20] EUROCONTROL, "European Network Operations Plan 201-2019/22," Brussels, 2018.

[21] M. Frech, F. Holzäpfel, A. Tafferner and T. Gerz, "High-Resolution Weather Data Base for the Terminal Area of Frankfurt Airport," *Journal of Applied Meteorology and Climatology,* Vol. 46, pp. 1913-1932, 2007.

[22] F. Holzäpfel, "Probabilistic Two-Phase Wake Vortex Decay and Transport Mode," *Journal of Aircraft,* Vol. 40, pp. 323-331, 2003.

[23] C. W. Schwarz and K.-U. Hahn, "Full-flight simulator study for wake vortex hazard area investigation," *Aerospace Science and Technology,* Vol. 10, pp. 136-143, 2006.

[24] F. Holzäpfel, L. Strauss, C. Schwarz, "Assessment of Dynamic Pairwise Wake Vortex Separations for Approach and Landing at Vienna Airport," in *AIAA Aviation 2019*, Dallas, 2019.

[25] F. Holzäpfel, "Effects of Environmental and Aircraft Parameters on Wake Vortex Behavior," *Journal of Aircraft,* Vol. 51, pp. 1490-1500, 2014.

[26] R. Horonjeff, F. X. McKelvey, W. J. Sproule and S. B. Young, Planning & Design of Airports, McGraw-Hill, 2010.

[27] R. de Neufville and A. Odoni, Airport Systems - Planning Design and Management, New York: McGraw-Hill, 2003.

[28] EUROCONTROL, "Challenges of Growth 2013, Task 6: The Effects of Network Congestion in 2035," EUROCONTROL, Brussels, 2013.

[29] ICAO, "Guidance on A380-800 Wake Vortex Aspects," ICAO, 2008.

[30] A. R. Groskreutz and G. Ruiz Mayer, "Analysis of 2NM Separation for Minimal Pair Arrivals," in *SESAR Innovation Days*, Bologna, 2015.

[31] M. Frech and F. Holzäpfel, "Skill of an Aircraft Wake-Vortex Model Using Weather Prediction and Observation," *Journal of Aircraft,* Vol. 45, pp. 461-470, 2008.

[32] V. Cappellazzo, V. Treve and C. Chalon, "Design Principles for a Separation Support Tool Allowing Optimized Runway Delivery," in *ATIO Aviation Technology, Integration, and Operations Conference*, Atlanta, 2018.

[33] EUROCONTROL, "DDR2 Reference Manual For General Users 2.9.5," EUROCONTROL, 2018.

[34] G. van Baren, C. Chalon-Morgan and V. Treve, "The current practice of separation delivery at major European airports," in *Eleventh USA/Europs Air traffic management Research and Development Seminar*, Lisbon, 2015.

[35] F. Herrema, "Time Based Separation - Compression on final approach and Time Based Separation for optimized runway delivery," TU Delft, 2014.

[36] C. Morris, J. Peters and P. Choroba, "Validation of the Time Based Separation concept at London Heathrow Airport," in *Tenth USA/Europe Air Traffic Management Research and Development Seminar (ATM2013)*, Chicago, 2013.

[37] F. Herrema, V. Treve and R. Curran, "Typical additional spacing-buffer to apply at 4DME for delivering separation minima," in *34th Digital Avionics System Conference DASC*, Prague, 2015.

[38] L. Spinoso, G. Coville and C. Roberts, "Analysis of the Excess Inter-Arrival Time Distribution," in *Integrated Communications Navigation and Surveillance (ICNS) Conference*, Herndon, 2014.

[39] EUROCONTROL, "Standard Inputs for EUROCONTROL Cost-Benefit Analyses 8.0," EUROCONTROL, Brussels, January 2018.

[40] P. Agnew and Hoad, D. J., "Climatology Study of World Airports in the Context of Wake Vortex Behaviour Class," Met Office UK, 2002.

1.4 Ground-based Wake Vortex Prediction in the En-route European Airspace

Alexander Lau[1], Jan Berling[2], André Koloschin[2] Frank Holzäpfel[3], Ingo Sölch[3]

[1] *Air Transportation Systems*
[2] *Hamburg Technical University (TUHH)*
[3] *Institute of Atmospheric Physics*

The L-bows working package 1.4 *Wake Vortex Predictions from Take-off to Landing* deals with ground-based prediction of en-route wake turbulence encounters in the European airspace. Due to an increasing overall volume of air traffic with required navigation performance within highly congested en-route airspaces, wake turbulence encounters above flight level 100 are becoming more frequent during the last years. The prediction of en-route wake vortex encounters provides information about airspaces with an increased encounter probability as well as specific characteristics of potential encounters. Apart from safety-related benefits, this information may be applied during flight- and capacity planning processes. Two different types of models are coupled with each other: an air traffic flow management model and a wake vortex decay and transport model. The results provide information about the predicted number of en-route encounters, dominant spatial encounter configurations and their locations.

1. Introduction

The encounter of wake vortices at least means a reduction of comfort but may also lead to a fatal safety threat for the intruder aircraft. Therefore, a detailed understanding of the possible behavior of wake vortices in all flight phases is important to most efficiently reduce the effects on flight operations and passenger comfort. A few studies of wake vortex encounters at cruise altitudes have been published [[1],5,[13],[15]]. The Aviation Safety Reporting System (ASRS) associates 28% of wake vortex reports with takeoff and climb, 25% for cruise, and 47% for approach and landing in the US-American airspace in a time frame extending from February 1999 to November 2009 [12].

The highly congested European airspace with its complex structure of traffic flow patterns promotes the appearance of different en-route wake turbulence encounter configurations according to a higher number of possible spatial configurations of the wake vortex and the intruder aircraft trajectory. This is generally related to the analysis of the European air traffic network structure. With continuously increasing traffic demand during the last decades, which is also expected for the upcoming years, the possibility of wake turbulence encounters increases within en-route airspaces. The EASA Safety Information Bulletin No. 2017-10 [1] therefore specifically addresses the issue of en-route wake turbulence encounters. It describes the general wake vortex behavior in the form of a descending or ascending wake center and the possibility of lateral drift caused by the influence of wind. The possible impact on the intruder aircraft may appear with a strong rolling moment when the wake vortex impacts along the aircraft's longitudinal axis. Furthermore, vertical acceleration and loss of control may occur.

This study focuses on the prediction and detection of wake vortices within the framework of a comprehensive air traffic simulation using numerical weather prediction data. In this context, ground-based (pre-)tactical predictions of wake vortex *corridors* in the European en-route airspace are performed, which are valuable to generate an information on the characteristics, the location and the number of potential wake turbulence encounters during cruise flight. To achieve this information, two comprehensive models are applied to predict and to integrate wake vortex corridors into a European Air Traffic Management Network (EATMN) model. Flight plan- and meteorological data for each flight as part of a daily traffic sample is compiled individually. Based on operational flight plan (OFP) trajectory data, which is processed by an air traffic flow management tool suite (Network Flow Environment, NFE), probabilistic wake vortex corridors are computed by the Airborne Probabilistic Two-Phase Wake Vortex Decay and Transport Model (P2P[a]). Therefore, both models have been adapted to efficiently predict wake vortex corridors. This allows for an identification of potential en-route encounters in the case of an intruder aircraft entering a corridor residing along the aircrafts planed trajectory.
This article has been published as AIAA Paper [9].

2. Technical Background

The applied models have been developed independently from each other at DLR Air Transportation Systems and DLR Institute of Atmospheric Physics. The initial concept envisages the use of a comprehensive network model covering the en-route flight phase on the one hand and a sophisticated wake vortex prediction model on the other hand. The following chapters provide additional model information.

2.1 Network Flow Environment (NFE)

The Network Flow Environment is a tactical ATFM tool suite for the representation of the European airspace system and for the allocation of tactical short-term air traffic flow and capacity management (ATFCM) measures for the demand-capacity-balancing (DCB) process in the flight planning phase [11]. NFE allocates departure slots and pre-flight alternative routes according to realisitc tactical DCB in Europe. Departure slots result in (pre-) departure ATFM delay of flights planned to enter highly congested network elements along their individual estimated trajectory. The approach comprises both types of capacity-afflicted network elements: ATC sectors and airports.

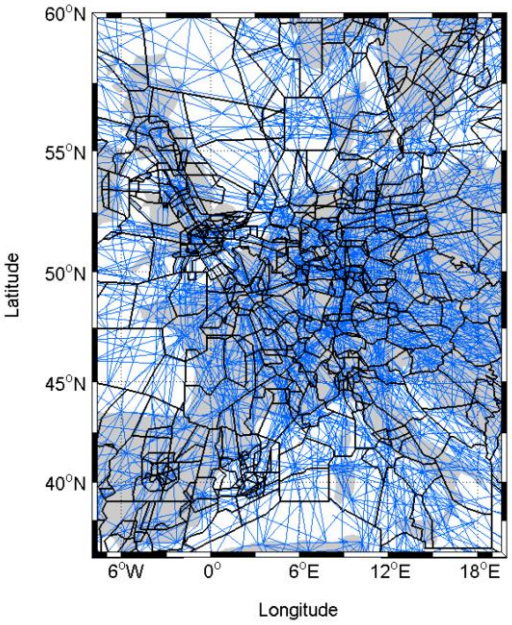

Figure 1. *Central European ATS route- and airspace-network representation within NFE*

NFE contains two main functions: i) data preparation and processing, and ii) demand-capacity-balancing. Apart from traffic data, network infrastructural (ATS route- and airspace-network data, see Figure 1) and impact data

like strong wind or convection are processed. These different data types need to be matched according to the time-frame, granularity and domain of the defined scenario. A heuristic functional algorithm as well as a linear large-scale optimization architecture for slot allocation are implemented, which is described in detail in Lau et al. (2015) [10]. The allocation of departure slots according to an overall system delay minimization is performed by a binary-integer optimization module to handle comprehensive ATFM optimization problems with acceptable computation effort.

2.2 Airborne Probabilistic Two-Phase Wake Vortex Decay and Transport Model (P2Pa)

The Airborne Probabilistic Two-Phase Wake Vortex Decay and Transport Model (P2P^a) is a version of the P2P models [8], which has been optimized for a fast aircraft-based prediction of wake vortex *corridors* [7]. Like P2P, the further developed P2P^a considers aircraft parameters, which characterize the position, strength and size of the wake vortex. Additionally, meteorological parameters determining the decay and the transport of wake vortices are considered, which are wind, temperature and turbulence. Typical input uncertainties are taken into account within the probabilistic wake vortex prediction influencing the geometric wake vortex corridor dimensions. The corridors are made of wake elements (ellipses) along the flight path, which are re-generated according to defined time granularity. The ellipses are specified by their position and their geometric dimension and form the corridors when connected to each other. A probability of residence of the vortex centers is assigned to each ellipse. This measure refers to all generated ellipses and can be set to 90%, 95% or 99%. For the current study the probability is set to 99% leading to large vortex ellipses and high numbers of encounters. A sensitivity analysis of wake vortex behavior in cruise flight related to different environmental parameters [6] deduces the following ranking of impact parameters i) wind, ii) thermal stratification, iii) turbulence, iv) aircraft position, v) aircraft mass, and vi) wing load factor. The required meteorological data is obtained from the COSMO-EU model [14]. The meteorological data and the respective gradients are obtained by spatial and temporal interpolation. The COSMO-EU grid covers the whole European airspace with a grid-size of 7 km. The vertical dimension covers 40 layers from ground to a height of 24 km. The weather prediction data is available in hourly granularity.

3. Methodology

The methodological approach is based on the definition of potential encounters according to Figure 2, which provides a representative encounter example in which two aircraft are flying in opposite directions on vertically neighbored route segments TOSIL-QEBEC and RUDUM-SEPAR. At time (*t*-*a*) with *a* representing the wake age at the encounter shown in Figure 2d), the initial wake element and the corresponding ellipse is generated behind the generator aircraft *G*. This is shown in the top-left Figure 2a), which indicates, that the wake center resides within the ellipse behind the generator aircraft as part of the corridor. It descends without being drifted laterally due to the absence of lateral wind components, which is shown in the top-right Figure 2b). Within the European RVSM airspace with a standard separation of 1000 ft between flight levels, the corridor descends into the next lower flight level onto the flight path of the intruder

aircraft *E*, which is shown in Figure 2c). At time t, the intruder aircraft *E*(t) is located inside the corridor representing a potential wake turbulence encounter.

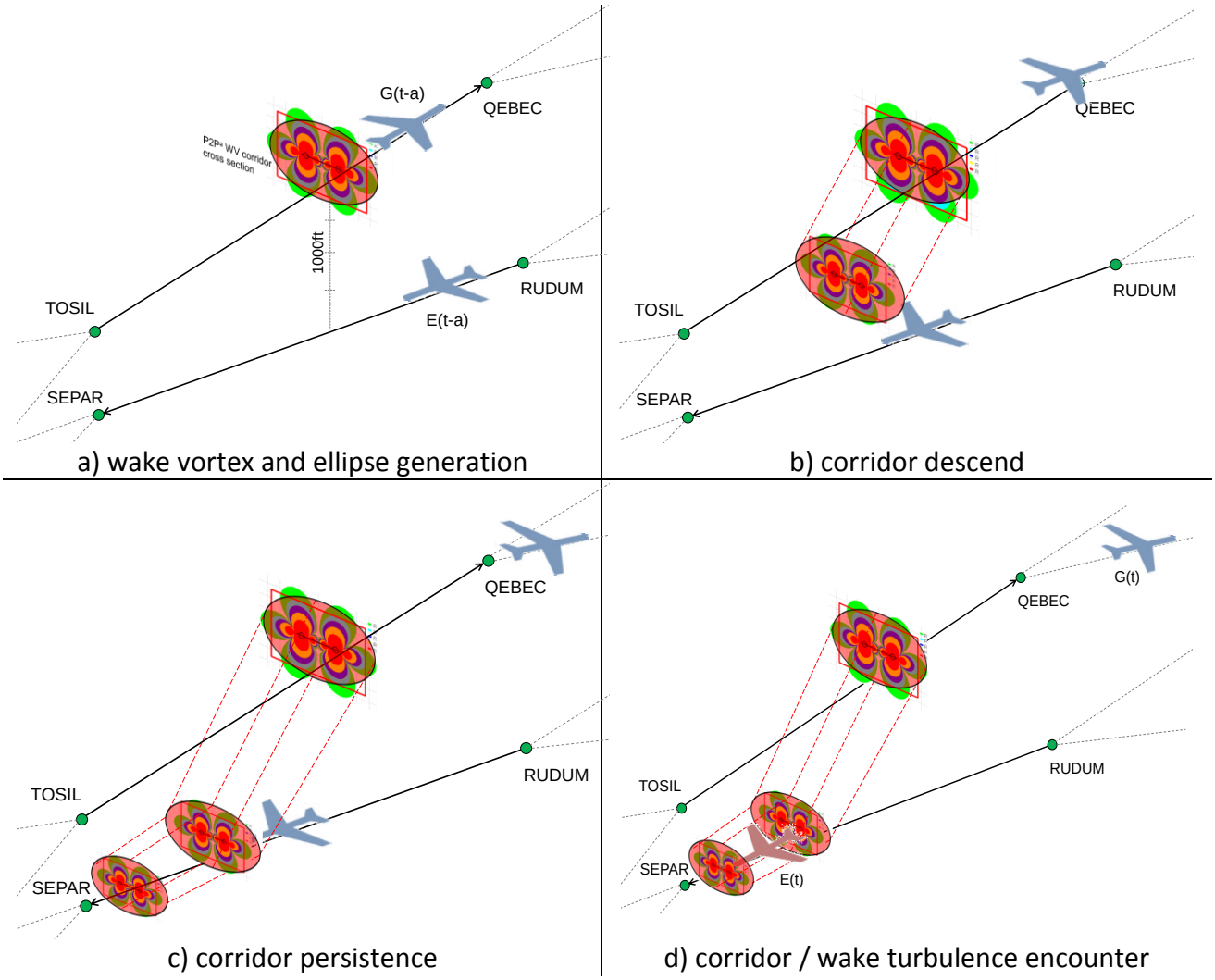

Figure 2. *Exemplary wake turbulence encounter (G: generator aircraft, E: encounter/intruder aircraft, a: wake age)*

The NFE serves as the main working instance addressing P2P[a] service to deliver the corresponding wake elements. To realize a workflow like shown in Figure 3, several steps concerning data processing and model interfacing are executed. In a first step, ATFM network infrastructure and traffic samples are extracted and processed within NFE. These samples usually comprise flight plan trajectories of a whole day in the European airspace. Flight plan data is provided by the EUROCONTROL Demand Data Repository (DDR2) [3], which contains individual mission parameters as well as detailed 4-dimensional flight plan trajectory data. These trajectories are initially divided into segments with defined boundary points representing navigation fixes or waypoints. Based on the actual mission planning process, the information may be adapted according to tactical needs. Flight plan data is methodologically

sufficient to be applied in the present study, since its predictive nature corresponds to the development of an encounter prediction functionality for the European airspace.

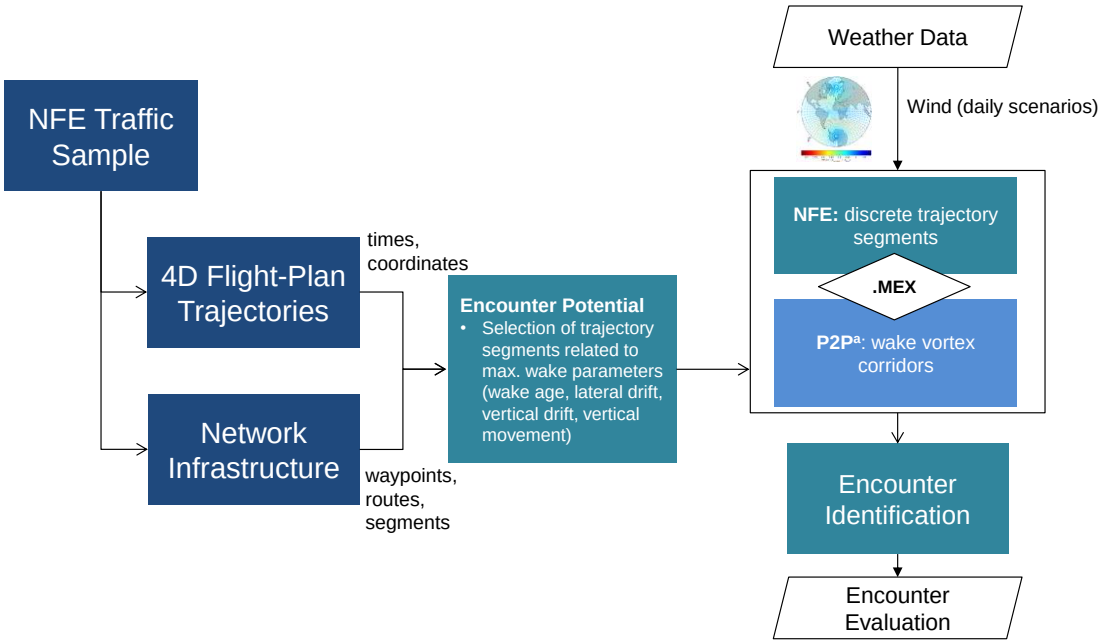

Figure 3. *Model workflow*

Prior to the computing of wake elements, potential conflicting generator-intruder pairs of aircraft have to be identified on the basis of potential conflicts between wake vortex corridors with intruder aircraft trajectories. Within a comprehensive flight plan data set, only a small fraction of aircraft pairs fulfills the encounter conditions given by its temporal and the spatial relations. Detailed P2Pa predictions are only conducted for aircraft pairs meeting all conditions listed in Table 1.

Table 1. *Wake corridor parameter bounds*

Wake Corridor Parameter	**Bounds**
Maximum lateral drift [m]	12.000
Maximum vertical descent [m]	600
Maximum wake age [sec]	360

Data processing functionalities of the NFE are established within MATLAB™. The interface between both models is therefore represented by a MATLAB™ executable (MEX) file since P2P^a is implemented in C++. The file is based on an already existing interface, but is adapted according to the application in the network context.

The final identification of potential wake vortex encounters is challenging due to high airspeeds in cruise flight[1]. Therefore, not only flight plan trajectory nodes are verified for

[1] Depending on individual configurations, encounters at cruising speed can only take a fraction of a second.

residing within a wake vortex corridor, but also trajectory segments in between trajectory nodes are verified such that potential short-term encounters are not missed. This approach is executed with flight plan trajectories with a granularity exact to the second.

4. Results and Discussion

An evaluation of potential en-route encounters within the European airspace comprises different types of parameter evaluations. Two out of 180 days representing different wind situations are evaluated to identify the impact of wind mainly on wake drift and number of encounters. Figure 4 provides average wind speeds and standard deviations of the whole set of 180 days in the first 6 months in 2014. Wind data is obtained from the ECMWF European Centre for Medium-Range Weather Forecasts [4]. It covers 24 measuring locations at European airports throughout the EATMN. Strongest average wind speeds with over 40 m/s occur at 14th February 2014, lowest average wind speeds with about 15 m/s occur at 3rd June 2014. The average wind speed of all days considered is about 23 m/s prevailing on 10th April 2014.

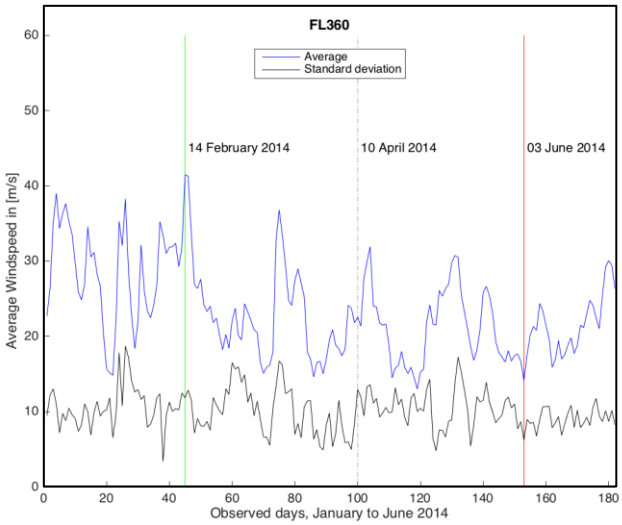

Figure 2. *Average wind speeds of 180 days observed from January to June 2014*

Wind speeds have been evaluated within a vertical layer between FL245 and FL400. Figure 5 provides the wind situations for both selected days at 12:00z for FL360. The grid-based wind fields indicate wind speeds up to 100 m/s. 14th February (hereinafter referred to as “strong wind day”) is characterized by strong winds from south-westerly directions over the Bay of Biscay and the British isles turning to north-westerly winds within the German airspace. 3rd June (hereinafter referred to as “low wind day”) is mainly characterized by winds speeds of around 20 m/s with peaks of about 55 m/s over the Bay of Biscany.

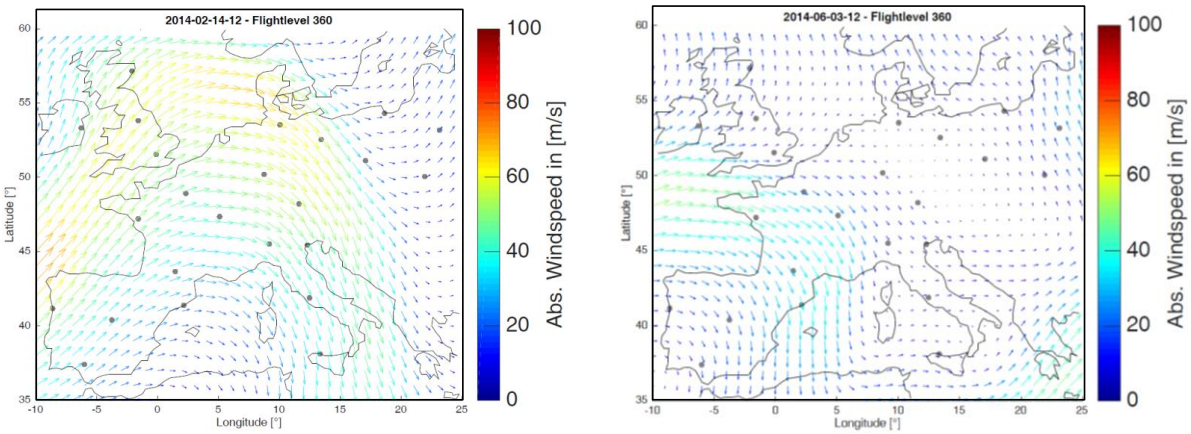

a) strong wind day a) low wind day

Figure 5. *Windfields of the selected days at 12:00z, FL360. The grey dots represent aerodrome locations applied for the average wind measurements*

4.1 Number of Encounters

As described in chapter 3, a predicted encounter is defined as the residence of the intruder aircraft within the wake turbulence corridor of the generator aircraft. The probabilistic elliptical volumes are supposed to contain the wake vortex centers with a probability adjusted to 99% considering estimated uncertainties of all input parameters needed for the wake vortex predictions. Because real wake vortices cover only a small fraction of the probabilistic volumes, the number of real encounters would be substantially lower than the predicted potential encounters reported here. Table 2 provides general quantitative results on both selected days. The total number of operational flight plan trajectories depends on traffic demand on the individual day, whereas inconsistent flight plans are filtered out of the evaluation set of trajectories.

Table 2. General Prediction Results

	low wind day	**strong wind day**
Trajectories [total number]	25.704	21.404
Intruder trajectories [total number]	8.336	5.436
Encounters [total number]	18.649	10.147

The share of intruder trajectories for which at least one encounter along the trajectory path is predicted, differentiates for both days. On the low wind day, 32.4% of all trajectories are classified as intruder trajectories whereas on the strong wind day, only 25.4% show at least one predicted encounter. The strong wind day features a lower share of predicted encounters, which is related to the lower total number of trajectories and therefore a decreased probability of encounter-prone situations concerning a necessary geometric relation of a corresponding trajectory pair (encounter configurations, see Figure **7**). Additionally, the lower share of predicted encounters is related to the predominant wind situation. A high share of encounters occurs for aircraft pairs, which do not represent a safety relevant wake turbulence category.

Both scenarios indicate similar distributions of predicted encounter durations. Most encounters have a duration of about two seconds. This is justified by typical diameters of probabilistic wake turbulence corridors of several hundred meters and air speeds of a few hundred meters per second. Nevertheless, encounter durations of more than 30s exist indicating configurations of intruder aircraft flying on almost parallel tracks for a longer time period.

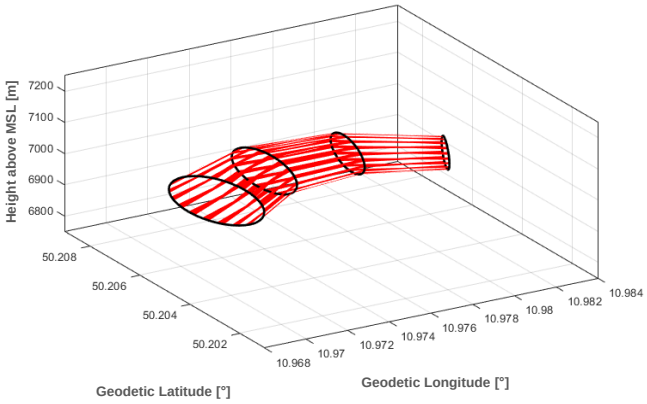

Figure 4. *Exemplary wake corridor design for one-minute resolution*

4.2 Corridor Design and Encounter Configuration

Figure 6 provides an impression on the geometric design of a wake vortex corridor. The time granularity with which the wake

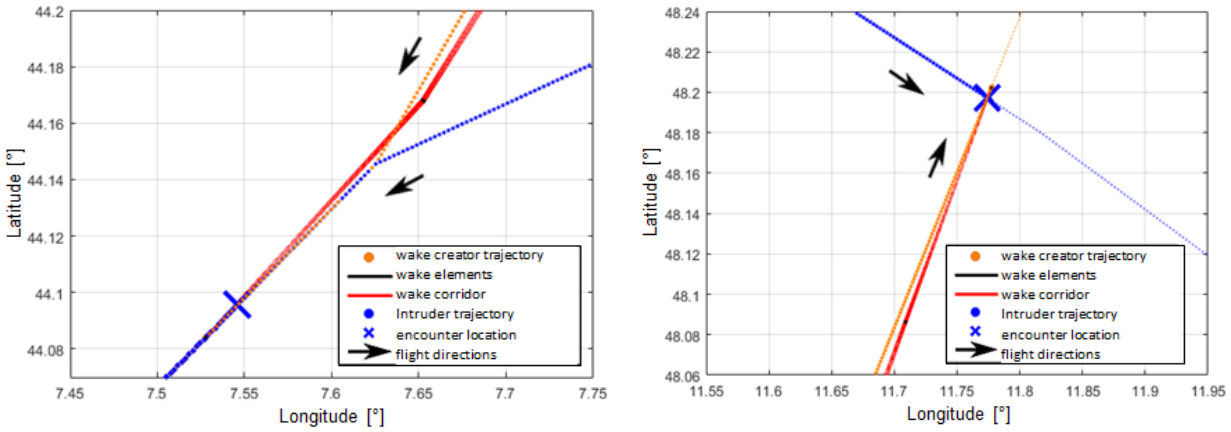

a) merging trajectories b) crossing orthogonal trajectories

Figure 3. *Typical encounter configurations*

elements (ellipses) are computed influences computation efficiency, which decreases with increasing data amounts. Therefore, the default P2P[a] output setting of one wake element per second is reduced to one element per minute, by which the amount of data to be handled is

reduced by a factor of 30. Figure **6** depicts the linear design of the corridor elements between the ellipses. Consequently, the final design of a corridor in terms of its 2-dimensional shape is affected by the defined temporal output granularity of wake elements.

Figure 7 provides typical encounter configurations. Different configurations are possible, whereas aircraft may fly on same, opposite or crossing flight tracks. Aircraft with different vertical speeds are also likely to be classified as a possible encounter pair as long as their trajectories fulfill the geometric relations according to table 1. The provided example of Figure **7**a) shows two merging aircraft trajectories in a low wind scenario. A lateral corridor drift does not appear so that the intruder aircraft penetrates the vortex corridor some nautical miles behind the merging point. Another typical encounter configuration is shown in Figure **7**b) on crossing orthogonal trajectories. It shall be mentioned, that air traffic control (ATC) would ensure sufficient radar separation especially at crossing points to not allow any conflict states between aircraft below en-route separation minima. The application of flight plan trajectories without a representation of ATC separations increases the total number of predicted encounters within this study compared to encounters possibly taking place during realistic operations.

4.3 Encounter Locations

Visualizations of encounter locations are shown separately for the lower and the upper en-route airspace. In this study the lower airspace is defined with a vertical dimension between FL100 and FL195, since in Europe, the upper information region (UIR) is generally defined above FL195 and up to FL660. This allows for a better encounter differentiation of aircraft during climb or (initial) approach phases and those, which are most likely in cruise flight.

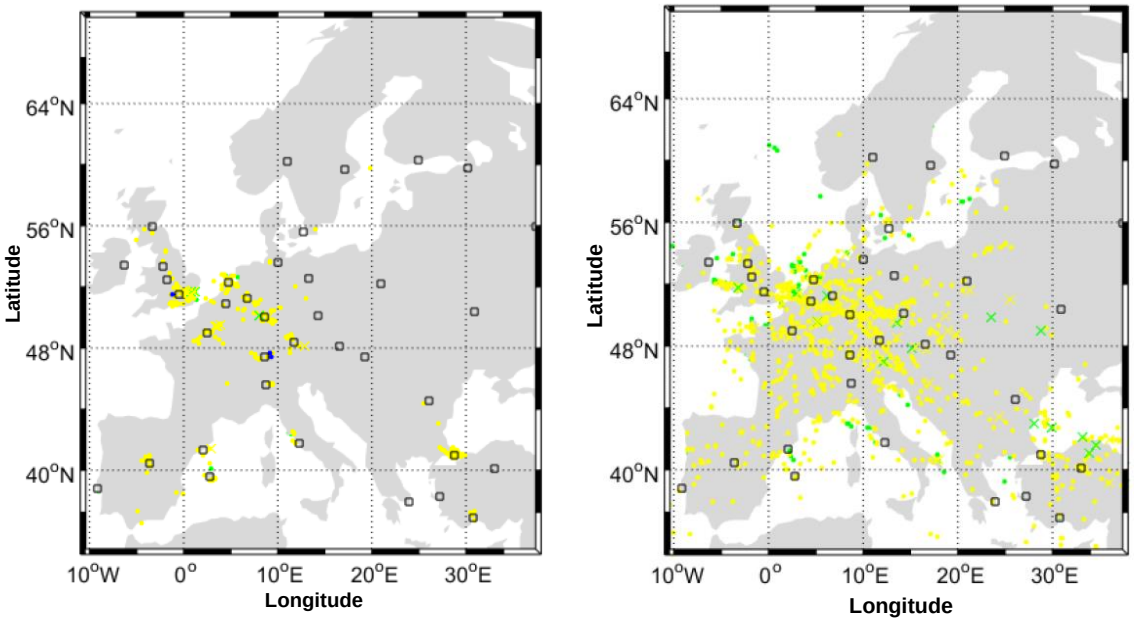

a) low wind day, FL100 – FL195

b) low wind day, FL196 – FL660

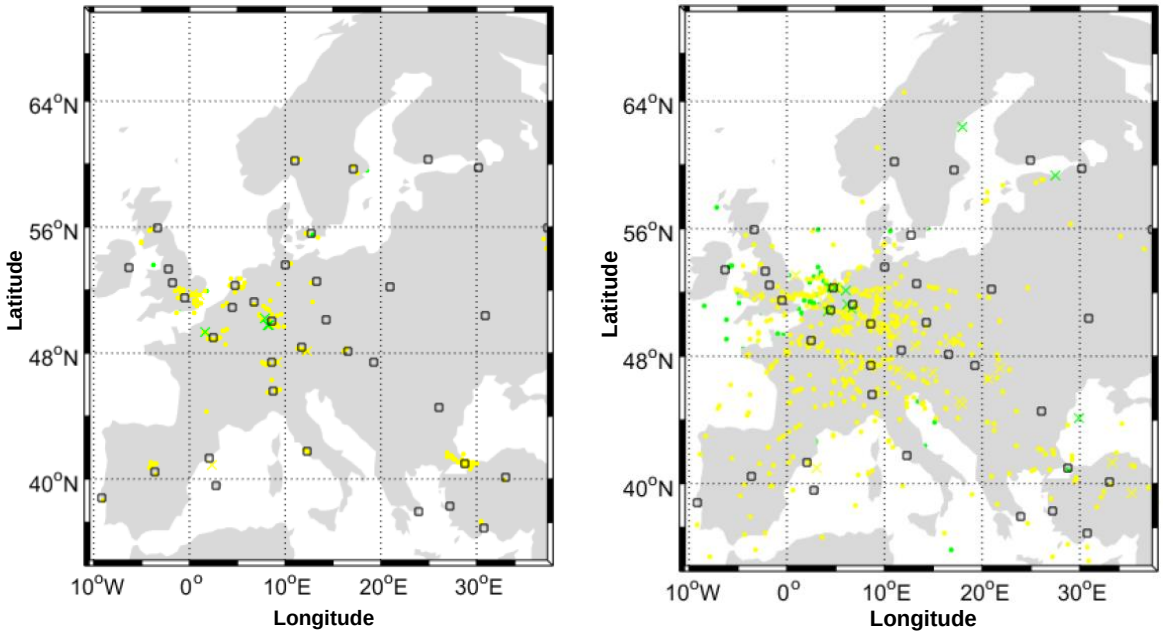

c) strong wind day, FL100 – FL195 d) strong wind day, FL196 – FL660

Figure 8. *Encounter locations, yellow dots: heavy-medium pairing, yellow crosses: super-medium pairing, green dots: heavy-heavy pairing, green crosses: super-heavy pairing*

Figure 8 provides mappings of encounter locations within the defined lower and the upper en-route airspace across Europe for both selected days. Encounter concentrations in the vicinity of hub airports like London Heathrow (EGLL), Paris Charles-de-Gaulle (LFPG) and Frankfurt/Main (EDDF) can be identified especially for the lower airspace, whereas in the upper airspace encounters mainly occur along congested ATS routes. This can be attributed to a higher traffic density with a higher complexity of crossing flight trajectories within these airspaces. The most frequent wake turbulence category pair is medium behind heavy type of aircraft, whereas heavy behind heavy and heavy behind super pairings also occur.

On the low wind day, 2.463 safety-relevant potential encounters at or above the required radar separation are predicted in total. Most of them occur within the upper en-route airspace along the air traffic service routes, where the wake corridor resides along the generator trajectory due to low lateral wind components. 1.563 encounters are associated to medium behind heavy aircraft pairs, whereas 807 encounters are associated to heavy behind heavy aircraft pairs. On the strong wind day, about 40 % less encounters are predicted related to the reduced number of relevant aircraft pairs. The number of safety-relevant predicted potential encounters has to be set into relation to the high number of flights throughout a day within the European airspace. Moreover, due to the probabilistic nature of wake corridors, only a small fraction of the predicted corridor penetrations represents an encounter with resulting critical rolling moments on the intruder aircraft.

The influence of wind is clearly represented by the different numbers of encounters of both days. It is obvious, that wind-induced lateral vortex drift decreases the number of encounters along a trajectory segment. On the other hand, specific wind direction in combination with

specific encounter configurations may lead to increased encounter probabilities. One typical case is stated by two flights flying at the same route segment in opposite directions. Even if these flights have vertical separations and lateral offsets, wind may lead to wake drift into intruder`s flight path. Strategic lateral offsets of the intruder aircraft in upwind direction could avoid such encounters.

The analysis of occurrence of different encounter geometries implies that the vortex drift away from intruder`s trajectories is statistically outweighing the vortex drift into intruder`s trajectories. Thus the lower number of encounters on the strong wind day can be interpreted as not only resulting from the lower number of trajectories but also from the effect of vortex drift.

5. Outlook

It is intended by the authors to provide steps to further develop this work but also to describe the opportunity for adding an additional modeling instance to detail the shape of the wake vortex corridor. The application of this methodology to a larger set of traffic samples is certainly one of the obvious activities to gain more insights on wake-vortex encounter statistics. Therefore, DLR`s Simplified Hazard Area Prediction Method – SHAPe [16] shall be integrated into the workflow to better assess the potential encounter safety risk. Moreover, a sensitivity analysis of different maximal wake corridor values shall be conducted.

An application of historic trajectory radar data would provide post-operational and therefore more realistic results to validate wake-vortex predictions like presented in this study. This would allow for a more reliable classification of wake encounters and thereby reduce the predicted number of encounters. Based on these validation activities, NFE`s ATFM optimization function shall be adapted to reduce demand within airspaces with increased wake encounter potential. It is intended to adapt ATFM optimization cost functions and to set up a feasibility study on wake encounter cost models within the ATFM problem.

References

[1] Brown, A. P. (2008): Wake Vortex Considerations in the Analysis of Recorded Data from the Upset to Flight AC190, Rept. LTR-FR-289, National Research Council Canada, Ottawa, Canada, p. 44.

[2] EASA European Aviation Safety Agency (2017): Safety Information Bulletin No. 2017-10, En-route Wake Turbulence Encounters, Köln, Germany.

[3] EUROCONTROL (2017): DDR2 Reference Manual for General Users, ed. 2.9.3, Brussels.

[4] ECMWF European Centre for Medium-Range Weather Forecasts (2015), ERA Interim, Daily, http://apps.ecmwf.int/datasets/data/interim-full-daily/levtype=ml/ (2015).

[5] Hoogstraten, M., et al. (2015): An improved understanding of en route wake-vortex encounters, Journal of Aircraft, Vol. 52, No. 3, pp. 981-989. doi: 10.2514/1.C032858.

[6] Holzäpfel, F. (2014): Effects of Environmental and Aircraft Parameters on Wake Vortex Behavior, Journal of Aircraft, Volume 51, Issue 5, pp. 1490-1500, doi: 10.2514/1.C032366.

[7] Holzäpfel, F. and Tchipev, N. (2013): Advanced Airborne Wake Vortex Prediction Model P2P[a], Model Design and Specification, Application, Verification, and Implementation Test Cases, SESAR P9.11, D2.2-1 / D2.2-2, 5.2.2013, 49 pages.

[8] Holzäpfel, F. (2003): Probabilistic Two-Phase Wake Vortex Decay and Transport Model, Journal of Aircraft, Vol. 40, No. 2, 2003, pp. 323–331.

[9] Lau A., Berling J., Koloschin A., Holzäpfel F., Linke F., Wicke K. (2018): Ground-based Wake Vortex Prediction in the En-route European Airspace, , AIAA Paper 2018-2879, AIAA Aviation Forum, Atlanta, GA, pp. 9.

[10] Lau A., Berling J., Linke F., Gollnick V., Nachtigall K. (2015): Large-Scale Network Slot Allocation with Dynamic Time Horizons, 11th USA/European Air Traffic Management Research and Development Seminar (ATM 2015), Lissabon, Portugal.

[11] Lau A., Budde R., Berling J., Gollnick V. (2014): The Network Flow Environment: Slot Allocation Model Evaluation with Convective Nowcasting, 29th Congress of the International Council of the Aeronautical Sciences (ICAS), St. Peterburg, Russia.

[12] Münster, C. and C. Schwarz (2010): Auswertung von Wirbelschleppenmeldungen im US Aviation Safety Reporting System (ASRS), Institutsbericht, IB 111-2010/33, Deutsches Zentrum für Luft- und Raumfahrt, Institut für Flugsystemtechnik, Braunschweig, p. 17.

[13] Nelson, R. C. (2006): Trailing vortex wake encounters at altitude - A potential flight safety issue?, AIAA Paper 2006-6268.

[14] Schättler U., Doms G., Schraff C. (2018): A Description of the Nonhydrostatic Regional COSMO-Model, Part VII: User`s Guide, www.cosmo-model.org (04/16/2018).

[15] Schumann, U. and R. Sharman (2015): Aircraft wake-vortex encounter analysis for upper levels, Journal of Aircraft, Vol. 52, No. 4, pp. 1277-1285. doi: 10.2514/1.C032909.

[16] Schwarz C. and Hahn K.-U. (2011): Simplified Hazard Area Prediction Method – SHAPe, Institutsbericht, IB 111-2011/31, Deutsches Zentrum für Luft- und Raumfahrt, Institut für Flugsystemtechnik, Braunschweig.

2.1 Concept Study of a Michelson-Interferometer-based UV Direct-Detection Doppler Wind Lidar for the Near-field, Range-resolved Characterization of Gusts, Turbulence and Wake Vortices

Jonas Herbst and Patrick S. Vrancken

Institute of Atmospheric Physics

In today's air transport, gusts, turbulence and wake vortices in clear air at all altitudes are met unexpectedly by the flight crew. These events engender increased fatigue of the material (like wing roots), decrease passengers' comfort and even may cause damage to the plane or injuries to the passengers and cabin crew. Current mitigation methods like separation rules or important safety margins in aircraft design are costly and inefficient.

Advanced mitigation by active alleviation of gusts, turbulence and wake vortices [Ehlers et al. 2015] demands a reliable onboard sensing system for the measurement of wind speeds in the near-field (50 – 200 m) ahead of the aircraft independent of atmospheric conditions. Today, a sensor system fulfilling the multitude of requirements is not available.

In this work, a concept for a near-field UV direct-detection Doppler Wind Lidar (DWL) sensor is presented. The forward-pointing sensor is part of a proposed full alleviation system which uses the reconstructed wind field for a fast reaction of the flight controller and subsequent action of the control surfaces of the aircraft [Fezans et al. 2015].

Fringe-imaging direct-detection DWLs work independently of the aerosol scattering ratio, which is an important design criterion for flights in cruising altitude [3, 4]. The Doppler signal (wind speed) is derived from determining the shift of the interferogram of the backscattered light. Ultraviolet light maximizes the backscattered Rayleigh signal. Field-widening is necessary for range-resolved detection in the near-field [Stelmaszczyk et al. 2005] where large étendues may be obtained. Two-wave interferometers like the fringe-imaging Michelson (FIMI) [Bruneau 2002] and Mach-Zehnder interferometer (FIMZ) [Cézard et al. 2009]] allow for field-widening [Hilliard and Shephard 1966].

In our work, a monolithic FIMI is designed with an inclination of the mirrors such that a single linear fringe is obtained. The linear fringe can be imaged on a fast linear detector, like a photomultiplier tube or avalanche photodiode array, what allows for range-resolved detection. Due to the monolithic design, together with temperature stabilization and fast referencing, the orientation and position of the fringe is thermo-mechanically stabilized in order to minimize possible biases.

An end-to-end lidar simulation is used to estimate the performance of the sensor. It considers the airborne WALES/DELICAT transmitter [9, 10], an ideal Michelson instrument function, a uniform and stabilized illumination, convolution with the backscattered spectrum, a sequential reference measurement, stochastic speckle light distributions, detector noise and solar background noise. Digital averaging is applied prior to the evaluation with a Downhill simplex fit [Nelder and Mead 1965] of a cosine-shaped fit function, in order to average both speckle distributions and detector noise. A range gate length of 20 m is assumed. At wind

speeds typical for gusts, standard deviations smaller than 1 m/s are obtained, independent of the atmospheric conditions at different measurement points within a distance of 50 – 130 m in front of the aircraft. Such a sensor may be a suitable candidate for an aimed full alleviation system.

1. Introduction

Currently, no airborne sensor system is available for the characterization of complex wind fields of turbulent structures in clear-air atmosphere. A reliable assessment of imminent turbulence encounters and mitigation of those events is thus impossible nowadays.

Wake Vortices, Gusts and Turbulences are characterized by inhomogeneous wind fields, which induce undesired aerodynamic forces on the aircraft structures. Unintended deviations from flight trajectory, fatigue of the materials, a reduction of passengers' comfort and an increased risk of injuries and damages of the aircraft are direct consequences. Onboard sensor systems require compactness, high reliability, stability, speed and local precision. These preconditions are most likely to be met by lidar [Vrancken 2016]. Wind speed components can be measured along the Line-of-Sight (LoS) of the laser beam with Doppler Wind Lidars (DWL). DWLs measure frequency changes of the light backscattered from scattering centers moving in the wind field. In order to measure the full wind field a scanning of the laser beam is necessary.

In this report we summarize the principle of our selected type of direct DWL [Herbst and Vrancken 2016], i.e. a fringe-imaging Michelson interferometer and estimate its performance using an end-to-end simulation.

Fig. 1 shows a simplified scheme of a system for online alleviation control of turbulent wind fields containing a DWL. This report was published in the context of the ONEAR-DLR Aerospace Symposium 2016.

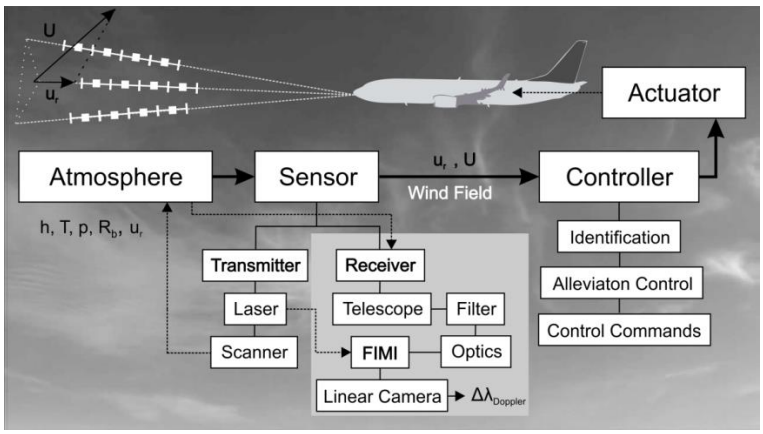

Figure 1: System for online alleviation control with FIMI lidar sensor concept (grey shaded box).

2. Lidar receiver principle and design

The sensor system contains the transmitter (laser) and a receiver to determine the 3D wind field. The reconstructed wind field information will be fed to a controller unit identifying turbulent structures such as wake vortices or gusts via special algorithms [1, 2] and routines in order to infer special alleviation control commands for moving aircraft control surfaces. It is essential for the reconstruction of the turbulent wind field from a reduced number of measurement regions, that wind speeds can be measured with low standard deviations [Ehlers et al. 2015], independent of the atmospheric conditions, i.e. altitude (h), temperature (T), pressure (p), density (ρ), and aerosol backscattering ratio ($R_b = (\beta_{Aer} + \beta_{Mol})/\beta_{Mol}$), and especially in clear air ($R_b = 1$).

Low standard deviations are however very challenging, because of the varying low signal strengths and coherence of the backscattered light, as well as the very short required maximum measurement time ($\lesssim$0.1 s). Furthermore bias can be induced by thermo-mechanical instabilities and laser beam pointing instabilities (about 0.4 m/s per µrad).

The standard deviations are thus determined by the transmitter properties and the type of receiver. A pulsed UV laser (355 nm) is used as transmitter due to the high level of Rayleigh scattering ($\beta_{Ray} \propto \lambda^{1/4}$). Also, eye-safe design is more straightforward than for visible wavelengths.

The grey box in Fig. 1 shows the receiver part. It consists of a telescope, a narrow sunlight background suppressing filter, optics, a fringe imaging Michelson interferometer and a linear detector array (camera). We describe in the following the working principle of DWL receivers.

DWL receivers can be classified into coherent and incoherent (direct). Coherent DWLs use infra-red (IR) light due to high backscattering from aerosols, whereby the Doppler shift is determined from the beat of the spectrally narrow aerosol-backscattered signal with a local oscillator reference. Coherent DWLs are a proven and accurate technology at low altitudes (ground to boundary layer), where the required coherence is given by sufficient aerosol concentration. However, coherent DWLs are not reliable in clear air and at high altitudes (during the long cruise phase of an aircraft), where the concentration of aerosols usually is very low [Vaughan et al. 1995].

This is why direct DWLs are considered in this work since both the spectrally narrow aerosol backscatter as well as the broad molecular (Rayleigh-Brillouin) backscatter may be spectrally analysed. Direct DWLs may consist of filters, which transmit only a certain spectral bandwidth. From the amount (ratio) of UV light which is transmitted through the filters the Doppler frequency shift can be determined (cf. Double Edge technique). In our case the filter is an interferometer used in fringe-imaging mode, i.e. its interference fringe is imaged on a position-sensitive detector. From the shift of the inference pattern the Doppler shift is determined. Such a setup was tested on an aircraft for the measurement of wind speeds in the EC FP5 AWIATOR project [Rabadan et al. 2010]. It used a multi-wave interferometer, a Fabry-Perot interferometer (FPI). Such an FPI, when properly illuminated, produces interference rings and the Doppler shift is determined from the change of the radii. This principle is however disadvantageous, because slow 2D detector arrays (e.g. CCD) have to be used, which makes this principle inappropriate for range-resolved measurements of wind

speeds, and because analysis is time consuming and prone to errors [Hirschberger and Ehret 2011].

Range–resolving, though, allows for collecting wind data in multiple distances in front of the aircraft along the line of sight of the laser beam, with the advantage that more wind field information can be acquired in short time.

Two-wave interferometers are better suited, because they can be built with a net inclination of the mirrors in the interferometer arms such that a single linear fringe is produced. Unlike for the Fizeau interferometer (also a multi-wave interferometer), a compensating plate can be inserted in one of the interferometer arms. This compensation stabilizes the instrumental interference contrast for angular distributed light (high etendue), which is a direct consequence of the large FOV of the telescope required for near-field, range-resolved detection, since total overlap [Stelmaszczyk et al. 2005] should be reached already at a close distance of ~50 m in order to maximize the signal. The linear, in amplitude cosine-shaped fringe can be imaged on fast linear array detectors (e.g. photomultipliers or photodiodes) suitable for range-resolved detection. The fringe shape (cosine) is independent of the atmospheric conditions, except for a change of the so-called atmospheric contrast, which decreases down to 66% for pure Rayleigh scattering (Rb = 1). This principle was proposed by [Bruneau 2002] considering a Mach-Zender interferometer, optimized for pure Rayleigh scattering. It was adopted for a Michelson interferometer and experimentally tested by [Cézard et al. 2009]].

We decided to use the fringe-imaging Michelson interferometer technique (FIMI), because it is considered easier to be realized in a monolithic way, which is necessary for thermo-mechanical stability of the fringe position and orientation under flight conditions. A nonpolarizing, cubic beamsplitter (30 x 30 mm) is optically contacted to a glass block with a mirror coated rear surface (glass arm). Fused silica glass is selected to minimize absorption. The other arm will consist of spacers holding the second, slightly inclined mirror (17.8 µrad). The length-ratio of the arms is matched to achieve a field-widening compensation [Hilliard and Shephard 1966] at a mean incident angle of 2 degrees. In this way the FIMI can be used in tilted configuration. This allows imaging both the transmitted and the reflected interference patterns on individual linear PMT-arrays. This method should increase the performance, because the otherwise wasted reflected light can be used for processing as well. The optical path difference (28 mm) between the arms is optimized for pure Rayleigh scattering. The mirrors are polished and coated with λ/20 precision to ensure a linear fringe. Anti-reflection coatings and high quality beam splitter coatings ensure a high instrumental contrast. The spacer material can be fabricated as a composite of fused silica and calcium fluoride to tune the linear expansion coefficient to minimize the temperature tuning rate, i.e. the shift of the fringe position with temperature. Additionally the interferometer will be mounted in a temperature stabilized container (± 10 mK/min) such that the estimated bias in Doppler wind speed measurement is around 0.02 m/s /s. Temperature stabilization is necessary for averaging over multiple transmitter pulses during a period of e.g. 0.1 s. Long-term stability will be guaranteed by fast referencing. A fiber is used to delay the reference light with respect to the received signal light. A combination of beam stabilization and fiber optical mode scrambling can be used to stabilize the far-field distribution illuminating the fringe-imaging

Michelson interferometer (FIMI). Optical mode scrambling may be improved with the help of a two-lens optical scrambler. Vibration of the fiber will be used to lower the speckle contrast of reference light and signal light backscattered by aerosols.

3. End-to-end simulations of Doppler wind lidar system

In a performed end-to-end simulation possible biases are assumed to be minimized. The illumination function is uniform and stable. The laser has the same properties as the WALES/DELICAT transmitter [Wirth et al. 2009, Vrancken et al. 2015], i.e. an energy per pulse of 80 mJ , a repetition rate of 100 Hz, and a pulse-to-pulse frequency jitter of 1 MHz in the UV during 60s. Moreover, an ideal Michelson instrument function with an instrumental contrast of 98% is considered and a perfect linear fringe is obtained. The instrument function is convolved with the Rayleigh-Mie spectrum of the backscattered Doppler shifted signal light, to obtain the signal interference fringe. An according reference fringe is simulated as well. A simulated wind speed of 10 m/s is set. The signal and reference light distributions are downsampled to the 12 pixels of the detector and stochastic speckle noise is added. The speckle patterns are modelled in a simplified way, as arrays of 48 x 48 pixels, where each array element obeys a gamma-type intensity distribution with a speckle contrast of 1 for reference light and a reduced speckle contrast for the partially coherent signal light. From the speckle patterns linear light distributions are calculated by integration in one dimension, and those light distributions are multiplied with the downsampled interference patterns for each pulse and range gate. Multiple range gates with a length of 20 m between 50 and 200 m are considered.

Fig. 2 shows a schematic aircraft travelling at a speed of 250 m/s with the transmitter beam pointing in one direction only (no scanning). The simulation also includes detector noise using standard equations for photomultiplier tubes (PMT), i.e. thermal noise current, shot noise of dark current and signal photocurrent, and solar background light current. The solar background radiation in the atmosphere is considered with 300 W/m².sr.µm. A field-of-view (FOV) of 4 mrad is supposed. The resolution of the analog-to-digital converter is assumed to be 14 quantization bits. The saturation level can be set to the expected maximum signal light current by adjustment of PMT gain. The reference photocurrent is set for optimum use of the quantization levels. The relative shift between the simulated signal and reference light distributions is determined with a “downhill simplex fit” (Nelder-Mead method) [Nelder and Mead 1965] without use of derivatives and converging very safely. The fit function is of the form:

$$f(w,x) = w_0 (1 + w_1 \cos(x + w_2)) + w_3 \qquad (1)$$

where w_0, w_1, w_2, and w_3 are the respective fit parameters for amplitude, contrast, shift and background. The Doppler shifts are obtained from w_2. In order to decrease the speckle contrast, detector noise and final standard deviation, the signal of a multitude of pulses is digitally averaged prior to the evaluation. For signal light ten pulses are averaged, for reference light 1000 pulses. Laser jitter is omitted because it has no influence on the results. 50 trials of the simulated measurement procedure are performed and the mean and standard deviation of the obtained LoS wind speeds are calculated. Simulations are carried out for two different atmospheric conditions: h = 10,000 m, R_b = 1, and h = 1,000 m, R_b = 6. Backscattering

coefficients are obtained from altitude dependent pressures and absolute temperatures obtained from an atmospheric model after Collis and Russel [Collis and Russel 1976]. The signal of h = 1,000 m, R_b = 6 is damped in order to obtain the same signal intensities as in case of h = 10,000 m, R_b = 1. The resulting standard deviations of the simulated Doppler wind measurement are plotted as a function of range in Fig. 2.

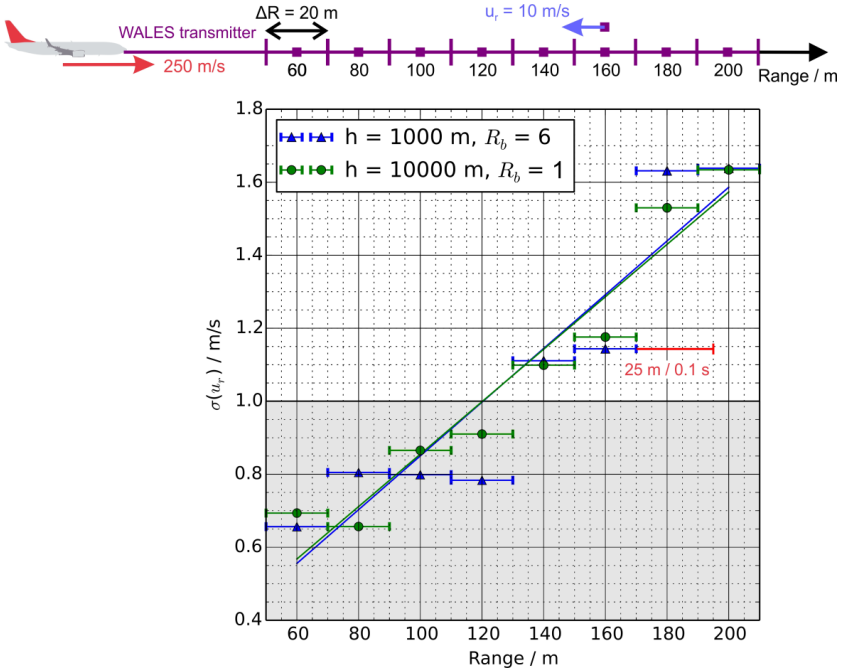

Figure 2: Results of the End-to end simulation with the WALES transmitter: Standard deviation of the determined wind speed for 50 trials as a function of range. For each trial ten pulses are digitally averaged during a time of 0.1 s. During this time the aircraft covers a distance of 25 m.

The mean values converge to the simulated wind speed of 10 m/s. A linear trend of increasing standard deviation with range is observed, in line with expectations. The different atmospheric conditions do not show to have any effect on the result, i.e. no effect of atmospheric contrast is apparent. The speckles of the reference light are efficiently averaged. Standard deviations below 1 m/s are obtained in a distance of 50 – 120 m.

The signal strength seems to be the dominant factor of influence. Signal averaging during 0.1 s further blurs the measurement volume. We assume that in tilted configuration (offering two measurement channels, i.e.) the FIMI will allow for shorter digital averaging times. These standard deviations are small enough for wake vortex mitigation algorithms as proposed by Ehlers et al. [Fezans et al. 2015] to work.

However, Ehlers et al. [Ehlers et al. 2015] considered different scanning geometries with at least three vertical and three horizontal scanning directions and one measurement point (MP) at 60 m with up to five MPs along the laser beam for wakes. Fezans et al. [Fezans et al. 2015] consider the scanning geometry with just 3 x 3 x 1 MPs and a scan field-of-view of +/-10° in vertical and +/-16° in lateral direction to be too sensitive to the encounter geometry and

insufficiently robust. The authors show that their Online Wake Identification (OWI) algorithm performs better at smaller range gate lengths (e.g. 15 m) than at longer blur depths of 30 m [Ehlers et al. 2015]. The high number of scanning directions requires high update rates and short digital averaging times. The authors considered an update rate of 10 Hz for 9 points [Fezans et al. 2015]. With the here described system we expect an update rate of 10 Hz for up to 8 MPs along one direction, however only 4 MPs fulfill the requirement of $\sigma(ur) < 1$ m/s. In order to obtain a wind vector at least three scanning directions would be necessary. This would give an update rate of 3.3 Hz (optimistic 6.6 Hz for the tilted configuration of the FIMI) at the most for 12 (overlapping) MPs in a scanning triangle as shown in Fig. 1. The authors have not yet checked the robustness of their algorithms for such a low number of scanning directions, which will be interesting to note. It should also be checked, whether higher standard deviations (> 1 m/s) are tolerable, especially in the case of gusts and turbulence [Fezans et al. 2015].

4. Conclusion

To conclude we have described a receiver system suitable for an online alleviation control system. A (tilted) fringe-imaging field-widened Michelson interferometer is likely to reach the maximum performance (standard deviations and update rates) achievable with current transmitter and detector technology, for measurements of wind speeds in the near-field in front of an aircraft. Range-resolved measurements, made possible by field-widening and linear fringes, which can be evaluated with current linear PMT-array technology, would be a major improvement. Low standard deviations below 1 m/s of the end-to-end simulation in the near-field of 50 – 120 m independent of the atmospheric conditions suggest that the principle is valuable. A monolithic, temperature-stabilized design together with optical fiber scrambling and speckle reduction is expected to limit the biases to a minimum. The challenges of range-dependence of signal strengths as well as speckle and detector noise implying relatively long digital averaging times remain.

References

J. Ehlers, D. Fischenberg, and D. Niedermeier, “Wake impact alleviation control based on wake identification,” Journal of Aircraft pp. 1–13 (2015).

N. Fezans, J. Schwithal, and D. Fischenberg, “In-flight remote sensing and characterization of gusts, turbulence, and wake vortices,” Presented at the Deutscher Luft- und Raumfahrtkongress, Rostock, Germany, 22 - 24 September. (2015)

G. J. Rabadan, N. P. Schmitt, T. Pistner, and W. Rehm, “Airborne lidar for automatic feedforward control of turbulent in-flight phenomena,” Journal of Aircraft 47, 392–403 (2010).

M. C. Hirschberger and G. Ehret, “Simulation and high-precision wavelength determination ofnoisy2d fabry–pérot interferometric rings for direct-detection dopplerlidar and laser spectroscopy,” Applied Physics B 103, 207–222 (2011).

K. Stelmaszczyk, M. Dell’Aglio, S. Chudzy´ nski, T. Stacewicz, and L. Wöste, “Analytical function for lidar geometrical compression formfactor calculations,” Applied Optics 44, 1323–1331 (2005).

D. Bruneau, “Fringe-imaging mach-zehnder interferometer as a spectral analyzer for molecular doppler wind lidar,” Applied Optics 41, 503–510 (2002).

N. Cézard, A. Dolfi-Bouteyre, J.-P. Huignard, and P. H. Flamant, “Performance evaluation of a dual fringe-imaging Michelson interferometer for air parameter measurements with a 355 nm rayleigh-mie lidar,” Applied Optics 48, 2321–2332 (2009).

R. L. Hilliard and G. G. Shepherd, “Wide-angle Michelson interferometer for measuring Doppler line widths,” Journal of the Optical Society of America 56, 362–369 (1966).

M. Wirth, A. Fix, P. Mahnke, H. Schwarzer, F. Schrandt, and G. Ehret, “The airborne multi-wavelength water vapor differential absorption lidar wales: system design and performance,” Applied Physics B 96, 201– 213 (2009).

P. Vrancken, M.Wirth, G. Ehret, B. Witschas, H. Veerman, R. Tump, H. Barny, P. Rondeau, A. Dolfi-Bouteyre, L. Lombard, “Flight Tests of the DELICAT Airborne LIDAR System for Remote Clear Air Turbulence Detection,” In 27th International Laser Radar Conference (ILRC), New York City, USA (2015).

J. A. Nelder and R. Mead, “A simplex method for function minimization,” The Computer Journal 7, 308–313 (1965).

P.S. Vrancken, “Airborne remote detection of turbulence with forward-pointing LIDAR,” In: Sharman, R., Lane, T. (Eds.) Aviation Turbulence - Processes, Detection, Prediction, Springer, doi: 10.1007/978-3-319-23630-8 (2016).

J. Herbst, P. Vrancken, “Design of a Monolithic Michelson interferometer for Fringe-Imaging in a Near-Field, UV, Direct Detection Doppler Wind Lidar,” Applied Optics, submitted (2016).

J.M. Vaughan, D.W. Brown, C. Nash, S.B. Alejandro, G.G. Koenig, “Atlantic atmospheric aerosol studies: 2. Compendium of airborne backscatter measurements at 10.6 μm. Journal of Geophysical Research: Atmospheres, 100(D1), 1043-1065 (1995).

R. T. H. Collis and P. B. Russell, “Lidar measurement of particles and gases by elastic backscattering and differential absorption,” in “Laser Monitoring of the Atmosphere,” , Vol. 14 of Topics in Applied Physics, E. D. Hinkley, ed. (Springer Berlin Heidelberg, 1976), pp. 71–151.

2.2 Performance of on-board wake vortex prediction systems employing various meteorological data sources

Ingo Sölch[1], Frank Holzäpfel[1], F. Abdelmoula[2], Dennis Vechtel[2]

[1] *Institute of Atmospheric Physics*, [2] *Institute of Flight Systems*

In this work the accuracy of wake vortex predictions of DLR's Wake Encounter Avoidance and Advisory System (WEAA) is analyzed by means of data gathered from a flight test campaign in April 2014. The system is based on airborne data exchange between aircraft and allows pilots to avoid potentially dangerous wake vortex encounters. As the vortex evolution is strongly controlled by atmospheric parameters, the acquisition of meteorological data is crucial for WEAA. The accuracy of the wake vortex predictions is investigated, employing first the current Automatic Dependent Surveillance (ADS-B) standard, which is then extended by additional meteorological data transmitted via telemetry, or data from numerical weather predictions.

1. Introduction

Currently air traffic is foreseen to grow in the near future, leading to an increased demand on capacity in air space (EUROCONTROL, 2004). To enable a high throughput in the terminal manoeuvering area near airports, but also en-route, novel air traffic management procedures are investigated for example in the new SESAR 2020 project (SESAR, 2012). There, a self-separation of air traffic is envisaged, accompanied by a delegation of responsibility to the flight crew. This additional work load might only be addressed by pilots, if they are guided by advanced safety tools. The minimum separation distances between aircraft are also likely to be reduced in near future in order to further increase air space capacity (Treve & Rooseleer, 13 May 2014). Among other factors this contributes to a potential increase of the risk of hazardous wake encounters in the future. Therefore, a wake vortex encounter warning system, as one of the mentioned safety tools, may become necessary to alleviate this emerging risk.

Recently, a prototype of such a system, the DLR Wake Encounter Avoidance and Advisory system (WEAA), was successfully demonstrated in flight trials onboard the DLR research aircraft A320 ATRA (Advanced Technologies Research Aircraft) and with DLR's Falcon 20 as wake generator. The system is not intended to directly influence the spacing between aircraft, but increases the situational awareness of the flight crew and suggests small tactical avoidance maneuvers. To enable a robust prediction of the evolution and trajectories of the wake vortices, atmospheric parameters, e.g. wind speed or stratification, have to be known as precisely as possible.

Currently, the use of high-resolution weather data in flight deck management systems and applications is limited. Position and state data of nearby aircraft and atmospheric parameters are available via an air-to-air data link as defined in the automatic dependent surveillance (ADS-B) standard. However, meteorological measurement data is usually not broadcast, although the data is available. Such information is downlinked by the aircraft meteorological data relay (AMDAR) from selected aircraft (Painting, 2003) to improve the number of observations used for data assimilation into numerical weather prediction models. By using aircraft-transponder data the number of AMDAR-type information could be enhanced to obtain wind and temperature information (Mode-S) (de Haan, 2011). However, these approaches are not applicable for airborne wake prediction relying on frequently updated meteorological estimates at the locations of aircraft on close trajectories. Some approaches exist using ADS-B information of multiple aircraft to estimate wind, temperature and pressure (de Leege et al., 2013). However, the algorithms are mainly applicable in spatially limited areas around airports. Recently, a method has been patented to derive the horizontal wind vector with increased accuracy from the data broadcasted via ADS-B (Holzäpfel, 2013).

Meteorological forecasts of state-of-the-art numerical weather prediction (NWP) models are also used by controllers at the ground for the greater part. For airborne applications, Troxel & Reynolds (2015) used NWP forecasts to study the feasibility of NextGen navigation procedures such as 4D-Trajectory Based Operations which are highly dependent on high-accuracy wind data. They found considerable

spread in the error distributions of NWP wind forecasts. At any single time or location, forecast errors may be considerably larger than the aggregate mean. Thus, the attributed error tolerance of each procedure or system has to be monitored carefully, to be applicable. Emerging ensemble prediction methods may assist the systems, by providing flow-dependent error covariance estimates (Houtekamer & Mitchell, 1998; Harnisch & Keil, 2015). Lee et al. (2009) used a time-lagged ensemble to account for the uncertainty in wind forecast for aircraft trajectory predictions. Recently, high-resolution wind grids are uplinked to aircraft, to enhance on-board flight management system predictions, such as time and fuel estimates (Bienert & Fricke, 2013; AVTECH Sweden AB, 2012).
The purpose of this work is twofold: firstly, the performance of the WEAA system for the flight campaign in 2014 shall be thoroughly investigated in its existing setup. Secondly, the role of additional meteorological input data sources on the performance and accuracy of the wake predictions shall be analyzed.

Starting from that input data, which is already transmitted via ADS-B nowadays, we systematically add or modify the meteorological data sources, to highlight possibilities and benefits for on-board wake predictions. This includes additional aircraft derived measurement data, which is already available but not yet transmitted operationally. The fusion of data from different aircraft may enhance the prediction accuracy. de Jong et al. (2014) demonstrated the benefit of wind-profile estimation using airborne sensors for continuous-descent operations. We will extend the analysis from pure measurement-based data to NWP forecasts, interpolated to the actual aircraft trajectory. We want to encourage the ongoing attempts, to extend the ADS-B standard (RTCA WP-YY Prepared by: WVTT) or to use additional numerical weather prediction output, driven by the perception that this may be valuable for novel airborne but also for ground-based safety tools.
In Section 2 the WEAA system will be introduced together with the field campaign in April 2014. Different sources of meteorological input used in this study and evaluation methods for wake prediction using flight data are introduced in Section 3. Results of the WEAA system with different input data types are presented in Section 4. Sources of error and sensitivity analysis of the system are discussed in Section 5. Section 6 summarises the results and implications for future development and tests of the system.

2. The WEAA system and the wake vortex encounter flight tests

The wake encounter avoidance and advisory system (WEAA) is currently developed at DLR in collaboration of Airbus, developed from previous work on wake vortex prediction tools. This section gives a brief introduction to the WEAA system and its functionality, followed by a short description of a flight test campaign conducted in April 2014 for demonstration of the wake prediction and conflict detection algorithms. The data gathered during these flight tests are used for the analysis of the system's performance presented here.

2.1. Wake encounter avoidance and advisory system

The intended purpose of the system is a light-weight application, running on board an aircraft, which should predict imminent encounters with wake vortices of other nearby aircraft, warn the pilot and, if possible, guide him through an evasive maneuver. Currently WEAA does not utilize any wake detection equipment, such as LiDAR instrumentation. The wake prediction is based on a probabilistic wake prediction model that estimates the current and future positions of wake vortices from surrounding aircraft. Based on traffic data, meteorological data and sensor data, such as inertial reference and air data, the wake habitation volume is calculated. For these wakes a severity assessment and a conflict detection between the wake volume and the own flight path is performed. Once a conflict is predicted, the conflict resolution algorithm calculates, if possible, an evasive trajectory, which is free of any conflict with the wake, other traffic or terrain. The aircraft performance and navigational limitations are taken into account in theses calculations. The wake is displayed to the pilot (at least on the navigational display) and the evasive trajectory is fed into the flight guidance system or the autopilot. In the current development phase the traffic prediction, the wake prediction and the conflict detection as well as the cockpit display have been realised and tested successfully in flight (see section 2.2.). In further development phases, WEAA will be expanded by a wake avoidance functionality, i.e. evasive trajectories will be generated, which shall lead the aircraft around the predicted wake hazard volumes. As the evasive maneuvers should consume as little airspace as possible, they need to be small-scale. Hence, the prediction of the

wake habitation volumes needs to be as accurate as possible. The accuracy of the prediction strongly depends on the accuracy of the required input data, which is based on aeronautical and meteorological measurements of the own aircraft, and/or transmitted via ADS-B from other aircraft (Bauer et al., 2014). Figure 1 illustrates the working principle of the wake prediction functionality of the system. The actual wake predictions are performed by the airborne version of the P2P model (Holzäpfel, 2003) termed P2P^a. P2P^a is a real-time capable probabilistic two-phase wake vortex prediction model. The real-time capability is required, because wake evolutions are continuously calculated with a temporal resolution of 1 second along the actual flight path and a prediction horizon of 120 seconds along the intended flight track. P2P^a accounts for the effects of wind, wind shear, turbulence, stable thermal stratification, and ground proximity. The model equations are based on the analytical description of the decaying potential vortex and have been adapted to large eddy simulation results and field measurement data (Holzäpfel, 2006). Due to the turbulent nature of the atmosphere no deterministic forecast of the wake is performed but a probabilistic one that considers the uncertainties of the input parameters. The probabilistic model design distinguishes between the parameters that can be directly modelled by propagation of uncertainty and parameters that are considered via multiple solutions of the non-linear model equations employing different combinations of input parameters and model constants. This results in ellipses at each prediction gate in which the vortex pair resides with a specified certainty level. In addition to the vortex position also the remaining strength of the vortices in terms of a circulation is calculated. In future application a multi-model ensemble for wake vortex predictions could be used to capture the model uncertainty of wake vortex decay and increase the prediction accuracy compared to a single model forecast (Körner et al., 2015).

As wake vortex behavior is dominantly controlled by atmospheric influences, the acquisition of meteorological data is crucial for WEAA. For the prediction of the wake of an aircraft, P2P^a needs the actual aircraft mass M, heading Ψ, true airspeed TAS, position $\mathbf{x}$, span width b, and the bank and flight path angles of the wake generating aircraft. As meteorological input wind speed v and direction α, temperature T, eddy dissipation rate ϵ, and static air pressure p, as well as linear gradients of temperature $\frac{\partial T}{\partial z}$, wind speed $\frac{\partial v}{\partial z}$, and wind direction $\frac{\partial \alpha}{\partial z}$ at the wake prediction positions are required. The input data has to be provided in terms of a mean value and standard deviation, which are translated into uncertainty envelopes of the wake predictions by P2P^a. In general, the lateral displacement of the wake is mainly controlled by the wind drift and to a lesser extent by the change in wind speed and direction during the descent of the vortex. The descent in turn is controlled initially by the vortex strength and the separation distance of the vortex pair, and later on, by the temperature gradient and turbulence, i.e. the eddy dissipation rate, which will weaken the circulation of the vortex until final decay (Greene, 1986).

2.2. Wake vortex encounter flights April 2014

For demonstration and evaluation of the already existing system components under operational conditions, flight tests were conducted with the DLR research aircraft A320 ATRA (Advanced technologies research aircraft, A320) and the DLR Falcon 20 during three days in April 2014. The Falcon acted as a wake generating aircraft, while the ATRA tried to hit the wake of the Falcon intentionally in order to verify the position of the wake vortices predicted by the WEAA system, which was operated on board the ATRA. The Falcon was chosen as generating aircraft because it is sufficiently small to generate relatively weak vortices, which do not pose threat to the vastly heavier ATRA. An extra telemetry link was operated between the two aircraft to substitute and simulate an ADS-B like transmission of aeronautical and measurement data, because the Falcon was not equipped with an ADS-B transmitter at that time. On board the ATRA, the received data were converted to mimic the ADS-B protocol format. This way the WEAA system does not recognize any differences between data coming from telemetry receiver or from ADS-B. Furthermore, the telemetry link gave the opportunity to transfer additional data, which was currently not transmitted via ADS-B, such as wind information. All required data on the own aircraft are registered and stored with a frequency of 50 Hz and the Falcon data with 1 Hz. This way the accuracy of the WEAA predictions can be investigated a posteriori with different input data sets or sources of varying accuracy based on the collected data. The WEAA predictions were transferred to an experimentally installed human-machine interface in the cockpit of ATRA. Upcoming conflicts on the ATRA flight path with the Falcon wake were detected and displayed to inform the pilots.

To hit the wake vortices intentionally they need to be visible. Therefore, persistent contrails were

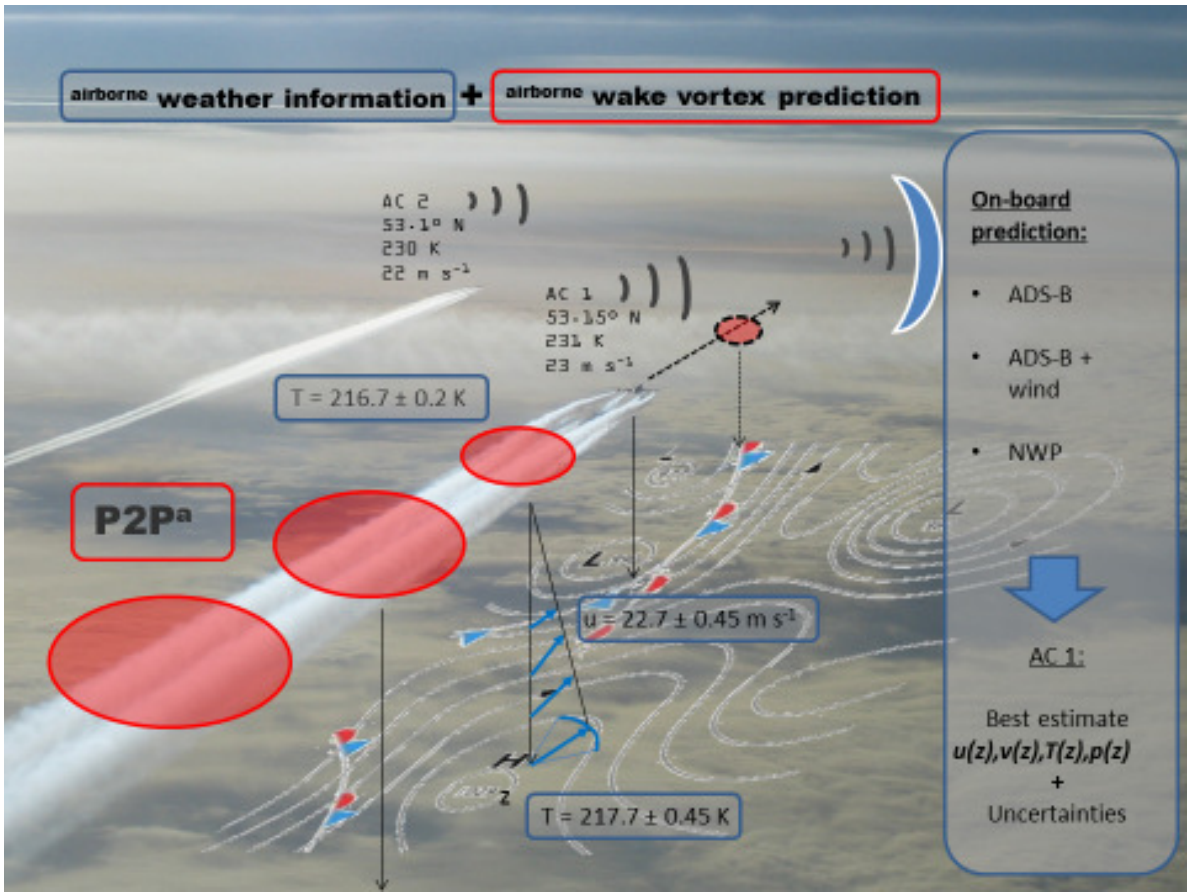

Figure 1: Graphical illustration of the onboard WEAA system from the perspective of the own aircraft. Two other aircraft AC1 and AC2 are flying in the vicinity and transmit aeronautical and meteorological information (i.e. via ADS-B) to the own ship. Based on this data or other sources of meteorological input (ADS-B+, and NWP), a mean atmospheric state and related uncertainties at the position of AC 1 and AC 2 are deduced, which are required for the onboard probabilistic wake vortex predictions. Those are performed at distinct way points on the actual and future trajectory (dashed arrow) of the wake generating aircraft by the P2P^a model. The model calculates mean positon $\mathbf{x_p}$ and elliptical uncertainty envelopes with horizontal semi-axis a and vertical semi-axis b for the habitation volumes of the vortex pair. Thus, at every output time step a complete picture of the trailing wake volume of an aircraft and its remaining strength is available. Picture taken by T. Jurkat during the CONCERT campaign 2008 (Voigt et al., 2010).

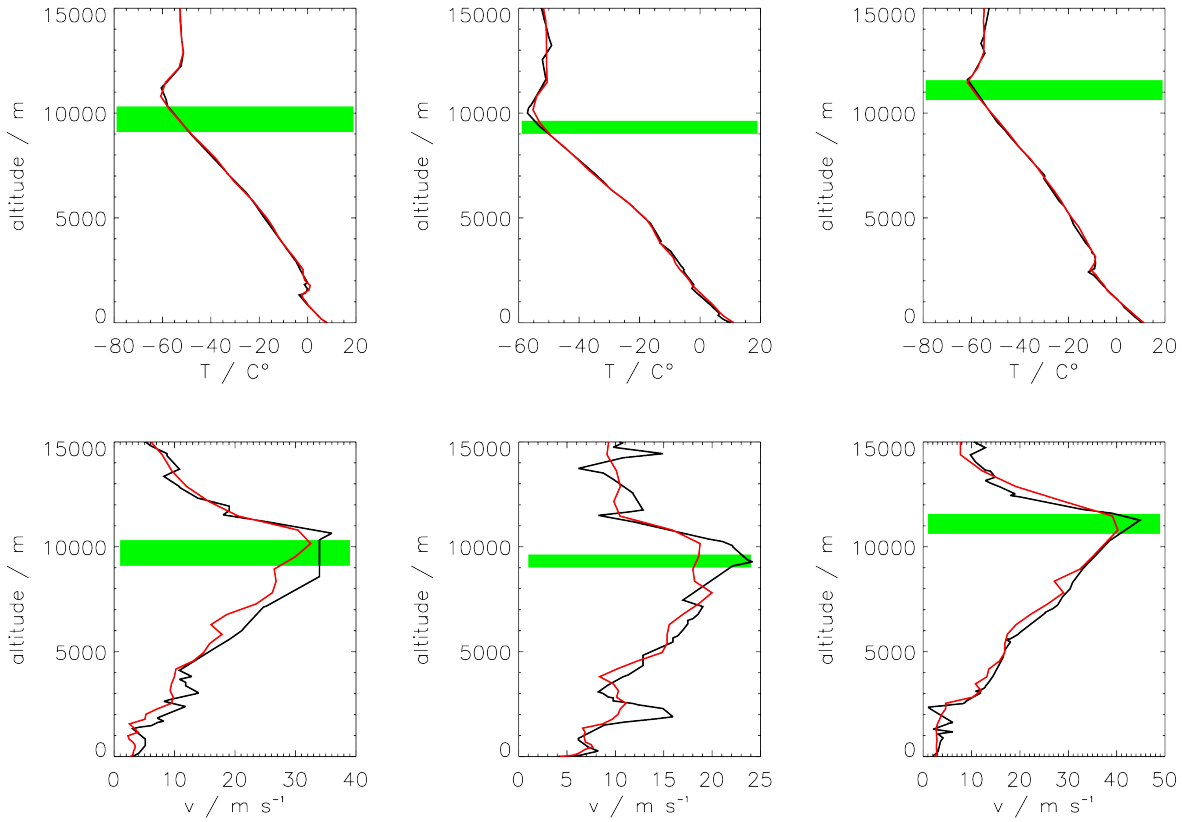

Figure 2: Vertical soundings of temperature (a-c) and wind speed (d-f) on 10th (a,d), 11th (b,e), and 16th (c,f) of April 2014 from operational 12 UTC radiosonde launches from Greifswald station (lat=54.10 °N, lon=13.40 °E) (solid lines). Additionally the corresponding vertical profiles of the 3 h COSMO-DE forecast starting at 09 UTC for 10th and 16th, and the 6 h forecast starting at 06 UTC for the 11th of April, respectively are shown (red solid line). The height range in which encounters were detected on the given date is also indicated (green area).

required for the flight test, acting as visible markers of the approximate vortex locations. However, the exact position of the wake vortex pair does not necessarily match with all visible parts of the contrail, because also in the secondary wake at the initial flight height a visible contrail may exist and may even dominate for weak contrails (Unterstrasser, 2014). During the flights different maneuvers were performed in order to hit the wake at varying distances behind the Falcon. By flying ATRA in trail of the Falcon the accuracy of the wake prediction could be verified. For verification of the conflict detection this method was not useful. For this the ATRA hit the wake of the Falcon at larger angles with more straight flight paths some minutes in advance for both aircraft. This way, the prediction accuracy of the conflict detection could be verified very well, and it showed a timely prediction accuracy of below one second, even if the encounter was more than one minute ahead.

Figure 2 shows vertical soundings of the atmosphere for temperature and wind speed from the nearby radiosonde station in Greifswald for all three campaign days on the 10th, 11th, and 16th of April. On the 10th and 16th the cold point tropopause (temperature minimum) is at a height of around 11 km accompanied by a strong jet (up to 45 m s^{-1}) with northerly wind direction right below. On 11th of April a weak frontal passage has been observed with a drop in tropopause height to 10 km and reduced wind speeds of 25 m s^{-1} now from westerly directions. All encounters were reported in regions slightly below the indicated tropopause height, except for 16th of April, where the aircraft may have entered the stratosphere with the typical reversal of the temperature gradient. Table I lists mean values of aeronautical and meteorological parameters met during the actual encounter situations on each day.

Table I: Mean values of aeronautical parameters, atmospheric parameters, and resulting wake properties for the encounters on each individual campaign day. These are true air speed and mass of the Falcon, and cross wind in the aircraft frame of reference v_{cross}, temperature, static air pressure, temperature gradient , and base 10 logarithm of the eddy dissipation rate (in units of m^2 s^{-3}), respectively. The latter two atmospheric parameters are derived from the COSMO model output, all others are Falcon measurements. On each day N_{enc} encounters are reported. Here, Δy and Δz_m represent the lateral and vertical displacement of the reported vortex position from the location where it was generated, respectively. Δz_p is a predicted mean by P2P^a with corresponding simulated vortex ages T_a. Note that there might be considerable fluctuations among individual parameters from encounter to encounter.

Day	10/04/2014	11/04/2014	16/04/2014
TAS [m s^{-1}]	200.5	202.1	198.6
M [kg]	11618	11004	11559
v_{cross}, [m s^{-1}]	25.87	22.78	37.91
T, [K]	219.3	220.2	215.0
p, [hPa]	265.2	279.5	224.2
$\frac{\partial T}{\partial z}$, [K m^{-1}]	-0.00666	-0.00568	-0.00475
$\log(\epsilon)$	-4.69	-4.44	-4.17
N_{enc}	18	12	14
Δy, [m]	899	901	1487
Δz_m, [m]	35.1	57.2	68.9
Δz_p, [m]	41.3	38.5	52.9
T_a [s]	34.8	39.1	39.2

Between 12 and 18 encounters were flown in a time frame between 60 and 90 minutes. On the 16th of April the strongest cross wind speeds prevailed and led to lateral displacements of the Falcon wake of 1500 m on average during its descent. The mean age of these vortices was $T_a \approx 35$ s, when ATRA hit the wake (T_a is derived from the P2P^a output). Even the rather strong prevailing wind speeds did not degrade the mentioned prediction accuracy of the conflict detection.

3. Methodology

In the standard setup of the WEAA system, which was used in the flight trials, the $^{am+}$fusion algorithm is operated, to estimate the atmospheric input parameters. It has been developed at DLR under subcontract to Airbus and skillfully fuses both the information of the own and the Falcon transmitted measurements. Since it is an on-board system, all information has to be accessible on board the own aircraft.

3.1. Sources of meteorological input

To systematically study the influence of the quality and source of meteorological input data on the performance of the on-board wake vortex predictions, we extend the system a posteriori by three additional algorithms, which generate the input data. They increase in their degree of complexity or amount of additional data required. Starting from the most simple setup then the algorithms considered line up as follows

- ADS-B (**A0**): only aeronautical information from telemetry is used. The meteorological parameters have to be deduce either from measurements of the own aircraft or climatological knowledge.
- ADS-B+ (**A1**): besides the aeronautical information, now, additional meteorological data is taken from the telemetry transmission. In addition to the standard protocol, we assume that wind speed information and temperature is transmitted from the Falcon.
- $^{am+}$fusion (**A2**): built on the ADS-B+ standard, $^{am+}$fusion is a state-of-the-art algorithm to perform a best guess of the meteorological input data by a statistical approach.

Table II: List of the data sources for the algorithms considered for aeronautical information AI, temperature T, wind speed and direction, eddy dissipation rate ϵ, and linear temperature, wind speed and wind direction gradients. The sources are: transmission via telemetry from Falcon based on today's standard (ADS-B), additional transmission of wind data and temperature from telemetry (ADS-B+), measurement from the own on-board sensors (ATRA), a combination of own data and telemetry data from the Falcon ($^{am+}$fusion), climatologically derived information (Clim), and the use of data from numerical weather prediction forecasts (NWP).

Algorithm	*AI*	*T*	*wind*	ϵ	*gradients*
A0	ADS-B	ATRA	ATRA	ATRA	Clim
A1	ADS-B	ADS-B	ADS-B+	ATRA	Clim
A2	ADS-B	$^{am+}$fusion	$^{am+}$fusion	ATRA	$^{am+}$fusion
A3	ADS-B	NWP	NWP	NWP	NWP

- NWP (**A3**): if the latest data from a numerical weather prediction model before take-off were available, the atmospheric parameters may be interpolated to the position of the wake generating aircraft in space and time.

Table II lists the different algorithms and the sources used, to quantify the various input parameters for the wake prediction in the extended WEAA versions in this work.

In all measurement-based algorithms the eddy dissipation rate ϵ, is deduced from structure functions based on the high frequency wind speed measurements of ATRA according to Meischner et al. (2001). Vertical gradients of temperature and wind cannot be inferred from line measurements of a single aircraft during cruise. Without additional data from other aircraft, those are based on climatological mean profiles in **A0** and **A1**. For temperature such a climatology is based on data from Gettelman et al. (2011) and Hoinka (1998). A threshold pressure level is used to distinguish between tropospheric and stratospheric conditions as a function of latitude. No seasonal dependence is considered here. Data sets for the gradients in wind speed and wind direction are presented in Houchi et al. (2010). Due to the high natural variability in the gradients, sufficiently large uncertainty ranges have to be attributed to the climatological mean values.

3.1.1. ***A0*** *- ADS-B*

This is the simplest algorithm under consideration. Concerning the meteorological information, it may easily be operated with data available on board an aircraft today. Only the aeronautical information is required from the other aircraft, the Falcon in our case. The WEAA system predicts wake vortices generated by aircraft, which are in close vicinity of the own aircraft. Therefore, it may suffice to deduce the atmospheric parameters from the own measurement data and extrapolate them to the position of the Falcon. Gradients are based on climatologically prescribed values. Derived wind speed and direction and the eddy dissipation rate are kept unchanged, while temperature and pressure are adopted according to the vertical displacement by the assumed temperature gradient and the barometric formula, respectively. Because the measurement data is available at a high frequency from the on-board sensors of the own aircraft (50 Hz), the data may be averaged (1 s interval), which allows to reduce the uncertainty due to the measurement noise. The errors attributed to a single measurement are given in Table III with values based on Schwartz & Benjamin (1995) and Drüe et al. (2008). An additional representativeness error, due to the horizontal displacement between the position of the Falcon and the location of the ATRA measurement, is attributed. Its size is based on classical turbulence theory via the structure functions, deduced from the own wind speed and temperature measurements.

3.1.2. ***A1*** *- ADS-B+*

In the extended ADS-B+ format we assume that the additionally transmitted temperature and wind data from the Falcon aircraft by telemetry were part of the ADS-B protocol. Then, only eddy dissipation rate has to be derived from the own high-frequency measurements. All other input parameters may be

Table III: Errors (1σ values) attributed to the direct sources of meteorological data for west-east wind component u, south-north wind component v, static air temperature T, and static pressure p. The values reflect the sensor errors attributed to an aircraft derived measurement (AC) or the interpolated COSMO-DE model output.

error	*AC*	*NWP*
u, v	2 m s^{-1}	1.5 m s^{-1}
T	1 K	1 K
p	30 Pa	100 Pa

taken directly from the Falcon measurement data received via telemetry with the attributed measurement accuracy. Gradients are again based on the climatology.

3.1.3. ***A2*** - $^{am+}$*fusion*

Now, both, the own measurement data and the data received via telemetry from other aircraft is used to estimate the atmospheric state at the position of the wake generating aircraft. $^{am+}$fusion is the standard algorithm in use for the WEAA and was operated in the flight trials. It fuses the data sources of Falcon (ADS-B+) and ATRA, to provide a best estimate of the required meteorological data, including their vertical gradients. The actual uncertainty levels for the meteorological variables are statistically estimated with the actual measurement accuracy considered as given in Table III.

3.1.4. ***A3*** - *NWP*

This algorithm differs significantly from the previous ones, because solely data from a numerical weather prediction model is used. This implies that either the required four-dimensional field of the model output has to be uploaded before take-off and stored on board the aircraft, if the system should remain autonomous, otherwise a bi-directional air-ground data link has to be established. It may suffice to upload wind, temperature, and turbulence fields in a corridor along the requested flight trajectory.
In this study weather prediction data is taken from the operational runs of the COSMO-DE of the Deutscher Wetterdienst (DWD). COSMO-DE is a regional, non-hydrostatic, convection permitting model with the highest resolution in the operational forecast chain of DWD. It has a horizontal grid spacing of approximately 2.8 km on 50 vertical levels (Baldauf et al., 2011). Model runs are updated every 3 hours with 21-hour forecasts and output is available in an hourly interval. Here, we use the most recent forecast run, which is available before ATRA's take-off. Wind, temperature, pressure and also vertical gradients of temperature, wind and eddy dissipation rate may then be spatially interpolated to the Falcon positions along its flight track. Every hour the according model fields are updated with the new weather prediction data, but no temporal interpolation between two consecutive forecast hours is performed.
Figure 2 shows vertical profiles of wind speed and temperature of the corresponding model data, compared to the radiosonde data at Greifswald station. In general the agreement between the observed and predicted temperature profiles seems very satisfactory. The general structure of the temperature and wind profiles, especially the position of the tropopause and the jets right below are well predicted. For the height range, where the encounters have been detected, the largest deviations are present on the 11th of April. These and also smaller scale discrepancies may be explained by forecast errors, but also by small scale atmospheric fluctuations, which are not resolved in the numerical model.
The attributed accuracy of the forecast model is given in Table III with error assumptions for the COSMO-DE model from Schraff et al. (2015).

4. Results

4.1. Validation of predictions with measured encounter data

To assess the quality of the wake predictions by the WEAA system, and by that, the quality of the different meteorological input sources, we will use the reported encounter data from the flight campaign. Figure 3 shows an example of an encounter situation for 11th of April. The displayed wake volume

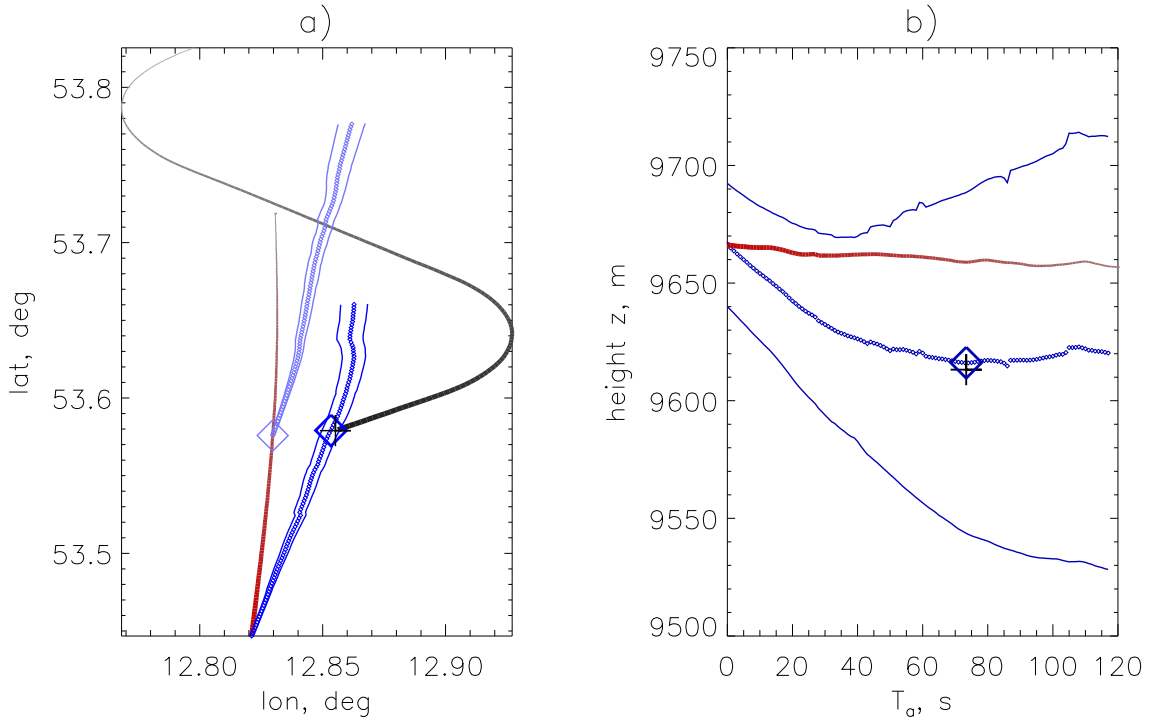

Figure 3: Spatio-temporal plot of the horizontal (a) and vertical (b) flight tracks, predicted wake volumes and detected wake encounter position of a single encounter on 11th April. In the horizontal plot the trajectories of the Falcon (red) and ATRA (black) are depicted. To illustrate their temporal evolution, they are displayed up to 150 seconds in the past, increasing in color and width until the actual time t_{enc} of the reported encounter (black plus sign). For the actual interpolated wake volume predictions (dark blue) the mean position and the 99 % confidence intervals are shown and the wake element closest to the reported encounter position is marked (dark blue diamond). This wake vortex was generated earlier by the Falcon on the trajectory (light blue diamond) with an attributed trailing wake at that time (light blue). The observed drift of the wake element due to the wind is, therefore, about 1600 m to the east. Similarly, the wake of the Falcon is shown in the vertical plot with mean position (dotted blue) and the extension of the 99 % ellipses (solid blue) at t_{enc} and the time evolution of the Falcon trajectory is illustrated in its temporal evolution. Here, the height of the wake elements are plotted against their predicted age T_a.

predictions are performed with the standard algorithm **A2** as it was operated in the flight campaign. An updated wake volume of the trailing wake behind the Falcon is available each second in the current setup of WEAA. In other words, each second a new wake vortex element is initialised at the Falcon position and its evolution in time is predicted for the actual aeronautical and meteorological input parameters. The trailing wake volume, therefore, consists of a sequence of wake elements with increasing age, while the vortex descends behind the aircraft. The wake volume at the exact reported encounter time t_{enc} has most likely to be interpolated in time between two consecutive output steps. Those two wake elements within the interpolated volume with the minimal distance to the reported encounter position are then spatially interpolated to arrive at that element which is evaluated against the reported encounter. Both the deviation from the expected mean position and the acknowledged uncertainty envelopes are validated. In the case of the encounter in Figure 3 the encounter was well predicted by the WEAA system. The system estimates that the wake element encountered had an age of 72 seconds and both its vertical and horizontal position were well predicted. The uncertainty envelopes were large enough, to capture the observed deviation.
To evaluate the general prediction quality, all reported encounters are processed as described above. To standardise the results, each observed deviation in horizontal (dy) and vertical (dz) direction is normalised by the attributed ellipse sizes a and b for the uncertainty envelopes of the predictions.

$$dy^* = \frac{dy}{a}; \quad dz^* = \frac{dz}{b} \tag{1}$$

Thus, for a correctly predicted encounter situation, the normalised deviations dy^* and dz^* have to lie inside a circle of unity radius around the predicted mean position. Missed encounters will have normalised deviations with a radius $dr^* > 1$. Figure 4 shows the results for 11th of April with the standard algorithm **A2** in the lower left panel. Here, standard error bars are added to the reported encounter positions, due to the flight engineer's response time, setting the time flag for an encounter, and the inaccuracy of the altitude of both aircraft. Nine out of the twelve encounters detected on that day are well predicted.

4.2. Accuracy of predictions with different meteorological input sources

Now we will start to compare the results from the predictions with the alternative meteorolgical input data sets to the standard system. One has to keep in mind that the accuracy of the wake vortex predictions of P2P^a may depend non-linearly on the given input data and, therefore, also P2P^a is implicitly evaluated, but e.g. the vortex displacement by the wind is mostly linear, in particular as the vortices of the Falcon do not descend far and vertical gradients in wind are of minor importance (see Section 5.).
At a first glance Figure 4 shows that the algorithm **A3**, the ADS-B based algorithm **A0** and the standard algorithm **A2** have an equal number of well predicted encounters. The prediction quality of the WEAA system fed with the meteorological input from **A1** is very poor. While, in lateral direction, the deviations of the reported encounter positions from the predicted mean are mainly centered around the mean in **A0**, **A2** and **A3**, they seem to be shifted to the left in algorithm **A1**. A large number of reported encounters lies well outside the predicted uncertainty envelopes, if the direct Falcon measurements are used. One encounter (number 2 in Figure 4) on that day is not captured correctly by any of the different versions of the prediction system. Here, the encounter was reported at lower altitudes than expected by any of the P2P^a predictions, regardless which input source is used. At the current state we could not clarify, if there is an error in the reported position, or in the wake prediction. In vertical direction the deviations from the predicted mean position are equally distributed among the algorithms. In most of the cases the reported encounters were detected below the centre line. This is expected, because the uncertainty envelopes for the vertical descent of the vortex are not equally distributed in P2P^a. In the majority of the cases we expect the vortices to reside in the lower part of the ellipse (Holzäpfel, 2006). Vortices may be deflected at strong vertical wind shear layers and travel upward again (Proctor & Ahmad, 2011). To compensate these, rather sparse, events the uncertainty envelopes are shifted upward.
From Figure 4 a hit rate may defined as the ratio of well predicted encounters to the total number of encounters detected on the corresponding campaign day. A summary of the performance of all algorithms and campaign days is given in Figure 5. The upper right panel confirms that **A0**, **A2**, and **A3** have a similar number of well predicted encounters, expressed as a hit rate, for the actual flight data obtained on 11th of April. **A1** has a very poor hit rate. The reasons for the unsatisfactory result of **A1** will be further

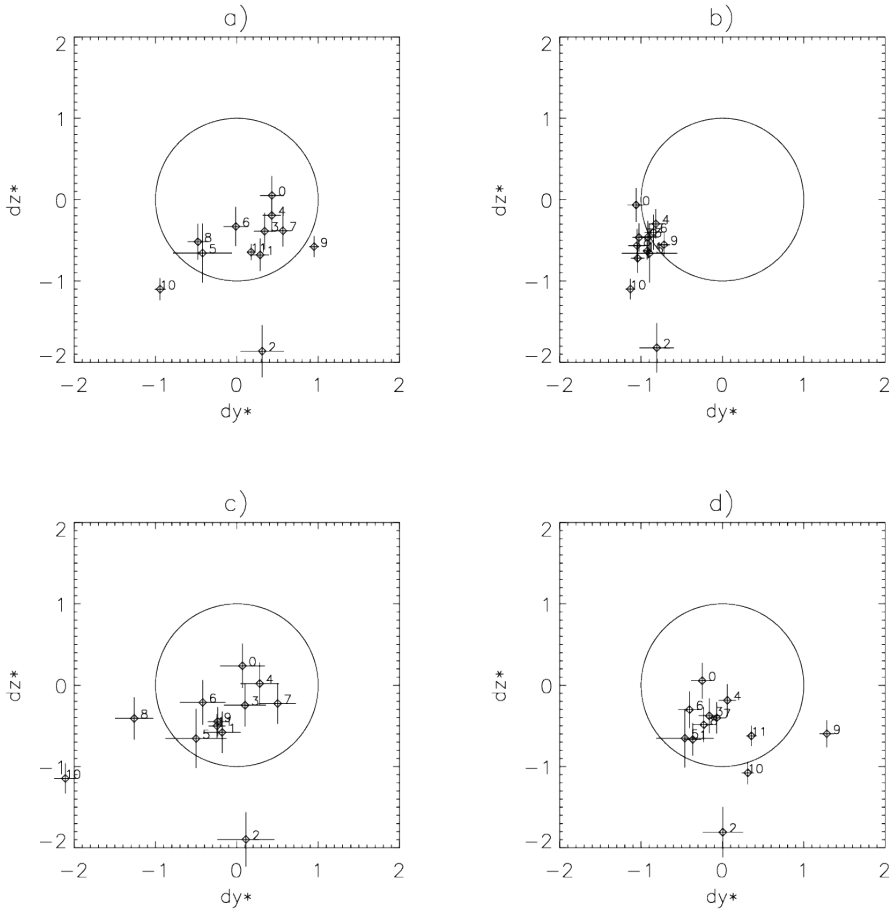

Figure 4: Distribution of normalised horizontal deviations dy^* and vertical deviations dz^* of the detected encounters from the predicted mean position for algorithms **A0** (a), **A1** (b), **A2** (c), and **A3** (d) on 11th April. Each diamond labeled with an unique number represents an encounter event with lateral and vertical error bars added, reflecting the assumed uncertainty in the reported encounter position. All distances are normalized by the predicted ellipse semi-axis. Therefore, correctly predicted encounter lie inside the circles with radius $dr^* = \sqrt{dy^{*2} + dz^{*2}} = 1$.

discussed in section 5.. The attributed or estimated uncertainty levels for each meteorological input variable in an individual algorithm (see also Table IV) are translated into different sizes of the probabilistic envelopes predicted by P2P^a. For **A2** these are rather small, both for the lateral and vertical semi-axis of the ellipses, while for the other algorithms they are considerably larger, with the largest values for **A1**. Here, the mean value of the wind speed is most uncertain, as it is derived from a single measurement transmitted via ADS-B and consequently only accurate up to the assumed measurement precision. In an operational setup a small ellipse size is desirable, because the alleviation maneuver can be more gentle. However, with increasing size, it is more likely that the predicted uncertainty envelope is sufficiently large to cover all deviations from the reported encounter positions. Therefore, both, the mean value and the standard deviation for each input parameter has to be well predicted to give an optimal solution. The results do not change considerably if the errors in the experimentally determined encounter position are considered, except for **A1** which then varies between a hit rate of 0.0 and 0.575. Generally, none of the algorithms is able to achieve the optimal hit rate of 0.99 on that day like it is intended by design of the system.
Another significant value is the mean distance of the reported encounter position and the predicted P2P^a mean values. Here, the smallest deviation is achieved for **A2** ($dr \approx 63$ m) followed by **A3** ($dr \approx 73$ m), **A0** ($dr \approx 105$ m) and at last **A1** ($dr \approx 212$ m). This implies that the wake positions predicted by **A2** are closest to the observed values.
On the 10th of April the hit rate of **A1** improved considerably and achieves values comparable to **A0** and **A2**. Compared to 11th of April also the hit rate of the NWP based predictions of **A3** improved. The latter algorithm predicts the wake closest to the reported positions with a mean distance $dr \approx 63$ m, comparable to **A2**, reaching a slightly higher value with $dr \approx 65$ m. The last campaign day on 16th of April shows the worst results for the measurement-based algorithms, in contrast to the NWP based predictions by **A3** with a hit rate of 0.85. On that day also the mean distances dr are the largest of all three campaign days. This may partly be explained by the considerable displacement of $\Delta y = 1487$ m in the mean by the high prevailing wind speed (see Table I). Thus, a similar relative error in wind speed will lead to higher misplacement of the predicted encounter positions. The values of dr are still well below 100 m for **A3** and **A2**, while the two algorithms which use either the Falcon or ATRA data are shifted by about 200 m. **A0** and **A1** also do not achieve hit rates greater than 0.55, even in the best scenario at the upper end of the error bar.
The last panel in Figure 5 is an overall result for all three campaign days. **A3** outperforms the measurement based algorithms for the hit rate (0.85). For the measurement based algorithms **A2** has the highest hit rate (0.725), followed by **A0** (0.65) and **A1** (0.4). Also the observed misfit between the mean simulated and reported vortex position is small with $dr \approx 70$ m for **A2** and **A3** and well below 10% of the mean lateral displacement Δy. For the other, measurement based, algorithms it is about 10% and 20% for **A0** and **A1**, respectively.

Generally, it is important to keep the sizes of the 99 % uncertainty ellipses in mind. They are the smallest for **A2**. In lateral direction the ellipse sizes are also well below 10% of the mean drift, here. They are considerably larger ($\sim 15\%$) for all other algorithms.
Also the vertical ellipse sizes are small in **A2**. However, the attributed uncertainty envelopes are large compared to the mean overall descent distances of the vortices (see Table I). A considerable part of the uncertainty is explained by the inaccuracy of the reported aircraft altitudes. Especially in the beginning, it is reflected by the initial size of the uncertainty envelopes at an age $T_a < 20$ s in Figure 3. With increasing age the uncertainties of all other parameters gain importance and the vertical ellipse sizes further inflate.

5. Discussion

In this section we want to discuss aspects and implications of the results obtained. First of all the reason for the poor performance of **A1** is investigated, as one would expect that directly available measurement data at the position of the vortex generation from the Falcon aircraft may be the most valuable information.

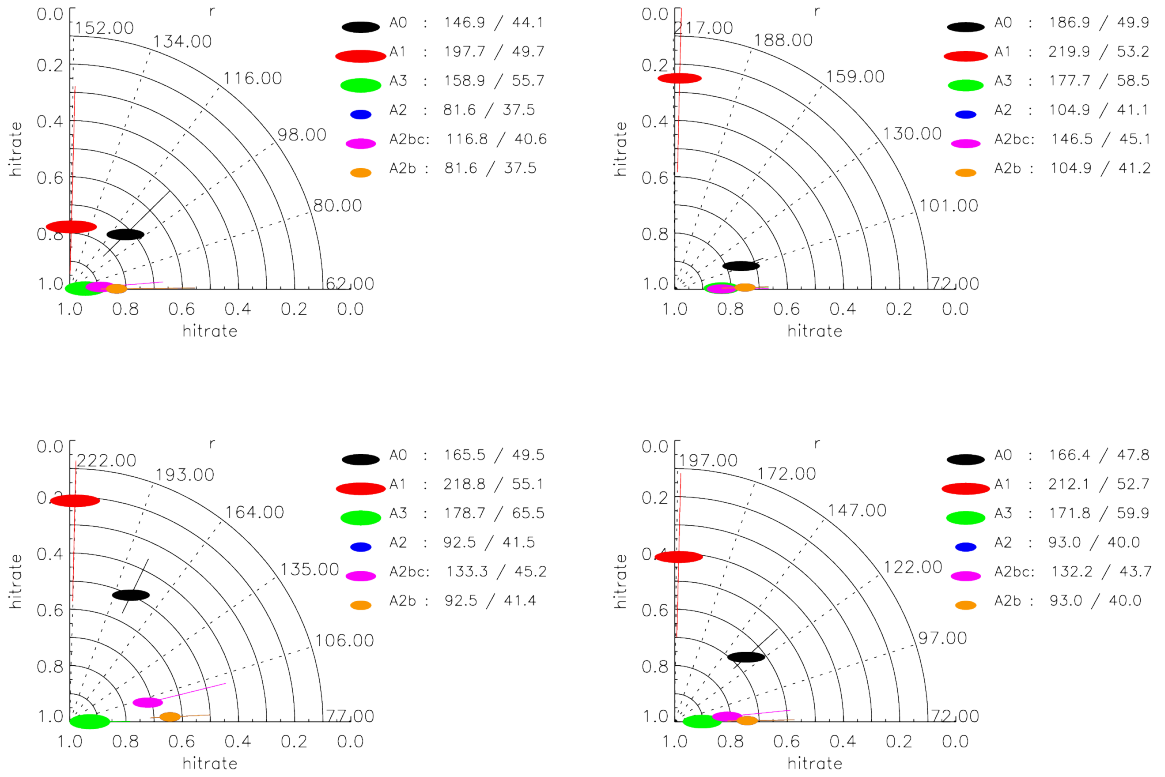

Figure 5: Summary of the performance of algorithms **A0** (black symbol), **A1** (red symbol), **A2** (blue symbol), and **A3** (green symbol) on 10th (a), 11th (b), 16th of April (c), and the mean for all three days combined (d). The radius of the polar coordinate system is the achieved hit rate and the azimuth an average distance dr of the detected encounter to the predicted mean position of the individual algorithms. The attached standard error bars indicate the achievable minimal and maximal hit rate, considering the uncertainties in the detection of the real wake vortex position. The performance of an algorithm decreases with increasing distance to the origin and to the x-axis. The legends to the right of each plot indicate the mean lateral/vertical ellipse semi-axis sizes in metres for the 99 % uncertainty envelopes of P2P^a's wake vortex predictions (upper numbers), which is also reflected in the symbol sizes. The normalised displacement of the barycentre of the detected encounters to the predicted mean position in horizontal and vertical direction is also indicated (lower numbers).

5.1. Bias in wind and temperature measurement

It is apparent from Figure 4, that the lateral displacement of the wake vortices is incorrectly predicted by **A1** on 11th of April. The barycentre of the normalised deviations in the horizontal direction is 0.936, close to the uncertainty ellipse size (see Figure 5). This is also the case for all other days with a value of 0.88 on average. The actual shift of the predicted mean position is nearly twice as large as in the other algorithms with $dr \approx 200$ m. The most likely reason for this weak prediction quality is a bias in the wind speed measurement of the Falcon aircraft, because the lateral vortex displacement is mainly controlled by the wind drift. Figure 6 compares the NWP values and those winds derived from the Falcon and ATRA measurement in an aircraft-centred frame of reference as a function of incident wind direction, on 11th of April. While for the ATRA derived wind no distinct dependency on relative wind direction is visible, there seems to be a sinusoidal deviation for the Falcon derived wind. This may be related to a known error in the mounting of the ILS system of the aircraft of about 1°. A sinusoidal function of the incident direction fits the observed deviations well, also for the two remaining campaign days. In general, also the pilots of the ATRA were forced to maneuver a lot, due to the experimental setup, and the wind measurements by the aircraft may be degraded (Drüe, 2011).
If the wind speed data transmitted from the Falcon aircraft is corrected for this bias, the wake vortex predictions and input generation for **A1** may be rerun, to investigate its influence. Because **A2** also fuses the Falcon measurements, the calculations are also repeated for the standard algorithm. A summary of the resulting performance as mean of all three campaign days is given in Figure 7 . Now **A1** and **A2** are replaced by $\mathbf{A1_c}$ and $\mathbf{A2_c}$, which are corrected for the Falcon bias. Most striking is the substantial improvement of $\mathbf{A1_c}$. Its hit rate increases from 0.4 to 0.9, better than for the NWP based algorithm, and, concerning the error bar, at least 0.775. The mean displacement is $dr \approx 80$ m now. The size of the uncertainty ellipses has not changed. Also $\mathbf{A2}_c$ improves. The hit rate increases slightly from 0.725 to 0.775, and the already acquired small displacement of **A2** further reduces from $dr \approx 70$ m down to $dr \approx 59$ m for $\mathbf{A2_c}$. This corresponds to only 5% of the mean lateral displacement Δy.
This result has two major implications. First, if wind were to be additionally transmitted via ADS-B, these measurements have to be very accurate, if calculations are solely based on this information. A bias may be very likely, and predictions of P2P^a may be misleading, as shown in the results of **A1**. In contrast, if the measurements were very accurate, the additional information would be very valuable and would increase prediction accuracy distinctly. However, also in this case the NWP derived wind fields seem to be almost equally accurate. The impact of the bias was, to some extent, already compensated in the standard algorithm **A2**. However, in the corrected version $\mathbf{A2_c}$ the barycentre of the deviations is further reduced from -0.3618 down to -0.2127.

The actual accuracy in the measurement data has to be reflected in the attributed standard deviations for each input parameter, the wind speed and direction in this case. The different approaches in each algorithm arrive at different values for these uncertainty envelopes, as compiled in Table IV for 11th of April. P2P^a translates them into final 99 % confidence intervals, and these were especially small in **A2**. Up to now, the standard algorithm assumes, that the errors in the measurement data are unbiased, but we have seen, that this is not the case for the Falcon wind data. Even if the correction is applied, it may only partly remove the bias. To study the effect of the ellipse sizes on the hit rate, additional runs have been performed with modified error assumptions for the wind data. $\mathbf{A0_{pc}}$ and $\mathbf{A2_{pc}}$ add an additional bias contribution of 1 m s^{-1} to the estimated uncertainty for the wind values of versions $\mathbf{A0_c}$ and $\mathbf{A2_c}$, respectively. In contrast $\mathbf{A1_{bc}}$ and $\mathbf{A3_{bc}}$ use a reduced error assumption (0.5 m s^{-1}) for the individual wind component data of the aircraft and NWP, respectively. Resulting standard deviations may again be taken from Table IV for $\mathbf{A0_{pc}}$, $\mathbf{A2_{pc}}$, and $\mathbf{A3_{bc}}$. Figure 7 shows that now the uncertainty envelopes for the modified version $\mathbf{A2_{pc}}$ are comparable to that of the standard versions **A0**, $\mathbf{A1_c}$ (with the bias correction applied), and **A3**. With the inflated uncertainty allowances $\mathbf{A2_{pc}}$ improves the hit rate up to that of the previously best algorithm $\mathbf{A1_c}$ and even minimizes the deviation between observed and predicted mean encounter position. In turn, if the error margins are reduced in $\mathbf{A1_{bc}}$ and $\mathbf{A3_{bc}}$, their performance drops below that one of $\mathbf{A2_c}$ with the small ellipse sizes. Also the inflation of the uncertainty assumption in $\mathbf{A0_{pc}}$ improves the hit rate from 0.65 to 0.8. However, even a mean horizontal ellipse size of $a = 267.9$ m (already 25 % of the mean lateral drift Δy) does not suffice, to compensate the observed deviations of $dr \approx 138$ m.

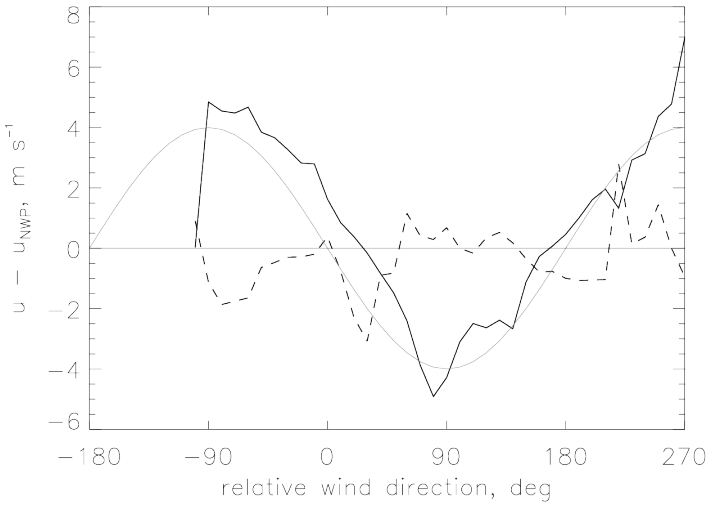

Figure 6: Mean difference of aircraft-derived wind speed data to the NWP predictions as a function of wind direction relative to the aircraft $\alpha - \Psi$, with α as meteorological wind direction and the aircraft heading Ψ on 11th of April for flight altitudes above 9000 m. Aircraft data is from **A1** with Falcon wind measurements data (solid black) and **A0** the ATRA extrapolated wind (dashed black) . Additionally, an empirically fitted functional dependency for the difference to the Falcon derived winds of the form $-\tilde{v}\sin(\alpha - \Psi)$ is shown (solid gray). The amplitude is set to $\tilde{v} = 4$ m s^{-1}.

Table IV: Mean meteorological estimates for encounter situations on 11th of April for the four standard algorithms and some of the modified versions from Figure 7 (in brackets). Shown are the estimated mean values $\pm$ the attributed standard deviations. If the latter are printed in bold, the deviations are set purely empirically.

Parameter / Algo	A0 (A0_pc)	A1 (A1_c)	A2 (A2_pc)	A3 (A3_bc)
v [m s^{-1}]	22.43 $\pm$ 1.58 (22.43 $\pm$ 2.58)	21.13 $\pm$ 2.00 (22.34 $\pm$ 2.00)	21.66 $\pm$ 0.58 (22.21 $\pm$ 1.59)	22.99 $\pm$ **1.5** (22.99 $\pm$ **0.5**)
α [deg]	267.66 $\pm$ 4.05 (267.66 $\pm$ 6.63)	263.41 $\pm$ 5.71 (263.41 $\pm$ 5.17)	266.15 $\pm$ 1.57 (264.87 $\pm$ 4.12)	268.36 $\pm$ 3.76 (268.36 $\pm$ 1.25)
$\log(\epsilon)$	-4.86 $\pm$ 0.69	-4.86 $\pm$ 0.69	-4.86 $\pm$ 0.69	-4.44 $\pm$ **0.50**
$\frac{\partial}{\partial z}(\log(\epsilon))$ [m^{-1}]	0.0 $\pm$ **0.001**	0.0 $\pm$ **0.001**	0.0 $\pm$ **0.001**	-0.0001 $\pm$ **0.001**
T [K]	219.7 $\pm$ 1.17	220.2 $\pm$ 1.00	220.0 $\pm$ 0.36	219.6 $\pm$ 1.00
ρ [kg m^{-3}]	0.441 $\pm$ 0.0025	0.442 $\pm$ 0.0021	0.442 $\pm$ 0.0008	0.442 $\pm$ 0.008
$\frac{\partial \alpha}{\partial z}$ [deg m^{-1}]	0.0 $\pm$ 0.010	0.0 $\pm$ 0.010	-0.0021 $\pm$ 0.0089	0.0086 $\pm$ **0.001**
$\frac{\partial v}{\partial z}$ [s^{-1}]	0.0 $\pm$ 0.003	0.0 $\pm$ 0.003	-0.0010 $\pm$ 0.0036	-0.0017 $\pm$ **0.001**
$\frac{\partial T}{\partial z}$ [K m^{-1}]	-0.0010 $\pm$ 0.0040	-0.0010 $\pm$ 0.0040	-0.0052 $\pm$ 0.0015	-0.0057 $\pm$ **0.001**

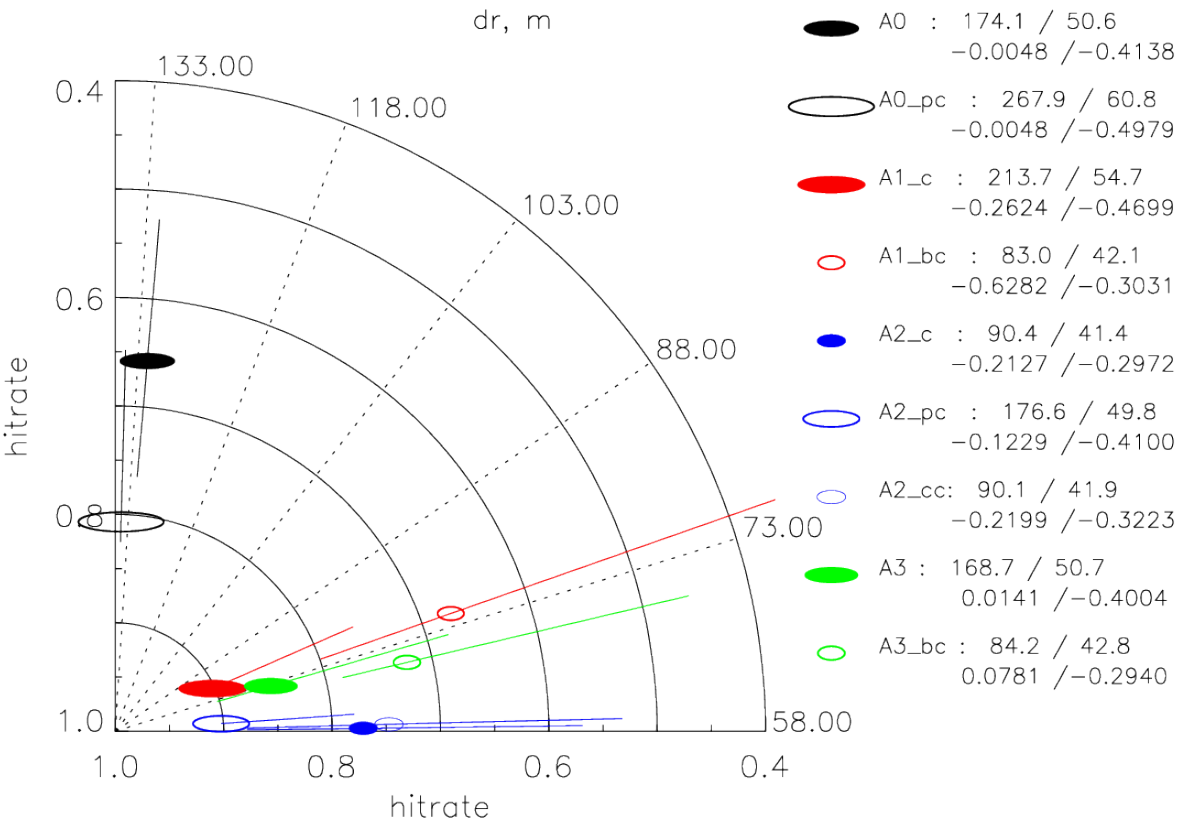

Figure 7: Similar to Figure 4, but only the mean performance on all three campaign days is shown. Only algorithms A0 and A3 are shown in the standard setup, $\mathbf{A1_c}$ and $\mathbf{A2_c}$ are corrected for the wind speed bias (solid symbols). The alternatives $\mathbf{A1_{bc}}$, and $\mathbf{A3_{bc}}$ prescribe smaller wind errors, while in $\mathbf{A0_{pc}}$ and $\mathbf{A2_{pc}}$ an additional constant bias contribution is added to the wind speed uncertainty (open symbols). In $\mathbf{A2_{cc}}$ not the estimated gradients are assumed, but the climatological values as in **A0** or **A1** (Table IV gives further details on the attributed standard deviations on 11th of April).

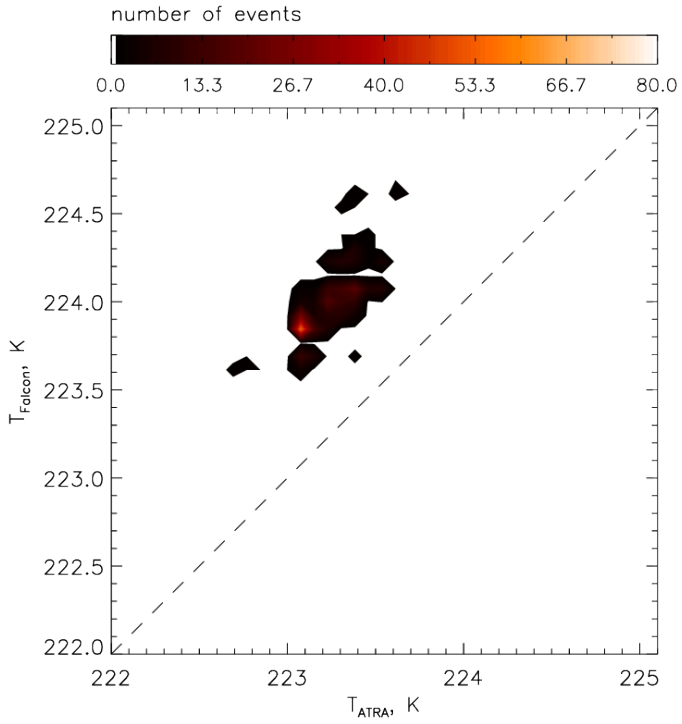

Figure 8: Correlation between the temperature measurements of the ATRA versus the Falcon aircraft during formation flights on 11th of April. A bin width of 0.1 K is used to generate the plot. Additionally, the one-to-one correlation is shown (dashed line).

5.2. The role of temperature and wind gradient estimation

Not only the wind speed, but also temperature measurements may be biased. As shown in Figure 8, there seems to be also a temperature offset of $\delta T \sim 0.8$ K between the measurements of the two aircraft, while they were flying in formation during the calibration of the height measurement on each campaign day. Compared to the NWP output, the bias seems to be attributable to the Falcon data. For the actual wake predictions the exact value of the static air temperature T is less important, but the change in temperature with height $\frac{\partial T}{\partial z}$, because the latter determines the buoyancy forces when the vortex descents and is heated adiabatically. Therefore, at least the relative temperature difference between the two aircraft should be accurately known if gradients shall be estimated from the data.

Actually, we investigate three different methods, to deduce a temperature gradient for the predictions in this work. The climatological approach, the approach based on measurement data of both aircraft during descent or ascent and relative temperature differences observed on different altitudes, or an approach based solely on NWP forecast data. The deduction of gradients from measurement data alone has to be done very carefully. If only two temperature measurements from both aircraft at different altitudes are available, the error in the gradient for a given measurement inaccuracy is large if the height difference of the aircraft is small and decreases with increasing separation. If the height difference gets too large, small scale features may be missed. A close inspection of the temperature profiles measured by the radiosonde in Figure 2, reveals some distinct changes in the profile over vertical distances less than 500 m. Examples are the two temperature inversions between 1 km and 5 km altitude on the 10th and 16th of April, respectively. Another important feature is the tropopause, where the gradient may even change sign over a small altitude range. For our work, no exact temperature gradient measurement is available, therefore, in a first step, we compare the gradients derived from **A1** and **A2** to the NWP derived data, because the modelled profiles are in agreement with the radiosonde data (compare Figure 2).

On 10th of April Figure 9 shows, that the COSMO model predicts gradients between -0.0075 K m^{-1} and -0.0055 K m^{-1} in the region where encounters have been detected. The climatologically

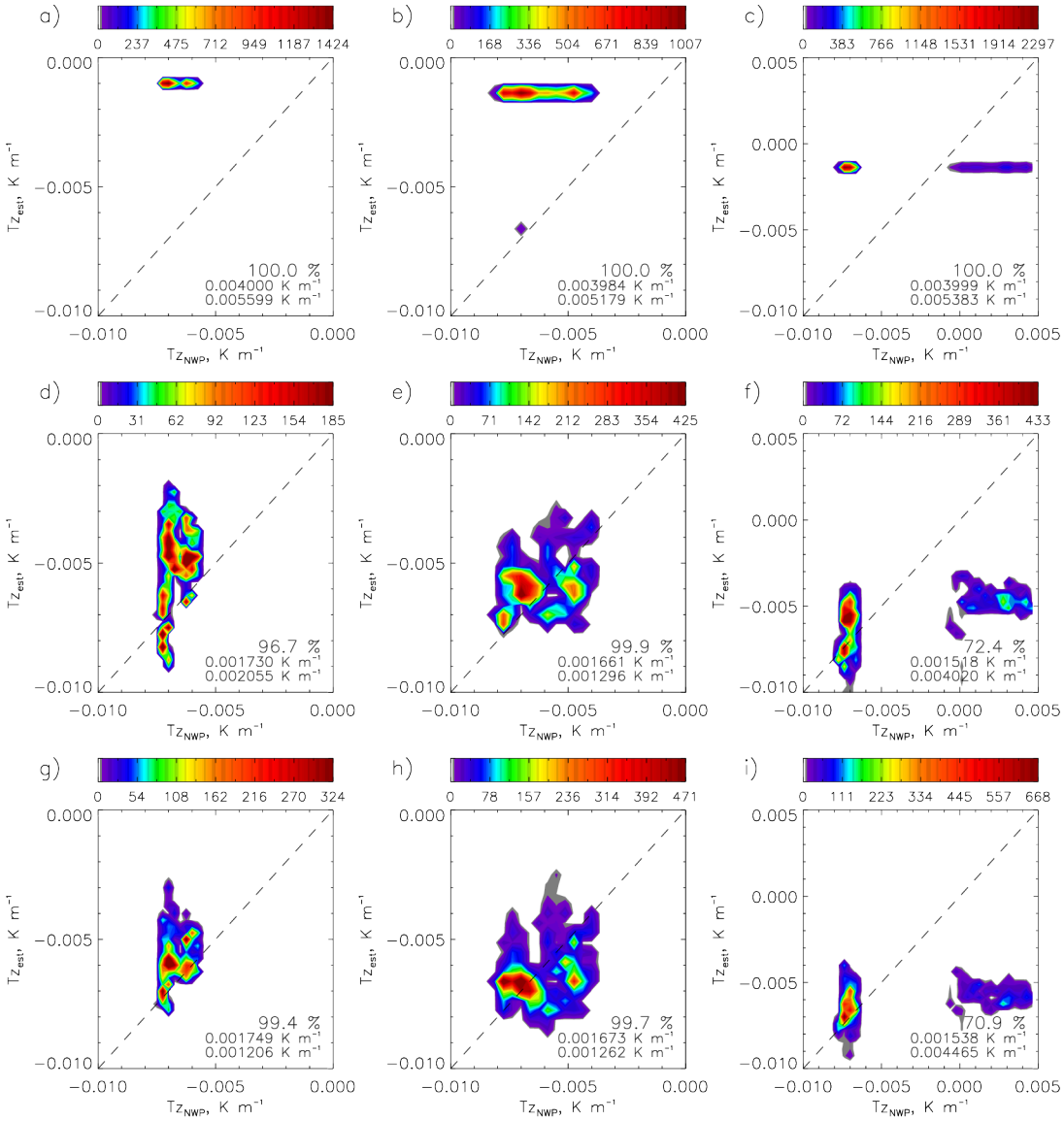

Figure 9: 2D histograms (with color-coded number of events) of the temperature gradients $\frac{\partial T}{\partial z}$ derived from **A3** (NWP model output) versus **A1** (a-c), versus **A2** (d-f), and a special version of **A2** with an automatic correction for a temperature bias (g-i) for 10th of April (a,d,g) 11th of April (b,e,h) and 16th of April (c,f,i) for flight altitudes above 9000 m. The upper number in each panel corresponds to the percentage of data points, for which the NWP-based value is located within the 3σ uncertainty range predicted by **A1**, **A2**, and the modified version of **A2**. The lower two numbers are the mean attributed uncertainty allowance (1σ) of each algorithm and the actual mean standard deviation of the corresponding algorithm to the NWP-derived values, respectively.

based algorithm **A1** already attributes stratospheric values for this altitude range and given latitude. Considering the close vicinity of the tropopause, deduced from the profiles in Figure 2, this seems reasonable. The measurement based estimates of **A2** predict tropospheric values, but an enlarged spread between -0.009 K m^{-1} and - 0.0025 K m^{-1}.
On 11th of April the variation of the NWP predicted values is larger, with tropospheric values between -0.008 K m^{-1} and -0.004 K m^{-1}. Again, for **A1** almost exclusively stratospheric gradients are proposed. The predictions of **A2** are in better agreement with the model derived values, although a slight shift to larger values is present.
For the last campaign day on 16th of April, the situation is different, in so far, that now model derived values show stratospheric influences with occasional predictions of positive gradients. In contrast, the measurement derived values of **A2** do not show any positive values. A close inspection of temperature measurements during ascents of one single aircraft reveals no evidence of positive gradients. In every case, temperature decreases with increasing height. This fact discloses a possible error source of the model derived gradients. The COSMO model uses 50 vertical levels with decreasing resolution with increasing height. At 11 km the resolution is approximately 800 m. Therefore, the sharp gradient in temperature change at the tropopause can not be fully resolved and due to the interpolation stratospheric values are erroneously attributed to the atmosphere below the Falcon. Furthermore, the model may only partly predict small scale deviations, caused by small scale turbulence or clouds, and higher natural variability may be expected in the actual temperature gradients.

For the probabilistic approach pursued in the WEAA system, the accurate prediction of the corresponding uncertainty has to be well defined. Despite the above mentioned difficulties in deriving the gradients by **A3**, we will use them to judge the suitability of the uncertainty levels attributed to the gradients from the climatological based algorithm **A1**, and the measurement based estimates of **A2**. While the errors are fixed empirically in the first one, they are automatically derived in the second algorithm. For algorithm **A1**, the deviation from the NWP value is consistently enclosed by the 99 % envelopes on all three campaign days (compare Figure 9). The climatologically derived standard deviation chosen is quite large with 0.004 K m^{-1}. However, the actual root mean square deviation of the estimated gradients to the model predicted values is even larger, about ~ 0.005 K m^{-1}. The large spread is mainly caused by the distinctly different gradients for the attributed stratospheric values and the predicted tropospheric ones. For the two first campaign days also **A2** predicts accurate uncertainty levels. Here, the standard deviation is considerably smaller, 0.0017 K m^{-1}, and close to the root mean square difference to the NWP values between 0.002 K m^{-1} on the 10th and 0.0013 K m^{-1} on 11th of April. On the last campaign day, the root mean square difference is much larger and only 72 % of the estimates have a standard deviation set large enough. However, as mentioned above, the NWP-derived stratospheric values may be misinterpreted. So, the evaluation on 16th of April should be handled carefully.

As mentioned in section 5.1., the Falcon temperature measurement is biased, and every estimation of gradients based on that data may also be erroneous. A modified version of the standard algorithm **A2** was tested in this work, which tries to automatically detect a bias in temperature. Here, not the absolute temperature value is targeted but the correction of the temperature difference between two aircraft. Therefore, the total bias is attributed to one single aircraft, the Falcon in our case. The gradients resulting from estimates of this additional algorithm are also shown in Figure 9. On the first two campaign days, the centres of the 2D histograms move closer to the one-to-one correlation and the root mean square deviation is reduced to a value of 0.0012 K m^{-1} for both days.

There seems to be quite a large spread in the actual mean values of the predicted gradients from one algorithm to another. However, referring to Figure 4, the vertical displacement of the encounter positions is not very different between **A0**, **A2**, and **A3**. Figure 10 shows deterministic wake evolutions calculated by D2P for the Falcon aircraft and a larger one, similar to an A320, for tropospheric and stratospheric conditions. The difference in descent distance is much less sensitive to the temperature gradient in case of the small Falcon aircraft. Due to the smaller descent distances less work has to be done against the stability. Therefore, the spread in the estimated temperature gradients does not affect the resulting wake volumes considerably. In Figure 7 experiment $\mathbf{A2_{cc}}$ uses the climatological gradients from **A0** and **A1** instead of the estimated ones and the effect on the overall performance is very small.

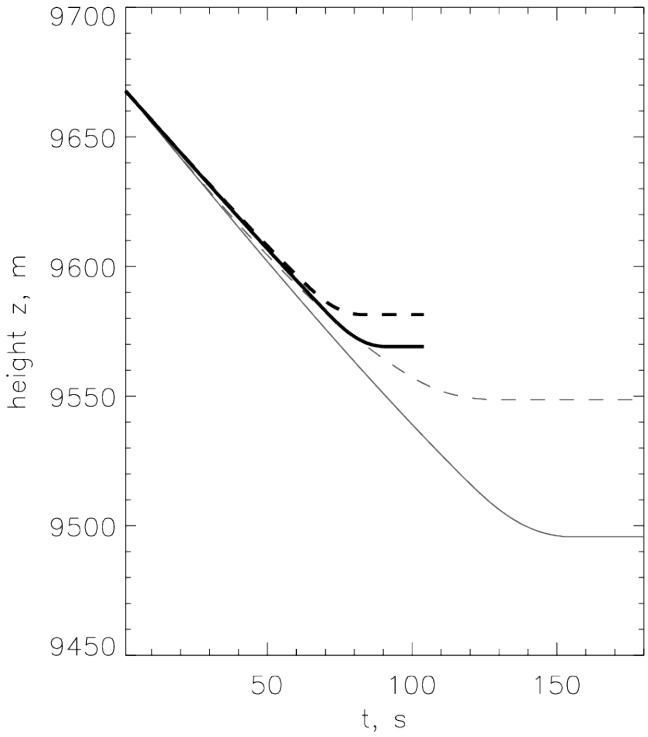

Figure 10: Deterministic D2P calculation for the temporal descent of the wake vortex for the Falcon aircraft (thick black) and an A320 aircraft (thin grey) for an initial altitude of 9658 m. Shown is the sensitivity of the prediction to a change of the temperature gradient from typical tropospheric conditions $\frac{\partial T}{\partial z} = -0.0065$ K m^{-1} (solid lines) to stratospheric conditions $\frac{\partial T}{\partial z} = 0.0$ K m^{-1} (dashed lines).

6. Conclusion

In this work the wake vortex advisory and avoidance system WEAA has been evaluated using data from an encounter flight campaign in April 2014. Special emphasis was laid upon the role of meteorological input on the accuracy of probabilistic wake vortex predictions.

Starting from an algorithm which is based on standard ADS-B information, we further investigated the performance of the system for an enhanced ADS-B protocol, and for numerical weather prediction data. The wake volumes predicted by the different versions of the algorithms were evaluated with the reported encounter positions on the three campaign days.

For the ADS-B based algorithm **A0** about 65 % of the reported encounters have been correctly predicted. The rather large mean distance between reported and predicted encounter positions, is very likely caused by wrong estimates of the atmospheric wind. Due to the small size of the vortex generating aircraft the role of atmospheric stability was of minor importance and we were mainly addressing the predicted drift of the wake vortex system by the wind and the attributed uncertainty envelopes.

By design, the achieved hit rate of the WEAA system should be 99 %. The lower rate for **A0** may be partly explained by an inadequate setting of the attributed uncertainties of the input parameters. However, even an increase of the expected uncertainties of the wind input in $\mathbf{A0_{pc}}$ could not compensate all remaining error sources. Additional errors in the aeronautical parameters, but also non-Gaussian error distributions or errors in the actual vortex predictions and in the reported vortex positions could be present. Further, the rather low number of 44 reported encounters may be insufficient for reliable statistical estimates.

For setup **A1** the wind speed and temperature was added to the transmitted data from the vortex generator Falcon. Due to a bias in the Falcon wind speed data the performance of this algorithm was very poor. Only 40 % of the encounters have been well predicted and the overall deviation was large with $dr \approx 192$ m. If the bias is partly corrected (setup $\mathbf{A1_c}$), the results improve considerably and 90 % of the encounters are well detected with a reduced mean deviation of $dr \approx 80$ m. If the accuracy of the wind measurement of the wake generating aircraft was very high, the extended ADS-B+ format would be very valuable and would increase prediction accuracy distinctly.

Even if the bias is present the fusion of the measurement data of both the leading and the following aircraft in an ADS-B+ setup, like it is done in the standard algorithm **A2**, outperforms the other measurement-based algorithms, with a prediction accuracy of 72.5 %. The algorithm attributes very small uncertainty envelopes in the meteorological estimates and consequently the predicted 99 % uncertainty envelopes of the wake volumes were small. In the current version of the algorithm no bias is assumed, but Gaussian measurement errors. If we account for an additional bias term, $\mathbf{A2_{pc}}$ even outperforms $\mathbf{A1_c}$.

Forecast from a numerical weather prediction model was also investigated an an additional data source for the WEAA system. Only model data, which would have been available before take-off was used. The acquired performance of **A3** was very good. 85 % of the encounters were well predicted and the mean deviation was $dr \approx 70$ m. The attributed uncertainty envelopes seem to be set adequately. If the error assumptions were more strict, $\mathbf{A3_{bc}}$ would achieve a result comparable to **A2**.

Due to the low vertical resolution of the weather prediction model data, temperature gradients derived from the model output may have been erroneous on the 16th of April. However, the estimation of gradients from measurement data is also demanding. If no additional data source than the own aircraft is available, climatological values may be used.

For future campaigns investigating the performance of WEAA or wake vortex predictions in general, we would propose to use a larger aircraft as generator, for the gradient information to become distinctly visible in the wake vortex evolution and descent. We would further suggest to schedule the flights below and above the tropopause, to examine the behavior of the system in these different regimes and also in situations when crossing from one layer to the other. Due to the nature of the experimental setup, the pilots were forced to maneuver a lot, in order to hit the wake behind the Falcon. This is a situation where the wind and temperature measurements by the aircraft may be degraded during rapid ascent or turning maneuvers. In a more common situation for such an on-board system straighter flight paths can be assumed which may in turn enhance the prediction quality of the measurement-based algorithms.

Acknowledgements

The authors gratefully acknowledge contributions of other colleagues from DLR for their commitment during the flight campaign. Part of the component development for WEAA has been performed under contract to Airbus and we gratefully appreciate the discussions with Dr.-Ing. Sebastian Kauertz. We would further like to thank Stephan Körner for the provision of the D2P calculations and Dr. Simon Unterstrasser for a critical and constructive review of the manuscript.

References

AVTECH Sweden AB (2012), *Aventus NowCast: Great fuel savings by accurate wind information*. Product Sheet.

Baldauf, M., Seifert, A., Förstner, J., Majewski, D., Raschendorfer, M., Reinhardt, T. (2011), Operational Convective-Scale Numerical Weather Prediction with the COSMO Model: Description and Sensitivities. *Mon. Wea. Rev.*, Vol. 139, pp. 3887–3905. doi:10.1175/MWR-D-10-05013.1.

Bauer, T., Vechtel, D., Abdelmoula, F., Immisch, T. (2014), In-flight wake encounter prediction with the wake encounter avoidance and advisory system. *AIAA*, Vol. 2014-2333. doi:10.2514/6.2014-2333.

Bienert, N., Fricke, H. (2013), Real-time wind uplinks for prediction of the arrival time and optimization of the descent profile. *3rd ENRI international workshop on ATM/CNS*, pp. 1–6. Electronic Navigation Research Institute, Tokyo. EN-045.

de Haan, S. (2011), High-resolution wind and temperature observations from aircraft tracked by Mode-S air traffic control data. *J. Geophys. Res.*, Vol. 116, No. D10111, pp. 1–13. doi:10.1002/2010JD015264.

de Jong, P. M. A., van der Laan, J. J., in 't Veld, A. C., van Paassen, M. M., Mulder, M. (2014), Wind-profile estimation using airborne sensors. *Journal of Aircraft*, Vol. 51, No. 6, pp. 1852–1863. doi:10.2514/1.C032550.

de Leege, A. M. P., van Paassen, M. M., Mulder, M. (2013), Using automatic dependent surveillance-broadcast for meteorological monitoring. *Journal of Aircraft*, Vol. 50, No. 1, pp. 249–261. doi:10.2514/1.C031901.

Drüe, C. (2011), Reconstruction of aircraft trajectories from AMDAR weather reports. *J. Atmos. Oceanic Technol.*, Vol. 28, No. 7, pp. 921–932. doi:10.1175/2011JTECHA1499.1.

Drüe, C., Frey, W., Hoff, A., Hauf, T. (2008), Aircraft type-specific errors in AMDAR weather reports from commercial aircraft. *Q.J.R. Meteorol. Soc.*, Vol. 134, No. 630, pp. 229–239. doi:10.1002/qj.205.

EUROCONTROL (2004), Challenges to Growth 2004 Report (CTG04). Vol. 1.0.

Gettelman, A., Hoor, P., Pan, L., Randel, W., Hegglin, M., Birner, T. (2011), The extratropical upper troposphere and lower stratosphere. *Rev. Geophys.*, Vol. 49, pp. RG3003. doi:10.1029/2011RG000355.

Greene, G. C. (1986), An approximate model of vortex decay in the atmosphere. *Journal of Aircraft*, Vol. 23, pp. 566–573. doi:10.2514/3.45345.

Harnisch, F., Keil, C. (2015), Initial conditions for convective-scale ensemble forecasting provided by ensemble data assimilation. *Mon. Wea. Rev.*, Vol. 143, pp. 1583–1600. doi:10.1175/MWR-F-14-00209.1.

Hoinka, K. (1998), Statistics of the global tropopause pressure. *Mon. Wea. Rev.*, Vol. 126, No. 12, pp. 3303–3325.

Holzäpfel, F. (2003), Probabilistic Two-Phase Aircraft Wake-Vortex Decay and Transport Model. *Journal of Aircraft*, Vol. 40, pp. 323–331.

Holzäpfel, F. (2006), Probabilistic Two-Phase Aircraft Wake-Vortex Model: Further Development and assessment. *Journal of Aircraft*, Vol. 43, pp. 700–708. doi:10.2514/1.16798.

Holzäpfel, F. (2013), Verfahren und Vorrichtung zum Ermitteln des Horizontalwindes an Bord eines Luftfahrtzeugs. Patent DE 10 2012 007 147.

Houchi, K., Stoffelen, A., Marseille, G. J., De Kloe, J. (2010), Comparison of wind and wind shear climatologies derived from high-resolution radiosondes and the ECMWF model. *J. Geophys. Res.*, Vol. 115, No. D22123.

Houtekamer, P., Mitchell, H. (1998), Data assimilation using an ensemble Kalman filter technique. *Mon. Wea. Rev.*, Vol. 126, No. 3, pp. 796–811.

Körner, S., Ahmad, N., Holzäpfel, F., VanValkenburg, R. (2015), Mulit-model ensemble wake vortex prediction. *AIAA*, Vol. 2015-3173. doi:10.2514/6.2015-3173.

Lee, A., Weygandt, S., Schwartz, B., Murphy, J. (2009), Performance of trajectory models with wind uncertainty. *AIAA*, Vol. 2009-5834.

Meischner, P., Baumann, R., Höller, H., Jank, T. (2001), Eddy dissipation rates in thunderstorms estimated by doppler radar in relation to aircraft in situ measurements. *J. Atmos. Oceanic Technol.*, Vol. 18, pp. 1609–1627.

Painting, D. (2003), *Aircraft meteorological data relay (AMDAR) reference manual*. Secretariat of the World Meteorological Organisation, Geneva - Switzerland. WMO-No. 958.

Proctor, F., Ahmad, N. (2011), Crosswind shear gradient affect on wake vortices. *AIAA*, Vol. 2011-3038.

RTCA WP-YY Prepared by: WVTT (2015), *Suggested standards development activities to move forward with aircraft-derived data for wake vortex, air traffic management, and meteorological applications*. RTCA, Inc. DRAFT. RTCA Paper No. 118-15/PMC-1331.

Schraff, C., Reich, H., Rhodin, A., Schomburg, A., Stephan, K., Periáñez, A., Potthast, R. (2015), Kilometre-scale ensemble data assimilation for the COSMO (KENDA). *Q.J.R. Meteorol. Soc.*, Vol. in review.

Schwartz, B., Benjamin, S. (1995), A comparison of temperature and wind measurements from ACARS-equipped aircraft and rawinsondes. *Weather and Forecasting*, Vol. 10, No. 3, pp. 528–544.

SESAR (2012), European ATM Master Plan. *SESAR Consortium*, Vol. 2.0.

Treve, V., Rooseleer, F. (13 May 2014), RECAT-EU proposal, validation and consultation. *WakeNet Europe 2014 Workshop*.

Troxel, S., Reynolds, T. (2015), Use of numerical weather prediction models for NextGen ATC wind impact studies. *AIAA*, Vol. 2015-2890. doi:10.2514/6.2015-2890.

Unterstrasser, S. (2014), Large eddy simulation study of contrail microphysics and geometry during the vortex phase and consequences on contrail-to-cirrus transition. *J. Geophys. Res.*, Vol. 119, No. 12, pp. 7537–7555. doi:10.1002/2013JD021418.

Voigt, C., Schumann, U., Jurkat, T., Schäuble, D., Schlager, H., Petzold, A., Gayet, J.-F., Krämer, M., Schneider, J., Borrmann, S., Schmale, J., Jessberger, P., Hamburger, T., Lichtenstern, M., Scheibe, M., Gourbeyre, C., Meyer, J., Kübbeler, M., Frey, W., Kalesse, H., Butler, T., Lawrence, M. G., Holzäpfel, F., Arnold, F., Wendisch, M., Döpelheuer, A., Gottschaldt, K., Baumann, R., Zöger, M., Sölch, I., Rautenhaus, M., Dörnbrack, A. (2010), In-situ observations of young contrails ? overview and selected results from the CONCERT campaign. *Atmos. Chem. Phys.*, Vol. 10, No. 18, pp. 9039–9056. doi:10.5194/acp-10-9039-2010.

List of publications emerging from the project

Bauer, Tobias; Vechtel, Dennis; Abdelmoula, Fethi; Immisch, Thomas: In-Flight Wake Encounter Prediction with the Wake Encounter Avoidance and Advisory System, AIAA AVIATION 2014, June 2014, http://dx.doi.org/10.2514/6.2014-2333.

Berling J.; A. Lau, V. Gollnick: Strategic Conflict Probabilities in the European Air Traffic Management Network DGLR 2016.

Dambowsky, Falk; Abdelmoula, Fethi; Müller, Adrian: Wirbelschleppen: DLR testet Warnsystem bei Flugversuchen, DLR Pressemitteilung, 14.04.2014, http://www.dlr.de/dlr/desktopdefault.aspx/tabid-10081/151_read-9997.

Dambowsky, Falk; Bauer, Tobias; Heider, Jens: Wirbelschleppen umfliegen: Neues System im Flugversuch erprobt, DLR Pressemitteilung, 20.12.2016, www.dlr.de/dlr/desktopdefault.aspx/tabid-10081/151_read-20497.

Gerz, Thomas; Frank Holzäpfel, Anton Stephan, Takashi Misaka: Aircraft wake vortices: Theory, simulation, experiment and mitigation options, Abstract of a Keynote Speech for the 3rd International Retreat on Vorticity Aerodynamics (IRVA-3) August 2016 in Beijing, China, 4 pages.

Heel, Tobias: Numerical Simulation of the Impact of Plate Lines on Aircraft Wake Vortices during the WakeOP Measurement Campaign, Master's Thesis, TU München, TUM-AER-2014-06.

Herbst, Jonas, Vrancken, Patrick: Concept Study of a Michelson-Interferometer-based UV Direct-Detection Doppler Wind Lidar for the Near-field, Range-resolved Characterization of Gusts, Turbulence and Wake Vortices, Proceedings of the ONERA-DLR Aerospace Symposium (ODAS),Jun 16.

Herbst, Jonas, Vrancken, Patrick: Design of a monolithic Michelson interferometer for fringe imaging in a near-field UV direct-detection Doppler wind lidar, OSA Appl. Opt., Vol. 55, No. 25, Sep 16, http://doi.org/10.1364/AO.55.006910.

Holzäpfel, Frank: Effects of Environmental and Aircraft Parameters on Wake Vortex Behavior, Journal of Aircraft, Volume 51, Issue 5, 2014, pp. 1490-1500, 2014, http://dx.doi.org/10.2514/1.C032366.

Holzäpfel, Frank; Anton Stephan, Stephan Körner, Takashi Misaka: Wake Vortex Evolution During Approach and Landing With and Without Plate Lines, AIAA SciTech 2014, 52nd Aerospace Sciences Meeting, AIAA-2014-0925, National Harbor, Maryland, 13-17 January 2014, 13 pages.

Holzäpfel, Frank; Anton Stephan: Aircraft Wake Vortex Evolution During Approach and Landing With and Without Plate Lines, Gauss Centre for Supercomputing, January 2014, http://www.gauss-centre.eu/gauss-centre/EN/Projects/ScientificEngineering/_node.html.

Holzäpfel, Frank; Anton Stephan, Tobias Heel: Wake Vortices of Landing Aircraft, High Performance Computing in Science and Engineering, Editors: S. Wagner, A. Bode, H. Satzger,

M. Brehm, LRZ, Bayerische Akademie der Wissenschaften, Garching/Munich 2014, pp. 134-135.

Holzäpfel, F.; A. Stephan, N. Tchipev, T. Heel, S. Körner, T. Misaka: Impact of Wind and Obstacles on Wake Vortex Evolution in Ground Proximity, AIAA Aviation, 6th AIAA Atmospheric and Space Environments Conference, AIAA 2014-2470, 16-20 June 2014, Atlanta, GA, 16 pages, http://dx.doi.org/10.2514/6.2014-2470.

Holzäpfel, Frank: Flugzeug-Wirbelschleppen – von der Grundlagenforschung zur Anwendung, promet, Jahrg. 39, Heft 1/2, Aktuelle Aspekte der Flugmeteorologie II - Mit dem Wetter leben, 2014, pp. 14-22.

Holzäpfel, F.; A. Stephan, T. Heel, S. Körner Enhanced: Wake Vortex Decay in Ground Proximity Triggered by Plate Lines, 4th EASN Workshop, Flight Physics & Aircraft Design, RWTH Aachen, 27.-29. Oktober 2014, 12 pages .

Holzäpfel Frank: A380 Wake Vortex Measurements at Tarbes Airport in October 2014, Report on measurement campaign, Institut für Physik der Atmosphäre, 30 March 2015, 26 pages.

Holzäpfel, F.; N. Tchipev, A. Stephan: Wind Impact on Single Vortices and Counterrotating Vortex Pairs in Ground Proximity, AIAA Aviation 2015, 7th AIAA Atmospheric and Space Environments Conference, AIAA 2015-3174, 22-26 June 2015, Dallas, TX, 13 pages, http://dx.doi.org/10.2514/6.2015-3174.

Holzäpfel, F.; A. Reinke, C. Schwarz et al.: Aircraft Wake Vortex State-of-the-Art & Research Needs, WakeNet3-Europe 201 pages, 10. Nov 15, http://dx.doi.org/10.17874/BFAEB7154B0.

Holzäpfel, F.; A. Stephan, T. Heel, S. Körner: Enhanced Wake Vortex Decay in Ground Proximity Triggered by Plate Lines, Aircraft Engineering and Aerospace Technology, Vol. 88, Issue 2, 2016, pp. 206-214, http://dx.doi.org/10.1108/AEAT-02-2015-0045.

Holzäpfel, Frank; Nikola Tchipev, Anton Stephan: Wind Impact on Single Vortices and Counterrotating Vortex Pairs in Ground Proximity Flow, Turbulence and Combustion, Volume 97, Issue 3, October 2016, pp 829–848, http://dx.doi.org/10.1007/s10494-016-9729-2.

Holzäpfel, Frank: Analyse potentieller Wirbelschleppen Einflüge am Flughafen Wien (LOWW), Gutachten, 67 Seiten, 12. Apr 16.

Holzäpfel, Frank: Analysis of potential wake vortex encounters at a major European airport, Proceedings of the International Conference of the EASN Association, 6th EASN International Conference on Innovation in European Aeronautics Research, Porto, Portugal, 18.-21. October 2016, pages 223-238.

Holzäpfel, Frank: Surface Structure on a Ground Surface for Accelerating Decay of Wake Turbulence on the Short Final of an Approach to a Runway, Patent, Republic of Singapur, 192217, 12. May 2016.

Holzäpfel, Frank: Surface Structure on a Ground Surface for Accelerating Decay of Wake Turbulence on the Short Final of an Approach to a Runway, Patent, Japan, 5745099, 2016.

Holzäpfel, Frank: Surface Structure on a Ground Surface for Accelerating Decay of Wake Turbulence on the Short Final of an Approach to a Runway, Patent for Austria, France, Great Britain, Spain, Switzerland.

Holzäpfel, Frank: Analysis of potential wake vortex encounters at a major European airport, Aircraft Engineering and Aerospace Technology, Vol. 89, Issue 5, 2017, pp. 634-643, http://dx.doi.org/10.1108/AEAT-01-2017-0043.

Jung, Bernadette: Von erhofften Turbulenzen und unverhofften Schwierigkeiten, DLR-Magazin 144, Nov 14.

Knabe, F.; M. Schultz: A New Way to Indicate Airport Airside Performance from an Economic Perspective, Transportation Research Procedia, Volume 14, 2016, Pages 3771–3780, http://dx.doi.org/10.1016/j.trpro.2016.05.462.

Körner, S.; F. Holzäpfel: Multi-Model Wake Vortex Prediction, 4th EASN Workshop, Flight Physics & Aircraft Design, RWTH Aachen, 27.-29. Oktober 2014, 11 pages .

Körner, Stephan; Nash'at N. Ahmad, Frank Holzäpfel, Randal L. VanValkenburg: Multi-Model Ensemble Wake Vortex Prediction, AIAA Aviation 2015, 7th AIAA Atmospheric and Space Environments Conference, AIAA 2015-3173, 22-26 June 2015, Dallas, TX, 22 pages, http://dx.doi.org/10.2514/6.2016-3438.

Körner, S.; F. Holzäpfel: Multi-Model Ensemble Wake Vortex Prediction, Aircraft Engineering and Aerospace Technology, Vol. 88, Issue 2, 2016, pp. 331-340, http://dx.doi.org/10.1108/AEAT-02-2015-0068.

Körner, Stephan: Multi-Model Ensemble Wake Vortex Prediction, Doktorarbeit, RWTH Aachen, Institut für Luft- und Raumfahrtsysteme, 2016.

Körner, Stephan; Frank Holzäpfel, Nashat Ahmad, Randal van Valkenburg: Multi-Model Ensemble Wake Vortex Prediction – Further Development and Probabilistic Assessment, AIAA AVIATION 2016, 8th AIAA Atmospheric and Space Environments Conference, AIAA Paper 2016-3438, Washington, D.C., 13–17 June 2016, http://dx.doi.org/10.2514/6.2016-3438.

Körner, Stephan; Nashat Ahmad, Frank Holzäpfel, Randal van Valkenburg: Multimodel Ensemble Methods for Prediction of Wake-Vortex Transport and Decay, Journal of Aircraft, Vol. 54, No. 5, 2017, pp. 1849-1859. http://dx.doi.org/10.2514/1.C034287.

Kroll Norbert, Schwamborn Dieter, Hennings Holger, Kügeler Edmund, Kohlgrüber Dieter, Köcke H., Spangenberg Holger, Holzäpfel Frank, Ess Peter, Schreiber Andreas, Kier Thiemo, Nagel Björn: DLR Leitkonzept "Virtuelles Produkt" Stand der Wissenschaft und Technik, EB 124-2016/908, 78 Seiten.

Lau, A.; J. Berling, F. Linke, V. Gollnick, K. Nachtigall: Large-Scale Network Slot Allocation with Dynamic Time Horizons, 11th USA/Europe ATM Seminar, 2015, www.atmseminar.org.

Maibach, Malte: Sensitivitätsanalyse des Wirbelschleppenwarn- und -ausweichsystems WEAA, DLR-IB-FT-BS-2016-32, Jan 16.

Misaka, Takashi; Shigeru Obayashi, Anton Stephan, Frank Holzäpfel, Thomas Gerz, Kazuhiro Nakahashi: Numerical Simulation of Jet-Wake Vortex Interaction, AIAA SciTech 2014, 52nd Aerospace Sciences Meeting, AIAA-2014-0926, National Harbor, Maryland, 13-17 January 2014, 9 pages 2014.

Misaka, Takashi; Frank Holzäpfel, Thomas Gerz: Large-Eddy Simulation of Aircraft Wake Evolution from Roll-Up until Vortex Decay; AIAA Journal, Vol. 53, No. 9, September 2015, pp. 2646 – 2670, http://dx.doi.org/10.2514/1.J053671.

Misaka, Takashi; Shigeru Obayashi, Anton Stephan, Frank Holzäpfel, Thomas Gerz: Sensitivity Analysis of Wake Vortex Parameters Measured by Doppler Lidar, AIAA Aviation 2015, 7th AIAA Atmospheric and Space Environments Conference, AIAA 2015-3023, 22-26 June 2015, Dallas, TX, 10 pages. http://dx.doi.org/10.2514/6.2015-3023.

Nachtigall, K.; F. Knabe, F. Hesse: Entwicklung von Steuerungsstrategien in der prätaktischen Planung in Reaktion auf kapazitätsreduzierende Wetterphänomene am Flughafen, DLRK 2016, http://www.dglr.de/publikationen/2016/420134.pdf.

Rohlmann, D.: Numerische Simulation des Einflusses des Fahrwerks und des Bodeneffekts auf die Umströmung einer Transportflugzeugkonfiguration, DLRK 2016, http://www.dglr.de/publikationen/2016/420170.pdf.

Rohlmann, D.: Numerical Simulation of the Influence of the Landing Gear and the Ground Effect on the Flow around a Transport Aircraft Configuration, submitted to CEAS Aeronautical Journal, 2017.

Schrall, Jürgen: Numerical Optimization of Plate Line Design, Master's Thesis FernUni Hagen, 2017.

Smalikho, I.N.; V.A. Banakh, F. Holzäpfel, S. Rahm : Method of radial velocities for the estimation of aircraft wake vortex parameters from data measured by coherent Doppler lidar, Optics Express, Vol. 23, No. 19, pp. A1194-A1207, 2015.

Sölch, Ingo; Frank Holzäpfel, Fethi Abdelmoula, and Dennis Vechtel: Performance of on-board wake vortex prediction systems employing various meteorological data sources , J. Aircraft, Vol. 53, Issue 5, pp. 1505-1516, 2016, http://arc.aiaa.org/doi/abs/10.2514/1.C033732.

Stephan, Anton; Frank Holzäpfel, Takashi Misaka, Reinhard Geisler, Robert Konrath: Enhancement of aircraft wake vortex decay in ground proximity - Experiment versus Simulation, CEAS Aeronautical Journal, Volume 5, Issue 2, 2014, pp. 109-125, http://dx.doi.org/10.1007/s13272-013-0094-8.

Stephan, Anton; Frank Holzäpfel, Takashi Misaka: Hybrid simulation of wake-vortex evolution during landing on flat terrain and with plate line, International Journal of Heat and Fluid Flow, Vol. 49, 2014, pp. 18-27, 2014, http://dx.doi.org/10.1016/j.ijheatfluidflow.2014.05.004.

Stephan, A.; F. Holzäpfel, T. Misaka: Simulation of Aircraft Wake Vortices During Landing with Decay Enhancing Obstacles , No. 2014_0796, ICAS 2014, St. Petersburg, 7.-12. September 2014, 10 pages.

Stephan, Anton; Jürgen Schrall, Frank Holzäpfel: Numerical Optimization of Plate Line Design for Enhanced Wake-Vortex Decay, AIAA AVIATION 2016, 8th AIAA Atmospheric and Space Environments Conference, AIAA Paper 2016-3135, Washington, D.C., 13–17 June 2016, http://dx.doi.org/10.2514/6.2016-3135.

Stephan, Anton ; Stefan Zholtovski, Frank Holzäpfel: The effect of gusts on aircraft wake vortices – one-way and two-way coupling of RANS and LES codes, Proceedings of the

International Conference of the EASN Association, 6th EASN International Conference on Innovation in European Aeronautics Research, 18.-21. October 2016, pages 784-800.

Stephan, Anton; Jürgen Schrall, Frank Holzäpfel: Numerical Optimization of Plate-Line Design for Enhanced Wake-Vortex Decay, J. Aircraft, Vol. 54, No. 3 (2017), pp. 995-1010., http://dx.doi.org/10.2514/1.C033973.

Stephan, Anton; Stefan Zholtovski, Frank Holzäpfel: The effect of gusts on aircraft wake vortices, Aircraft Engineering and Aerospace Technology, Vol. 89, Issue 5, 2017, pp. 692-702, https://doi.org/10.1108/AEAT-01-2017-0032.

Takeshima, Yuriko; Takashi Misaka, Shigeru Obayashi, Frank Holzäpfel, Hiroshi Kato, Shigeo Takahashi, Issei Fujishiro: Topological Approach to Multisensory Realization of Wake Turbulence, AIAA Aviation, 6th AIAA Atmospheric and Space Environments Conference, AIAA 2014-2335, 16-20 June 2014, Atlanta, GA, 7 pages .

Vechtel, D.; A. Stephan, F. Holzäpfel Simulation Study of Severity and Mitigation of Wake-Vortex Encounters in Ground Proximity, J. Aircraft, Vol. 54, No. 5 (2017), pp. 1802-1813, http://arc.aiaa.org/doi/abs/10.2514/1.C033995.

Veerman, H., Vrancken, P., Lombard, L.: Flight testing delicat–A promise for medium-range clear air turbulence protection, In European 46th SETP and 25th SFTE Symposium, Jun 14.

Vrancken, Patrick, Witschas, Benjamin, Wirth, Martin, Ehret, Gerhard, et al.: Flight tests of the DELICAT airborne LIDAR system for remote clear air turbulence detection, The 27th International Laser Radar Conference (ILRC 27), New York City, USA, Edited by B. Gross; F. Moshary; M. Arend; EPJ Web of Conferences, Volume 119, id.14003, Jul 15, https://doi.org/10.1051/epjconf/201611914003.

Vrancken, Patrick, Wirth, Martin, Ehret, Gerhard, et al.: Airborne forward-pointing UV Rayleigh lidar for remote clear air turbulence detection: system design and performance, OSA Appl. Opt. Vol. 55, No. 32, Nov 16, http://dx.doi.org/10.1364/AO.55.009314.

Vrancken, Patrick: Airborne remote detection of turbulence with forward-pointing LIDAR, In Sharman, Lane (Eds.) Aviation Turbulence (pp. 443-464). Springer International Publishing,.Sep 16.

Wang, C.H. John ; D. Zhao, J. Schlüter, A. Stephan, F. Holzäpfel: Effect of Ground Obstacle of Different Aspect Ratio on Wake Vortex Dissipation, AIAA AVIATION 2016, 8th AIAA Atmospheric and Space Environments Conference, AIAA Paper 2016-3134, Washington, D.C., 13–17 June 2016, http://dx.doi.org/10.2514/6.2016-3134.

Wang, C.H. John; D. Zhao, J. Schlüter, A. Stephan, F. Holzäpfel: Effect of Ground Obstacle Separation Distance on Wake Vortex Dissipation, AIAA AVIATION 2016, 34th AIAA Applied Aerodynamics Conference, AIAA Paper 2016-4176, Washington, D.C., 13–17 June 2016, http://dx.doi.org/10.2514/6.2016-4176.

Wang, C.H. John; Dan Zhao, Jörg Schlüter, Frank Holzäpfel, Anton Stephan: LES study on the shape effect of ground obstacles on wake vortex dissipation, Aerospace Science and Technology, Volume 63, April 2017, Pages 245–258, http://dx.doi.org/10.1016/j.ast.2016.12.032.

Echos in Media

allewetter: Wirbelwarner sollen fliegen sicherer machen, Hessischer Rundfunk Fernsehen, 08.05.2014, http://www.hr-online.de/website/fernsehen/sendungen/index.jsp?rubrik=2254.

Braunschweiger Zeitung Forschungsbeilage, Braunschweiger Zeitung,13.09.2016.

Cockpit der Zukunft, Arte Xenius, 09.10.2015.

Deutsche Experten erforschen Wirbelschleppen, fluege.de, 22.04.2014, http://news.fluege.de/a-bis-z/deutsche-experten-erforschen-wirbelschleppen/64932.html.

Developing a Wake Turbulence Warning System, flightradar24 blog, 22.12.2016, https://blog.flightradar24.com/blog/developing-a-wake-turbulence-warning-system/.

DLR entwickelt Wirbelschleppen-Warnsystem, Luft- und Raumfahrt, Juli-Aug 14.

DLR-Forscher testen Wirbelschleppen-Warnsystem, airliners.de, 17.04.2014, http://www.airliners.de/dlr-forscher-testen-wirbelschleppen-warnsystem/32200.

DLR's effort to create a wake turbulence warning system, twitter flightradar24, 22.12.2016.

DLR testet Wirbelschleppenwarnsystem bei Flugversuchen, airportzentrale.de, 14.04.2014, http://www.airportzentrale.de/dlr-testet-wirbelschleppenwarnsystem-bei-flugversuchen/32354/.

Flugsicherheit verbessern - Künstliche Hurrikane in der Luft vorhersagen, ingenieur.de, 15.04.2014, http://www.ingenieur.de/Branchen/Luft-Raumfahrt/Kuenstliche-Hurrikane-in-Luft-vorhersagen.

Gefährliche Wirbel, AERO International, 07.04.2014, http://www.aerointernational.de/.

Gefährliche Wirbelschleppen (Sendung Zeitfragen, ca. 5 min Beitrag), DeutschlandRadio Kultur, 10.07.2014, http://www.deutschlandradiokultur.de/luftfahrt-gefaehrliche-wirbelschleppen.976.de.html?dram:article_id=291405.

Flugversuche zu einem Wirbelschleppenassistenzsystem, DLR facebook, 23.12.2016.

Новая система предупредит пилота о вихревых следах vpk.name, 21.05.2014, http://vpk.name/news/110652_novaya_sistema_predupredit_pilota_o_vihrevyih_sledah.html

ILA Sonderausgabe Aviation Week, 20.05.2014.

Luftfahrt DLR-Forscher entwickeln System, das vor Wirbelschleppen warnt, Deutschlandfunk, 17.06.2014, http://www.deutschlandfunk.de/meldung-forschung-aktuell.678.de.html?drn:news_id=370974.

Luftsicherheit: Wirbelwarner soll Fliegen sicherer machen, Spiegel online, 12.04.2014, http://www.spiegel.de/wissenschaft/technik/wirbelschleppen-dlr-testet-warnsystem-fuer-flugzeuge-a-963876.html.

Neues System bannt gefährliche Wirbelschleppen, Die Welt, 18.06.2014, http://www.welt.de/129199357.

Neues Warnsystem soll Flugzeuge schützen, N24.de, 18.06.2014 .

Schlaglöcher in der Luft, Süddeutsche Zeitung, 14.05.2014.

Warnung für Flugzeuge - Software erkennt gefährliche Luftwirbel, Deutschlandfunk, 24.04.2014, http://www.deutschlandfunk.de/warnung-fuer-flugzeuge-software-erkennt-gefaehrliche.676.de.html?dram:article_id=283615.

Wibbly-wobbly-Wirbelschleppe, Subway, Dez 15.

Wirbelschleppen: DLR testet Warnsystem bei Flugversuchen, FLUG REVUE, 14.04.2014, http://www.flugrevue.de/flugzeugbau/systeme/wirbelschleppen-dlr-testet-warnsystem-bei-flugversuchen/562052.

Wirbelschleppen - Die unsichtbare Gefahr, WDR 5 - Leonardo 30.05.2014, http://www.wdr5.de/sendungen/leonardo/luftwirbelwarnsystem100.html.

Wirbelschleppenforschung, MDR Umschau, 11.11.2014.

Wirbelschleppen, WDR 5 – Leonardo, 12.02.2015.

Wissenschaftler forschen weiter an Wirbelschleppenwarnsystem, airliners.de, 10.01.2017, http://www.airliners.de/wissenschaftler-wirbelschleppenwarnsystem/40463.

Wirbelschleppen - Gefährliche Schönheit, Flugrevue, 06.03.2017 .

Wirbelschleppen bringen kleine Flugzeuge in Gefahr, Saarbrückener Zeitung, 19.04.2017.

ISSN 1434-8454

ISRN DLR-FB—2019-16